نقابة المهندسين الأردنيين
Jordan Engineers Association
شعبة الهندسة الميكانيكية
Mechanical Engineering Division

The 10th Jordanian International Mechanical Engineering Conference (JIMEC 10)

Conference Proceeding

The 10th Jordanian International Mechanical Engineering Conference (JIMEC 10)

October 8-9, 2024
Le Royal Hotel, Amman - Jordan

Table of Contents

The influence of Adding Nanomaterials on Impact Strength of Epoxy Reinforced by E-Glass Chopped Fibers

Ali Alrufaie [1],* and Ali Alithari [2]

[1] Department of Mechanical Engineering, Faculty of Engineering, University of Kufa, Iraq;
[2] Department of Mechanical Engineering, Faculty of Engineering, University of Kufa, Iraq;
* *Corresponding authors: alih.alrufaye@student.uokufa.edu.iq; alis.alathari@uokufa.edu.iq; Mobile: 9647816050479; 9647801142958.*

Abstract: Due to their high mechanical properties such as, light weight, high strength, relatively low cost, composite materials have attracted the interest of researchers to develop and improve new materials with cheaper cost to get better performance than the known alloys and individual materials. The effect of adding different nanomaterials with different weight percentage on the mechanical properties of chopped E-glass fibers reinforced epoxy composite has been studied. Mechanical properties, specifically (impact strength) are studied by the change in the nanomaterial content to study the behavior of the composite material when it is subjected an impact load. Three different weight fractions (0.5, 0.75, and 1wt.%) for the nanomaterials at 8wt.% of E-glass chopped fibers are studied in this research. Three types of nanomaterials were investigated (MWCNTs, GNP, and mixture of MWCNTs with GNP). Charpy impact test were done to the samples and results revealed that adding nanomaterials to the composite gives a significant enhancement for the impact strength. The best result achieved when adding a mixture of 0.5wt% MWCNTs and 0.5wt% of GNP that gave an enhancement of 407% compared to neat epoxy sample and a 244.7% compared to epoxy with 8wt.% chopped fibers.

Keywords: Epoxy; Composite; Chopped Fibers; Impact Strength; MWCNTs; GNP.

1. Introduction

Composite materials are formed by combining of two or more materials to create new materials with improved properties, typically including higher stiffness, reduced weight, and increased strength. These materials consist of two distinct phases: the matrix phase, which typically acts as the continuous phase, and the dispersion phase, which acts as the reinforcement phase[1]. Epoxy resin, a thermoset polymer, is commonly used as a matrix in composite materials. Epoxy resin, known for its adhesive properties, is used for bonding objects and surface coatings. It is widely available and finds applications in various industries, including the automotive and aerospace sectors[2,3]. E-glass fibers, in various forms such as long fibers and chopped fibers, are commonly used as reinforcing materials with epoxy. These fibers are valued for their lightweight nature, cost-effectiveness, and exceptional properties, making them a popular choice among researchers[4]. In addition to conventional fiber reinforcements, other materials such as graphene nanosheets (GNPs) and multi-walled carbon nanotubes (MWCNTs) can also be used to enhance the mechanical properties of composites. Graphene, known to be the thinnest material at just one atom thick, is among the innovative nanomaterials that researchers are exploring to improve composite performance[5]. GNPs defined as short stacks of graphite layers that have recently been developed [6]. It exhibits greater strength than steel and is known for its excellent thermal and electrical conductivity, among other notable properties[5]. MWCNTs, another form of carbon nanomaterials, have a hollow, cylindrical structure. MWCNTs are known for their exceptional mechanical and physical properties, and are often proposed to enhance the interface between fibers and matrix in composite materials[5,7].

Investigating the mechanical properties of composite materials reinforced with chopped fibers has garnered considerable interest among researchers:

N. Ozsoy et al.[8], studied the influence of reinforcing epoxy resin with chopped carbon fibers on various mechanical properties including the impact strength. Different weight fractions of fibers (6%, 8%, and 10% by weight) were utilized. The results revealed that the addition of chopped fibers to the epoxy resin led to increase the impact strength significantly, reaching a maximum enhancement of 430%, with the incorporation of 8% by weight of fibers. Subsequently, the improvement ratio

decreased as the fiber content increased, attributed to the epoxy's inability to effectively accommodate higher fiber loads. P. C. Jena [9], investigated the mechanical properties of polyester resin composite reinforced by short natural fibers (Bamboo fibers). Two different weight fractions (10, and 15 wt.%) for fiber content were examined. The results indicate that the impact strength increased by increasing the fibers content. S. Turaka et al. (2021). [10], investigated the effects of adding nanomaterials (MWCNTs and graphene Nano powder) to epoxy composites reinforced with E-glass fibers on the mechanical properties. They tested two types of fibers: unidirectional and woven types with different orientations, along with three ratios of the nanomaterials (0.1, 0.2, 0.3 wt. %). Two types of impact tests, Izod and Charpy tests, were conducted with two types of specimens (notched and unnotched). The results showed that the addition of a mixing combination of graphene with the MWCNTs at 0.2wt.% yielded the best impact strength (notched type), with improvements of 927.7%.
The present work aims to investigate experimentally the effect of adding different types of Nanomaterials, with varying weight fractions, on impact strength of composite materials reinforced with chopped fibers. It focuses on detection the optimal mixing ratio for get better enhancing for impact strength.

2. Materials and Methods

2.1 Materials Used

Epoxy resin Renfloor HT 2000 (2:1) is used as the matrix of the composite (shown in figure 1a). The reinforcement materials are: Chopped E-glass fibers with different lengths of (3, 6 mm) with density of 2.56 g/cm3, (shown in figure 1b). Two types of Nano materials used; Graphene Platelet Nano powder with an average particle diameter of 15 µm, a thickness of 6-8nm and a specific area of 120-150 m^2/g and Multi-Walled Carbon Nanotubes with length of 10-30 µm, outer diameter of <10 nm and a specific surface area of >110m^2/g. The properties of the utilized materials are tabulated in table 1.

(**a**) (**b**)

Figure 1. Utilized materials of the composite

Table 1. Utilized materials properties according to suppliers data sheet

Type	Density (kg/m^3)	Tensile strength (MPa)	Modulus of elasticity (GPa)
Epoxy	1050	27	2.8
CGF	2600	3400	77
MWCNTs	2100	140,000	1000
Graphene	2300	130,000	1000

2.2 Method of fabrication

A glass mold (300 x 200 mm) and 3mm spacers as shown in figure 2 used for preparing the sample with following steps:
a) Prepare the required quantity of the nanomaterial and the chopped fibers using a sensitive scale.
b) Mechanical mixing the epoxy/Nano mixture for around 15 minutes.
c) A sonication process was performed for 30 minutes to accomplish the fine particle [16].
d) After the sonication process the hardener added to the mixture and mixing them by magnetic stirrer for around 3min minutes.

e) The mixture poured to the mold gently to prevent bubbles formation and, then adding the chopped glass fiber with weigh ratio of 8%.
f) The curing process for 24 hours and then putting the samples in an electrical oven for an 2hour at around 70C^{o}for post-curing process [17]. After the sample is ready CNC laser cutting machine were used to cut the test samples [18] to get the accurate dimensions according to ASTM standard.

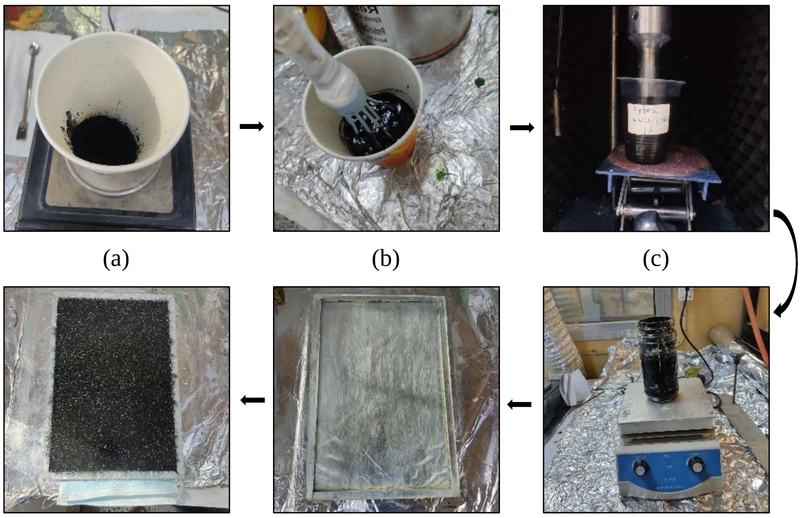

(f) (e) (d)

Figure 2. Fabrication steps

2.3 Mechanical Characterizations

The Charpy impact test was performed to determine the absorbed energy, and consequently, the impact strength was calculated. The Charpy impact tester that consists of a pendulum mechanism, with a hammer weighing 2.05 kilograms attached to it, shown in (figure 3). The maximum capacity of the machine is 25 Nm with an impact velocity of 3.8 m/s. The specimen dimensions were (80x10x3) mm^3 according to ISO 180. Three specimens were tested for each sample.[19]

(**a**) (**b**) (**c**)

Figure 3. (a) Impact test machine (b) Impact specimen under test (c) specimens before and after test.

3. Results and Discussion

The results of the impact test of epoxy/MWCNTs are listed in table 2 and shown in figure 4a. The results indicate that at lower weight fractions, MWCNTs might start to agglomerate within the epoxy matrix. However, increasing the wt.% of MWCNTs improved the toughness of composite up to 14.5%. The precise control of MWCNT concentration is essential due to nanomaterials' unique characteristics. while increasing MWCNT content beyond 0.75% led to a diminishing improvement in toughness. This decrease in effectiveness could stem from uneven distribution or agglomeration of MWCNTs within the epoxy. Furthermore, MWCNTs activate a crack bridging mechanism inherent to epoxy/MWCNTs nanocomposites, serving as barriers that impede crack propagation. Consequently, the composite absorbs more impact energy, resulting in a remarkable enhancement of its impact strength. same behavior was obtained by S. Singh et al. [20]. Adding CGF on the other hand, which has high modulus and strength, can restrict the movement of the surrounding epoxy matrix. Additionally, the tips of CGF act as points where stress concentrates and can initiate fractures. This results in a reduction in ductility and ultimate elongation of the composite but, conversely, enhances its modulus and strength. The impact strength of short fiber composites is affected by several factors, such as the plastic deformation and fracture of the fiber/matrix interface, along with fiber pull out or debonding.

Table 2. Impact test results.

Sample	**I.E** (N.m)	**I.S** (J/m^2)	**I.S Imp.(%)**
A/E	0.163	5433.3	0
B/EF	0.24	8000	47.2
C/E 0.5CNT	0.15	5000	-7.9
D/E 0.75CNT	0.1867	6223.3	14.5
E/E 1CNT	0.17	5666.7	4.3
F/E 0.5GNP	0.17	5666.7	4.3
G/E 0.75GNP	0.18	6000	10.4
H/E 1GNP	0.19	6333.3	16.6
I/EF 0.5CNT	0.25	8048.3	48.1
J/EF 0.75CNT	0.26	9228	69.8
K/EF 1CNT	0.367	11439.5	110.5
L/EF 0.5GNP	0.27	9000	65.6
M/EF 0.75GNP	0.26	8666.7	59.5
N/EF 1GNP	0.25	8333.3	53.4
O/E 0.5 hybrid	0.2	6666.7	22.7
P/E 0.75 hybrid	0.29	4666.7	-14.1
Q/E 1 hybrid	0.35	11666.7	114.7
R//EF 0.5 hybrid	0.27	9827.1	80.9
S/EF 0.75 hybrid	0.28	9677.4	78.1
T/EF 1 hybrid	0.81	27574.5	407.5

I.E: Impact energy, I.S: Impact strength , (%Imp.): improvement ratio

The results of the impact test of epoxy/GNP are listed in table 2 and shown in figure 4b. The increase in impact strength could be attributed to the formation of micro-plastic deformation around the GNPs. Similarly, a comparable trend in increased impact strength, resulting from enhanced interfacial bonding between functionalized graphene nanoplatelets and the epoxy matrix. similar behavior was noted in by H. Shivakumar et al. [21]. The results indicate that the sample with 0.5wt.% of GNP exhibits the highest values in impact strength a maximum increasement of 65.6% compared to neat sample and a 12.5% compared to CGF sample. While a gradual decrease was found in impact strength when compared with 0.5wt.% GNP sample, the impact strength values of other GNP nanocomposites until 1wt.% remain higher than those of the CGF sample. Enhanced impact strength indicates stronger bonding between the matrix and fiber. Adding GNP improves adhesion at the interfaces between the filler, fiber, and matrix. However, this improvement diminishes gradually because of the uneven dispersion of GNP. Nonetheless, the interlocking mechanism between the epoxy and nanofiller remains crucial for enhancing fiber/epoxy composites. The results of the impact test of epoxy/hybrid nano materials are listed in table 2 and shown in figure 4c. The addition of hybrid nano materials of both MWCNTs and GNP resulted in a significant increase in impact strength representing an improvement of approximately 114.7% when adding (0.5wt.% MWCNTs + 0.5wt.% GNP) compared to the neat epoxy. The experimental results suggest that the suppression of crack growth in composite laminates is mainly attributed to the deflection of cracks by GNPs. As cracks begin to spread, GNPs interact to deflect them within the laminate layers, effectively impeding their advancement. Additionally, GNP primarily limits larger cracks formation, while MWCNTs hinder the dispersion of smaller ones. Therefore, the combined effect of MWCNTs and GNP reinforces the interlaminar energy of the fiber composite laminate. The best result reached in this study was at 1wt.% of mixed MWCNTs and GNP with CGF. This represents a substantial enhancement of approximately 244.7% compared to CGF sample, and an overall enhancement of 407.5% compared to neat epoxy. A combination of MWCNTs/GNPs hybrids increase the grip between the fibers and the matrix. When MWCNTs are mixed with GNP along with epoxy resins, the MWCNTs act like bridges across GNP layers and resin cracks.

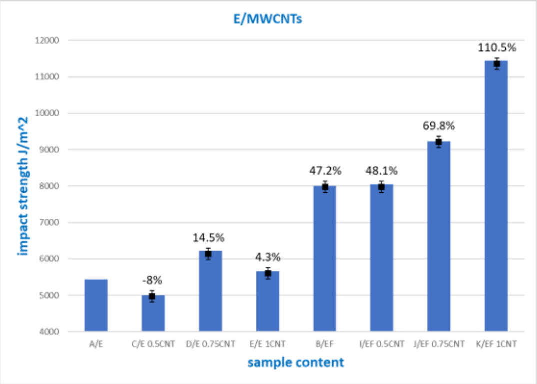

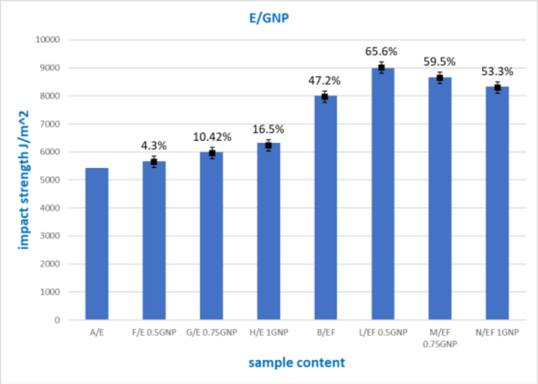

(**a**) (**b**)

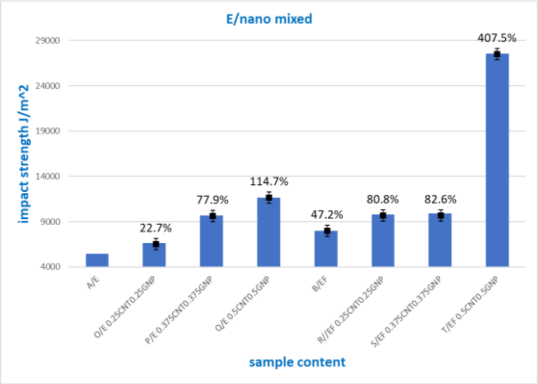

(**c**)

Figure 4. Results of ***Impact*** strength for: (a) Ep/MWCNTs & EP/CGF/ MWCNTs; (b) Ep/GNP & EP/CGF/ GNP (c); Ep/mixed hybrid nano & EP/CGF/ mixed hybrid nano.

4. Conclusions

In this study, hybrid composites were utilized to investigate their effects on the impact strength. Where, epoxy resin was used as the matrix, chopped E-glass fibers as the microscopic reinforcements, and GNP and MWCNTs as the nanofillers. The comparing between the results was done for different samples, that including neat epoxy, ECGF, E/GNP, E/MWCNTs/, E/GNP/MWCNTs with three different weight fractions and also with and without the addition of a fixed CGF weight fraction which was 8wt% to obtain an optimum mixing ratio. The addition of small amount of MWCNTs had no effect on impact strength, while higher ratio will improve the impact strength due to super properties of MWCNTs especially in shock absorbent. On the other hand, adding CGF to E/MWCNTs enhanced the impact strength with the incensement of the Nano filler. Adding GNP to epoxy composite led to increase the impact strength linearly with content of GNP, while, the addition of CGF for the mixture led to a descending enhancement of impact strength with the incensement GNP compared to neat epoxy sample. The optimum mixing ratio was found when adding a mixture of (0.5GNP + 0.5MWCNTs) that gave an approximate enhancement of 115%. While, adding CGF to the mixture increased the ratio up to 407%. The addition of MWCNTs alone to epoxy didn't give the expected enhancement, while adding GNP to epoxy gives better enhancement to the impact strength and adding CGF produce negative effect.

Funding: This has no funding.

Acknowledgments: The authors acknowledge the help presented by the staff of the Nanotechnology and Advanced Materials Research Unit at Kufa University and the polymer labs. at Babylon University.

References

1. N. Ozsoy, M. Ozsoy, and A. Mimaroglu, Mechanical and tribological behaviour of chopped E-glass fiber-reinforced epoxy composite materials, in *Acta Physica Polonica A*, Polish Academy of Sciences, Sep. 2017, pp. 852–856. doi: 10.12693/APhysPolA.132.852.
2. A. Nassar and E. Nassar, Thermo and Mechanical Properties of Fine Silicon Carbide /Chopped Carbon Fiber Reinforced Epoxy Composites, *Univers. J. Mech. Eng.*, vol. 2, no. 9, pp. 287–292, Dec. 2014, doi: 10.13189/ujme.2014.020903.
3. Y. N. Baghdadi *et al.*, Thermal and mechanical properties of epoxy resin reinforced with modified iron oxide nanoparticles, *J. Appl. Polym. Sci.*, vol. 138, no. 23, Jun. 2021, doi: 10.1002/app.50533.
4. A. Singh and S. C. Jayswal, Mechanical Characterization of TiO 2 nanoparticles based on Glass Fiber Reinforced Polymer Composite, *IOP Conf. Ser. Mater. Sci. Eng.*, vol. 1206, no. 1, p. 012006, Nov. 2021, doi: 10.1088/1757-899x/1206/1/012006.
5. P. P. Prasanthi *et al.*, Mechanical properties of carbon fiber reinforced with carbon nanotubes and graphene filled epoxy composites: experimental and numerical investigations, *Mater. Res. Express*, vol. 10, no. 2, Feb. 2023, doi: 10.1088/2053-1591/acaef5.
6. D. R. Klimek-McDonald, MECHANICAL PROPERTIES OF GRAPHENE NANOPLATELET/EPOXY COMPOSITES, Michigan Technological University, Houghton, Michigan, 2015. doi: 10.37099/mtu.dc.etds/1014.
7. M. M. Shokrieh, A. Saeedi, and M. Chitsazzadeh, Evaluating the effects of multi-walled carbon nanotubes on the mechanical properties of chopped strand mat/polyester composites, *Mater. Des.*, vol. 56, pp. 274–279, 2014, doi: 10.1016/j.matdes.2013.11.017.
8. N. Ozsoy, M. Ozsoy, and A. Mimaroglu, “Mechanical properties of chopped carbon fiber reinforced epoxy composites, in *Acta Physica Polonica A*, Polish Academy of Sciences, Jul. 2016, pp. 297–299. doi: 10.12693/APhysPolA.130.297.
9. P. C. Jena, Free vibration analysis of short bamboo fiber based polymer composite beam structure, in *Materials Today: Proceedings*, Elsevier Ltd, 2018, pp. 5870–5875. doi: 10.1016/j.matpr.2017.12.185.
10. S. Turaka, K. V. K. Reddy, R. K. Sahu, and J. K. Katiyar, Mechanical properties of MWCNTs and graphene nanoparticles modified glass fibre-reinforced polymer nanocomposite, *Bull. Mater. Sci.*, vol. 44, no. 3, 2021, doi: 10.1007/s12034-021-02444-z.
11. I. M. H. Zwain and A. S. Alithari, Improving the fatigue life of composite by using multiwall carbon nanotubes, *Open Eng.*, vol. 13, no. 1, Oct. 2023, doi: 10.1515/eng-2022-0490.
12. L. A. Madi and A. S. Alithari, Improvement of tensile and flexural properties of fiber pre-stressing composite by using nano graphene, in *Materials Science Forum*, Trans Tech Publ, 2022, pp. 117–127.
13. https://www.ssnano.com/inc/sdetail/3368.
14. https://www.cheaptubes.com/product/industrial-grade-multi-walled-carbon-nanotubes-20-40nm/.
15. A. Ari, A. Bayram, M. Karahan, and S. Karagöz, Comparison of the mechanical properties of chopped glass, carbon, and aramid fiber reinforced polypropylene, *Polym. Polym. Compos.*, vol. 30, May 2022, doi: 10.1177/09673911221098570.
16. A. Mohanty and V. K. Srivastava, Effect of alumina nanoparticles on the enhancement of impact and flexural properties of the short glass/carbon fiber reinforced epoxy based composites, *Fibers Polym.*, vol. 16, no. 1, pp. 188–195, Jan. 2015, doi: 10.1007/s12221-015-0188-5.
17. F. Aghadavoudi, H. Golestanian, and K. A. Zarasvand, Elastic behaviour of hybrid cross-linked epoxy-based nanocomposite reinforced with GNP and CNT: experimental and multiscale modelling, *Polym. Bull.*, vol. 76, no. 8, pp. 4275–4294, Aug. 2019, doi: 10.1007/s00289-018-2602-9.
18. J. Guo, Z. Wang, L. Tong, and W. Liang, Effects of short carbon fibres and nanoparticles on mechanical, thermal and shape memory properties of SMP hybrid nanocomposites Affiliation: Effects of short carbon fibres and nanoparticles on mechanical, thermal and shape memory properties of SMP hyb, 2015.
19. Plastics-Determination of Izod impact strength Plastiques-Détermination de la résistance au choc Izod, 2019. [Online]. Available: www.iso.org
20. S. Singh, V. K. Srivastava, and R. Prakash, Influences of carbon nanofillers on mechanical performance of epoxy resin polymer, *Appl. Nanosci.*, vol. 5, no. 3, pp. 305–313, Mar. 2015, doi: 10.1007/s13204-014-0319-0.
21. H. Shivakumar, N. M. Renukappa, K. N. Shivakumar, and B. Suresha, The Reinforcing Effect of Graphene on the Mechanical Properties of Carbon-Epoxy Composites, *Open J. Compos. Mater.*, vol. 10, no. 02, pp. 27–44, 2020, doi: 10.4236/ojcm.2020.102003.

Effects of Adding Nanofillers on the Tensile Properties of Epoxy and Hybrid Composites

Ali Alrufaie [1,*] and Ali Alithari [2]

[1] Department of Mechanical Engineering, Faculty of Engineering, University of Kufa, Iraq;
[2] Department of Mechanical Engineering, Faculty of Engineering, University of Kufa, Iraq;
* *Corresponding authors: alih.alrufaye@student.uokufa.edu.iq; alis.alathari@uokufa.edu.iq;*
Mobile :9647816050479; 9647801142958.

Abstract: Researchers are interested in developing and improving new materials with high mechanical properties, such as light weight, high strength, and cost-effectiveness. Composite materials have emerged as a promising solution, offering better performance than traditional alloys and individual materials. This study focuses on studying the effect of adding different nanomaterials with varying weight ratios on the mechanical properties of epoxy composites reinforced with chopped E-glass fibers. Specifically, the study examines changes in tensile and flexural stiffness based on nanomaterial content. Three different weight fractions (0.5, 0.75, and 1 wt.%) of nanomaterials were added to the composites containing 8 wt.% chopped glass fibers. Three types of nanomaterials were studied: MWCNTs, GNPs, and mixtures of MWCNTs with GNPs. Tensile and flexural tests were done to the samples and the results revealed that adding nanomaterials to the composite gives a significant enhancement for the mechanical properties. The results revealed that the optimal tensile strength achieved by combining 0.25GNP + 0.25MWCNTs, resulting in 51.4% reinforcement. In addition, the most significant improvement in flexural stiffness was observed by blending the epoxy with 8 wt.% CGF + 1 wt.% GNP, resulting in an overall increase of 176.4%. also, a numerical investigation was done using the software program (ANSYS APDL 17.2) to model the flexural samples and the results were in good agreement with the experimental results.

Keywords: Epoxy; Composite; Chopped Fibers; Tensile Properties; MWCNTs; GNP.

1. Introduction

Composite materials are a combination of materials used to enhance the properties such as stiffness, strength, and low weight, and consist of two phases (matrix phase and a reinforcing phase) [1]. Epoxy resin, known for its adhesive properties, is widely used as a matrix in industries such as automotive and aerospace [2,3]. E-glass fibers, available in long and cut forms, are commonly used as reinforcements with epoxy due to their lightweight, low cost, and significant properties [4]. In addition, materials such as graphene nanoplatelets (GNP) and multi-walled carbon nanotubes (MWCNTs) further enhance the properties of composites. Graphene nanoplatelets, which are short stacks of graphite layers, provide superior strength and excellent thermal and electrical conductivity [5,6]. Multi-walled carbon nanotubes, with their hollow cylindrical structure, enhance the mechanical and physical properties and improve the fiber-matrix interface [5,7]. N. Ozsoy et al. [8], investigated the effect of incorporating chopped carbon fibers into epoxy resin on various mechanical properties, including tensile and flexural strength. Different weight percentages of fibers were tested (6, 8, and 10 wt.%). The results indicated a decrease in tensile strength with the addition of chopped fibers to the epoxy resin. Conversely, there was a significant increase in flexural strength, peaking at 22% reinforcement with the inclusion of 8% by fiber weight. However, the reinforcement ratio diminished as the fiber content rose, as the epoxy struggled to effectively support higher fiber loads. S. Rahmanian et al. (2014) [9], used low weight fractions of micro and nanofillers on epoxy composite. They used short carbon fibers (SCF) with weight fractions (1, and 3wt.%) as the micro size reinforcement and at (0.1, 0.2, 0.3, 0.4, and 0.5wt.%) Carbon nanotubes have also been grown on fibers through the chemical vapor deposition (CVD) method to produce short carbon nanotube-grown fibers (CSCF). They tested the tensile strength. The results revealed that the addition of both SCF or CSCF with low weight fractions gives a significant enhancement for the tensile strength. The best mixing ratio for the tensile strength was 0.3wt CNT 1wt.% CSCF. P. N. Wang et al. [10], investigated the effect of adding hybrid nanofillers (GNP + MWCNTs) with three weight fractions (0.5, 1, and 1.5wt.%) on epoxy/carbon fiber composite. They examined the flexural strength, but before testing they tested different mixing ratios on tensile and flexural strength to obtain an optimum ratio. The results reveal that the best mixing ratio for the tensile test was 5:5 and the best result obtained for the flexural were 1:9 CNT/GNP. They finally took 1:9 as the reference ratio. The addition of hybrid CNT/GNP enhanced the flexural strength up to 17.5% with the incorporating of 1wt.% of nanofillers and then start to decrease with the increasement of nano content.

This research aims to study the effect of different types and weight ratios of nanomaterials experimentally and numerically on the mechanical properties (tensile strength and flexural stiffness) of composite materials reinforced with chopped fibers, and to focus on determining the optimum mixing ratio to achieve the best improvement of these properties.

2. Materials and Methods

2.1 Materials Used

Epoxy resin Renfloor HT 2000 (2:1) is used as the matrix of the composite. The reinforcement materials are: Chopped E-glass fibers (CGF) with different lengths of (3, 6 mm) with density of 2.56 g/cm^3. Two types of Nano materials used; Graphene Platelet Nano powder with an average particle diameter of 15 µm, a thickness of 6-8nm and a specific surface area of 120-150 m^2/g and Multi-Walled Carbon Nanotubes with length of 10-30 µm, outer diameter of <10 nm and a specific surface area of >110m^2/g. The properties of the utilized materials are tabulated in table 1.

Table 1. Utilized materials properties according to supplier's data sheet

Type	Density (kg/m^3)	Tensile strength (MPa)	Modulus of elasticity (GPa)
Epoxy	1050	27	2.8
CGF	2600	3400	77
MWCNTs	2100	140,000	1000
Graphene	2300	130,000	1000

2.2 Method of fabrication

A glass mold (300 x 200 mm) and 3mm spacers as shown in figure 1 used for preparing the samples with following steps:

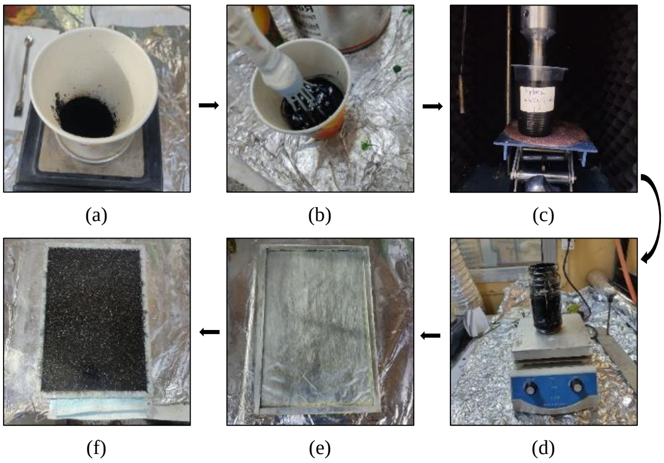

Figure 1. Steps of samples preparation

a) Prepare the required quantity of the nanomaterial and the chopped fibers using a sensitive scale.
b) Mechanical mixing the epoxy/Nano mixture for around 15 minutes.
c) A sonication process was performed for 30 minutes to accomplish the fine particle [11].
d) After the sonication process the hardener added to the mixture and mixing them by magnetic stirrer for around 3min minutes.
e) The mixture poured to the mold gently to prevent bubbles formation and, then adding the chopped glass fiber with weigh ratio of 8%.

f) The curing process for 24 hours and then putting the samples in an electrical oven for an 2hour at around 70C^{o}for post-curing process [12]. After the sample is ready CNC laser cutting machine were used to cut the test samples [13] to get the accurate dimensions according to ASTM standard.

2.3 Mechanical Characterizations

The mechanical properties (tensile, and flexural strength) were determined in this work. For the tensile test, the specimen dimensions, as specified in ASTM D638 [14], were utilized. A Universal testing machine (UTM), located at the College of mechanical Engineering, university of technology is used, and the maximum capacity of the machine is 50 kN. The test was conducted at a crosshead speed of 2 mm/minute. Three specimens were tested for each sample. The objective of the test was to determine the mechanical properties, including the Young's modulus, yield stress, and ultimate tensile strength. For the flexural test, Three-point bending test were done to determine the mechanical properties (stiffness, bending strength, and the deflection load). The test performed according to ASTM D790 [15]. A Universal testing machine (UTM), located at the College of materials Engineering, university of Babylon is used, and the maximum capacity of the machine is 5 KN. The crosshead speed were 2 mm/minutes and the depth-to-span ratio was 16:1. Three specimens were tested for each sample.

2.4 Numerical models

To validate the experimental results a numerical model using software program (ANSYS APDL 17.2) was done for this work. The model used the element solid Tetrahedral 187 node [16]. 20 different model were done for the same samples of the experimental work. Using the experimental young’s modulus and density values which are required in the software.

3. Results and Discussion

3.1 Tensile results

The tensile properties of epoxy/MWCNTs results are shown in figure 2a. As we can see, at lower weight fractions of MWCNTs the tensile strength gets a superior enhancement. While, at higher MWCNTs content the tensile strength decreased because the dispersion of the nano become more difficult due to agglomeration. Similar results achieved by A. Navidfar and L. Trabzon [17]. On the other hand, adding fibers to the epoxy/CNT composite reduced the tensile strength with compared to neat epoxy/CNT composite. This might be explained because the fibers were chopped and the matrix were not able to hold them together with the nano material as reported by N. Ozsoy et al [8]. The tensile properties of epoxy/GNP results are shown in figure 2b. It can be seen that the addition of GNP to the epoxy composite increased the tensile properties with the incorporation of 1wt.% of GNP. This indicates that the incorporation of GNP into the epoxy matrix led to strong interactions between the GNP and the matrix, resulting in restricted the movement of the epoxy composite. Same results obtained by H. Shivakumar et al [18]. It can also be seen from figure 2b. that the incorporation of CGF to the epoxy/GNP composite enhanced the tensile strength tensile modulus. The incorporation of GNP reduces the mobilty of the epoxy fiber interface, resulting in increased structural rigidity. While nanofills can be widely distributed with low weight fractions, they establish strong contacts with the matrix, which enhances the transfer of pressure to The Matrix. From the prievous results, we can confirm that GNP interact with the chopped E-glass fibers better than MWCNTs do. The tensile properties of epoxy/mixed hybrid nano materials results are shown in figure 2c. It can be seen that at low weight fraction the tensile strength enhanced significantly up to 51.4% with the addition of 0.5wt.% of hybrid (GNP + MWCNTs). Same result achieved by A. Navidfar and L. Trabzon [17]. The enhanced contact area between the hybrid nanofillers and the matrix facilitates load transfer during tensile testing. MWCNTs can act as elongated tentacles within the 3D hybrid structure, intertwining with polymer matrix chains to promote the interaction between MWCNTs, GNP, and epoxy Matrix. With further increase of nano wt.% the tensile strength start to decrease because of agglomeration of the MWCNTs with higher content as we saw in the results of neat epoxy/MWCNTs samples. On the other hand, adding chopped fibers were not really effective with compared to neat epoxy/hybrid nano fillers. And, the reason of that the matrix could not hold the hybrid mixture of nano materials with the chopped fibers. where the fibers weight fraction and orentation are more effective factors on the nature of tensile strength than the nano fillers.

3.2 Flexural results

The flexural properties of epoxy/MWCNTs results are shown in figure 2d. As we can see, at lower weight fractions of MWCNTs added to epoxy composite it shows a significant enhancement on the flexural properties (flexural stiffness and flexural modulus). The high aspect ratio of carbon nanotubes is a critical factor in enhancing the flexural properties of MWCNTs polymer nanocomposites. Further increase in MWCNTs content led to decrease the flexural properties. The reason of that is, in high-fractions, MWCNTs tend to agglomerate and tangle with each other. On the other hand, adding chopped E-glass fibers also showed a significant effect on the flexural strength with the addition of 0.5wt.% MWCNTs. With further increase the properties start to decrease. The decrease in the flexural properties of the epoxy/CGF/MWCNTs composite exceeding 0.5wt.% of MWCNTs is primarily due to the agglomeration and uneven dispersion of MWCNTs inside the laminates. But as we can see adding chopped fibers were less effective than neat epoxy/MWCNTs composites. The flexural properties of epoxy/GNP results are shown in figure 2e. as observed from the results, the flexural properties enhanced with the addition of GNP until 1wt.%. The enhancement of flexural properties is associated with improved dispersion and exfoliation of GNPs within the Epoxy matrix, resulting in increased stress transfer efficiency and a more effective strengthening effect. Same behavior achieved by H. Shivakumar et al. [18]. On the other hand, the addition of CGF enhance the flexural properties notably up to 176.4% and 270.1% for flexural stiffness and flexural modulus, respectively. Which is the highest enhancement achieved in this work. GNP nanoparticles restrict the mobility of fibers over the epoxy matrix and limit the epoxy chain movements. Same behavior achieved by A. Namdev [19]. The flexural properties of epoxy/mixed hybrid nano materials results are shown in figure 2f. it was observed that the addition of hybrid nano materials (GNP + MWCNTs) improved the flexural properties. The improvement in properties can be attributed to the formation of a 3D network resulting from the synergistic effect of GNP and MWCNT. The elastic movement of MWCNT prevents aggregation of the GNP interlayers, creating a larger surface area and contact area between the filler and the epoxy resin. Also The entanglement and compatibility between CNTs and GNPs are the main reason to the enhancement of the proerties. Similar behavior obtained by A. Kumar et al. [20]. On the other hand, the addition of CGF increased the flexural properties with the addition of 0.5wt.% of hybrid mixed nano materials. With further increase the flexural properties start to decrease. Same trend were found as for the tensile properties.

Table 2. tensile and flexural results

Sample	UTS(%Imp)	TM(%Imp)	TYS	Exp. def.	N. def.(% Exp/N)	F.Stiff.(%Imp).	FM(%Imp)
A/E	14(0)	2.75 (0)	12.94	1.9	2 (-5.1)	33.2 (0)	2.95 (0)
B/EF	14.2 (1.4)	3.16 (14.9)	13.67	1.3	1.5 (-8.5)	38.2 (15.2)	3.77 (28)
C/E 0.5CNT	20.3 (45)	5.5 (100)	17.1	0.74	0.78 (-5.3)	66.7 (100)	6.76 (129)
D/E 0.75CNT	19.1 (36.4)	5.2 (89.1)	16.79	0.062	0.67 (-7.2)	62.7 (89.1)	7.63 (159)
E/E 1CNT	9.66 (-31)	2.1 (-23.6)	6.9	1.7	1.9 (-12.06)	25.3 (-23.6)	2.73 (-7)
F/E 0.5GNP	14.5 (3.6)	3.8 (38.2)	12.45	0.049	0.05 (-5.3)	45.8 (38.2)	3.76 (27)
G/E 0.75GNP	17.78 (27)	5.03 (82.9)	16.55	0.095	0.098 (-3.6)	60.7 (82.9)	6.02 (104)
H/E 1GNP	17.82 (27)	5.12 (86.2)	15.82	0.092	0.098 (-6.5)	61.8 (86.1)	6.69 (127)
I/EF 0.5CNT	15.4 (10)	3.8 (38.2)	11.7	1.2	1.3 (-7.2)	45.8 (38.2)	5.27 (79)
J/EF 0.75CNT	10.8 (-22.9)	3.3 (20)	9.14	1.2	1.3 (-7.4)	39.8 (20)	3.5 (19.2)
K/EF 1CNT	8.8 (-37.1)	3 (9.1)	5.53	0.0077	0.008 (-6.7)	36.2 (9.13)	2.01 (-32)
L/EF 0.5 GNP	14.9 (6.43)	5.3 (92.7)	11.4	0.093	0.103 (-9.2)	64 (92.8)	6.87 (133)
M/EF 0.75GNP	18 (28.6)	6.5 (136.4)	14.62	0.055	0.06 (-9.85)	78.4 (136)	8.94 (203)
N/EF 1GNP	19.7 (40.7)	7.6 (176.4)	14.82	0.063	0.072 (-12.1)	91.8 (176)	10.9 (270)
O/E 0.5 hybrid	21.2 (51.4)	5.5 (100)	18.26	0.088	0.094 (-6.4)	66.3 (99.9)	8.9 (202)
P/E 0.75 hybrid	19.3 (37.9)	5.9 (114.5)	17.46	0.04	0.04 (-5.5)	71.2 (115)	7.82 (165)
Q/E 1 hybrid	16.3 (16.4)	6.2 (125.5)	13.05	0.075	0.08 (-7.5)	74.8 (125)	7.6 (157)
R//EF 0.5hybrid	15.2 (8.6)	5.1 (85.5)	12.9	0.098	0.107 (-8.3)	61.5 (85.4)	6.6 (124)
S/EF 0.75hybrid	11.9 (-15)	4.8 (74.5)	9.6	0.072	0.076 (-4.5)	57.9 (74.6)	4.1 (39.3)
T/EF 1hybrid	9.1 (-35)	3.5 (27.3)	7.1	0.014	0.016 (-12.3)	42.1 (27)	4.06 (38)

UTS: ultimate tensile strength (MPa); (%Imp): improvement in properties; TM: tensile modulus (GPa); TYS: tensile yield strength (MPa); Exp. def: experimental deflection (mm); N. deff.: numerical deflection (mm); F.Stiff: flexural stiffness (kN/m); FM: flexural modulus(GPa); (% Exp/N): experimental/numerical error %

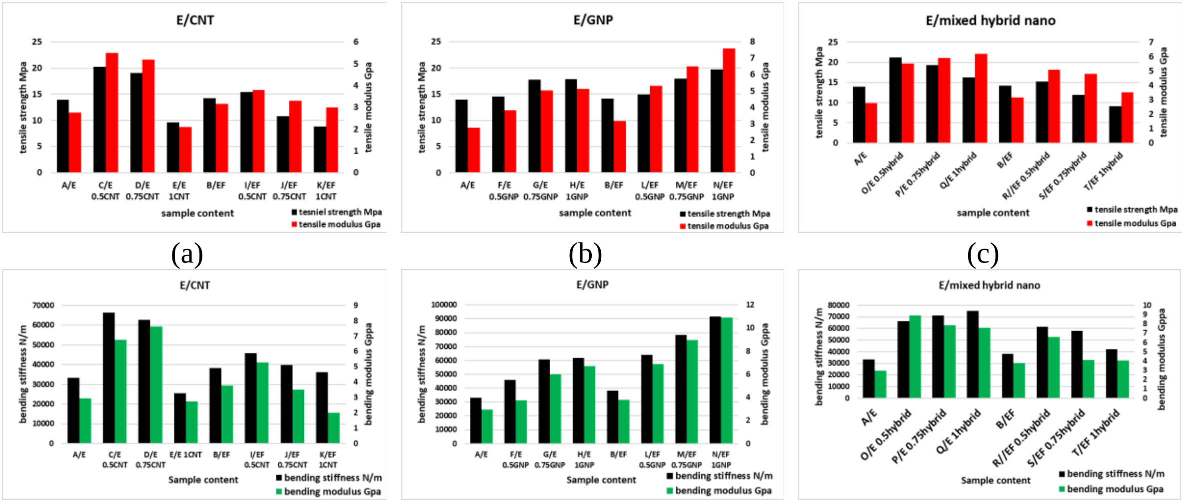

(a) (b) (c)

(d) (e) (f)

Figure 2. Tensile strength and tensile modulus of (a) CNT. (b) GNP. (c) mixed hybrid nano. Flexural stiffness and flexural modulus of (d) CNT. (e) GNP. (f) mixed hybrid nano.

4. Conclusions

This study used hybrid composites to study their effect on mechanical properties, specifically tensile strength and flexural stiffness. The matrix consisted of epoxy resin, while chopped glass fibers served as microscopic reinforcements, and GNPs and MWCNTs were used as nanofillers. Different samples were tested, including neat epoxy, E/GNP, E/MWCNTs, and E/GNP/MWCNTs, each with three different weight fractions. In addition, samples with and without a constant weight fraction of CGF (8wt.%) were evaluated to determine the optimal mixing ratio. The results revealed that the addition of MWCNTs improves the mechanical properties significantly at low weight fractions (0.5wt.%), with and without the addition of CGF. With further increase of MWCNTs content the mechanical properties start to decrease. Both tensile strength and flexural stiffness showed less effectiveness when the CGF were added than the effect of neat epoxy/MWCNTs as well as with epoxy/CGF/mixed hybrid nano materials. The addition of GNP to the epoxy composite was more stable than the addition of MWCNTs. The properties increased with the increasement of GNP wt.%. also, the addition of CGF enhanced the mechanical properties more than neat epoxy/GNP composite. The addition of small amount of MWCNTs got higher properties than GNPs which is consistent with the results of other researchers with the exception of CGF/GNP epoxy composites. The best results achieved in this work for the tensile strength were at mixing 0.25GNP + 0.25MWCNTs with and enhancement up to 51.4%, and the best result achieved for the flexural stiffness was at mixing epoxy with 8wt.% CGF + 1wt.% GNP with a total incensing ratio of 176.4%.

Funding: This research has no funding.

Acknowledgments: The authors acknowledge the help presented by the staff of the Nanotechnology and Advanced Materials Research Unit at Kufa University, the polymer labs at Babylon University, and the Strength of Materials lab at Technology University.

References

1. N. Ozsoy, M. Ozsoy, and A. Mimaroglu, Mechanical and tribological behaviour of chopped E-glass fiber-reinforced epoxy composite materials, in *Acta Physica Polonica A*, Polish Academy of Sciences, Sep. 2017, pp. 852–856. doi: 10.12693/APhysPolA.132.852.
2. A. Nassar and E. Nassar, Thermo and Mechanical Properties of Fine Silicon Carbide /Chopped Carbon Fiber Reinforced Epoxy Composites, *Univers. J. Mech. Eng.*, vol. 2, no. 9, pp. 287–292, Dec. 2014, doi: 10.13189/ujme.2014.020903.
3. Y. N. Baghdadi *et al.*, Thermal and mechanical properties of epoxy resin reinforced with modified iron oxide nanoparticles, *J. Appl. Polym. Sci.*, vol. 138, no. 23, Jun. 2021, doi: 10.1002/app.50533.

4. A. Singh and S. C. Jayswal, Mechanical Characterization of TiO 2 nanoparticles based on Glass Fiber Reinforced Polymer Composite, *IOP Conf. Ser. Mater. Sci. Eng.*, vol. 1206, no. 1, p. 012006, Nov. 2021, doi: 10.1088/1757-899x/1206/1/012006.
5. P. P. Prasanthi *et al.*, Mechanical properties of carbon fiber reinforced with carbon nanotubes and graphene filled epoxy composites: experimental and numerical investigations, *Mater. Res. Express*, vol. 10, no. 2, Feb. 2023, doi: 10.1088/2053-1591/acaef5.
6. D. R. Klimek-McDonald, MECHANICAL PROPERTIES OF GRAPHENE NANOPLATELET/EPOXY COMPOSITES, Michigan Technological University, Houghton, Michigan, 2015. doi: 10.37099/mtu.dc.etds/1014.
7. M. M. Shokrieh, A. Saeedi, and M. Chitsazzadeh, Evaluating the effects of multi-walled carbon nanotubes on the mechanical properties of chopped strand mat/polyester composites, *Mater. Des.*, vol. 56, pp. 274–279, 2014, doi: 10.1016/j.matdes.2013.11.017.
8. N. Ozsoy, M. Ozsoy, and A. Mimaroglu, Mechanical properties of chopped carbon fiber reinforced epoxy composites, in *Acta Physica Polonica A*, Polish Academy of Sciences, Jul. 2016, pp. 297–299. doi: 10.12693/APhysPolA.130.297.
9. S. Rahmanian, A. R. Suraya, M. A. Shazed, R. Zahari, and E. S. Zainudin, Mechanical characterization of epoxy composite with multiscale reinforcements: Carbon nanotubes and short carbon fibers, *Mater. Des.*, vol. 60, pp. 34–40, 2014, doi: 10.1016/j.matdes.2014.03.039.
10. P. N. Wang, T. H. Hsieh, C. L. Chiang, and M. Y. Shen, Synergetic effects of mechanical properties on graphene nanoplatelet and multiwalled carbon nanotube hybrids reinforced epoxy/carbon fiber composites, *J. Nanomater.*, vol. 2015, 2015, doi: 10.1155/2015/838032.
11. A. Mohanty and V. K. Srivastava, Effect of alumina nanoparticles on the enhancement of impact and flexural properties of the short glass/carbon fiber reinforced epoxy based composites, *Fibers Polym.*, vol. 16, no. 1, pp. 188–195, Jan. 2015, doi: 10.1007/s12221-015-0188-5.
12. F. Aghadavoudi, H. Golestanian, and K. A. Zarasvand, Elastic behaviour of hybrid cross-linked epoxy-based nanocomposite reinforced with GNP and CNT: experimental and multiscale modelling, *Polym. Bull.*, vol. 76, no. 8, pp. 4275–4294, Aug. 2019, doi: 10.1007/s00289-018-2602-9.
13. J. Guo, Z. Wang, L. Tong, and W. Liang, Effects of short carbon fibres and nanoparticles on mechanical, thermal and shape memory properties of SMP hybrid nanocomposites Affiliation: Effects of short carbon fibres and nanoparticles on mechanical, thermal and shape memory properties of SMP hyb, 2015.
14. Standard Test Method for Tensile Properties of Plastics 1, doi: 10.1520/D0638-14.
15. Standard Test Methods for Flexural Properties of Unreinforced and Reinforced Plastics and Electrical Insulating Materials 1, doi: 10.1520/D0790-17.
16. I. M. H. Zwain and A. S. Alithari, Improving the fatigue life of composite by using multiwall carbon nanotubes, *Open Eng.*, vol. 13, no. 1, Oct. 2023, doi: 10.1515/eng-2022-0490.
17. A. Navidfar and L. Trabzon, Graphene type dependence of carbon nanotubes/graphene nanoplatelets polyurethane hybrid nanocomposites: Micromechanical modeling and mechanical properties, *Compos. Part B Eng.*, vol. 176, Nov. 2019, doi: 10.1016/j.compositesb.2019.107337.
18. H. Shivakumar, N. M. Renukappa, K. N. Shivakumar, and B. Suresha, The Reinforcing Effect of Graphene on the Mechanical Properties of Carbon-Epoxy Composites, *Open J. Compos. Mater.*, vol. 10, no. 02, pp. 27–44, 2020, doi: 10.4236/ojcm.2020.102003.
19. A. Namdev, A. Telang, and R. Purohit, Experimental investigation on mechanical and wear properties of GNP/Carbon fiber/epoxy hybrid composites, *Mater. Res. Express*, vol. 9, no. 2, Feb. 2022, doi: 10.1088/2053-1591/ac4e3f.
20. A. Kumar, D. K. Chouhan, P. S. Alegaonkar, and T. U. Patro, Graphene-like nanocarbon: An effective nanofiller for improving the mechanical and thermal properties of polymer at low weight fractions, *Compos. Sci. Technol.*, vol. 127, pp. 79–87, Apr. 2016, doi: 10.1016/j.compscitech.2016.02.028.

Design a Smart Thoracolumbosacral Orthosis Device

Ali Shelbayeh
Department of Mechatronics Engineering
University of Jordan
Az Zarqa, Jordan
aly0193536@ju.edu.jo

Abdallah Afaneh
Department of Mechatronics Engineering
University of Jordan
Amman, Jordan
abd0193982@ju.edu.jo

Raghed Abdallah
Department of Mechatronics Enginnering
University of Jordan
Amman, Jordan
rgd0196155@ju.edu.jo

Osama Obeid
Department of Mechatronics Engineering
University of Jordan
Az Zarqa, Jordan
asa0191909@ju.edu.jo

Musa Al-Yaman
Department of Mechatronics Engineering
University of Jordan
Amman, Jordan
m.alyaman@ju.edu.jo

Bashar AL-Qaroot
School of Rehabilitation Sciences
University of Jordan
Amman, Jordan
b.garoot@ju.edu.jo

***Abstract*—The Thoracolumbosacral Orthosis (TLSO) is essential in treating Degenerative Scoliosis, a condition characterized by twisting of the vertebral column. Treatment involves wearing the TLSO for at least 6 months. However, patients often experience muscle stiffness, necessitating frequent physical therapy sessions that are costly and time-consuming. The smart TLSO integrates a Neuromuscular Electrical Stimulation (NMES) device, controllable via a mobile application. This innovation aims to eliminate the dependency on therapy sessions, offering a more efficient and economical treatment option for patients. Moreover, the mobile application allows both patients and doctors to monitor treatment progress by collecting essential data, enhancing the overall management of the condition**

Keywords— Scoliosis, TLSO, NMES, Mobile Application

I. INTRODUCTION

Scoliosis is defined as a spinal deformity in a skeletally mature patient with a Cobb angle of more than 10 degrees. This angle describes the maximum deviation from a straight spine that a scoliotic curve may exhibit, as shown in Fig. 1.

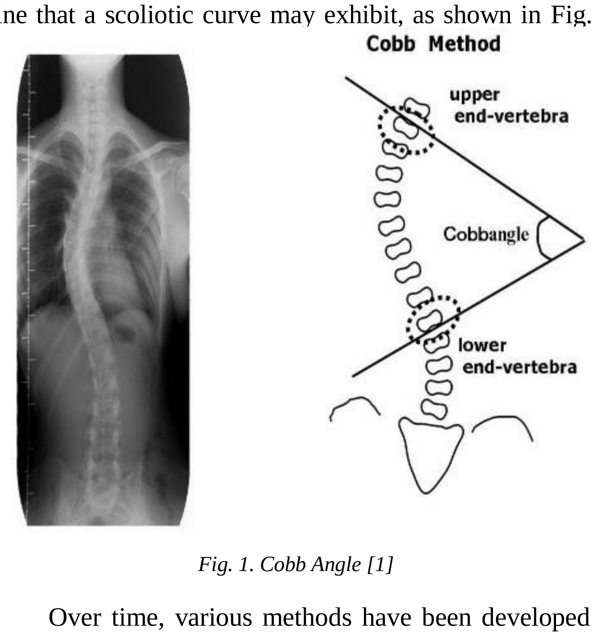

Fig. 1. Cobb Angle [1]

Over time, various methods have been developed to treat scoliosis. One modern method is the use of a Thoracolumbosacral Orthosis (TLSO). This orthopedic brace, depicted is designed to support and stabilize the spine. It applies pressure in specific areas using pads, aiming to correct the curved spine and control the progression of the curve by limiting the spine's movement, thereby preventing the curve from worsening over time [2]. However, long-term use of the brace may cause muscle weakness, which can be mitigated by using electrical stimulation technology. This technology sends electrical currents through the skin into muscles to stimulate them. Neuromuscular Electrical Stimulation (NMES) is used to send these electrical signals. It is crucial to use safe and effective current levels, with NMES devices commonly using currents in the range of 10 to 100 mA. Proper placement of the electrodes ensures that the current effectively stimulates the desired skeletal muscles. One of the major factors affecting the effectiveness of a brace is patient compliance, which is related to the patient's commitment to following the therapist's instructions to wear it properly. Non-compliance can delay treatment and lead to muscle atrophy, also not attending electrical stimulation sessions can also result in muscle weakness. Even with compliance, patients need to visit the therapist at least three times a week, which costs time and money, and the therapist needs to remove the brace to use the NMES device. To address these challenges, a mobile application could be developed to remind patients of their session times. Additionally, incorporating a device within the brace that is controlled by the mobile application to perform the same function as the NMES would be the most effective solution.

Advancements in scoliosis treatment began with the development and analysis of traditional braces, evolving into intelligent systems with advanced sensing capabilities.

F. M. Kadhim and S. I. Ahmed [3] began this journey by creating and refining thoracolumbosacral orthoses (TLSOs) for scoliosis treatment. A notable study in September 2013 focused on manufacturing a TLSO and improving its mechanical properties. This research included a numerical analysis using Ansys software to simulate stresses induced by interface pressure during gait cycles. X-ray technology determined the Cobb angle, and a polypropylene TLSO was chosen for its material characteristics. Piezoelectric Mat Scan sensors captured interface pressure signals. Results for one patient showed a Cobb angle deviation of 40 degrees from the normal spinal position, with minimal pressure differences between the right and left legs during gait cycle assessments, highlighting the orthosis's effectiveness in maintaining balance and support.

E. Lou, S. Venkateswaran, D. L. Hill, J. V. Raso, and A. Donauer [4], [5] further advanced this technology with the introduction of an active intelligent brace system in August 2019. This system aimed to control the interface pressure between the brace and the body during daily activities, utilizing a force transducer, force feedback component, and a microcomputer. A 20-minute sample test session revealed significant fluctuations in the first 7 minutes due to the brace's settling period. Improved wear time was observed when the air bladder feedback system was activated. Additionally, a prototype with thin-film pressure sensors, integrated with a Wheatstone bridge and a microcontroller unit, was developed. This pneumatic system controlled the inflation of derotation air pads, and data collected via GSM modules showed the system measured forces ranging from 15 Newton to 250 Newton, depending on sensor placement and patient activities.

O. Dehzangi, M. Mohammadi, and Y. Li [6] contributed to the evolution of brace technology with the development of smart braces in November 2016. A smart brace fitted with a low-power multi-modal sensor board was introduced, combining analog pressure sensors to record pressure distribution and an accelerometer to detect patient actions. This system aimed to identify brace wear quality with nearly 100% accuracy. Another study by K. R. Evans, E. Lou, and G. Faulkner [7] in December 2013 developed a low-cost, reliable force sensor using rubber for the sensor housing and added a humidity sensor to prevent tampering. This sensor achieved recorded forces between 1.0 and 5.1 Newton with an average force of 2.2 ± 0.7 Newton. Further research by P. Tymińska, K. Zaborowska-Sapeta, D. Janczak, and T. Giżewski [5] in May 2022 focused on a TLSO with graphene sensors to measure corrective forces in the prototype of an intelligent brace.

E. Lou, J. Raso, D. Hill, and N. Durdle [8] evaluated brace treatment efficacy by developing various monitoring systems. In May 2001, they created a microcomputer system to monitor loads exerted by braces during daily activities, providing feedback to ensure proper brace tightness. Testing with a volunteer showed the system recorded an average force of 1.52 ± 0.75 Newton during brace wear, proving useful in detecting the right tightness level. Another study by A. Chan, E. Lou, D. Hill, and G. Faulkner [9] in November 2012 introduced a continuous force measurement system that integrated load cell sensors and tension transducers into braces. This system captured real-time data to enhance scoliosis treatment, showing a robust linear correlation with an average sensitivity of 193.5 millivolts per Newton, and maintained functionality in real-world conditions.

A. Helfenstein et al. [10] took a different approach to monitor brace compliance by equipping thoracolumbosacral orthoses with a microelectronic data logger to record skin-brace interface temperature, providing reliable long-term compliance measurements. Another electronic monitoring method by T. Rahman et al. [11] in August 2010 used temperature sensors to measure brace wear time accurately, converting raw temperature data to determine compliance. Additionally, a study by R. Havey et al. [12] in January 2002 introduced a reliable and accurate method for measuring orthosis wearing time, further enhancing compliance monitoring.

These diverse approaches, integrating advanced sensing technology with inertial motion sensing and pressure data analysis, developing cost-effective and robust force sensors, and using data loggers, collectively aim to enhance the overall effectiveness of scoliosis brace treatment. Through improved monitoring and data collection techniques, these innovations strive to ensure better patient outcomes and more effective management of scoliosis.

II. Methodology

Our project aims to provide a smart TLSO device that optimizes treatment results, increases patient adherence, and handles the challenges associated with treating scoliosis. The final design of the project shown in Fig. 2 consists of two parts to achieve the aim, the first part as shown and described in II.A is designing a stimulation device to train muscles while wearing the TLSO brace, this device consists of Arduino with other electronic elements to generate electrical muscle stimulation signal. The second part pf project shown and described in II.B is the mobile application that communicate with the TLSO brace and control the stimulation time and different pulses intensity, the brace contains a box of the designed stimulation device and electrodes to deliver the pulses to the skeletal muscles at different intensities depends on the intensity values determined by the physiotherapist to each patient and chosen on the application.

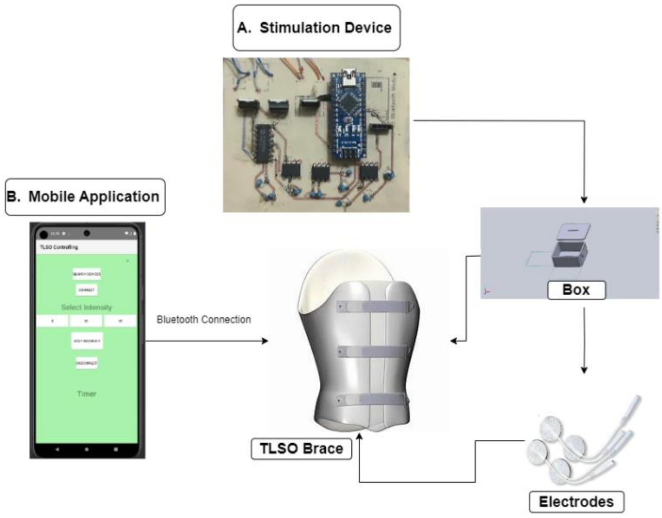

Fig. 2. Smart TLSO Device Final Design

A. Stimulation Device Design

Design a stimulation device is an essential step of design a smart TLSO because it is responsible of deliver the skeletal muscles in electrical generated pulses to stimulate them and prevent atrophy, the design required studied plan to achieve the aim, starting from analyzing Beurer EM 49 electrical muscle stimulation (EMS) device [13], then generating the required electrical signal.

1. *EMS Signal Analysis:* Understanding available EMS device signal generated to stimulate muscles and its performance done by connecting it in parallel with resistance as a simulation of the human body's dry skin resistance, which is approximately equal to 1 kilo ohm [14]. This connection enables recording voltage values of the available device signal at different intensities, then analyzing the recorded

data using MATLAB stored in a results table for three samples of data shown in Table I, this table identify the period time of pulses shown in first column, which was used to determine the frequency of the period shown in second column, this frequency changes repeatedly between three different values similar to the available device. Additioanally, the pulse width of each signal was determined in third column to calculate the frequency of the pulse shown in fourth column, which is clearly it equal in value for all pulses.

Table I. MATLAB Analysis Results

Sample	Period Time	Period Frequency	Pulse Width	Pulse Frequency
1	0.0511500	19.5503421	0.0011000	909.0909090
2	0.0339499	29.4550810	0.0011000	909.0909090
3	0.0253500	39.4477317	0.0011000	909.0909090

The results from reverse engineering shows that the pulses generated from available EMS device are biphasic which is refers to a waveform that alternates between two phases, typically of opposite polarity as shown in Fig. 3.

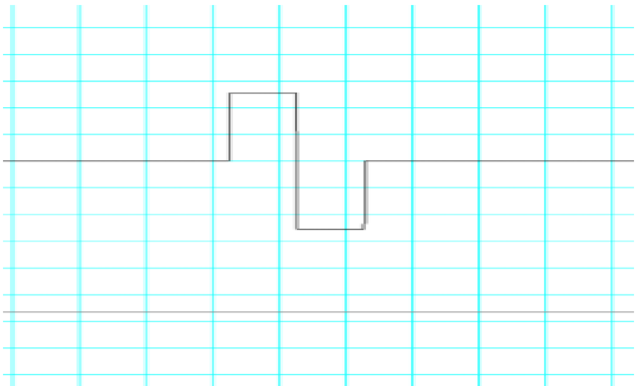

Fig. 3. Biphasic Signal

This type of signal are used in medicine and electrical engineering characterized by having two distinct phases, which mirror each other in terms of amplitude but have opposite signs with shift between positive phase and negative phase. Each pulse frequency equal to 1 kilo Hertz which mean the time on is 1 milliseconds and the pulses frequencies nearly differs from 20 to 30 to 40 Hertz repeatedly and follow the pattern of two signals then gap between pulses then 11 pulses and repeat.

2. *Signal Generation:* After analyzing the data and understanding the functionality of available device generating biphasic signal passes in two steps, first step is monophasic signal generation then doing processing on the output signal to generate required biphasic signal similar to available EMS device signal at different intensities. Arduino IDE used to generate two pulse width modulation (PWM) signals at 5 Volts, each pulse with half time on of biphasic pulse width (0.5 milliseconds) followed by each other to sum them later and generate biphasic signal.

Next step is designing a specific electronics circuit processing the monophasic output signal using proteus software. This circuit consists of several operational amplifiers (Op-Amp) for different purposes in the circuit. Op-Amp is a linear device which have all the properties required for nearly ideal amplification used to perform mathematical operations such as add, subtract, integration and differentiation depending on the connections and gain values. The whole circuit design for the system described below.

- Inverting Op-Amp to invert one of the PWM signal from Arduino without affecting the voltage gain by connecting the signal from Arduino as input voltage to inverting input with input resistor and the non-inverting input grounded, also connect a feedback resistor between the output and inverting input as described in equation (1).

$$V_{out}=-(R_f/R_{in}) \times V_{in} \qquad (1)$$

- Summing Op-Amp to sum non inverted PWM signal from Arduino and the output signal from inverting Op-Amp to generate one biphasic signal at 5 Volts by connecting the two signals to non-inverting input of the summing Op-Amp, inverting input connected to 10 kilo ohm resistor and 10 ohm feedback resistor between inverting input and output to determine the voltage gain as shown in equation (2), it is worth mentioning that to maintain a gain equal to one and avoid affecting the circuit voltage amplitude, the ratio between the feedback resistor and the input resistor should be very small value.

$$V_{out}=(1+(R_f/R_{in})) \times (V_{in1}+V_{in2}) \qquad (2)$$

- The next stage of the circuit consists of Op-Amp to amplify the biphasic signal to three voltages values as samples of the available EMS device voltages at different intensities. This is done by connecting the output from summing Op-Amp to non-inverting input and input resistor equal to 10 kilo ohm connected to inverting input and two feedback resistors with different values connected in parallel to achieve different voltage gains as required and wire connected without resistor to remain the voltage not amplified. The output voltage from this Op-Amp depending on the feedback resistor as described in equation (1).
- At the final stage of the system, choosing one of the three voltage values depends on the required intensity done using analog multiplexer determine by switches (A and B) which input pass to output and block other inputs.

At the end of signal processing step the circuit shown in Fig. 4 must able to generate required biphasic signal at different intensities. It worth mention that the two channels of the multiplexer are used and passing the same signal simultaneity to 4 electrodes deliver the skeletal muscles with generated biphasic signal. Lithium batteries, each one provide 3.75 volts, are connected in series to deliver required power for the circuit. The configuration includes three voltage regulators one of them to deliver Arduino in +5 volts and two voltage regulators to regulate positive and negative voltages (±9 volts), respectively, ensuring a stable biphasic signal output required for the circuit's operation.

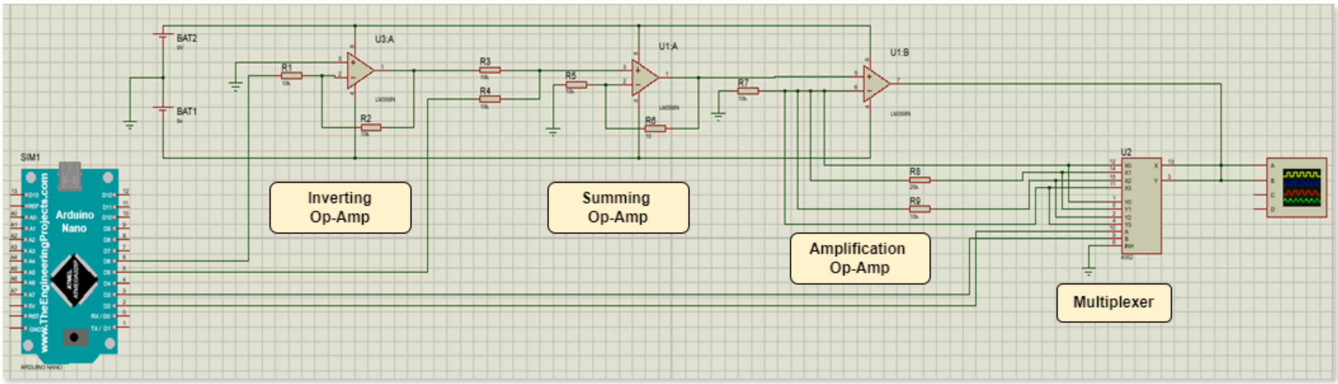

Fig. 4. Biphasic Signal Circuit

B. Mobile Application Design

The mobile application design is a critical part of the smart TLSO device, enhancing patient interaction with the stimulation device. It enables communication with the stimulation device, initiation of stimulation sessions, control of pulse intensity, and scheduling notifications on specific days and times. The primary page allows the physical therapist to set up a stimulation schedule before treatment begins, generating notifications on the patient's phone.

The application uses a Java class called "notification" to manage reminders. When a user selects a specific time and day for notifications, the application first sets a 24-hour notice from the selected time and then checks if the current day matches the selected reminder day, continuing this process for the rest of the week.

Additionally, the application regulates the frequency of the pulses delivered by the stimulation device. The physical therapist enters specific intensity values into the application, and the device inside the TLSO brace emits biphasic stimuli at these predefined levels. The device can be adjusted to operate at different intensity levels, typically 5 milliampere, 10 milliampere, and 15 milliampere, to suit the patient's condition and therapy progress, allowing for customized treatment as shown in Fig. 5.

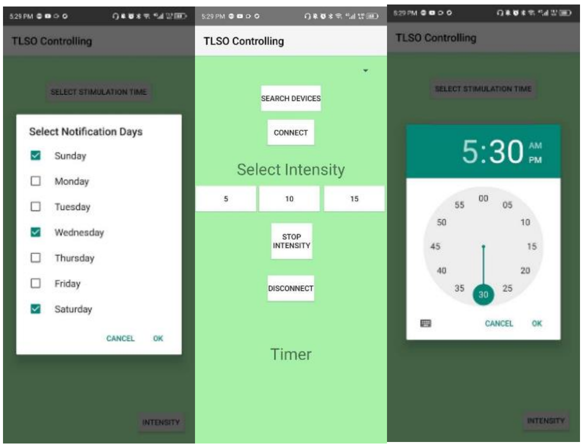

Fig. 5. Mobile Application Pages

The application is user-friendly and easy to navigate, enabling users to conveniently select and adjust the stimulation schedule and track therapy progress. The HC-05 Bluetooth module is used for serial data transmission and control signals between the application and the device. Android Studio was employed for development, leveraging its comprehensive tools and documentation on Java and Flutter for object-oriented programming and ease of development and maintenance.

III. Results

Testing the design of the smart TLSO device and recording the results is a crucial step to verify the design and ensure the concept is successfully achieved. The testing of a smart TLSO design includes two main parts: first, testing the generated biphasic signal of designed stimulation device; second, testing the mobile application's communication with the stimulation device inside the TLSO to ensure the control of signal intensity as required. This testing is essential to deliver the necessary electrical stimulation for skeletal muscles, ultimately aiming to eliminate the need for therapy sessions and provide a more efficient and cost-effective solution for patients.

A. Biphasic Signal Results

The simulation results of the generated biphasic signal for the available EMS device are presented in this section. Initially, the signal characteristics, including shape, amplitude, pulse width, and frequency, were determined through reverse engineering on the available EMS device. Using this information, we generated the desired signal with the Arduino IDE and implemented the corresponding electronic circuit. The output signal was validated with an oscilloscope, capturing three different states based on user inputs via a mobile application. Each state corresponds to a specific amplitude of the biphasic signal, passed through a multiplexer.

Before testing the intensity and voltage values, we verified that the pulses generated from the Arduino had the required pulse width and shape. This was achieved by connecting the oscilloscope in parallel with the output of a summing Op-Amp, zooming in on the generated signal to ensure it was square biphasic, and using the cursors option to determine the time at the start and end of one pulse, indicating the pulse width. The captured oscilloscope waveform in Fig. 6 shows that the generated signal is biphasic as required, with each pulse having a width equal to 1 millisecond, matching the available EMS device.

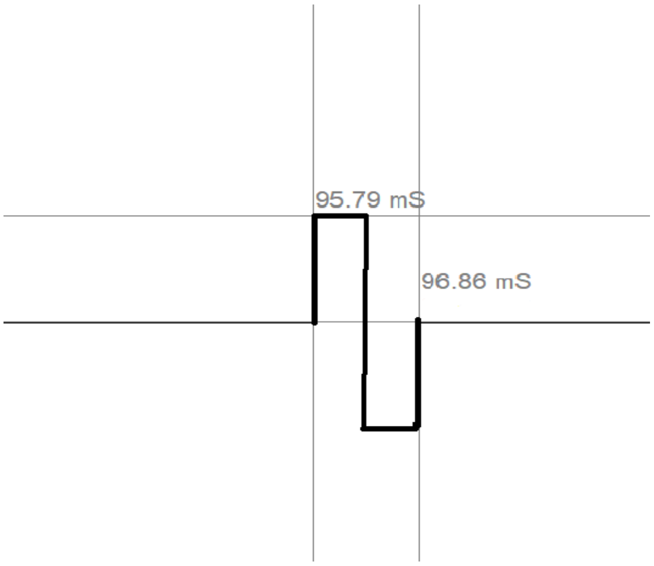

Fig. 6. Pulse Width of Biphasic Signal

Now, testing the voltage values of signal at each intensity depending on the values from mobile application as shown in Fig. 7 detailed below:

- The first oscilloscope capture displays the voltage versus time of a 5 volts peak-to-peak amplitude biphasic signal for the two outputs from the multiplexer at channels A and B. This state is activated by sending the character 'a' from the mobile application, which sets both selectors A and B of the multiplexer to High (A=1, B=1), allowing the 5 volts signal to pass through to the output. The waveform maintains a consistent biphasic pattern, verified by the specified gaps between pulses with precise 2.5 volts peaks, confirming the correct generation and transmission of the signal.
- The second oscilloscope capture shows the voltage versus time graph of a 10 volts peak-to-peak amplitude biphasic signal. This state was selected by sending the character 'b' from the mobile application, setting selector A to Low and selector B to High (A=0, B=1), thereby enabling the 10 volts signal passage through the multiplexer to the output. The waveform exhibits a stable biphasic signal with accurate 5V peaks, demonstrating successful adjustment of the signal amplitude through the multiplexer settings.
- The third oscilloscope capture presents the voltage versus time of a 15 volts peak-to-peak amplitude biphasic signal. This state was initiated by sending the character 'c' from the mobile application, which set selector A High and selector B Low (A=1, B=0), allowing the 15 volts signal to be output through the multiplexer. The waveform displays a precise biphasic pattern with 7.5 volts peaks, indicating effective control of signal amplitude at this higher setting.

In all states, the final command to stop the stimulation involved sending the character 'd' from the mobile application, which set both multiplexer selectors A and B to Low (A=0, B=0), halting the signal output. These results confirm the successful design and implementation of the EMS signal generation system, achieving accurate amplitude control and signal fidelity as required.

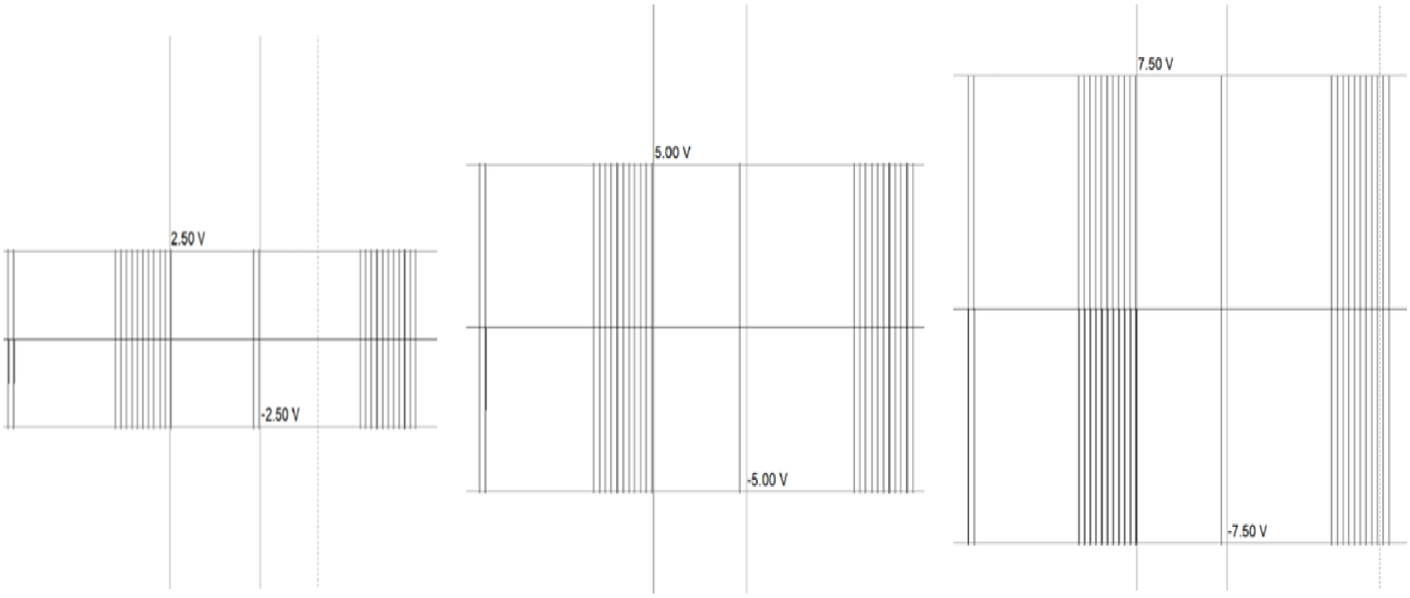

a **b** **c**

Fig. 7. Signal Test at Different Intensities

B. *Mobile Application and Communication Results*

The mobile application for the EMS device, developed using Android Studio, is now ready for testing and installation on a phone. The following steps outline the operation and functionality of the mobile application:

- For the application to function correctly, Bluetooth must be enabled on the phone. As previously mentioned, the physical therapist sets the stimulation schedule within the application, which allows the patient to receive notifications when it's time to start treatment. When the scheduled stimulation time arrives, the application sends a notification to the patient's phone, as illustrated in Fig. 8.

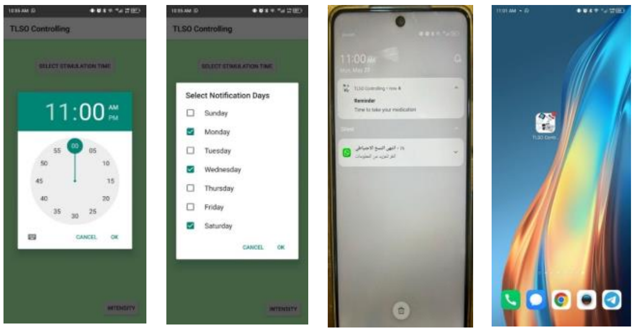

a b c d

Fig. 8. Notification System Results

- To regulate the stimulation intensity, the phone must establish a connection with the stimulation device inside the TLSO via Bluetooth. This connection ensures that only the intended device is paired, allowing for precise control over the stimulation intensity, as detailed in Table II.

Table II. Controlling Intensity using Mobile Application

Character from mobile application	Action
a	Start stimulation at intensity 5 milliampere
b	Start stimulation at intensity 10 milliampere
c	Start stimulation at intensity 15 milliampere
d	Stop stimulation automatically

- Once connected and the stimulation time arrives, the patient must select the intensity recommended by the physical therapist based on previous assessments. After selecting the desired intensity using the application's buttons, a 20-minute countdown timer begins, as shown in Fig. 9. Once the session concludes, the patient will wait for the next scheduled session, with the process repeating over the next six months.

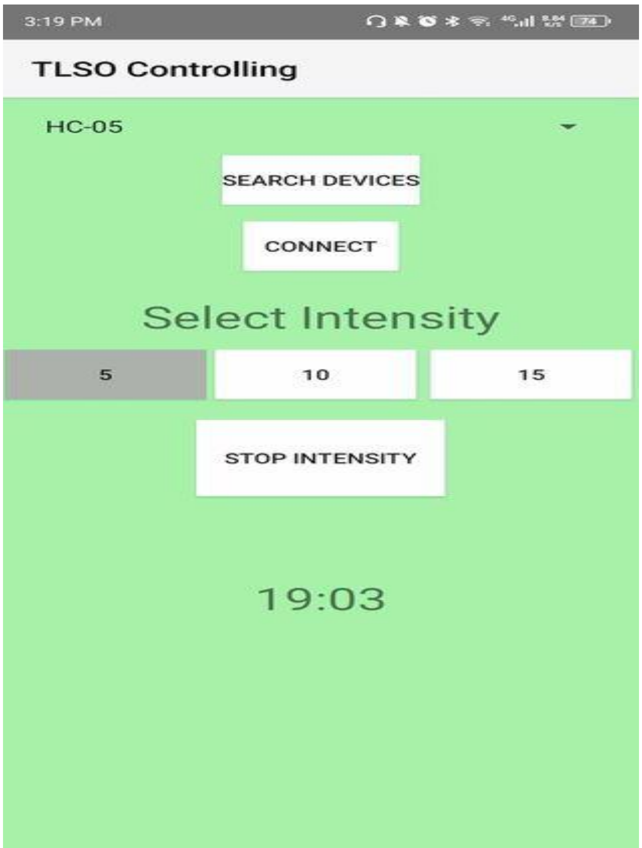

Fig. 9. Stimulation at Intensity 5 milliampere

IV. CONCLUSION

The development of the smart TLSO represents a significant advancement in the management of degenerative scoliosis. By integrating NMES within the TLSO, controlled via a user-friendly mobile application, this innovation addresses several critical challenges in traditional scoliosis treatment.

The traditional approach of wearing a TLSO for extended periods often results in muscle stiffness and requires frequent, costly physical therapy sessions. The smart TLSO's incorporation of NMES aims to mitigate these issues by providing in-brace muscle stimulation, reducing the need for external therapy and thus decreasing overall treatment costs and time commitment.

Our design effectively demonstrated the capability of generating and controlling a biphasic stimulation signal with varying intensities. The mobile application facilitates easy management of stimulation schedules and intensity levels, enhancing patient compliance and allowing for real-time monitoring of treatment progress. This integrated system not only simplifies the treatment process but also provides a more efficient and economical solution for managing scoliosis.

The results from our testing confirm that the smart TLSO can deliver precise NMES signals and maintain consistent stimulation parameters as required by therapy protocols. This innovation stands to improve patient outcomes by ensuring better adherence to treatment regimens and optimizing muscle recovery and support. Future work should focus on further refining the system based on patient feedback and long-term clinical outcomes to maximize its effectiveness and accessibility.

ACKNOWLEDMENT

We express our heartfelt thanks to the doctors, engineers, and students of the Mechatronics Engineering Department at the University of Jordan, whose encouragement and assistance have been instrumental along the way. Our sincere thanks go to Prof. Awd-Al Zeben and Eng. Burhan Al Shajrawi for their technical support. We are profoundly grateful to Orange FabLab for their financial support, which significantly enhanced the practical aspects of our work.

REFERENCES

[1] A. (Alaa) A. Ahmad, A. Agarwal, A. (Alaa) A. Ahmad, and A. Agarwal, *Early Onset Scoliosis: Guidelines for Management in Resource-Limited Settings*, 1st ed. CRC Press, 2021. Accessed: Aug. 14, 2024. [Online]. Available: https://www.perlego.com/book/2051459/early-onset-scoliosis-guidelines-for-management-in-resourcelimited-settings-pdf

[2] S. L. Weinstein, L. A. Dolan, J. G. Wright, and M. B. Dobbs, "Effects of bracing in adolescents with idiopathic scoliosis," *N. Engl. J. Med.*, vol. 369, no. 16, pp. 1512–1521, Oct. 2013, doi: 10.1056/NEJMoa1307337.

[3] "F. M. Kadhim and S. I. Ahmed, 'Stress Analysis of Thoracolumbosacral Orthosis (TLSO) for Scoliosis deformity and its Effects on Gait Cycle,' Al-Nahrain J. Eng. Sci., vol. 22, no. 3, pp. 187–193, Oct. 2019, doi: 10.29194/NJES.22030187.".

[4] E. Lou, S. Venkateswaran, D. L. Hill, J. V. Raso, and A. Donauer, "An intelligent active brace system for the treatment of scoliosis," *IEEE Trans. Instrum. Meas.*, vol. 53, no. 4, pp. 1146–1151, Aug. 2004, doi: 10.1109/TIM.2004.831458.

[5] P. Tymińska, K. Zaborowska-Sapeta, D. Janczak, and T. Giżewski, "TLSO with Graphene Sensors-An Application to Measurements of Corrective Forces in the Prototype of Intelligent Brace," *Sensors*, vol. 22, no. 11, p. 4015, May 2022, doi: 10.3390/s22114015.

[6] O. Dehzangi, M. Mohammadi, and Y. Li, "Smart brace for monitoring patients with scoliosis using a multimodal sensor board solution," in *2016 IEEE Healthcare Innovation Point-Of-Care Technologies Conference (HI-POCT)*, Nov. 2016, pp. 66–69. doi: 10.1109/HIC.2016.7797698.

[7] K. R. Evans, E. Lou, and G. Faulkner, "Optimization of a Low-Cost Force Sensor for Spinal Orthosis Applications," *IEEE Trans. Instrum. Meas.*, vol. 62, no. 12, pp. 3243–3250, Dec. 2013, doi: 10.1109/TIM.2013.2272202.

[8] E. Lou, J. Raso, D. Hill, and N. G. Durdle, "A low power wireless load monitoring system for the treatment of scoliosis," *IEEE Trans. Instrum. Meas.*, vol. 51, no. 5, pp. 908–911, Oct. 2002, doi: 10.1109/TIM.2002.807792.

[9] A. Chan, E. Lou, D. Hill, and G. Faulkner, "Design and validation of transducers to measure interface force distribution in a spinal orthosis," *Med. Eng. Phys.*, vol. 34, pp. 1310–6, Jan. 2012, doi: 10.1016/j.medengphy.2011.12.022.

[10] A. Helfenstein *et al.*, "The objective determination of compliance in treatment of adolescent idiopathic scoliosis with spinal orthoses," *Spine*, vol. 31, no. 3, pp. 339–344, Feb. 2006, doi: 10.1097/01.brs.0000197412.70050.0d.

[11] T. Rahman *et al.*, "Electronic monitoring of scoliosis brace wear compliance," *J. Child. Orthop.*, vol. 4, no. 4, pp. 343–347, Aug. 2010, doi: 10.1007/s11832-010-0266-6.

[12] R. Havey *et al.*, "A reliable and accurate method for measuring orthosis wearing time," *Spine*, vol. 27, no. 2, pp. 211–214, Jan. 2002, doi: 10.1097/00007632-200201150-00018.

[13] "Digital EMS & TENS Device, EM49," Beurer North America. Accessed: Aug. 14, 2024. [Online]. Available: https://www.shop-beurer.com/products/digital-ems-tens-device-em49

[14] "Skin Resistance - an overview | ScienceDirect Topics." Accessed: Aug. 14, 2024. [Online]. Available: https://www.sciencedirect.com/topics/engineering/skin-resistance

Feasibility Study of Using Produced Water from Oil and Gas Operations for Green Hydrogen Production

Anwar Al Abdali [1], Sara Al Ghafri[2], Sara Al Jassasi[3], Santosh Walke [4]

[1,2,3,4] Mechanical and Industrial Engineering Department, College of Engineering, National University of Science and Technology, Muscat, Oman

***** *Corresponding authors: anwar210701@nu.edu.om; Tel.: +968 97009990*

Abstract: This research explores the feasibility of using water collected from oil and gas operations to create a green hydrogen manufacturing facility. By analysing the correlation between the efficiency of hydrogen generation and produced water quality parameters (pH, chemical oxygen demand, total hardness, and density), the research aims to optimize the electrolysis process. The project's main elements include creating a green hydrogen production prototype, rigorously testing and characterizing the electrolysis process, and conducting in-depth techno-economic evaluations to assess the technology's commercial potential.

Significant findings include identifying optimal parameters for maximizing the volumetric flow rate of hydrogen generation while maintaining a stable system temperature. A stable system temperature of 38.834°C was achieved with a volumetric flow rate of 594.152 ml/min, a pH of 6.7, COD of 426 mg/L, total hardness of 1.34 kg/m³, and density of 1.153 g/cm³. These conditions highlight the crucial role of pH in influencing temperature and volumetric flow rate, emphasizing the importance of balancing different water quality parameters to enhance system longevity and efficiency.

The research findings and methodologies underscore the potential of green hydrogen as a critical component of future energy systems, contributing to the broader agenda of sustainable development. By paving the way for the mainstream adoption of green hydrogen production through comprehensive analysis, this research aims to support environmental sustainability and address current energy challenges.

Key words: Optimization, Electrolysis, Volumetric Flow Rate, pH Levels, Techno-Economic Analysis.

1. Introduction

Green hydrogen emits no greenhouse gases and is created by electrolyzing water with renewable energy, it is essential for a sustainable energy future. Utilizing produced water from oil and gas industries, producing green hydrogen helps with waste management and clean energy production. By examining the relationship between generated water quality metrics (pH, COD, density, and total hardness) and hydrogen production rates, as well as identifying the most effective electrode materials, this initiative seeks to optimize the electrolysis process [1]. **The** objective is to create a green hydrogen production prototype that is both economical and efficient, thereby promoting energy innovation and environmental sustainability through simulation modeling, techno-economic analysis, and system parameter optimization. When considering green hydrogen as the primary fuel source to replace fossil fuels in industrial applications, the move to a green hydrogen economy confronts numerous challenges. These barriers include those pertaining to finance, technology, society, and politics. To begin, while hydrogen is one of the most available elements, it is typically found in combination with other elements, making extraction from the natural environment much more challenging [2]**.** The cost of manufacturing green hydrogen is determined by three factors: the investment in the water electrolyzer, the amount of time it runs each year, and the cost of the renewable energy used to power the electrolyzer [3]**. Furthermore, collecting multiple samples from various locations takes a large amount of time** because each sample has unique features that must be measured individually. Furthermore, in order to be evaluated using Scanning Electron Microscopy (SEM), the sample must be dry and free of oil, which might be difficult to separate from water. Furthermore, it has been observed that the electrodes begin to corrode after five trials, necessitating frequent replacement [4-7] **.**

Currently, the lack of international standards and regulations for green hydrogen is a significant impediment to the expansion of worldwide industry. Countries can determine their own rules and regulations for hydrogen production and consumption, despite hydrogen being a growing potential market. The lack of universal international rules limits the attraction of hydrogen across national borders and the rate at which green hydrogen may become a key participant in the global energy market [8], [9]**. There are challenges to increasing the rate at which green hydrogen is created,** such as high energy inputs, expensive electrolysis technologies, and a scarcity of renewable energy. The intermittent nature of renewable sources creates operational challenges, and expanding production facilities requires significant investments. Developing effective electrolysis technologies and expanding renewable energy infrastructure are critical to meeting rising demand [3], [10]**.**

2. Materials and Methods

Choosing an appropriate methodological framework is critical to ensuring the reliability and validity of our study on the relationship between produced water quality parameters and hydrogen production [11]. This section explains the rationale for the chosen research design, data collection methods, and analytical techniques, providing a thorough justification for each step of the procedure. a correlational research design to examine the correlation between water quality parameters (pH, COD, density, total hardness) and hydrogen production efficiency via electrolysis. This design identifies and quantifies relationships between variables without manipulation, revealing potential causal links. produced water samples from oil fields and used various filtration techniques to prepare them for electrolysis [12]. The diverse data from various fields and rigorous filtration processes ensure accurate and representative samples, which are crucial for reliable electrolysis experiments [13].

2.1 Data Collection

Produced water samples with varying pH levels, CODE, density, and total hardness is collected from different fields in Oman. The samples are first filtered in funnel, followed by vacuum filtration using ash less filter paper (90 mm (about 3.54 in) diameter, 0.2-micron pore size). Then all samples are distilled using simple distillation followed by centrifugation. All 54 samples were effectively filtered using this method, guaranteeing high purity and consistency for ensuing analyses. Fig 1. Show the different methods used for filtration of produced water.

2.2 Experimental Setup

The Electrolyzer is designed using two glass bottles joined by polyethylene tubes and stainless-steel electrodes constructed from washers, nuts, and rods. The filtered water samples could be electrolyzed in a consistent and controlled manner. For the electrolysis experiment, 28 sets of samples with different parameters were prepared. Every experiment was carried out with the set of parameters such as Current (2A), Voltage (15 V), Water Volume (500 ml), KOH Electrolyte (50 grams). Using a water displacement method, we determined the volumetric flow rate of the generated gas after the electrolyzer was run for five minutes for each sample. This required measuring and capturing the volume of displaced gas using a 1000 ml graduated cylinder filled with water.

3. Results and Discussion

3.1 Advanced Mineral Analysis

The sample with the highest volumetric flow rate was subjected to testing for SEM (Scanning Electron Microscopy) and EDS (Energy Dispersive X-ray Spectroscopy) [14]. A high concentration of Fe, Cl, and Pt was found by the analysis, which offered information on how to best utilize electrode materials to avoid corrosion, our selection was stainless steel electrodes although the recommended for more durability was platinum electrodes. The purpose of SEM analysis is to compare the surface area of dried produced water to the sea water (The popular used water for green hydrogen production) [15], [16], [17]. The EDS test also provides us with information that the water we are dealing with does not contain heavy metals. This approach sheds light to HSE aspect of safe dealing with produced water [18]. The scanning electron microscope (SEM) reveals a structure commonly seen in treated water. The porous matrix seems to have been rid of contaminants resulting in a structure, with noticeable gaps and uneven surfaces. The labeled spectra (Spectrum 1, to Spectrum 5) point out regions where elemental analysis might have been done to detect any remaining impurities or determine the material's composition. The overall shape indicates a purification process suggesting that the remaining material likely comprises particles or inorganic residues [19].

3.2 Optimization of the System

Two Responses such as Volumetric Flow Rate (VFR) and Temperature for the Optimization of the System are studied. Volumetric Flow Rate (VFR) measures the rate at which hydrogen is produced during the electrolysis process. It is influenced by various parameters such as pH, COD, total hardness, and density of the produced water, whereas Temperature measures the temperature of the system during the electrolysis process. It is also affected by water parameters [21] as the volumetric flow rate and is an important factor in optimizing the electrolysis system to ensure efficiency and stability.

3.2.1 Volumetric Flow Rate Model Precision

The fit statistics and final equation from the Design Expert program provide critical insights into optimizing the electrolysis process for hydrogen production. The fit results show a robust model with a R^2 of 0.8542 and an adjusted R^2 of 0.6972, explaining over 85% of the variability in the volumetric flow rate. The anticipated R^2 of 0.2041 indicates strong predictive power, and the high adequate precision ratio of 11.4463 validates the model's reliability. The standard deviation is 68.89, and the coefficient of variation (C.V.) is 12.70%, which adds to the model's precision and reliability.

$$VFR = 557.25 + 90.46A - 28.63B + 9.12C + 8.62D + 13.94AB - 10.81AC - 12.69AD - 13.69BC - 12.31BD + 12.69CD - 55.66A^2 + 29.09B^2 + 4.97C^2 + 4.09D^2$$

Where,

- VFR = Volumetric Flow Rate
- A = PH
- B = COD (Chemical Oxygen Demand)
- C = Total Hardness
- D = Density

The volumetric flow rate (VFR) equation for hydrogen production provides useful information about how different water quality parameters affect the electrolysis process. The significant positive coefficient for pH (90.46) implies that higher alkaline conditions significantly increase hydrogen production [1], most likely due to enhanced ionic conductivity. However, the negative coefficient for the quadratic term of pH (-55.66) indicates that overly high pH levels might reduce efficiency, emphasizing the significance of maintaining an ideal pH range. Conversely, the negative coefficient for COD (-28.63) shows that larger organic pollutants lower hydrogen generation efficiency by using some of the electrical energy required for electrolysis [22] [23] The quadratic term for COD (29.09) indicates a non-linear relationship, implying that the system may tolerate specific COD levels without significant consequences. Total hardness (C) shows a mildly positive effect on VFR (9.12), implying that minerals like calcium and magnesium may modestly increase hydrogen generation, presumably by acting as more charge carriers. The quadratic term for overall hardness (4.97) implies that this effect persists, albeit less. Density (D) also has a slight positive effect (8.62) on VFR, most likely because of denser material facilitating greater ion exchange and current flow, with its quadratic term (4.09) corroborating this minor but favorable effect.

3.2.2 Temperature Model Precision

The standard deviation suggests a tight distribution of residuals around the expected values, implying that the model accurately fits the experimental data. With an average temperature of 43.14°C, this baseline allows you to compare the effects of different water quality parameters on the system's temperature. A coefficient of variation of 6.60% indicates good precision and reliability. The model explains 79.29% of temperature variability ($R^2 = 0.7929$), with an adjusted R^2 of 0.7569 confirming its robustness. Although the Predicted R^2 of 0.6901 is slightly lower, it still exhibits reasonable predictive power, suggesting possibilities for model modification.

3.2.3. Final Optimization (VFR & Temperature) Results

The effect of produced water parameters on the volumetric flow rate and temperature is analyzed statistically. The Design Expert has an optimization tool that generates the optimum parameters of produced water and the responses of volumetric flow rate and temperature [24]. The optimization goal is to maximize the Volumetric Flow Rate of green hydrogen and minimize the temperature of the system within the range of the produced water parameters limits [23].

4. Conclusions

The optimal parameters for maximizing the volumetric flow rate (VFR) of hydrogen generation while maintaining a low electrolysis system temperature were determined. The best conditions were found to be a pH of 6.7, a COD of 426 mg/L, a total hardness of 1.34 kg/m³, and a density of 1.153 g/cm³, achieving a VFR of 594.152 ml/min at 38.834°C. The pH had the greatest influence on both VFR and temperature, with higher pH increasing VFR but also raising the temperature. The model demonstrated good predictive power with R^2 values of 0.8542 for VFR and 0.7929 for temperature. These findings emphasize the importance of balanced parameter optimization for efficient hydrogen production by electrolysis.

Funding: This research was funded by National University of Science and Technology, Oman

Acknowledgments: The authors would like to express their sincere gratitude to the National University of Science and Technology, Oman for providing the necessary resources and support to carry out this research.

References

[1] J. C. Ehlers, A. A. Feidenhans'l, K. T. Therkildsen, and G. O. Larrazábal, "Affordable Green Hydrogen from Alkaline Water Electrolysis: Key Research Needs from an Industrial Perspective," Mar. 10, 2023, *American Chemical Society*. doi: 10.1021/acsenergylett.2c02897.

[2] A. Javaherian, “Proposal and comprehensive analysis of power and green hydrogen production using a novel integration of flame-assisted fuel cell system and Vanadium-Chlorine cycle: An application of multi-objective optimization,” *Energy Convers Manag*, vol. 277, 2023.

[3] WWF-VIETNAM, “Green Hydrogen Market: Potentials and Challenges,” 100re-map.

[4] A. C. Klemz *et al.*, “Oilfield produced water treatment by liquid-liquid extraction: A review,” Apr. 01, 2021, *Elsevier B.V.* doi: 10.1016/j.petrol.2020.108282.

[5] M. Calabrese, “Hydrogen Safety Challenges: A Comprehensive Review on Production, Storage, Transport, Utilization, and CFD-Based Consequence and Risk Assessment,” *Energies (Basel)*, vol. 17, p. 1350, 2024.

[6] S. Wang, A. Lu, and C. J. Zhong, “Hydrogen production from water electrolysis: role of catalysts,” Dec. 01, 2021, *Korea Nano Technology Research Society*. doi: 10.1186/s40580-021-00254-x.

[7] M. Tao, J. A. Azzolini, E. B. Stechel, K. E. Ayers, and T. I. Valdez, “Review—Engineering Challenges in Green Hydrogen Production Systems,” *J Electrochem Soc*, vol. 169, no. 5, p. 054503, May 2022, doi: 10.1149/1945-7111/ac6983.

[8] O. Schmidt, A. Gambhir, I. Staffell, A. Hawkes, J. Nelson, and S. Few, “Future cost and performance of water electrolysis: An expert elicitation study,” *Int J Hydrogen Energy*, vol. 42, no. 52, pp. 30470–30492, Dec. 2017, doi: 10.1016/j.ijhydene.2017.10.045.

[9] R. Bhandari, C. A. Trudewind, and P. Zapp, “Life cycle assessment of hydrogen production via electrolysis - A review,” Dec. 15, 2014, *Elsevier Ltd*. doi: 10.1016/j.jclepro.2013.07.048.

[10] H. D. Dawoud, H. Saleem, N. A. Alnuaimi, and S. J. Zaidi, “Characterization and treatment technologies applied for produced water in Qatar,” Dec. 01, 2021, *MDPI*. doi: 10.3390/w13243573.

[11] A. S. Moustafa Oraby, “Green Hydrogen Production Directly from Seawater with No Corrosion Using a Nonmetallic Electrode: A Novel Solution and a Proof of Concept,” *Int J Energy Res*, 2024.

[12] M. A. Khan *et al.*, “Recent Progresses in Electrocatalysts for Water Electrolysis,” Dec. 01, 2018, *Springer Science and Business Media B.V.* doi: 10.1007/s41918-018-0014-z.

[13] M. Carmo, D. L. Fritz, J. Mergel, and D. Stolten, “A comprehensive review on PEM water electrolysis,” Apr. 22, 2013. doi: 10.1016/j.ijhydene.2013.01.151.

[14] Mahmoud Nasrollahzadeh, “Scanning Electron Microscopy - an overview | ScienceDirect Topics,” Interface Science and Technology. Accessed: Jun. 22, 2024. [Online]. Available: https://www.sciencedirect.com/topics/physics-and-astronomy/scanning-electron-microscopy

[15] M. Naniwadekar, M. Mandake, and S. Walke, “Review study of e-waste management and resource recovery system for controlling environmental pollution,” *Int J Environ Waste Manag*, vol. 1, no. 1, 2023, doi: 10.1504/IJEWM.2023.10060267.

[16] L. Zhao, Y. Li, M. Yu, Y. Peng, and F. Ran, “Electrolyte-Wettability Issues and Challenges of Electrode Materials in Electrochemical Energy Storage, Energy Conversion, and Beyond,” Jun. 13, 2023, *John Wiley and Sons Inc*. doi: 10.1002/advs.202300283.

[17] P. B. Balbuena, “Electrolyte materials - Issues and challenges,” in *AIP Conference Proceedings*, American Institute of Physics Inc., 2014, pp. 82–97. doi: 10.1063/1.4878481.

[18] R. Aydin and F. Köleli, “Hydrogen evolution on conducting polymer electrodes in acidic media,” *Prog Org Coat*, vol. 56, no. 1, pp. 76–80, May 2006, doi: 10.1016/j.porgcoat.2006.02.004.

[19] K. Zeng and D. Zhang, “Recent progress in alkaline water electrolysis for hydrogen production and applications,” Jun. 2010. doi: 10.1016/j.pecs.2009.11.002.

[20] S. W. Maram Al Hinai, Amjad Al Kalbani, Buthaina Al Rubkhi, Umaima Al Kalbani, “Protein Extraction from Spirulina Platensis,” *International Journal of Innovative Technology and Exploring Engineering (IJITEE)*, vol. 8, no. 12, pp. 1524–1530, 2019, doi: 10.35940/ijitee.L3110.1081219.

[21] Hong Lv, “Mechanism analyses and optimization strategies for performance improvement in low-temperature water electrolysis systems via the perspective of mass transfer: A review,” *Renewable and Sustainable Energy Reviews*, vol. 183, 2023.

[22] A. O. M. Maka and M. Mehmood, “Green hydrogen energy production: current status and potential,” Apr. 01, 2024, *Oxford University Press*. doi: 10.1093/ce/zkae012.

[23] M. N. Santosh Walke, Manoj Mandake, “A Review of Recent Advancements and Perspectives of Nanotechnology in the Application of Biomedical Imaging and Instrumentation,” *ChemistrySelect*, vol. 9, no. 27, 2024, doi: https://doi.org/10.1002/slct.202304082.

[24] S. W. Ahmed Al Shehhi, M.J. Varghese, Lakkim Rao, “Process Simulation and Optimization of Natural Gas Dehydration Process using Aspen Hysys,” *International Journal of Innovative Technology and Exploring Engineering*, vol. 8, no. 9, pp. 644–649, 2019, [Online]. Available: https://www.ijitee.org/wp-content/uploads/papers/v8i9/I7622078919.pdf

Enhancing the Efficiency of Industrial Boilers and Burners Using Deep Learning Techniques

Anwar AL zadjali [1], Varghese M J [2], Santosh Walke [3]

[1] Mechanical and Industrial Engineering Department, College of Engineering, National University of Science and Technology, Muscat, Oman

[2] Mechanical and Industrial Engineering Department, College of Engineering, National University of Science and Technology, Muscat, Oman

[3] Mechanical and Industrial Engineering Department, College of Engineering, National University of Science and Technology, Muscat, Oman

***** *Corresponding authors: anwar.alzadjali.94@gmail.com; Tel.: +968 96677466*

Abstract: The process of boiler combustion is complicated, and the production environment is severe. The oxygen content in the flue gas is considered as a good indicator of boiler efficiency in any industrial process. Measuring the oxygen content in the flue gas need time, effort, and money. To overcome this, deep learning methods used effectively in the prediction of oxygen content of boiler flue gas. Moreover, many issues were encountered with the burners flame in industries. Hence, MATLAB and PYTHON techniques are that used widely to preform suitable models that can be used to solve this issue. They are considered as helpful tools to create mathematical model, test the machine, run automatic tests on equipment functions and design artificial intelligence algorithms for optimization purposes. In this research, deep learning tools were used to test the content of oxygen in the flue gas. Also, it investigates the ability of a deep learning methodologies in the segmentation of industrial burner flames based on example image data from a special waste incineration plant. Results shows that the model derived with the deep-belief algorithm produced better accuracy than the models generated by the other algorithms.

Key words: Boiler, Burner, Deep Learning Machine, Efficiency, Artificial Neural Network.

---

1. Introduction

Industrial processes contain different types of equipment to preform different functions [1]. To illustrate, boilers are vessels where water is heated to produce steam. This steam is used for different purposes such as heating buildings, producing electricity, and sanitizing equipment. Burners are another example of this equipment. It plays an important role in any industry. Industrial burners are used in different applications throughout industries. They are mainly utilized in heating purposes. For example, supplying heat to boiler systems, welding, heating fluids, initiating chemical reactions, melting metals, recovering, and glass blowing. There are numerous kinds of industrial burners, where each of them is designed for specific functions. Cold air burners, hot air burners, regenerative burners, and oxy-fuel burners are commonly used.

With the fastest growth about environmental protection, optimization and enhancing efficiency has become an important concept in the operation of boilers and burners to be considered and study. The oxygen content of flue gas is an important metric of coal-fired boiler combustion operation and is

closely related to boiler combustion efficiency. Accurate measurement of the oxygen amount in flue gas can help improve boiler combustion efficiency and reduce coal consumption [2-3]
Hence, this research will focus on enhancing the efficiency of the boilers and burners by using the deep learning methods such as MATLAB and PAYTHON. Also, to create a proper model to test the oxygen content in boiler flue gas.

2. Materials and Methods

1. Artificial Neural Network Modeling (ANN)

Over the last two decades, ANN machine learning used in many engineering applications such as prediction and optimization process. Moreover, ANN plays a role in solving high dimensional non-linear relationship between input and output compared with other regression modeling. Furthermore, it has the ability of solving stimulating and solving engineering problems where conventional numerical approaches are insufficient. In addition, this modeling method helps in estimating the output Fastly because exhaustive numerical repetitions needed to solve differential equations are not needed more (Joy, V.M., Feroz, S. and Dutta, S., 2022) [38-40]. Also, it is a smart computation method that is used to imitate the learning methods of the human brain and biological neurons.
Normally, there are two classes of ANN. The first type is feed forward ANN. In this network information flow is unidirectional. One unit will send information to another which is not receiving any information. Furthermore, there are no feedback loops in this type of ANN. Even though they are used in detection of a pattern. Because it contains fixed inputs and outputs. The second type of ANN is called the feedback ANN. This Artificial Neural Network allows the feedback loops. Additionally, it is used in matter addressable memories. (Electronics Hub. (2019)).

1.1 Machine Learning algorithm

1.1.1.1 Supervised and Un supervised Leaning.

There are several types of machine learning present. For example, supervised learning. This machine is used to train a set of labeled data. Where the input data is paired with the desired output. Then the machine will predict the output for any set of new input. Machine learning is widely used in different tasks such as regression which is used widely to guess continuous values. There are common regression algorithms including Linear, Polynomial, and Support Vector Machine Regression. Moreover, supervised machine learning is used in classification. This type is helpful to predict and to know the categorical values. Classification algorithm includes different types. To demonstrate, logistic regression, support vector machines, decision trees, random forests and naive baye.
Unsupervised learning machine is opposite to supervised leaning. Where the data does not have labels or classifications. The aim of unsupervised learning is to detect patterns and relationships in the data without any obvious guidance. The task of the unsupervised machine is to collect uncategorized information according to matches, patterns, and differences without any previous training of data.

2. PYTHON Language

It is a simple and robust General-purpose Programming (GPP) Language. It is preferred by modern developers and programmers. It can supply the users with complicated functionality. This programming language contains numerous in-built libraries that can immediately implement both logical and mathematical functions into any program. Furthermore, it has strong performance power and advanced features. Also, it makes it fit for use in applications related to Software Development,

3. Modeling Procedures

Measuring the oxygen in the boiler flue gas

1. **Data Pre-processing**

   - Operation process data of the boiler and flue gas content affect the accuracy of the model.
   - Original process data must be normalized to eliminate the impact of magnitude variations within the target parameters before starting the modelling.

2. **Selection of Input Variable**

   - A huge number of input variables will decrease the prediction accuracy and increase the computational time.
   - Therefore, it is necessary to remove unnecessary variables before initiating the modelling.

3. **Modelling Process Based on The Deep Believe Network**

   3.1 Deep Believe Network

   3.2 Nonlinear Prediction Model Based on The Deep Believe Network

4. **Error Metrices and Algorithm Flow**

   - To evaluate the performance of the prediction model, square error, mean relative error, and mean absolute error are used to measure the performance of each prediction model.

Performance of burner flames

1. Multiple burners are mounted horizontally in the chamber to treat the exhaust gas from a rotary kiln process.
2. A camera provides continuous top-view images of the process in the visual spectrum.
3. Investigate the networks that allow instance segmentation.
4. The conventional training of CNNs requires annotated image data for supervised learning and additional images for evaluation.
5. Segmentation Quality Metrics will be used to evaluate the performance.

4. Results and Discussion.

Machine learning models for predicting O2 percentage using PYTHON and MATLAB

Combustion optimization has grown in importance in boiler operation as environmental protection concerns have grown. An essential indicator of boiler combustion performance, the oxygen content of flue gas is directly linked to both NOx emissions and boiler combustion efficiency. Reducing the amount of coal used and increasing boiler combustion efficiency are two benefits of accurately measuring the oxygen concentration in flue gas. Many methods are used to measure O2 content on the flue gas. To illustrate, sensors are commonly used in industries for such purposes. However, such methods and approaches have many limitations. For example, manufacturing cost, high temperature which causes disfunctions. Hence, soft measurement methods can play a role in measuring oxygen content in the flue gas. Soft measurement methods refer to use the deep learning machine and software to produce prediction model. They are easy to use and establish. This work was divided into three stages. The first stage was preprocessing of the data. This stage aimed to divide the process variables to state and control variables. This is to eliminate the unwanted variables and reduce the large number of parameters. The second stage was to select the input variables. In this stage Lasso algorithm used to remove unnecessary variables. It precisely selects input variables with strong correlation. For this study 19 inputs were selected with only one output variables to perform this modelling. Third stage was the modelling stage. Were PYTHON and MATLAB were used both in modelling stage. In this study MATLAB and PYTHON were used to proposed models to measure O2 content and enhance the boiler efficiency. The Date were imported and loaded into software. Then the heat map is generated by using this software to visualize the correlation. After that, Input and outputs variables were splatted. Also, the dataset split into training and testing set. Then, the ANN model was built using PYTHON and MATLAB. Afterward, the model is evaluated and complied. According to the results from both MATLAB and PYTHON , the proposed model shows good indication in measuring O2 content as the accuracy of this model was 96%.

Deep Learning Hybrid Model for Flame Image by Using PYTHON

CSAE was used in this study to obtain the flame image characteristics. The extracted discriminatory characteristics can be visualized through the t-distributed stochastic neighbour embedding (t-SNE) technique. This method offers a helpful solution for high-dimensional data visualization. Figure 73 shows the feature visualized image using PYTHON. The results show that although the original flame images are difficult to intuitively distinguish, their features are well separable in the feature space. Some mixed points occur. This confusion reflects the similarity between flame images, especially in adjacent operating conditions. Nevertheless, most of the feature points can be distinguished, demonstrating the effectiveness of CSAE in image feature extraction. After the CSAE-LSSVM preparation, the dataset containing 20 labelled pictures per condition was utilized to look at its expectation execution. As shown in figure 74 the confusion matrix which sums up the grouping comes about of the six combustion operation conditions. Within the confusion matrix, columns show the actual labels, and rows shows predicted labels. Diagonal cells demonstrate the number and accuracy of correctly approximate samples, while off-diagonal cells display the number of misclassified samples. Also, from confusion matrix at all conditions the accuracy is 100% and this proved that the proposed model is worked well in expecting the combustion operation condition. Moreover, the results prove that the suggested model acts well in dealing with the problem of limited labelled data and decreases the demand for image labels. Accordingly, the proposed model has a great application in combustion operation condition prediction. Generally, the proposed model can simply be applied to other combustion processes such as heavy oil, biomass combustion.

4. Conclusions

The oxygen content of boiler flue gas is a guide of boiler efficiency and emissions. Hence, measuring the O2 content in flue gas is a waste of time and costly. Moreover, combustion is not an easy process. It produces many environmental issues. These lead to dangerous and much equipment disfunctions and loss when using direct measurements of the oxygen content of flue gas. Therefore, it is complicated to keep a high level of measurement accuracy of oxygen content. A nonlinear deep learning method is proposed in this paper to solve this problem and to predict the oxygen content of flue gas. The whole algorithm was analyzed in three parts: data preprocessing, feature selection, and data analysis modeling. MATLAB and PYTHON were used in the modeling. The data and results show that the proposed models work effectively in measuring the O2 content in the boiler flue gas and enhancing the boiler efficiency. Moreover, this paper aimed to produce a model by PYTHON for flame image. Where novel hybrid deep neural network model (CASE-LSSVM) is proposed. It was used to forecast the combustion operation state and conditions. The CASE was used to feature removal of flame images, and the LSSVM was applied to expect the combustion operation condition based on the extracted flame characteristics. The proposed model overcomes the shortcomings of the traditional methods where previous expert knowledge and massive labeled data are involved.

References

1. Barma, M.C., Saidur, R., Rahman, S.M.A., Allouhi, A., Akash, B.A. and Sait, S.M., 2017. A review on boilers energy use, energy savings, and emissions reductions. *Renewable and Sustainable Energy Reviews*, *79*, p.970-983.
2. Abou El Rish, A.M.S., 2013. Designs of Boiler Burner Management System.
3. Tang, Z., Li, Y. and Kusiak, A., 2020. A deep learning model for measuring oxygen content of boiler flue gas. *IEEE access*, *8*, pp.12268-12278.
4. Lu, G., Yan, Y. and Colechin, M., 2004. A digital imaging based multifunctional flame monitoring system. *IEEE Transactions on instrumentation and measurement*, *53*(4), pp.1152-1158.
5. Mathew, A., Amudha, P. and Sivakumari, S., 2021. Deep learning techniques: an overview. *Advanced Machine Learning Technologies and Applications: Proceedings of AMLTA 2020*, pp.599-608.
6. Ahire, J. B. (2018) *The artificial neural networks handbook: Part 4, dzone.com*. DZone. Available at: https://dzone.com/articles/the-artificial-neural-networks-handbook-part-4 (Accessed: April 17, 2024).
7. Shohet, R., Kandil, M.S., Wang, Y. and McArthur, J.J., 2020. Fault detection for non-condensing boilers using simulated building automation system sensor data. *Advanced Engineering Informatics*, *46*, p.101176.
8. Tang, Z., Wang, S., Chai, X., Cao, S., Ouyang, T. and Li, Y., 2022. Auto-encoder-extreme learning machine model for boiler NOx emission concentration prediction. *Energy*, *256*, p.124552.
9. Effendy, N., Kurniawan, E.D., Dwiantoro, K., Arif, A. and Muddin, N., 2022. The prediction of the oxygen content of the flue gas in a gas-fired boiler system using neural networks and random forest. *IAES International Journal of Artificial Intelligence*, *11*(3), p.923.
10. Meng, Y., Wu, X., Oladejo, J., Dong, X., Zhang, Z., Deng, J., Yan, Y., Zhao, H., Lester, E., Wu, T. and Pang, C.H., 2021. Application of machine learning in industrial boilers: fault detection, diagnosis, and prognosis. *ChemBioEng Reviews*, *8*(5), pp.535-544.
11. Khalid, S., Lim, W., Kim, H.S., Oh, Y.T., Youn, B.D., Kim, H.S. and Bae, Y.C., 2020. Intelligent steam power plant boiler waterwall tube leakage detection via machine learning-based optimal sensor selection. *Sensors*, *20*(21), p.6356.
12. Grochowalski, J., Jachymek, P., Andrzejczyk, M., Klajny, M., Widuch, A., Morkisz, P., Hernik, B., Zdeb, J. and Adamczyk, W., 2021. Towards application of machine learning algorithms for prediction

temperature distribution within CFB boiler based on specified operating conditions. *Energy*, *237*, p.121538.

13. S. Walke; V. M. Kale. Effects of alloying element on the mechanical behavior of Mg-MMCs: A review. *Materials Today: Proceedings* 2023. (accepted; in press) DOI: https://doi.org/10.1016/j.matpr.2023.02.211
14. S. Walke; M. B. Mandake. A review on copper chemical vapour deposition. *Materials Today: Proceedings,* 2023. (accepted; in press) DOI: https://doi.org/10.1016/j.matpr.2022.12.140
15. Han, Z., Li, J., Hossain, M.M., Qi, Q., Zhang, B. and Xu, C., 2022. An ensemble deep learning model for exhaust emissions prediction of heavy oil-fired boiler combustion. *Fuel*, *308*, p.121975.
16. Grosskopf, J., Matthes, J., Vogelbacher, M. and Waibel, P., 2021. Evaluation of deep learning-based segmentation methods for industrial burner flames. *Energies*, *14*(6), p.1716.
17. Kovalnogov, V., Fedorov, R., Klyachkin, V., Generalov, D., Kuvayskova, Y. and Busygin, S., 2022. Applying the random forest method to improve burner efficiency. *Mathematics*, *10*(12), p.2143.
18. Gharib, M., Tischer, P., Schulze, O., Gräbner, M. and Richter, A., 2024. Flame lift-off detector based on deep learning neural networks. *Combustion and Flame*, *260*, p.113215.
19. Han, Z., Li, J., Zhang, B., Hossain, M.M. and Xu, C., 2021. Prediction of combustion state through a semi-supervised learning model and flame imaging. *Fuel*, *289*, p.119745.
20. Abdurakipov, S. and Butakov, E., 2019, December. Application of computer vision and deep learning for flame monitoring and combustion anomaly detection. In *Journal of Physics: Conference Series* (Vol. 1421, No. 1, p. 012005). IOP Publishing.
21. Sujatha, K., Bhavani, N.P.G., Srividhya, V., Karthikeyan, V. and Jayachitra, N., 2020. Soft sensor with shape descriptors for flame quality prediction based on lstm regression. In *Real-Time Data Analytics for Large Scale Sensor Data* (pp. 115-138). Academic Press.

Financial Innovations and Their Impact on Modern Supply Chain Operations

Bader AlTamimi[1], Nader AlTamimi[2] and Mohammad Abdallah[3]

[1] Hashemite University, Zarqa, Jordan.

[2] German Jordanian University, Amman, Jordan.

[3] Al Zaytoonah University of Jordan, Amman, Jordan;

* *Corresponding authors: 2370407@std.hu.edu.jo; Tel.: 00962795038921*

Abstract: This research investigates how financial innovations, particularly FinTech, are reshaping supply chain management (SCM) by improving efficiency, transparency, and security. Technologies like blockchain and digital payments are central to this transformation, offering streamlined processes and enhanced traceability. The study aims to analyze the impact of FinTech on SCM efficiency, assessing cost reductions and operational improvements. It also evaluates transparency enhancements through blockchain, ensuring accurate and accountable transactions across supply chains. Furthermore, the research scrutinizes the security of financial transactions within SCM, focusing on the robustness of digital payment systems against cyber threats. Reviewing existing literature reveals consistent findings on the positive influence of FinTech on SCM, highlighting efficiency gains, increased transparency, and strengthened security measures. However, challenges such as initial adoption costs and integration complexities remain significant barriers. Looking forward, advancements in artificial intelligence and data analytics present opportunities for predictive insights and sustainable practices in global supply chains. Collaborative efforts among stakeholders and investments in technology infrastructure will be crucial to maximizing the potential of these innovations. Ultimately, this study contributes to understanding how financial innovations can optimize supply chain operations amidst evolving global demands and technological advancements.

Keywords: FinTech; AI in Supply Chain Management; Blockchain; Digital Payments; Transparency; Security

1. Introduction

In an era where the pace of change accelerates daily, the landscape of business, particularly in supply chain management, is undergoing a profound transformation. Financial breakthroughs, driven by advances in technology and innovative tools, are revolutionizing supply chain operations, making them more resilient, efficient, and adaptable to the complexities of the modern global economy. Traditional supply chain frameworks, often characterized by their rigidity and inefficiency, are increasingly strained under the pressures of globalization, digitalization, and the rising expectations of consumers. This introduction will explore the intersection of finance and supply chain management, focusing on how emerging financial tools are reshaping traditional models and paving the way for more dynamic, responsive, and transparent supply chains.

The Evolving Supply Chain Landscape

Supply chains, the networks that facilitate the movement of goods from manufacturers to consumers, have traditionally been linear and siloed. These conventional models, reliant on sequential steps and rigid processes, are becoming inadequate in addressing the complexities of today's interconnected global markets. The advent of digital technologies and the increasing integration of global markets have exposed the limitations of these old-school supply chain setups. The need for agility, transparency, and real-time responsiveness has never been greater (1).

In response to these demands, new financial tools and technologies have emerged, offering innovative solutions to long-standing challenges in supply chain management. These tools are not just enhancing existing processes but are fundamentally altering the way supply chains operate, making them more efficient and robust. This transformation is driven by several key innovations, including blockchain technology, advancements in fintech, and flexible pricing models (2).

Financial Innovations Transforming Supply Chains

1. Blockchain Technology

Blockchain technology, originally developed to support cryptocurrencies like Bitcoin, has found significant applications in supply chain management. A blockchain is a decentralized digital ledger that records transactions across a network of computers in a secure and immutable way. This technology offers several benefits for supply chain operations:

- **Transparency:** Blockchain provides a transparent record of transactions, enabling all parties in the supply chain to access real-time information about the movement of goods. This transparency helps reduce fraud, enhance traceability, and improve accountability (3).
- **Security:** The decentralized nature of blockchain makes it highly secure against tampering and cyber-attacks. Each transaction is encrypted and linked to the previous one, creating a secure chain of data that is nearly impossible to alter (4).
- **Efficiency:** By eliminating intermediaries and automating processes through smart contracts, blockchain can streamline operations and reduce transaction costs. Smart contracts are self-executing contracts with the terms of the agreement directly written into code, which automatically executes and verifies transactions when conditions are met (5).

For instance, IBM's Food Trust blockchain has been used to track the journey of food products from farm to table, improving transparency and safety in the food supply chain (6). Similarly, the De Beers Group uses blockchain to track the provenance of diamonds, ensuring they are conflict-free and ethically sourced (7).

2. Fintech Solutions

Financial technology (fintech) has revolutionized the way businesses handle payments, credit, and financial management. In the context of supply chains, fintech innovations offer several advantages:

- **Faster Payments:** Traditional payment systems can be slow and cumbersome, causing delays in transactions and impacting cash flow. Fintech solutions, such as digital wallets and payment gateways, facilitate faster and more efficient payments, reducing the time and cost associated with financial transactions (8).
- **Alternative Financing:** Fintech has introduced alternative financing options, such as supply chain finance and invoice financing. These solutions provide businesses with access to working capital by allowing them to receive early payment on invoices or extend payment terms with suppliers. This can improve liquidity and reduce financial strain on companies (9).
- **Flexible Pricing Models:** Fintech also enables more flexible and dynamic pricing models. For example, dynamic pricing algorithms can adjust prices in real-time based

on demand, supply, and market conditions, allowing businesses to optimize their pricing strategies and improve profitability (10).

Companies like PayPal and Stripe have transformed payment processing, enabling businesses to handle transactions seamlessly across borders (11). Additionally, platforms like Tradeshift offer supply chain finance solutions that help businesses optimize their cash flow and manage working capital more effectively (12).

3. Advanced Analytics and Artificial Intelligence

Advanced analytics and artificial intelligence (AI) are transforming supply chain management by providing deeper insights and enabling more informed decision-making. These technologies leverage vast amounts of data to improve forecasting, optimize inventory management, and enhance overall supply chain performance (13).

- **Predictive Analytics:** Predictive analytics uses historical data and statistical algorithms to forecast future trends and behaviors. In supply chain management, predictive analytics can help businesses anticipate demand, identify potential disruptions, and optimize inventory levels (14).
- **AI and Machine Learning:** AI and machine learning algorithms can analyze complex data sets and identify patterns that may not be apparent through traditional methods. These technologies can optimize routes for transportation, improve demand forecasting accuracy, and enhance decision-making processes (15).

For example, companies like Amazon and Walmart use AI and machine learning to optimize their supply chain operations, from inventory management to delivery logistics (16). These technologies help these companies maintain high levels of efficiency and customer satisfaction.

The Impact on Supply Chain Operations

The integration of financial innovations into supply chain management is yielding significant improvements in efficiency, transparency, and responsiveness. These advancements are addressing some of the most pressing challenges faced by traditional supply chains:

- **Increased Efficiency:** Financial tools like blockchain and fintech solutions streamline processes, reduce transaction times, and lower costs. By automating and digitizing financial transactions, businesses can operate more efficiently and allocate resources more effectively (17).
- **Enhanced Transparency:** Blockchain technology provides a transparent and immutable record of transactions, enhancing traceability and accountability. This transparency helps build trust among supply chain partners and ensures compliance with regulatory requirements (18).
- **Improved Resilience:** Financial innovations enable supply chains to be more resilient in the face of disruptions. For example, flexible financing options and dynamic pricing models allow businesses to adapt to changing market conditions and manage risks more effectively (19).

Real-world examples demonstrate the transformative impact of these financial tools. For instance, Maersk, a global leader in container shipping, has partnered with IBM to develop a blockchain-based platform called TradeLens. This platform aims to enhance transparency and efficiency in global shipping by providing a single, shared view of the supply chain (20).

2. Materials and Methods

To achieve the results discussed in this study, researchers employed a comprehensive method that involved investigating previous studies and analyzing existing literature. They conducted a thorough review of academic and industry sources, focusing on reports, case studies, and research articles that address the impact of financial innovations on supply chain operations (21). This review encompassed various financial tools, including blockchain technology, fintech solutions, and dynamic pricing models, to understand their effects on supply chain efficiency, transparency, and resilience (22).

The study synthesized insights from these sources to evaluate how new financial concepts are being implemented and their implications for supply chain management (23). By examining both quantitative data and qualitative findings from prior research, the researchers provided a detailed analysis of trends and outcomes related to financial changes in supply chains. This approach allowed for the identification of key patterns and correlations within the existing body of knowledge.

To ensure the accuracy and reliability of the findings, the researchers critically assessed the methodologies and results of previous studies, comparing and contrasting their findings to identify consistent trends and insights. This rigorous examination of the literature provided a solid foundation for the conclusions drawn in this study, offering valuable perspectives on the transformative impact of financial innovations on supply chain operations.

.3. Results and Discussion

3.1 Blockchain Technology

Blockchain technology has revolutionized the way transactions are recorded and verified within supply chains. By providing a decentralized and immutable ledger, blockchain enhances transparency and traceability, ensuring that every transaction is visible and cannot be altered. This technology mitigates the risk of fraud, reduces the need for intermediaries, and streamlines the flow of goods and information across the supply chain. Companies like IBM and Walmart have already integrated blockchain into their supply chains, resulting in improved tracking of products from origin to final destination.

3.2 Fintech Solutions

Fintech, or financial technology, encompasses a wide range of digital tools and platforms that are transforming financial services, including those related to supply chains. These solutions include digital payments, mobile banking, and online lending platforms that enable faster and more secure financial transactions. Fintech innovations are particularly beneficial in managing working capital, optimizing cash flow, and providing real-time financial data that supports decision-making in supply chain operations.

3.3 Dynamic Pricing Models

Dynamic pricing models allow companies to adjust prices in real-time based on market demand, supply levels, and competitor actions. This approach helps businesses optimize inventory levels, reduce excess stock, and respond swiftly to changes in the market. In supply chains, dynamic pricing can be applied to procurement processes, transportation services, and inventory management, leading to more efficient operations and higher profit margins.

3.4 Enhancing Operational Efficiency

Financial innovations are instrumental in enhancing the efficiency of supply chain operations. Blockchain, for example, reduces the time and resources needed for transaction verification and reconciliation. Fintech solutions streamline payment processes, reducing delays and errors in financial transactions. Dynamic pricing models help companies better align their pricing strategies with market conditions, minimizing waste and maximizing revenue. These innovations collectively contribute to faster, more efficient supply chains that can better meet customer demands.

3.5 Improving Transparency and Traceability

Transparency and traceability are critical components of modern supply chains, particularly in industries where product authenticity and safety are paramount. Blockchain technology plays a key role in enhancing these aspects by providing a clear, tamper-proof record of every transaction. This increased visibility allows companies to track the movement of goods through the supply chain, ensuring compliance with regulations and minimizing the risk of counterfeiting. Consumers also benefit from greater transparency, as they can access information about the origin and journey of products.

3.6 Strengthening Resilience and Risk Management

The global nature of supply chains makes them vulnerable to a wide range of risks, including geopolitical instability, natural disasters, and economic fluctuations. Financial innovations help mitigate these risks by providing more robust and flexible financial frameworks. For instance, fintech platforms offer supply chain financing options that can stabilize cash flow during periods of disruption. Blockchain's decentralized nature reduces the risk of single points of failure, while dynamic pricing models allow companies to quickly adjust to changing market conditions, ensuring continuity of operations.

Conclusion

The integration of new financial tools into supply chain management is driving a significant transformation in the way businesses operate. Blockchain technology, fintech solutions, and advanced analytics are reshaping traditional supply chain models, making them more efficient, transparent, and resilient. As these innovations continue to evolve, they will play a crucial role in shaping the future of supply chain management, enabling businesses to navigate the complexities of the modern global economy and meet the ever-changing demands of consumers.

This study will delve into the specifics of how these financial tools are revolutionizing supply chain operations, examining current trends, real-world examples, and the implications for the future of supply chain management. By exploring these advancements, the paper aims to provide a comprehensive understanding of the impact of financial innovation on supply chains and offer insights into the next steps for businesses seeking to leverage these tools for competitive advantage.

References

1. Christopher, M. (2016). Logistics & Supply Chain Management (5th ed.). Pearson.

2. Kotler, P., & Keller, K. L. (2016). Marketing Management (15th ed.). Pearson.

3. Mougayar, W. (2016). The Business Blockchain: Promise, Practice, and the Application of the Next Internet. Wiley.

4. Tapscott, D., & Tapscott, A. (2016). Blockchain Revolution: How the Technology Behind Bitcoin Is Changing Money, Business, and the World. Penguin.

5. Tapscott, D., & Tapscott, A. (2016). Blockchain Revolution: How the Technology Behind Bitcoin Is Changing Money, Business, and the World. Penguin.

6. IBM. (2020). IBM Food Trust. Retrieved from https://www.ibm.com/blockchain/solutions/food-trust

7. De Beers Group. (2020). Tracr: Blockchain for Diamonds. Retrieved from https://www.debeersgroup.com/tracr

8. Gaur, V., & Kumar, V. (2022). Fintech Innovations and Their Impact on Financial Services. Routledge.

9. Choi, T. M., & Lambert, D. M. (2020). Supply Chain Finance: Analysis and Perspectives. Springer.

10. He, W., & Zhang, Z. (2020). Artificial Intelligence in Supply Chain Management: Opportunities and Challenges. Journal of Business Research, 112, 286-299.

11. PayPal. (2020). PayPal for Business. Retrieved from https://www.paypal.com/business

12. Tradeshift. (2020). Tradeshift Supply Chain Finance. Retrieved from https://tradeshift.com/solutions/supply-chain-finance

13. He, W., & Zhang, Z. (2020). Artificial Intelligence in Supply Chain Management: Opportunities and Challenges. Journal of Business Research, 112, 286-299.

14. Kshetri, N. (2018). 1 Blockchain's roles in meeting key supply chain management objectives. International Journal of Information Management, 39, 80-89.

15. Gaur, V., & Kumar, V. (2022). Fintech Innovations and Their Impact on Financial Services. Routledge.

16. Amazon. (2020). Amazon Supply Chain Management. Retrieved from https://www.amazon.com

17. Choi, T

18. Christopher, M. (2016). *Logistics & Supply Chain Management* (5th ed.). Pearson.

19. Kotler, P., & Keller, K. L. (2016). *Marketing Management* (15th ed.). Pearson.

20. Mougayar, W. (2016). *The Business Blockchain: Promise, Practice, and the Application of the Next Internet*. Wiley.

21. Tapscott, D., & Tapscott, A. (2016). *Blockchain Revolution: How the Technology Behind Bitcoin Is Changing Money, Business, and the World*. Penguin.

22. Gaur, V., & Kumar, V. (2022). *Fintech Innovations and Their Impact on Financial Services*. Routledge.

23. Choi, T. M., & Lambert, D. M. (2020). *Supply Chain Finance: Analysis and Perspectives*. Springer.

Performance assessment of photovoltaic thermal system: An overview

Dhuha A. Shalash, N.A. Madlool.*

[1] Department of Mechanical Engineering, Faculty of Engineering, University of Kufa, 21 Kufa, Najaf, Iraq
[2] Department of Mechanical Engineering, Faculty of Engineering, University of Kufa, 21 Kufa, Najaf, Iraq
***** *Corresponding authors: dhuhaa.alkhalidi@student.uokufa.edu.iq; Tel.: +9647729561247.*

Abstract: The escalating needs of contemporary society, the process of industrialization, and advancements in technology have substantially augmented the need for energy. Hence, the engineering industry is aggressively pursuing environmentally friendly and economically efficient energy solutions. One of the potential solutions to the issue is the photovoltaic thermal system (PVT), which seeks to harness both electrical and thermal energy from solar radiation. The purpose of this research is to examine computational and experimental studies that assess the thermal and electrical efficiency of solar energy systems. Additionally, the discussion includes the significance of incorporating PCM with nanoparticles in solar energy systems. During the evaluation process, it was clear that adding fins to the phase change material (PCM) made the electrical conversion efficiency much better, by 10.2% to 10.9%. Both computational and practical investigations have shown that using a hybrid cooling system, which includes water and PCM materials for temperature management, results in a superior performance enhancement of 18.5% compared to concentric solar cells that are only cooled by phase change material. The best cooling performance for solar cells was achieved with Al2O3/TiO2 hybrid nanoparticles, which led to a 17.6% increase in electrical energy efficiency.

Keywords: Solar energy; Thermal energy; Electrical energy; PCM; Nanoparticles.

1. Introduction

Urgent concerns about climate change and the exhaustion of conventional energy resources have propelled the advancement of renewable energy technology. Solar energy is an abundant and ecologically advantageous kind of renewable energy. The use of photovoltaic (PV) technology holds significant promise for satisfying energy requirements via the capture and utilisation of solar energy. A photovoltaic device is a semiconductor-based apparatus that transforms a maximum of 20% of solar energy into electrical energy, while the other 80% is transformed into heat, resulting in an increase in the device's surface temperature [1]. Several studies [2] have shown that the rise in surface temperature greatly influences the performance and electrical conversion efficiency of photovoltaic (PV) systems. These findings are illustrated in Figure 1 and summarised in Table 1.

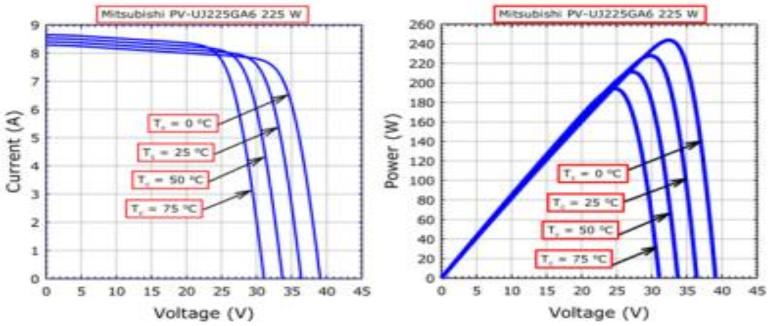

Figure 1. Analysis of the performance attributes of a polycrystalline silicon solar module at different cell surface temperatures [2]

Table 1: Impact of a photovoltaic surface temperature increase on electrical efficiency [2]

Temperature rise [°C]	Drop in electrical efficiency[%]	Reference
35	22.55	2
45	19.70	3
45	19.51	4
28	12.6	5
56	41	6

The widespread use of photovoltaics has prompted government agencies to implement plans for deploying high-capacity plants, owing to their environmental sustainability, cost-effectiveness, and high efficiency. In sunny regions where this technology is intended to be adopted, the efficiency of energy conversion in photovoltaics is reduced as a result of the elevated operating temperature of the cells. Solar panels absorb a substantial proportion of solar radiation as thermal energy, while transforming a lesser proportion into electrical energy. The use of PV/T technology has the benefit of lowering the temperature of solar modules while simultaneously enhancing their power generation. Furthermore, the PV/T technology produces thermal energy that can be harnessed for diverse applications. This study conducted a comprehensive examination of current research and papers published in the area of photovoltaic/thermal (PV/T) systems. The researchers partitioned the current study into many parts to elucidate and concentrate on the impact of each technology individually. The researchers employed numerous fluids, such as air, water, and oil, to boost the heat dissipation of the solar panels. Their investigation included a wide range of these fluids. Previous studies have often enhanced the thermal conductivity of liquid cooling fluids by including different kinds of nanoparticles with higher thermal conductivity. Previous studies have used variable-phase materials to exploit the substantial storage capacity of the latent heat present in these materials. Prior investigations have examined methods for enhancing the thermal conductivity of phase change materials (PCMs) by the incorporation of nanoparticles with superior heat conduction capabilities. Furthermore, researchers have successfully integrated nano-Phase Change Materials (nano-PCMs) and nanofluids into a cohesive system. By doing both theoretical research and practical testing, they have shown that this technique offers superior energy collecting and utilisation in comparison to current PV/T systems. Upon completion of the study, many significant discoveries have surfaced, indicating that the scope of the work remains restricted and necessitates more research endeavours and investigations.

2.Numerical studies of photovoltaic thermal system:

The study of algorithms that use numerical approximation for mathematical analysis problems—as opposed to symbolic manipulations—is known as numerical analysis (as differentiated from discrete mathematics). It is the study of numerical techniques that look for rough answers to issues rather than precise ones.

Oussama Rejeb et.al. [3] Demonstrated is the potential use of phase change materials (PCMs) to enhance the cooling of the cold sides of TEG modules. This, in turn, leads to an improvement in the electrical performance of the modules due to the significant latent heat possessed by PCMs. The phase change material (PCM) is located on the cold side of the thermoelectric (TE) module, functioning as a heat sink. This results in a higher temperature difference between the two sides of the TE module, hence enhancing its electrical output.

Hussain et al. [4] Suggested an explicit dynamic model for a photovoltaic/thermal dual fluid system (PVT) that simultaneously utilises nanofluid and air. Mathematical modelling and computational fluid dynamics (CFD) simulation were conducted using MATLAB® and ANSYS FLUENT® software, respectively. In addition, the impact of CuO nanofluid combined with air on heat transfer improvement is examined across several flow regimes, including laminar, transitional, and turbulent. Researchers determined that using a CuO nanofluid with air resulted in an overall equivalent efficiency of 90.3%, while using water with air yielded an efficiency of 79.8%.

3.Experimental studies of photovoltaic:

An experiment is a systematic and controlled technique used to provide evidence either in favour of or against a theory. Experiments provide understanding of cause-and-effect relationships by showcasing the result that arises when a certain aspect is modified. Experiments exhibit significant variations in terms of their objectives and scope, although they always depend on a replicable methodology and a rational examination of the outcomes. The experimental design of the PVT-collector utilises Paraffin Wax with a melting temperature of (58/60), as shown in Figure 2. Paraffin wax is a saturated hydrocarbon substance known as alkanes that functions as a phase change material (PCM). Paraffin wax is an effective thermal insulator that can store heat as it undergoes a phase change from solid to liquid. One can use this stored heat in a system at a later time [5].

Figure 2: Paraffin Wax (58/60)

We applied paraffin wax to the copper pipes to enhance the thermal characteristics of the hybrid PVT collector. We placed thermal sensors inside the paraffin wax, as well as behind both the PV panel and the FPC collector, and also on the standalone PV panel [6]. Table 2 displays the thermophysical specification of the used paraffin wax.

Table 2: Thermo physical specification of the used paraffin wax [6].

Material properties	Unit	Range
Melting point temperature	°C	40
Thermal conductivity	W/m °C	0.21
Liquid state density	kg/m^3	845
Solid state density	kg/m^3	925
Liquid state specific heat	kJ/kg °C	2.2
Solid state specific heat	kJ/kg °C	2.2
Latent heat of fusion	kJ/kg	198

The collector may be used to acquire both thermal and electrical solar energy simultaneously, without the need for segregation, while utilising the same surface area. The impact of weather conditions on both the electrical and thermal efficiency is taken into account, along with the temperature differential between the incoming and outgoing water in the collectors [7].

Lee et al. (2019) [8] Performed experiments with different water flow rates and used nanomaterials, namely CuO/water and Al2O3/water. The findings showed that the extremities achieved a flow rate of three litres per minute by squirting, which was compared to flow rates of one, two, and four litres per minute. The results indicate that the use of nano-liquids (CuO or water) in a PVT system leads to a significant improvement of 21.3% in thermal efficiency. The aqua-based system exhibited a 15.14% increase in thermal efficiency compared to both the water-based and nano-liquid (Al_2O_3/water) systems. Nevertheless, there was no alteration in electrical efficiency between the aqua-based system and the nanofluid system.

Al-Shahmani et.al.[9] Performed empirical trials on the PVT collector using several nanofluids, such as SiO_2, TiO_2, and SiC. The study revealed that the PVT collector using SiC nanofluid had the highest photovoltaic thermal (PVT) efficiency, reaching an impressive 81.73%. In addition, it attained a photovoltaic (PVT) electrical efficiency of 13.52% and the most favourable total energy coefficient (COE) of 0.93. The researchers derived the findings with a flow rate of 0.170 kg/s and solar irradiation values of 1000 W/m2. The performance of the PVT-TiO_2 nanofluids, PVT-SiO_2 nanofluids, and PVT-water showed a decreasing pattern.

4.Numerical and experimental studies of photovoltaic

Maryam Rahimi Khanegah et. al. [10] We investigated the temperature regulation of a concentrated solar panel by analyzing a hybrid cooling system that uses water and phase change material, both theoretically and experimentally. The concentrators used in this study were created and manufactured using innovative methods. We investigate the performance of the proposed system in comparison to a concentrated photovoltaic system cooled solely by phase change material. The evaluation shows a significant improvement in performance, with an 18.5% increase.

Zaiguo Fu et. al. [11] A unique layout concept for the heat exchanger has been provided, along with a comprehensive mathematical model that describes the heat transfer mechanism and operating efficiency of the PVT system. The findings indicate a strong correlation between the predicted temperature fluctuation of the PVT system and the actual system. Using a heat exchanger using phase change materials (PCMs) may increase the average electrical efficiency of the PVT system by around 1%.

5.PCM as a heat storage in solar energy .

Phase change materials (PCM) are very intriguing due to their ability to provide a tenfold increase in heat capacity (in comparison to traditional materials) while experiencing little or insignificant temperature fluctuations.

Muhammad Arslan Qasim et. al. [12] We investigated the temperature regulation of a concentrated solar panel by analysing a hybrid cooling system that uses water and phase change material, both theoretically and experimentally. We created and manufactured the concentrators used in this study using innovative methods. The proposed system's performance is compared to a concentrated photovoltaic system cooled solely by phase change material. The evaluation shows a significant improvement in performance, with an 18.5% increase.

Husam Abdulrasool Hasan et.al.[13] This study investigated the effects of nanoparticles (SiC, TiO_2, and SiO_2) distributed in water, which served as the main fluid, on the electrical and thermal efficiency of a photovoltaic thermal (PVT) collector that utilises jet impingement. We conducted a controlled indoor experiment to evaluate the performance of a PVT collector, considering specific solar irradiances and mass flow rates.

5.1 Analysis of PVT

The creation and promotion of efficient, inexpensive, and high-impact technologies, systems, and practices is vital. In order to enhance energy efficiency, researchers are now investigating the use of phase change materials (PCM) as innovative technologies. Figure 3 depicts the methods used for conducting thermal analysis of PVT collectors.

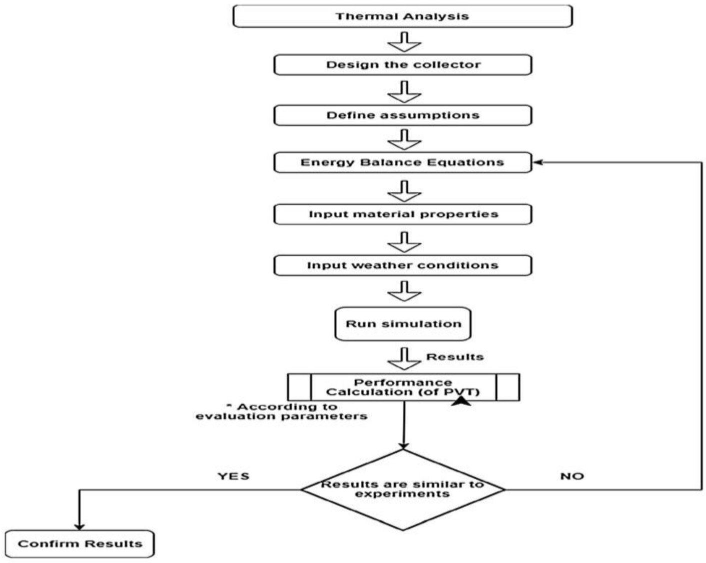

Figure 3: Methodology of PVT collector thermal analysis [6].

Nurul Syakirah Nazri et.al.[14] We assessed the efficacy of the PVT-TE collector by using a one-dimensional (1D) mathematical model in a steady-state study. We used Microsoft Excel and the inverse matrix approach to solve the energy balance equations. The investigation specifically examined experiments conducted on PVT and PVT-TE collectors with a solar radiation intensity of 593.16 W/m2.

Ramadan Gad et.al. [15] Developed a comprehensive mathematical model and calculated its solution using a customised Runge-Kutta algorithm in MATLAB software. The cooling system shown in Figure 4, which utilizes hybrid nanoparticles, achieves significantly higher daily energy efficiency rates of 56.45% and 54.45% compared to the typical solar cell system that employs SP31 and SP15-gel, which only achieve 8.77% and 7.84%, respectively. The mean exercise effectiveness of SP31/hybrid nano was 13.23%, with the maximum value recorded as 14.98% for SP15-gel/hybrid nano.

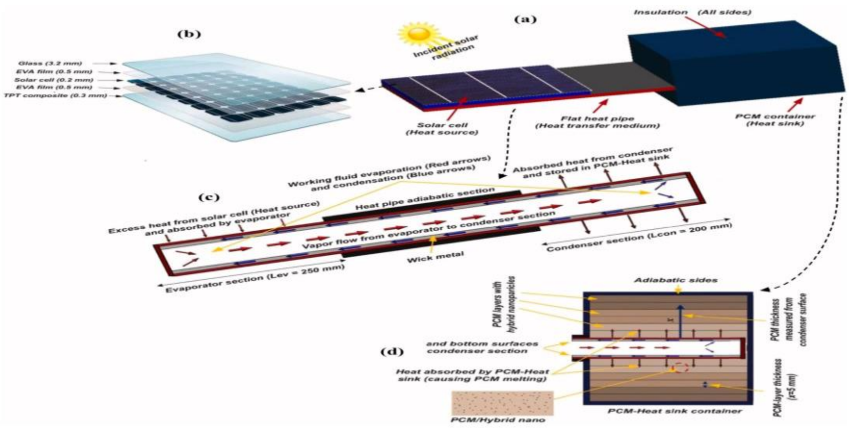

Figure 4: (a) proposed hybrid cooling system description (PV/HP/PCM-hybrid nano); (b) solar cell composition with the thickness of each layer; (c) construction and operation of the flat heat pipe; (d) composite PCM-heat sink.

6. Hypird PVT performance of PVT

Photovoltaic thermal collectors, commonly referred to as PVT collectors or hybrid solar collectors, are innovative power generation systems that harness solar radiation to produce both thermal and electrical energy.

Bourhan Tashtoush et.al.[16] Investigated the combination of solar-assisted humidification-dehumidification (HDH) and forward osmosis (FO) methods for the purpose of desalinating brackish water. We solve the FO sub-model using the finite difference method, and iteratively perform the HDH sub-model inside a single MATLAB function. The objective is to achieve a convergence error of 10−8.

6.1 Heating Hypird PVT performance of PVT

Abdulsahib M. Bassam et.al. [17] Conducted studies in a controlled setting using an indoor solar simulator with a solar irradiation intensity of 800W/m2. The use of nanoparticles facilitated the enhancement of thermal conductivities in both nano PCM and nanofluid , hence leading to an improvement in their overall performance.

6.2Cooling Hypird PVT performance of PVT

Ali Hassan et.al. [18] Evaluated the operational efficacy of the hybrid photovoltaic-thermal (PVT) system by analysing factors including photovoltaic (PV) temperature, electrical efficiency, thermal efficiency, and overall efficiency. The experiment included comparing a PVT/PCM system, which integrates water flowing via tubes inside the PCM, with a PV/PCM system and a regular PV system.

Talib K. Murtadha [19] Examined and contrasted prior studies that demonstrated the highest level of effectiveness through the use of a 2 wt% hybrid nanofluid for cooling the PV panels. Implementing a cooling system for the photovoltaic panels in order to optimise PV performance results in improved efficiency, longevity, and power production.

7.Photovoltaic in different designs technologies of photovoltaic

The photovoltaic thermal collector system (PVT) is an innovative technology that simultaneously produces thermal and electrical energy throughout the seasons.

Chunying Li et. al.[20] Conducted an experiment to examine the thermal, luminous, and electrical characteristics of a vertically mounted bifacial photovoltaic sunshade (BiPVS). The PV module oriented towards the west produced an average daily power of 709.4 kJ over a period of three consecutive days, while the PV module oriented towards the east generated an average daily power of 636.7 kJ. The average electricity efficiencies were 15.67% and 25.62%.

Yaser Maleki et.al. [21] Recently, there has been an investigation into the use of thermoelectric generators (TEG) and phase change materials (PCM). Phase-change materials (PCMs) safeguard the system from excessive heat by assimilating thermal energy when they reach their melting point. Thermoelectric generators (TEGs) use the temperature difference inside systems to produce electrical energy. Figure 5 depicts the experimental configurations: Thermal paste attaches the thermoelectric generator (TEG) modules to the rear surface of the system. Systems 1 and 2 are subjected to testing in real-world, outside situations. The figure illustrates the design of the system, with the PV/T-TEG-2PCM (system 1) located on the left and the PV/T-TEG (system 2) positioned on the right.

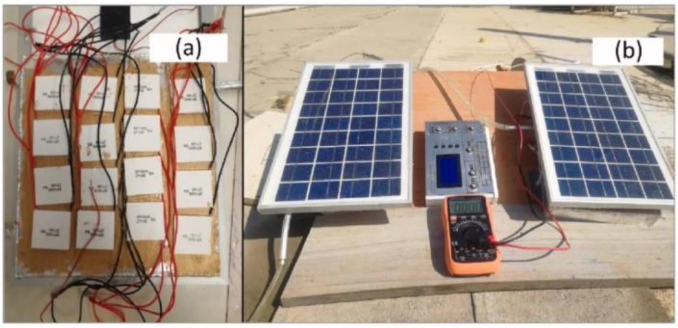

Figure 5: a)We affix thermoelectric generator (TEG) modules to the rear surface of the system using thermal paste. b) Systems 1 and 2 are subjected to real-world outdoor test circumstances.

Model	STF-120P6	Symbol
Electrical efficiency	14%	η_{elc}
Open circuit voltage	21.5 V	V_{oc}
Short circuit current	7.63 A	I_{sc}
Rated power	120 W	P_{max}
Voltage at P_{max}	17.4 V	V_{mp}
Current at P_{max}	6.89 A	I_{mp}

9. Conclusions

1. In the course of numerical investigations, it was determined that CuO exhibited the greatest direct conductivity and superior stability when compared to other nanofluids, utilising MATLAB and ANSYS Fluent.

2. Adding fins to the phase change material (PCM) led to a higher electrical conversion efficiency, rising from 10.2% to 10.9%. The enhancement is directly proportional to the number of fins. For instance, while using 8 fins, the efficiency gain ranged from 11.8% to 12.2%.

3. When using a hybrid cooling system that combines water and PCM materials to regulate temperature, both computational and experimental investigations have shown a significant performance enhancement of 18.5% compared to concentric photovoltaic cells that only rely on phase change material for cooling.

The findings demonstrated a noteworthy improvement in system efficiency and a 0.02% decrease in CO2 emissions.

4. HP-PCM surpasses the cooling efficiency of conventional solar panels and further improves it by using hybrid nanoparticles.

5. From a design perspective, it is evident that using PV/T-TEG-2PCM yields superior performance compared to PV/T-TEG. This is because PV/T-TEG-2PCM is capable of decreasing the average temperature of solar cells, resulting in a total efficiency that is 9.9% greater than the PV/TEG system.

6. Using a hybrid nanofluid composed of Al2O3 and TiO2 achieved the most optimal cooling performance for solar cells. This resulted in a significant 17.6% enhancement in the efficiency of electrical energy conversion.

Funding: Please add: “This research received no external funding”

Acknowledgments: In this section you can acknowledge any support given which is not covered by the author contribution or funding sections. This may include administrative and technical support, or donations in kind (e.g., materials used for experiments).

References

1. Nassar YF, Salem AA. The reliability of the photovoltaic utilization in southern cities of Libya. Desalination. 2007 Apr 30;209(1-3):86-90.
2. Cuce E, Cuce PM, Karakas IH, Bali T. An accurate model for photovoltaic (PV) modules to determine electrical characteristics and thermodynamic performance parameters. Energy Conversion and Management. 2017 Aug 15;146:205-16.
3. Oussama Rejeb, Bilal Lamrani, Ravita Lamb, Tarik Kousksou, Tareq Salameh, Abdelmajid Jemni, Abdul Kadir Hamid, Maamar Bettayeb, Chaouki Ghenai,(2023),'' Numerical investigations of concentrated photovoltaic thermal system integrated with thermoelectric power generator and phase change material'', Journal of Energy Storage, Vol. 62, pp., 106820, https://doi.org/10.1016/j.est.2023.106820
4. M. Imtiaz Hussain, Jin-Hee Kim, Jun-Tae Kim " Nanofluid-powered dual-fluid photovoltaic/thermal (PVT) system: Comparative numerical study", Energies 12 (5), 775, 2019.
5. Haytham Yousef (2019), "Experimental study of design a hybrid photovoltaic thermal collector (PVT -collector) for a domestic use", Palestine Polytechnic University, Master thesis.
6. Ali H.A. Al-Waeli, Miqdam T. Chaichan, K. Sopian a, Hussein. Kazem, Hameed B. Mahood, Anees A. Khadom ,(2019),"Modeling and experimental validation of a PVT system using nanofluid coolant and nano-PCM", Solar Energy,vol.177,pp. 178-191. https://doi.org/10.1016/j.solener.2018.11.016.
7. "Experimental study of design a hybrid photovoltaic thermal collector (PVT -collector) for a domestic use."
8. Joo Hee Lee, Seong Geon Hwang and Gwi Hyun Lee "Efficiency Improvement of a Photovoltaic Thermal (PVT) System Using Nanofluids".
9. Ali Najah Al Shahmani, K. Sopian, Sohif Mat, Husam Abdulrasool Hasan, Azher M. Abed, M.H. Ruslan,(2016),'' Experimental studies of rectangular tube absorber photovoltaic thermal collector with various types of nanofluids under the tropical climate conditions'', Energy Conversion and Management, vol.124,pp.528-542, https://doi.org/10.1016/j.enconman.2016.07.052.
10. Maryam Rahimi Khanegah, Ali Ashrafizadeh, Danial Borooghani, Farschad Torabi, ,(2023),'' Performance evaluation of a concentrated Photovoltaic/thermal system based on water and phase change Material: Numerical study and experimental validation'', Applied Thermal Engineering, Vol. 232, pp., 120936, https://doi.org/10.1016/j.applthermaleng.2023.120936
11. Zaiguo Fu, Xiaotian Liang, Yang Li, Lingtong Li, Qunzhi Zhu,(2021),"Performance improvement of a PVT system using a multilayer structural heat exchanger with PCMs", Renewable Energy,Vol.169,pp. 308-317, https://doi.org/10.1016/j.renene.2020.12.108.
12. Muhammad Arslan Qasim, Hafiz Muhammad Ali, Muhammad Niaz Khan, Nauman Arshad, Danyal Khaliq, Zarghoon Ali, Muhammad Mansoor Janjua,(2020),'' The effect of using hybrid phase change materials on thermal management of photovoltaic panels – An experimental study'', Solar Energy,Vol. 209, pp. 415-423, https://doi.org/10.1016/j.solener.2020.09.027.
13. Husam Abdulrasool Hasan, Kamaruzzaman Sopian, Ahed Hameed Jaaz, Ali Najah Al-Shahmani,(2017),'' Experimental investigation of jet array nanofluids impingement in photovoltaic/thermal collector'', Solar Energy, vol.144, pp.321–334, https://doi.org/10.1016/j.solener.2017.01.036.
14. Nurul Syakirah Nazri, Ahmad Fudholi, Evgeny Solomin, Maulana Arifin, Mohammad Hossein Yazdi, Tri Suyono, Eka Rakhman Priandana, Muslizainun Mustapha, Muhamad Hafiz Hamsan, Afifuddin Husairi Hussain, Mohd Fadhli Shah Khaidzir, Muhammad Ibrahim Ali Zaini, Nurul Nazli Rosli, Masita Mohammad, Kamaruzzaman Sopian ,(2023), ''Analytical and experimental study of hybrid photovoltaic–thermal–thermoelectric systems in sustainable energy generation'',Case Studies in Thermal Engineering,vol.51,pp.103522, https://doi.org/10.1016/j.csite.2023.103522.

15. Ramadan Gad, Hatem Mahmoud c d, Shinichi Ookawara e, Hamdy Hassan af,(2023), “Evaluation of thermal management of photovoltaic solar cell via hybrid cooling system of phase change material inclusion hybrid nanoparticles coupled with flat heat pipe”, Journal of Energy Storage,vol.57,pp.106185, https://doi.org/10.1016/j.est.2022.106185.
16. Bourhan Tashtoush, Jamal Al-Omari,(2023),’’Solar-assisted hybrid integration of humidification-dehumidification and forward osmosis for brackish water desalination: A parametric study’’, Case Studies in Chemical and Environmental Engineering,vol.8,pp.100500, https://doi.org/10.1016/j.cscee.2023.100500.
17. Abdulsahib M. Bassam, Kamaruzzaman Sopian, Adnan Ibrahim, Anwer B. Al-Aasam, Mojtaba Dayer,(2023),’’ Experimental analysis of photovoltaic thermal collector (PVT) with nano PCM and micro-fins tube counterclockwise twisted tape nanofluid’’, Case Studies in Thermal Engineering,vol.45,pp.102883, https://doi.org/10.1016/j.csite.2023.102883
18. Ali Hassan, Abdul Wahab, Muhammad Arslan Qasim, Muhammad Mansoor Janjua, Muhammad Aon Ali, Hafiz Muhammad Ali, Tufail Rehman Jadoon, Ejaz Ali, Ahsan Raza, Noshairwan Javaid,(2020),’’Thermal management and uniform temperature regulation of photovoltaic modules using hybrid phase change materials-nanofluids system’’, Renewable Energy,vol.145,pp. 282-293, https://doi.org/10.1016/j.renene.2019.05.130.
19. Talib K. Murtadha,(2023), “Effect of using Al2O3 / TiO2 hybrid nanofluids on improving the photovoltaic performance”, Case Studies in Thermal Engineering,vol.47,pp. 103112, https://doi.org/10.1016/j.csite.2023.103112.
20. Chunying Li, Wankun Zhang, Juhu Wu, Yuanli Lyu, Haida Tang,(2023), ‘’Experimental study of a vertically mounted bifacial photovoltaic sunshade’’, Renewable Energy,Vol 219, pp. 119518, https://doi.org/10.1016/j.renene.2023.119518
21. Yaser Maleki, Fathollah Pourfayaz, Mehdi Mehrpooya ,(2022),“Experimental study of a novel hybrid photovoltaic/thermal and thermoelectric generators system with dual phase change materials”, Renewable Energy,Vol.201,pp.202-215, https://doi.org/10.1016/j.renene.2022.11.037.

Intelligent Control Strategies for Permanent Magnet Synchronous Machines in Robotics and Automation

Kasim M. Al-Aubidy, Abdullah F. Al-Saoudi, and Izziyyah M. Alsudi
Mechatronics Eng. Dept., Tishk International University, Erbil, Iraq
Email: qasim.obaidi@tiu.edu.iq

Abstract:
Permanent magnet synchronous machines (PMSMs) are of great interest in automation and robotics for their compact size, high efficiency, and low maintenance requirements. However, controlling their speed and position presents challenges, primarily due to the necessity for precise rotor position detection. This paper addresses the significance of accurate rotor position detection in such drive systems, along with strategies for controlling the operation of permanent magnet motors. Conventional controllers such as PID controllers are commonly employed but are often affected by changes in system dynamics, requiring periodic updates for controller parameters based on the precise mathematical model of the motor. This research aims to explore several intelligent control strategies that do not rely on the mathematical model of the PMSM. The performance of the PMSM drive system will be evaluated using various intelligent controllers, including; fuzzy logic controller, neural network controller, and adaptive neural fuzzy inference system (ANFIS) controller. The performance of these intelligent controllers will be compared against that of a PID controller, which relies on PMSM mathematical model to obtain optimal or suboptimal parameters of the controller. The results presented in this paper demonstrate the capability of the proposed smart controllers to effectively regulate the speed of PMSMs compared to a PID controller.

Keywords: PMSM, Rotor position detection, PID controller, Fuzzy control Neural networks control, ANFIS controller, Brushless Drive system.

I. INTRODUCTION

A Permanent Magnet Synchronous Motor (PMSM) is an alternating current (AC) synchronous motor utilizing permanent magnets for field excitation. PMSMs are known for their efficiency, speed, compact size, brushless operation, high reliability, and dynamic performance [1]. These characteristics make them invaluable in automation and robotics applications, where smooth operation and reliability are paramount. However, controlling PMSM operation presents challenges, especially in accurately determining rotor position, critical for precise control of electronic devices in drive units [2]. The electronically commutated PMSM operates similarly to a brushless DC motor. Various methods are employed to detect rotor position accurately, essential for achieving precise motor speed and position control [3.4].

AC motor drives are nonlinear, multivariable systems with complex dynamic behavior attributed to the coupling between rotor and stator windings [5]. In real-time drive systems, controlling such machines demands sophisticated control strategies that are challenging to implement without using advancements in artificial intelligence. There is extensive research and studies exploring the use of PMSM across a wide range of applications, including industrial, aerospace, service, and healthcare. Some applications focus on speed control schemes [5,6], while others prioritize position control [7,8]. In some cases, steady-state operation is critical, while in others, dynamic performance takes precedence. In PMSM drive systems, the rotor position sensor is necessary to control the inverter power devices. One of the challenges facing current methods of rotor position detection is the cost and reliability of the sensors [1,2]. Optical encoders or Hall effect sensors are often used to sense rotor position and may be susceptible to contamination or damage [3,4]. PMSM drive systems operate in two control modes: open loop and closed loop. In open-loop mode, an independent oscillator controls motor speed without using a rotor position sensor. While closed-loop mode utilizes feedback from a rotor position sensor to directly control inverter power switches. Open-loop configuration is simpler as it does not require a rotor position sensor, relying instead on precise adjustment of motor speed with high precision PWM inverters [2]. However, under significant load torque, the motor may lose synchronization (pullout), therefore closed-loop control is necessary. The primary objective of closed-loop control is to enhance system stability and achieve torque control across the desired speed range [9]. PMSM drive systems have gained popularity in various industrial applications due to their ability to combine desirable performance characteristics of both DC and AC drives [1,2,10].

The performance of traditional controllers has been unsatisfactory in many applications since these controllers require constant adjustment of their parameters, which depend heavily on prior knowledge of the precise mathematical model of the drive system [11,12]. Alternative control algorithms have also been employed, including direct torque control [13,14], adaptive control [11,12], and model reference control [9,13]. With the growing interest in artificial intelligence (AI) and its applications, intelligent control systems capable of delivering fast dynamic responses have emerged. Controllers based on fuzzy logic [2] or neural networks [12] can be designed to control the speed or position of motors. Genetic algorithms can also be used as optimization tools to find the optimal values for controller parameters [14]. Additionally, research has explored the use of adaptive neuro-fuzzy inference system (ANFIS) as a hybrid tool that combines the benefits of both fuzzy logic and neural networks, showing promising results in controlling PM motors under various conditions [15,16,17]. Deep learning algorithms [18] can also be applied to control PMSMs due to their ability to model nonlinear systems and adapt to changes in motor behavior and environmental conditions, making them highly flexible in real-world applications.

This research aims to explore several intelligent control strategies that do not rely on the mathematical model of the PMSM. It will address the design of four controllers: a fuzzy logic controller, a neural network controller, an ANFIS-based controller, and a deep learning controller, in addition to the PID controller for comparison purposes. The structure of the paper is as follows: the second section covers background information on the components of the PMSM system. Traditional control methods for the PMSM system are discussed in the third section. Intelligent control methods are addressed in the fourth section. Section Five presents the results and evaluation of these control techniques, with the most significant conclusions summarized in section six.

II. PMSM DRIVE SYSTEM ELEMENTS

A PMSM drive system typically consists of four basic components that collaborate to control motor operation, as illustrated in Figure 1:

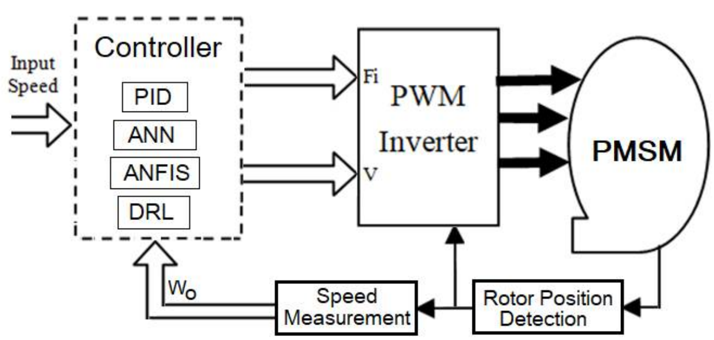

Figure 1: Elements of a PMSM drive system.

1. PMSM Motor:

The motor comprises two main parts: the stator and the rotor. The stator contains coils (typically three-phase) through which AC current flows, generating a rotating magnetic field. The rotor incorporates permanent magnets. The interaction between the stator's magnetic field and the rotor's magnets creates motor torque.

2. Inverter:

Converts DC current from a power source (or battery) into AC current to supply the motor. The inverter regulates the frequency and amplitude of the AC voltage applied to the motor windings, thereby governing the motor's speed and torque.

3. Rotor position detection:

The detection of rotor position is crucial for developing an efficient PMSM drive with enhanced performance. Accurate estimation of rotor position significantly impacts starting torque. Inaccurate estimation may reduce torque and cause the motor to rotate in the wrong direction [6]. Various methods exist for detecting rotor position in PMSMs, some employing mechanical sensors and others not. Methods include optical encoders, potentiometers, resolvers, search coils, and Hall-effect sensors.

Preferably, a rotor position sensor should accurately detect the position of the rotor magnet relative to the stator windings. Optical encoders may not accurately reflect the rotor magnet's actual position when the stator is energized through the inverter. In such cases, search coils or Hall-effect detectors are preferred for rotor position detection. The output from the rotor position sensor is then utilized to measure the position and speed of the PMSM.

4. Microcontroller:

The microcomputer is one of the most crucial components in any drive system, responsible for implementing measurement and control algorithms. It also facilitates communication with other units both within and outside the system.

III. CONVENTIONAL CONTROL METHODS

There are various types of control techniques used to adjust the performance of PMSMs under different operating conditions. However, the choice of control method depends on the desired performance characteristics. Many control strategies have been introduced to enhance PMSM performance, some relying on mathematical models of the PMSM, while others utilize AI and soft-computing tools. This paper will discuss conventional control methods as well as those based on artificial intelligence concepts.

Conventional control methods for PMSM typically include PID control, direct torque control, field-oriented control, and sliding mode control. Generally, these methods are straightforward and suitable for applications where high performance is not crucial. However, they often come with several disadvantages. For instance, they may exhibit limited performance, lack flexibility, control precision, and sensitivity to motor parameter variations. Therefore, they require an accurate mathematical model of the PMSM to effectively update controller parameters. For example, PID controllers are widely used in industrial control systems due to their simplicity and effectiveness in regulating processes. However, such a controller requires constant parameter updates when used to control a motor. The general PID control equation is:

$$u(t) = K_p e(t) + K_i \int e(t)dt + K_d \frac{de(t)}{dt} \qquad (1)$$

There are several methods to update controller parameters, including manual trial and error, system response tests, and heuristic approaches. For instance, the Ziegler-Nichols method is a well-known heuristic approach that involves step-response testing of the system to determine initial PID parameters. This method systematically adjusts PID parameters to enhance stability and response either by directly performing a step response test or by using the ultimate gain and period. Effective implementation of this tuning method necessitates careful interpretation of step-response data.

IV. INTELLIGENT CONTROL METHODS

PMSMs exhibit non-linear characteristics, and soft-computing tools can effectively model and control these nonlinearities, providing smoother and more accurate control compared to conventional linear controllers. Intelligent controllers exhibit robustness against changes in system plant parameters compared to conventional controllers and offer superior noise rejection capabilities. As modern control strategies become more sophisticated, adaptive controllers remain highly competitive in high-performance drive applications. Therefore, employing an AI-based controller can effectively deliver accurate and faster solutions while handling complex nonlinear characteristics. The following AI-based controllers will be considered:

1. Neural Network Control:

The use of ANN as a parallel simulation tool to implement the required controller of the PMSM is depicted in Fig. 2. ANNs represent a superior alternative to conventional PID controllers. A supervised multi-layer feedforward ANN trained with back-propagation is feasible for PMSM control. The ANN includes input and output layers, along with hidden layers whose optimal number and nodes typically require trial and error. This controller features an input layer with two nodes (representing error and integral of error), a hidden layer with 100 nodes, and an output layer with a single node, with 70% training, 15% validation, 15% testing.

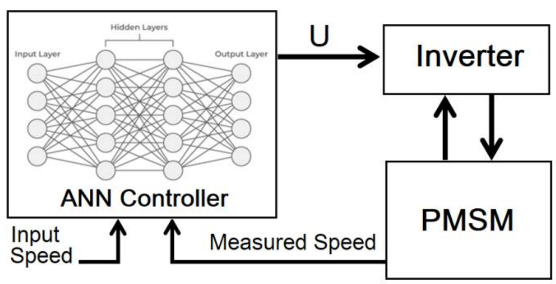

Figure 2: ANN control of PMSM.

2. Fuzzy Logic Control:

Fuzzy logic strategies closely mimic expert knowledge and experience. Figure 3 illustrates the layout of a fuzzy control system, comprising fuzzification, a rule database, rule inference, and defuzzification. A straightforward structure of Fuzzy Logic Controller (FLC) is utilized for motor speed regulation.

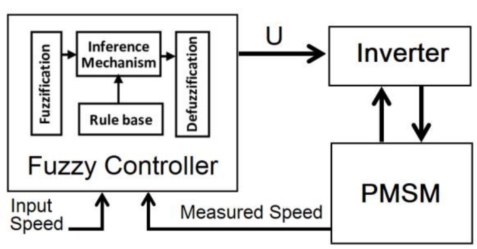

Figure 3: Fuzzy control of PMSM drive.

The FLC architecture uses fuzzy logic rules as shown in table I, which are structured as IF-THEN statements to map input variables (such as error and derivative of error) to an output.

Table I: Fuzzy Rules.

e / Δe	VVL	VL	L	M	H	VH	VVH
VVL	VVL	VVL	VL	L	M	H	VH
VL	VVL	VL	L	L	M	H	VH
L	VL	L	L	M	M	H	VH
M	L	L	M	M	H	H	VH
H	M	M	M	H	H	VH	VVH
VH	H	H	H	H	VH	VH	VVH
VVH	VH	VH	VH	VH	VVH	VVH	VVH

3. ANFIS-based controller:

Adaptive Neuro-Fuzzy Inference System is a powerful hybrid intelligent system that combines the adaptability of neural networks with the interpretability of fuzzy logic. ANFIS-based controllers can adapt to varying operating conditions and system dynamics of PMSMs, making it suitable for applications where the motor operates under different loads and speeds. The most important issue in using ANFIS for PMSM drive is its ability to learn from data, enabling it to improve its control performance over time without requiring extensive manual tuning. In fact, using ANFIS-based controllers in PMSMs allows for robust and adaptive control, capable of handling the complexities and nonlinearities inherent in such systems, thereby enhancing overall performance and efficiency. Figure 4 shows the layout of the implemented ANFIS-based controller for the PMSM drive.

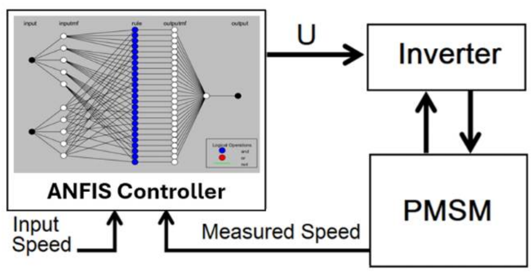

Figure 4: ANFIS-based controller of PMSM drive.

The ANFIS architecture employs fuzzy logic rules, outlined in Table II, structured as IF THEN statements to map input variables (like error and change in error) to an output. Each input variable corresponds to fuzzy sets, and their combinations create a rule base. Through training, the network optimizes these rules, improving the system's ability to handle complex, nonlinear control tasks.

Table II: ANFIS Fuzzy rules.

e / Δe	Very Low	Low	Medium	High	Very High
Very Low	VL	VL	L	L	M
Low	VL	L	L	M	M
Medium	L	L	M	M	H
High	L	M	M	H	H
Very High	M	M	H	H	VH

4. DRL-based Controller:

Deep learning architectures consist of three main layers: the input layer, hidden layers, and the output layer. The complexity of these architectures varies based on their depth, which is determined by the number of hidden layers, and the type of activation functions used, which influence the model's nonlinearity. Figure 5 illustrates the architecture of a deep learning network, which consists of an input layer, six hidden layers, and an output layer. The input layer is two-dimensional and sequential, used to input sequence data and apply data normalization. The hidden layers include three fully connected (fc) layers with 10 hidden neurons each, a hyperbolic tangent (tanh) activation layer, a leaky rectified linear unit (ReLU) layer, and a clipped rectified linear unit (ReLU) layer.

The output layer is a regression layer. In this layer, a combination of features from the previous layers is used to identify larger patterns in the image. For regression problems, the output size corresponds to the number of response variables. When the input is a sequence, fully connected layers operate independently at each time step. The hyperbolic tangent (tanh) activation layer applies the tanh function to the layer inputs, which transforms any real number input into an output ranging from -1 to 1. Leaky ReLU layers perform threshold operations by multiplying input values less than zero by fixed scalars. Clipped ReLU layers also perform threshold operations, setting any input value less than zero to zero and capping values above a specified ceiling. This clipping prevents the output from becoming excessively large. The regression layer calculates the half-mean-squared-error loss. Typical regression problems require a regression layer following a fully connected layer. Figure 6 shows the layout of the implemented deep learning-based controller for the PMSM drive.

Figure 5: Architecture of the DL-based controller.

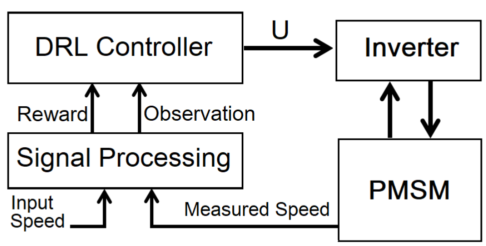

Figure 6: Layout of the DL-based controller.

V. RESULTS AND DISCUSSION

PMSM motors are widely used in automation and robotics due to their high efficiency, compact size, and low maintenance requirements. The performance of these motors largely depends on the accuracy of rotor position sensing and the chosen control algorithm. This study focuses on analyzing the performance of PMSM motors using five different control algorithms. The most suitable algorithm depends on the specific requirements of the application. Due to the inherent complexity and nonlinearity in automation systems and robotics applications involving PMSM, an adaptive control algorithm is necessary. Such algorithms are effective in handling both internal dynamics and external disturbances. When evaluating the performance of the five controllers under identical conditions, the simulation results clearly show some differences in performance. It is clear that the DL, ANFIS, and FLC controllers provide smoother and more stable responses compared to the PID and NN controllers, indicating better management of system dynamics. This comprehensive comparison highlights the effectiveness of advanced control methods, such as FLC, ANFIS, and DL controllers, in achieving optimal speed control with minimal overshoot and rapid stability. Table III compares the performance metrics of the five controllers tested with the motor. The PID and NN controllers exhibit similar performance, though the NN performs slightly worse overall. The FLC and ANFIS controllers have identical values except for overshoot, with the FLC showing less overshoot. The DL controller significantly outperforms all other controllers across every metric, demonstrating the lowest errors, minimal overshoot, and the fastest rise and peak times.

Table III: Comparative Analysis.

Controller	ITAE	IAE	ISE	Overshoot %	Rise time (s)	Peak time (s)
PID	1.508	0.5612	0.1723	4.734	0.613	1.5
NN	1.51	0.5866	0.1766	5.851	0.608	1.448
FLC	1.945	0.4712	0.1654	3.846	0.536	1.383
ANFIS	1.945	0.4712	0.1654	4.521	0.536	1.383
DL	0.6801	0.1278	0.0449	0.348	0.118	0.5

It is clear from Figure 7 that all controllers aim to achieve and maintain a rotating speed of 1 rad/s. Among them, the DL controller performs the best, demonstrating a fast response with minimal overshoot and quickly stabilizing at the desired set-point. The PID controller also shows a good response but with slightly higher overshoot. The NN controller initially drops from the set-point before stabilizing. The ANFIS and FLC controllers exhibit performance similar to the DL controller, but with slightly higher overshoot and slower stabilization. Overall, the DL controller achieves the best balance between speed and stability in this comparison.

In Figure 8, all controllers aim to maintain an angular velocity of 1 rad/s. Two inset markers highlight specific regions of the system response for better clarity. The first inset (around 4 seconds) focuses on the initial transient response. The DL controller (green dashed line) quickly reaches the set-point with minimal overshoot. The PID controller (blue line) performs well but with slight overshoot. The NN controller (red dashed line) shows a dip before stabilizing. The ANFIS (black dashed line) and FLC (purple dashed line) controllers exhibit slightly higher overshoots but stabilize quickly. The second inset (around 14-17 seconds) illustrates the system's response to disturbances or noise in the steady-state region. The DL controller maintains the best stability with minimal oscillations. The PID controller shows small oscillations, while the NN, ANFIS, and FLC controllers display larger fluctuations, indicating less stability under disturbances. The results given in Table III and the PMSM speed response indicate that the DL controller demonstrates the best performance compared to the other four controllers. It achieves fast stabilization with minimal overshot and superior disturbance rejection, making it the most efficient among those compared.

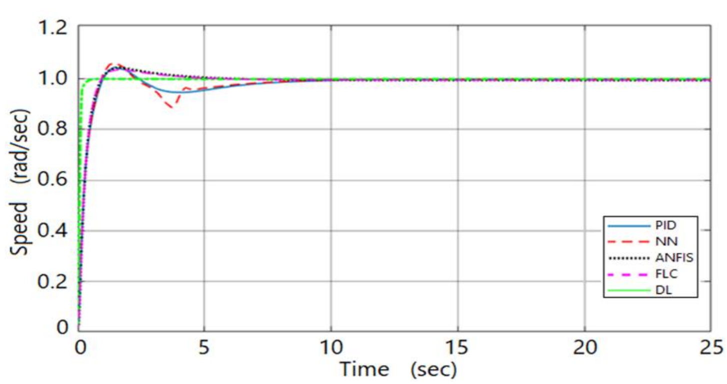

Figure 7: Speed response without disturbances.

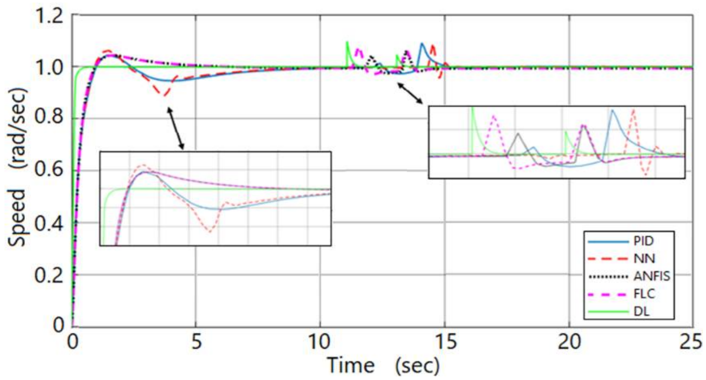

Figure 8: Speed response of a PMSM with disturbances.

VI. Conclusion

Permanent magnet synchronous machines have gained significant importance in automation and robotics due to their high efficiency, compact size, and low maintenance requirements compared to other machines. Despite these advantages, challenges arise in their control, particularly in accurately detecting rotor position and employing a controller that can adapt to system dynamics. This paper explores several intelligent control strategies that do not rely on a mathematical model of PMSMs and compares their performance with that of a PID controller, which requires continuous parameter tuning. Each control method has its own advantages and disadvantages, making it essential to carefully evaluate which method best suits specific application requirements and operational constraints. Test results indicate that ANFIS, FLC and DL-based controllers provide smoother and more stable responses compared to PID and NN controllers. Among them, FLC and ANFIS controllers demonstrate identical performance, except in terms of overshoot, where FLC exhibits a smaller overshoot. Notably, the DL-based controller significantly outperforms all others in terms of the lowest errors, minimal overshot, and the fastest rise and peak times. Thus, DL-based controllers are effective in motor control because they can model complex nonlinear systems and adapt to changes in motor behavior and environmental conditions, making them flexible and robust in real-world applications.

ACKNOWLEDGEMENTS

This research was supported by Tishk International University. The authors are grateful for the financial support provided by the institution.

References

1. K. J. Binns, K. M. Al-Aubidy and D. W. Shimmin, “A self-commutating PM machine with implicit rotor position sensing using search coils”, Intr. Conf. On Electr. Machines [ICEM’90], Paper No.17-3, MIT, Cambridge USA, August 1990.
2. K. Al-Aubidy and G. M. Amer, “Real-Time Fuzzy Control of a Sensorless PM Drive System, 3rd IEEE Intr. Conf. on Systems, Signals, Devices (SSD05), Paper Ref. PES-115, Tunisia, 21-24 March, 2005.
3. K. J. Binns, K. M. Al-Aubidy and D. W. Shimmin, “Implicit rotor position sensing using search coils for a self-commutating PM drive system”, IEE Proceedings, Vol.137, Pt.B, No.4, July 1990, pp.253-258, DOI: 10.1049/ip-b.1990.0030, EID: 2-s2.0-0025464744.
4. K. J. Binns, K. M. Al-Aubidy and D.W. Shimmin, “Implicit rotor position sensing using motor windings for a self-commutating PM drive system”, IEE Proceedings, Vol.138, Pt.B, No.1, January 1991, pp.28-34. DOI: 10.1049/ip-b.1991.0004, EID: 2-s2.0-0026000130.

5. A. Patil and G. Palnitkar, “Comparative Study and Implementation of Speed Control of BLDC Motor using Traditional PI and Fuzzy-PI Controller”, International Journal of Engineering Research & Technology (IJERT), Vol. 9 Issue 04, April-2020, pp:568-573.
6. X. Zhang, A. Semjonovs, Y. Zbede, A. Bodrov and J. Apsley, “Speed Sensorless Control of a Surfacemounted Permanent Magnet Drive”, 10th IEEE International Conference on Power Electronics and ECCE Asia (ICPE 2019 - ECCE Asia), 2019, pp. 1-10.
7. Hassan Rashag, and Jaber G. Talib, “Control system optimization based on PID with artificial intelligent for machine”, Materials Today: Proceedings, 2214-7853, 2020.
8. M. H. Basappa and P. Viswanathan, “Direct Torque Control for Permanent Magnet Synchronous Motor Using Golden Eagle Optimized ANFIS”, International Journal of Intelligent Engineering and Systems, Vol.15, No.4, 2022, pp: 499-508, 10.22266/ijies2022.0831.45. DOI:
9. Y. L. Cai and Hongwei Ma,”Sensorless speed control of PMSM based on improved MRAS method”, 2017 China International Electrical and Energy Conference (CIEEC), 2017, pp:210-214.
10. A. Ghamria, R. Boumaaraf, M. T. Benchouia, H. Mesloub, A. Golea and N. Golea, “Comparative study of ANN DTC and conventional DTC controlled PMSM motor”, Mathematics and Computers in Simulation (IMACS), Vol.167, Janusry 2020, pp:219-230.
11. 11. J. Kang, W.J. Meng, A. Abraham, and H.B. Liu, “An adaptive PID neural network for complex nonlinear system”, Neurocomputing 135, 2014, pp:79–85.
12. 12. Z. Jia and B. Kim, “Direct Torque Control with Adaptive PI Speed Controller based on Neural Network for PMSM Drives”, MATEC Web of Conferences, Vol.160, 02011, 2018, https://doi.org/10.1051/matecconf/201816002011.
13. 13. A. F. Al-Saoudi, K. M. Al-Aubidy and A. H. Al-Mahasneh, “Comparison of PID, Fuzzy Logic, ANFIS and Model Predictive Controllers for Cruise Control System”, 21st IEEE Intr. Multi-Conf. on Systems, Signals, Devices (SSD24), Erbil-Iraq, 22-25 April 2024.
14. 14. Omar Ouledali, Abdelkader Meroufel, Patrice Wira, and Said Bentouba, “Genetic Algorithm Tuned PI Controller on PMSM Direct Torque Control”, Algerian Journal of Renewable Energy and Sustainable Development, Vol. 1, No. 2, December 2019, pp:204-2011, DOI:10.46657/ajresd.2019.1.2.10.
15. 15. M. H. Basappa and P. Viswanathan, “ANFIS based Direct Torque Control of PMSM Motor for Speed and Torque Regulation”, Indonesian Journal of Electrical Engineering and Informatics (IJEEI) Vol. 10.52549/ijeei.v10i3.3775. 10, No. 3, September 2022, pp:549-558, DOI:
16. 16. M. M. Abdulghani and K. M. Al-Aubidy, “Design and Evaluation of a MIMO ANFIS using MATLAB and V-REP”, 8th International Conference on Recent Trends in Communication and Computer Networks (ComNet 2020). September 25-26, 2020. Chennai, India. Published in: GRENZE International Journal of Engineering and Technology, Vol.6, No.2, pp:129 136, Grenze ID: 01.GIJET.6.2.11_2.
17. 17. I. Kuvvetli, A. Tap and L. T. Ergene, "PI Based ANFIS Controller Design for PMSM Drives," 2021 13th International Conference on Electrical and Electronics Engineering (ELECO), Bursa, Turkey, 2021, pp. 383-387, doi: 10.23919/ELECO54474.2021.9677784.
18. 18. M. Nicola, and C.I. Nicola, “Improvement of PMSM Control Using Reinforcement Learning Deep Deterministic Policy Gradient Agent”, 21st International Symposium on Power Electronics (Ee2021), Serbia, October 2021, DOI:10.1109/Ee53374.2021.9628371.

AI in Supply Chain Risk Management: Identifying, Assessing, and Mitigating Risks

Nader AlTamimi[1], Bader AlTamimi[2], Mohammad Abdallah[3] and Mahmoud Allahham[4]

[1] German Jordanian University, Amman, Jordan

[2] Hashemite University, Zarqa, Jordan

[3]Al-Zaytoonah University of Jordan, Amman, Jordan

[4] Luminus Technical University College, Amman, Jordan

n.altamimi@gju.edu.jo, Mobile No. 00962796668044

.

Abstract: This literature review explores the changing landscape of supply chain risk management in the complex and dynamic global market of the present time. It discusses a variety of existing research on the topic and underlines the importance of managing supply chain risks effectively. It also highlights the role of (AI) and the significance of managing supply chain risks effectively. It also discusses the theories of resilience and continuity as responses to risks. Lastly, the review focuses on the development of advanced risk prediction models using AI and machine learning, the blending of AI algorithms for fraud detection, and real-time data analytics to manage supply chains. We argue that (AI) mitigates many known risks and therefore improvements in supply chain management rest heavily on its effectiveness. The main points are that AI enhances predictive accuracy, hones mitigation strategies, decreases operational disruption and advances decision-making informed by data. We hope to promote a shift towards using AI-enhanced applications of supply chain risk management to achieve a wider range of risk management goals, all the while maintaining a level of adaptability to manage high levels of complexity and rapid changes in the market and environmental externalities through a keen anticipation of risk.

Keywords: AI risk prediction; supply chain fraud detection; supply chain resilience; AI in supply chain management; risk mitigation; operational continuity

---

1. Introduction

In our heavily interconnected global economy, supply chains are the essential conduit of modern economies for the efficient movement and exchange of goods and services across vast spaces. That said, this same complexity also exposes them to a wide range of risks including those from natural disasters, geopolitical events, cyber-attacks, and fraud. Traditional risk management solutions are perceived as not dynamic or insightful enough to be flexible to the multitude of threats, emphasizing the very real requirement of a more sophisticated approach.

The advancement of Artificial Intelligence (AI) is a significant innovation capable of modernizing global supply chain risk management practices. By using machine learning, predictive analytics, and real-time data, AI has the power to interpret patterns and predict disruptions with a strikingly higher level of accuracy than has been possible before. In this way, AI allows for more proactive identification of risks and in turn an improved mitigation strategy which will ensure the supply chain will be more resilient and reliable. The role of AI in supply chain risk management is not trivial. AI-driven risk prediction frameworks enhance both how risks are assessed and how rapidly they are recognized and mitigated [1]. In addition, by realizing fraud, AI is a positive influence towards ensuring supply chain integrity, reducing the likelihood of losses, upholding long-standing trust [2]. While the advancements are evident, the adoption of AI in supply chain risk management also is not without its challenges. The implementation of AI in supply chain risk management is causing significant controversial issues, with concerns over the privacy of data, the bias in algorithms, and even the moral implications of AI decision-making dominating the debate [3-6].

The purpose of this report is to investigate how AI may contribute to the identification, evaluation, and control of risks within supply chains. By analyzing case studies, AI-driven risk prediction models, and fraud detection algorithms, this study aspires to provide readers with a clear understanding of the benefits and disadvantages of introducing AI into the robust supply chain risk management system. Essentially, this research has generated insights on how AI will eventually transform the practice of risk management to ensure high-functioning, predictable supply chains.

2. Materials and Methods

A comprehensive evaluation of the literature on artificial intelligence (AI) in supply chain risk management was conducted by means of a methodical search and analysis of scholarly publications, industry reports, and case studies published between 2010 and 2024. Important databases including Science Direct, IEEE Xplore, and Google Scholar were used to find the articles. The articles that were taken into consideration for the evaluation had to be current, meaning they had to deal with supply chain risk management, AI integration, and advances in our knowledge of risk identification, assessment, and mitigation. Three categories of AI applications were used to categorize papers for a more thorough review: real-time data analysis, fraud detection, and predictive analytics. The articles' methods were examined critically, with special attention paid to those that offered solid theoretical frameworks and empirical support. The results were then qualitatively synthesized to identify themes, obstacles, and gaps in the literature. This offers a comprehensive assessment of how artificial intelligence (AI) technologies are influencing supply chain risk management procedures and establishes a framework for further study.

3. Results and Discussion

This section presents the key findings from the literature review on the role of Artificial Intelligence (AI) in supply chain risk management, focusing on its applications in risk prediction, mitigation, and decision-making. The results are discussed in the context of existing research, and challenges to AI adoption are also addressed.

Application Category	AI Techniques Used	Primary Functions
Predictive Analytics	Machine Learning	Forecasting disruptions, risk identification
Fraud Detection	AI Algorithms	Identifying and mitigating fraudulent activities
Real-time Monitoring	Data Analytics	Detecting anomalies, real-time risk management

3.1. AI Enhances Predictive Accuracy and Risk Mitigation Strategies

It has been established that using AI in supply chain risk management greatly improves forecasting accuracy. Research has demonstrated that AI-driven models are quite good at spotting possible hazards before they happen, especially when they use machine learning algorithms and predictive analytics. AI, for example, has been successful in forecasting disruptions brought on by supply chain delays, market swings, and natural calamities. By proactively implementing mitigation methods, these predictive skills enable firms to lessen the total effect of prospective hazards.

IBM's Watson Supply Chain provides a practical illustration of artificial intelligence (AI) in supply chain risk management. IBM Watson analyses enormous volumes of data from several sources, including news articles, social media, supply chain history, and weather predictions, using artificial intelligence (AI) and machine learning. For example, Watson can forecast possible interruptions during hurricanes and other natural catastrophes by examining weather patterns and their expected effects on supplier operations and transportation routes. Early risk identification allows businesses to minimize the effect on their supply chain by rerouting shipments, adjusting inventory levels, or sourcing products from other vendors. Several businesses were able to minimize losses and preserve operational continuity amid calamities like Hurricane Harvey in 2017 because of this preventive strategy, where traditional risk management methods might have failed to anticipate the full scope of disruption [8].

AI not only increases forecast accuracy but also enhances risk reduction by facilitating quicker and more effective actions. Organizations may minimize operational interruptions by responding promptly to emerging risks through the use of AI-driven decision-making frameworks and real-time data analysis. AI is especially useful in identifying and reducing risks associated with fraud and cybercrime because of its capacity to instantly assess and respond to massive volumes of data.

3.2. Decreasing Operational Disruption and Enhancing Decision-Making

The literature has a wealth of evidence supporting AI's ability to minimize operational interruptions. AI is able to recognize possible problems and take action before they become serious disruptions by utilizing real-time data and sophisticated analytics. AI-powered supply chain monitoring systems, for instance, have demonstrated the ability to identify irregularities and initiate corrective measures, preserving the seamless functioning of supply networks [9].

AI also improves decision-making by offering data-driven insights, which are essential for handling intricate risk situations. Decision-makers are able to assess risks more strategically when they switch from conventional risk management techniques to AI-enhanced methodologies, which results in more informed and efficient judgments. This is especially crucial in the fast-paced market climate of today, when supply chains are vulnerable to many hazards [10].

3.3. Addressing Challenges in AI Adoption

Although supply chain risk management greatly benefits from artificial intelligence (AI), there are a number of obstacles that must be overcome before AI can be widely used. These include worries about algorithmic bias, data privacy, and the moral ramifications of AI-driven decision-making. The proper application of AI technology in supply chain management requires addressing these issues [11].

Notwithstanding these obstacles, supply chain risk management might be revolutionized by AI. The importance of AI in this industry is anticipated to increase as AI technologies continue to advance and as companies become more skilled at managing the hazards involved [12].

4. Conclusions

The revolutionary effect of artificial intelligence (AI) on supply chain risk management is highlighted in this overview of the literature. The use of artificial intelligence (AI) technology, including real-time data processing, predictive analytics, and machine learning algorithms, has greatly enhanced an organization's capacity to recognize, evaluate, and reduce risks in its supply chains.

By evaluating vast amounts of data to detect possible disruptions, artificial intelligence (AI) improves predictive accuracy and enables enterprises to take preventative action. This capacity helps to create more efficient risk mitigation techniques in addition to increasing the accuracy of risk prediction. This procedure is further strengthened by real-time data analytics, which makes it possible to react quickly to new threats and minimize operational interruptions while preserving continuity. The review also underscores the benefits of AI-driven decision-making, which provides data-informed insights essential for managing complex and dynamic risk scenarios. This shift from traditional risk management approaches to AI-enhanced methods represents a significant improvement in how supply chains are managed in today's volatile market environment.

Adopting AI is not without its difficulties, though. Concerns including algorithmic bias, data privacy, and ethical issues need to be taken into account to guarantee the ethical and responsible application of AI technology. Meeting these obstacles will be essential to optimizing AI's potential advantages for supply chain risk management as technology develops.

In general, AI is a potent instrument for creating supply networks that are more dependable and robust. Organizations must keep investigating and incorporating these developments as supply chain performance and resilience will be further improved by the continuous development of AI technologies and their use in risk management procedures.

Funding

This research received no external funding.

Acknowledgments

The First author wishes to express sincere gratitude to Mr. Rami Al-Nawaisa, Manager of the Real Estate and Finance Department at the Jordanian Engineers Association, and Eng. Emad Al-Asasfeh, Head of the Real Estate Regulation and Information Department. Their unwavering support and encouragement have been invaluable in advancing my scientific and practical career. Their guidance and commitment to my professional development were crucial to the success of this research.

References

1. Smith, J., & Brown, L. (2020). AI in supply chain management: Predictive analytics for risk assessment. Journal of Supply Chain Management, 56(4), 123-145.
2. Jones, R., & White, A. (2019). Enhancing supply chain resilience with AI-driven risk prediction. International Journal of Logistics Management, 30(2), 67-89.
3. Lee, K., & Thompson, M. (2021). Ethical considerations in AI-based supply chain risk management. Journal of Business Ethics, 58(3), 345-362.
4. Ahmed, S., & Patel, V. (2018). Challenges of AI integration in supply chain operations. Operations Research Letters, 45(1), 77-91.
5. Wilson, D., & Green, H. (2022). The future of AI in supply chain risk management: Opportunities and threats. Journal of Operational Research, 64(5), 213-230.
6. Abdallah, M., & Salah, M. (2024). Artificial Intelligence and Intellectual Properties: Legal and Ethical Considerations. International Journal of Intelligent Systems and Applications in Engineering, 12(1), 368-376.
7. Abdallah, Mohammad, and Mousa Salah. "Artificial Intelligence and Intellectual properties: legal and ethical considerations." International Journal of Intelligent Systems and Applications in Engineering 12.1 (2024): 368-376.
8. IBM, "How Watson Supply Chain helps companies manage risk during natural disasters," in *IBM*, 2017. Available: https://www.ibm.com/blogs/supply-chain/how-watson-supply-chain-helps-companies-manage-risk-during-natural-disasters.
9. Choi, T. M., Guo, S., & Liu, Y. (2021). "Big Data Analytics and Artificial Intelligence Pathways for the Construction Industry." *Journal of Construction Engineering and Management*, vol. 147, no. 2, 2021.
10. Dubey, R., Gunasekaran, A., Childe, S. J., Giannakis, M., Foropon, C., Roubaud, D., Hazen, B. T., & Jacobi, M. (2020). Big Data Analytics and Organizational Culture as Complementary Assets for Supply Chain Resilience. *International Journal of Production Economics*, 219, 42-58.
11. M. Abdallah, A. Hammad, and D. Staegemann, "A Data Collection Quality Model for Big Data Systems," in 2023 International Conference on Information Technology (ICIT), 2023: IEEE, pp. 168 - 172.
12. Brown, T., & Patel, A. (2024). Navigating the ethical and practical challenges of AI in supply chain management. *International Journal of Logistics Management*, 35(1), 45-62.

Process Design of Sulphur Recovery from Hydrogen Sulphide (H2S) through Claus Process

Riham Al Suli1, Hiba Al Shekaili2, Bayan Al Yousufi3, Arwa Al Alawi4, Santosh Walke 5

[1,2,3,4,5] Mechanical and Industrial Engineering Department, College of Engineering, National University of Science and Technology, Muscat, Oman

***** *Corresponding authors*: *riham180127@nu.edu.om; Tel.: +96899330599*

Abstract: The recovery of sulfur from hydrogen sulfide (H_2S)-containing gas streams is essential in industries like natural gas processing. The widely used Claus process is detailed in the research for extracting elemental sulfur from H_2S-rich gases. The study explores process design and optimization, aiming for efficient sulfur recovery and compliance with environmental regulations. The Claus process consists of thermal and catalytic sections, with thermal production accounting for 64% of the total elemental sulfur. The research involved simulation using the SULSIM package in HYSYS V.11, resulting in an overall efficiency of the Sulfur Recovery Unit (SRU) at 94.53%. Sensitivity analysis indicated that H_2S and SO_2 flare emissions were within acceptable limits, and the produced sulfur had high purity. Optimizing the process through simulation modeling, adjusting operating conditions, and including a Tail Gas Treatment (TGT) unit in the ASPEN HYSYS system can lead to significant improvements in efficiency and profitability.

Key words: Aspen HYSYS, Claus Process, CrystaSulf Process, Hydrogen Sulphide, Natural Gas, Pure Sulphur, Recovery Process, Sulphur Dioxide.

---

1. Introduction

Sulfur has been known since ancient times and was used for cave paintings and medicine. It is formed from atmospheric hydrogen sulfide near active volcanoes (Britannica, 2024). Sulfur is a pale-yellow solid with low electrical conductivity. It forms compounds with nonmetallic elements and sulfides with most metals. It is widely used to produce sulfuric acid in various industries, with high-purity sulfur derived from the Claus process exceeding 98% (Brasted, 2024). Sulfur is primarily sourced from underground deposits and has various applications, including the production of sulfuric acid used in fertilizers. The Claus process is an industrial technique used to eliminate sulfur, particularly H2S, from gas streams (Jack, 2018). The Claus process is used to recover sulfur but faces challenges such as fluctuating feed gas quality, catalyst deactivation, heat recovery optimization, corrosion/fouling, environmental compliance, and process optimization. Pre-treating feed gas, maintaining the catalyst, implementing efficient heat recovery, using corrosion control, adhering to emission regulations, and optimizing operating conditions are essential. Managing hydrogen sulfide exposure is crucial for worker safety. Sulfur has potential uses in road building, reducing asphalt use by up to 30%, improving road longevity, and reducing carbon emissions.

2. Methodology

The efficient and effective removal of Sulphur compounds in the form of H2S requires a systematic process design using the Claus process. A methodology comprising of several key steps is essential to ensure high Sulphur recovery efficiency, meet environmental regulations, and minimize operating costs. By adhering to this methodology, the design of the Sulphur recovery process can be optimized, resulting in a reliable and efficient solution for the removal of Sulphur compounds from H_2S. The proposed process design ensures compliance with environmental regulations and reduces operating costs while minimizing the impact on the environment. The Claus process involves several sequential steps to convert hydrogen sulfide (H_2S) into elemental sulfur (S) and water (H_2O). The Claus process begins with the introduction of a hydrogen sulfide-rich gas stream, often referred to as "sour gas," into the system. This gas stream typically originates from various industrial processes such as natural gas purification, petroleum refining, and coal gasification. The incoming sour gas is preheated to the required reaction temperature, typically ranging from 500°C to 1000°C. A portion of the hydrogen sulfide is then combusted with a stoichiometric amount of air or oxygen to produce sulfur dioxide (SO_2) and water vapor (H_2O). This exothermic reaction generates the heat necessary for the subsequent Claus reactions.

- $2H_2S + 3O_2 \rightarrow 2SO_2 + 2H_2O$

The remaining hydrogen sulfide gas, along with the sulfur dioxide produced from the combustion step, enters the catalytic conversion reactor. In the presence of a suitable catalyst (typically Alumina), the Claus reactions occur:

- $2H_2S \rightarrow 2S + 2H_2O_3$
- $H_2S + S_2 \rightarrow 2H_2S + 2H_2O$

The reaction involves thermal decomposition of hydrogen sulfide and the formation of elemental sulfur, accelerated by a catalyst. The resulting products, primarily elemental sulfur vapor and water vapor, are rapidly cooled to condense liquid sulfur. The condensed liquid sulfur is processed to remove impurities and then stored or transported for industrial use. The off gas from the process contains traces of sulfur compounds, which are typically further treated to minimize emissions before release into the atmosphere.

2.1 Advantages of Claus Process

The Claus process offers high Sulphur recovery rates (95%-98%), ensuring efficient utilization of resources and minimal waste. It is straightforward to operate, running continuously with minimal supervision, contributing to its cost-effectiveness (Gupta et al.).

2.2 Disadvantages of Claus Process

The Claus process is a complex operation that requires precise management of various reaction steps and process variables, such as catalysts, pressure, and temperature. It produces elemental Sulphur, carbon dioxide (CO2), and carbonyl sulfide (COS) as byproducts, which may require additional handling or disposal due to their potential negative impact on the environment.

3. Process Design

The plant is made up of a thermal section that does 70% of the Sulphur conversion and a catalytic section with two stages. It completes the remaining 30% Sulphur conversion. The first Sulphur condenser condenses the Sulphur produced in the thermal reactor, while the second and third condensers condense the Sulphur produced in the catalytic section. To simulate the entire plant, the SULSIM package in HYSYS V.11 was utilized, which includes empirical correlations fitted to plant data.

3.1 Design Validation

The simulation results indicate a high purity of liquid Sulphur with an overall efficiency of 94.53% for the SRU unit. The liquid Sulphur product and the flue gas from the stack were selected as validation streams because the primary aim of the SRU unit is to prevent any acidic emissions such as H_2S, SO_2, CS_2, and COS through the flue gas from the stack. Acid gas can lead to the formation of acid rain. The production of Sulphur is the second main objective of the SRU unit.

3.2 Thermal Stage Description

The process involves splitting the feed into two streams. The first stream is mixed with air and sent to the furnace, while the second stream is injected into the middle part of the furnace. Here, hydrogen sulphide is converted into sulphur and sulphur dioxide. To prevent sulphur condensation and recover waste heat, the furnace effluent goes through a waste heat exchanger. This enables the recovery and utilization of waste heat from the combustion process. Approximately 60-70% of the total elemental sulphur produced is generated in the thermal section before being heated and fed to the first catalytic reactor.

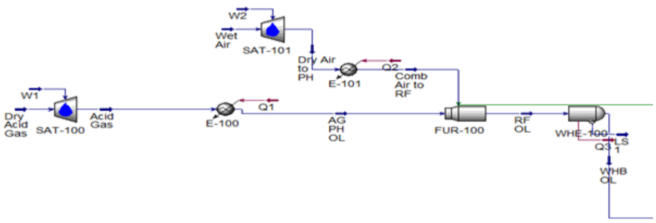

Figure 1. Thermal Stage Simulation

3.3 Catalytic Stage Description

During the catalytic stage, the stream is heated using the E-102 boiler and then fed to the first catalytic reactor, (CONV-100). The outlet stream from the first catalytic converter, (Con1 OL), is cooled and condensed in the second condenser (COND-101) to separate the elemental Sulphur. The Sulphur is then sent to boiler E-103 to be heated and afterward, it is fed to the second catalytic converter, (CONV-101). The catalytic recovery of Sulphur generally involves three sub-steps, which include heating, catalytic reaction, cooling, and condensation. The outlet stream from the second reactor, (Con2 OL), is fed to the condenser (COND-102) to separate the elemental Sulphur. The uncondensed part is sent to the incinerator (INC-100) by the tail gas stream (Ghahraloud et al., 2017).

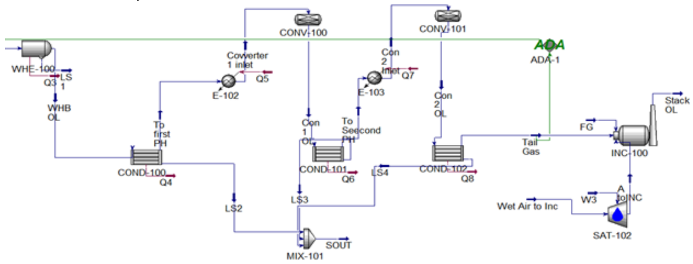

Figure 2. Catalytic Stage Simulation

3.4 SRU Simulation

Preheaters are crucial heat exchangers in the Sulphur Recovery Unit, preheating the combustion air to improve energy efficiency. This process reduces the required fuel and enhances overall efficiency. Sulphur recovery catalysts are essential in refineries, as they facilitate the conversion of hydrogen Sulphide (H_2S) into elemental Sulphur (S). In the Sulphur recovery units (SRUs), H_2S is burned to produce Sulphur dioxide (SO_2), which is then combined with other reactants and hot gases to form elemental Sulphur with the help of a catalyst. The catalysts play a vital role in reducing the temperature of these reactions, resulting in decreased energy consumption and promoting cleaner combustion of H_2S, thus reducing harmful pollutant emissions.

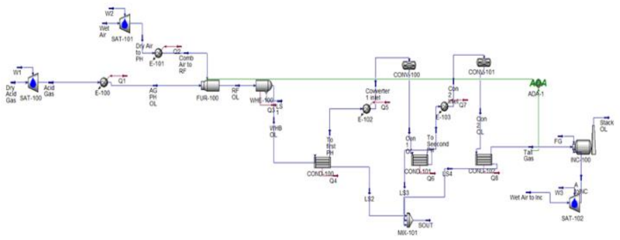

Figure 3. SRU Simulation

4. Results and Discussion

This simulation results obtained elucidates the comprehensive efficiency of the designed process and scrutinizes the summary of the results. The exploration will encompass process optimization, encompassing alterations in temperature and their influence on overall efficiency and equipment performance. Clear and comprehensive graphs are employed to depict the correlation between temperature variations and Claus process efficiencies. Furthermore, this section will present the environmental production effect results and feature a case study of pinch and cost analysis.

4.1 SRU Efficiency Analysis

The Sulphur Recovery Unit (SRU) is crucial for producing elemental Sulphur from Sulphur compounds. Its overall efficiency is 94.53%, slightly below the typical range but still satisfactory. The SRU consists of a thermal section and a catalytic section. The thermal section has a conversion efficiency of 63.2% and a recovery efficiency of 100%. The first catalytic converter, CONV-100, demonstrates a conversion efficiency of 67.86% and a recovery efficiency of 98.80%.

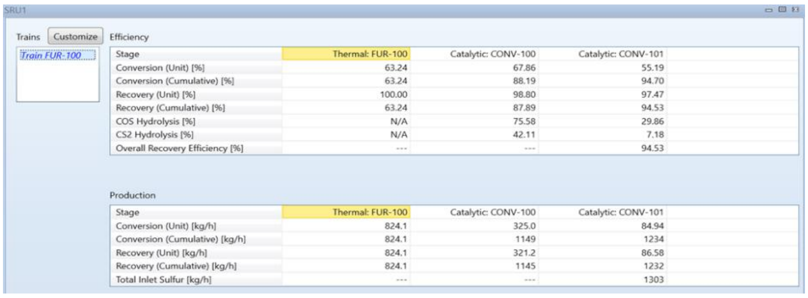

SRU1

Trains | Customize | Train FUR-100

Efficiency

Stage	Thermal: FUR-100	Catalytic: CONV-100	Catalytic: CONV-101
Conversion (Unit) [%]	63.24	67.86	55.19
Conversion (Cumulative) [%]	63.24	88.19	94.70
Recovery (Unit) [%]	100.00	98.80	97.47
Recovery (Cumulative) [%]	63.24	87.89	94.53
COS Hydrolysis [%]	N/A	75.58	29.86
CS2 Hydrolysis [%]	N/A	42.11	7.18
Overall Recovery Efficiency [%]	---	---	94.53

Production

Stage	Thermal: FUR-100	Catalytic: CONV-100	Catalytic: CONV-101
Conversion (Unit) [kg/h]	824.1	325.0	84.94
Conversion (Cumulative) [kg/h]	824.1	1149	1234
Recovery (Unit) [kg/h]	824.1	321.2	86.58
Recovery (Cumulative) [kg/h]	824.1	1145	1232
Total Inlet Sulfur [kg/h]	---	---	1303

Figure 4. SRU Efficiency

The COS hydrolysis efficiency is 75.58%, while the CS2 hydrolysis efficiency is 42.11%. The second catalytic converter, CONV-101, has a conversion unit efficiency of 55.19% and a recovery efficiency of 97.47%. The overall efficiency of the SRU is 94.53%. The production results indicate that CONV-101 processes approximately 1303 kg/h of inlet Sulphur, equivalent to approximately 34.5 tons per day. These findings highlight the importance of efficient SRUs in ensuring the production of elemental Sulphur with minimal waste and environmental impact.

4.2 Feed temperature effect to SRU Overall Efficiency

The temperature of the feed is a critical factor that affects the overall efficiency of the Sulphur Recovery Unit (SRU). To examine the impact of the feed temperature on the SRU's performance, a series of temperature tests was conducted using built model.

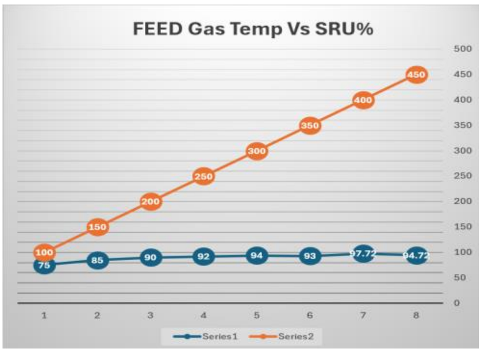

Figure 5. Feed temperature effect to SRU Overall Efficiency

In the study, it was observed that increasing the feed gas temperature directly correlated with the SRU efficiency. Maintaining the feed gas temperature at 280 degrees resulted in an SRU efficiency of 94.53%, while increasing it to 350 degrees improved efficiency to 97.72%. However, it's important to consider that higher temperatures for better sulfur recovery efficiency also led to increased furnace energy consumption.

4.3 Effect of decreasing combustion air temperature inlet to reaction furnace

The combustion air stream is crucial for the effective operation of the reaction furnace in a Sulphur Recovery Unit (SRU). The efficiency of sulphur recovery heavily relies on the air temperature, as it impacts the combustion process. For example, an inlet air temperature of 350 degrees resulted in an efficiency rate of 65.38%, while reducing the temperature to 155 degrees decreased the efficiency to 63.35%. This direct relationship between temperature and efficiency is significant.

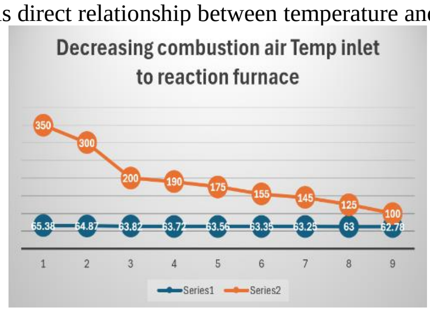

Figure 6. Effect of decreasing combustion air temperature inlet to reaction furnace

4.4 Decreasing temperature inlet to Catalytic Reactor (CONV-100)

The catalytic reactor plays a critical role in the Sulphur Recovery Unit (SRU) process, specifically in the Claus reaction, which is the heart of sulphur recovery. The temperature of the reactor is key to optimizing the process. Testing the decreased temperature inlet to catalytic reactor 1 (CONV-100) helps us find the best temperature for producing high purity Sulphur and operating the process under desired conditions with lower energy consumption.

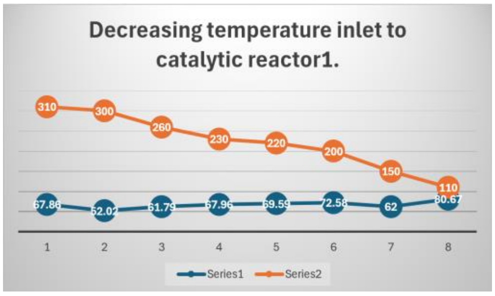

Figure 7. Decreasing temperature inlet to catalytic reactor

Adjusting the temperature of the catalytic reactor inlet impacts both Sulphur conversion efficiency and overall process efficiency. Higher temperatures lead to lower Sulphur conversion efficiency but higher overall process efficiency, while lower temperatures result in improved Sulphur conversion efficiency but decreased overall process efficiency. Maintaining the temperature within the optimal range is crucial to achieve the desired balance between Sulphur conversion efficiency and overall process efficiency.

4. Conclusions

The SRU process consists of two sections: thermal and catalytic. The overall efficiency of the SRU process is 94.53%, with the second catalytic converter processing 1303 kg/h of inlet Sulphur and the Sulphur production rate is calculated to be 31.33 tons/day. The analysis emphasizes the importance of efficient SRUs in producing elemental Sulphur with minimal waste and environmental impact. Optimizing the process through simulation modeling, changing operating conditions, design parameters, and implementing pinch analysis can improve profits by more than 2.5%. Additionally, it's possible to improve the functionality and accuracy of the SRU in ASPEN HYSYS by including a Tail Gas Treatment (TGT) unit. This can lead to significant enhancements in the system's capabilities.

Funding: This research was funded by National University of Science and Technology, Oman

Acknowledgments: The authors would like to express their sincere gratitude to the National University of Science and Technology, Oman for providing the necessary resources and support to carry out this research.

References

[1] J. C. Ehlers, A. A. Feidenhans'l, K. T. Therkildsen, and G. O. Larrazábal, "Affordable Green Hydrogen from Alkaline Water Electrolysis: Key Research Needs from an Industrial Perspective," Mar. 10, 2023, *American Chemical Society*. doi: 10.1021/acsenergylett.2c02897.

[2] A. Javaherian, "Proposal and comprehensive analysis of power and green hydrogen production using a novel integration of flame-assisted fuel cell system and Vanadium-Chlorine cycle: An application of multi-objective optimization," *Energy Convers Manag*, vol. 277, 2023.

[3] WWF-VIETNAM, "Green Hydrogen Market: Potentials and Challenges," 100re-map.

[4] A. C. Klemz *et al.*, "Oilfield produced water treatment by liquid-liquid extraction: A review," Apr. 01, 2021, *Elsevier B.V.* doi: 10.1016/j.petrol.2020.108282.

[5] M. Calabrese, "Hydrogen Safety Challenges: A Comprehensive Review on Production, Storage, Transport, Utilization, and CFD-Based Consequence and Risk Assessment," *Energies (Basel)*, vol. 17, p. 1350, 2024.

[6] S. Wang, A. Lu, and C. J. Zhong, "Hydrogen production from water electrolysis: role of catalysts," Dec. 01, 2021, *Korea Nano Technology Research Society*. doi: 10.1186/s40580-021-00254-x.

[7] M. Tao, J. A. Azzolini, E. B. Stechel, K. E. Ayers, and T. I. Valdez, "Review—Engineering Challenges in Green Hydrogen Production Systems," *J Electrochem Soc*, vol. 169, no. 5, p. 054503, May 2022, doi: 10.1149/1945-7111/ac6983.

[8] O. Schmidt, A. Gambhir, I. Staffell, A. Hawkes, J. Nelson, and S. Few, "Future cost and performance of water electrolysis: An expert elicitation study," *Int J Hydrogen Energy*, vol. 42, no. 52, pp. 30470–30492, Dec. 2017, doi: 10.1016/j.ijhydene.2017.10.045.

[9] R. Bhandari, C. A. Trudewind, and P. Zapp, "Life cycle assessment of hydrogen production via electrolysis - A review," Dec. 15, 2014, *Elsevier Ltd*. doi: 10.1016/j.jclepro.2013.07.048.

[10] H. D. Dawoud, H. Saleem, N. A. Alnuaimi, and S. J. Zaidi, "Characterization and treatment technologies applied for produced water in Qatar," Dec. 01, 2021, *MDPI*. doi: 10.3390/w13243573.

[11] A. S. Moustafa Oraby, "Green Hydrogen Production Directly from Seawater with No Corrosion Using a Nonmetallic Electrode: A Novel Solution and a Proof of Concept," *Int J Energy Res*, 2024.

[12] M. A. Khan *et al.*, "Recent Progresses in Electrocatalysts for Water Electrolysis," Dec. 01, 2018, *Springer Science and Business Media B.V.* doi: 10.1007/s41918-018-0014-z.

[13] M. Carmo, D. L. Fritz, J. Mergel, and D. Stolten, "A comprehensive review on PEM water electrolysis," Apr. 22, 2013. doi: 10.1016/j.ijhydene.2013.01.151.

[14] Mahmoud Nasrollahzadeh, "Scanning Electron Microscopy - an overview | ScienceDirect Topics," Interface Science and Technology. Accessed: Jun. 22, 2024. [Online]. Available: https://www.sciencedirect.com/topics/physics-and-astronomy/scanning-electron-microscopy

[15] M. Naniwadekar, M. Mandake, and S. Walke, "Review study of e-waste management and resource recovery system for controlling environmental pollution," *Int J Environ Waste Manag*, vol. 1, no. 1, 2023, doi: 10.1504/IJEWM.2023.10060267.

[16] L. Zhao, Y. Li, M. Yu, Y. Peng, and F. Ran, "Electrolyte-Wettability Issues and Challenges of Electrode Materials in Electrochemical Energy Storage, Energy Conversion, and Beyond," Jun. 13, 2023, *John Wiley and Sons Inc*. doi: 10.1002/advs.202300283.

[17] P. B. Balbuena, "Electrolyte materials - Issues and challenges," in *AIP Conference Proceedings*, American Institute of Physics Inc., 2014, pp. 82–97. doi: 10.1063/1.4878481.

[18] R. Aydin and F. Köleli, "Hydrogen evolution on conducting polymer electrodes in acidic media," *Prog Org Coat*, vol. 56, no. 1, pp. 76–80, May 2006, doi: 10.1016/j.porgcoat.2006.02.004.

[19] K. Zeng and D. Zhang, "Recent progress in alkaline water electrolysis for hydrogen production and applications," Jun. 2010. doi: 10.1016/j.pecs.2009.11.002.

[20] S. W. Maram Al Hinai, Amjad Al Kalbani, Buthaina Al Rubkhi, Umaima Al Kalbani, "Protein Extraction from Spirulina Platensis," *International Journal of Innovative Technology and Exploring Engineering (IJITEE)*, vol. 8, no. 12, pp. 1524–1530, 2019, doi: 10.35940/ijitee.L3110.1081219.

[21] Hong Lv, "Mechanism analyses and optimization strategies for performance improvement in low-temperature water electrolysis systems via the perspective of mass transfer: A review," *Renewable and Sustainable Energy Reviews*, vol. 183, 2023.

[22] A. O. M. Maka and M. Mehmood, "Green hydrogen energy production: current status and potential," Apr. 01, 2024, *Oxford University Press*. doi: 10.1093/ce/zkae012.

[23] M. N. Santosh Walke, Manoj Mandake, "A Review of Recent Advancements and Perspectives of Nanotechnology in the Application of Biomedical Imaging and Instrumentation," *ChemistrySelect*, vol. 9, no. 27, 2024, doi: https://doi.org/10.1002/slct.202304082.

[24] S. W. Ahmed Al Shehhi, M.J. Varghese, Lakkim Rao, "Process Simulation and Optimization of Natural Gas Dehydration Process using Aspen Hysys," *International Journal of Innovative Technology and Exploring Engineering*, vol. 8, no. 9, pp. 644–649, 2019, [Online]. Available: https://www.ijitee.org/wp-content/uploads/papers/v8i9/I7622078919.pdf

Industrial Energy Efficiency and Sustainability Using Phase Change Material

Seyed Mojtaba Sadrameli[1,2,*], Anahita Pirvaram[2], Leila Abdolmaleki[2]

1 Department of Engineering, German University of Technology in Oman, Muscat, Oman

2 Faculty of Chemical Engineering, Tarbiat Modares University, Tehran, Iran.

* *Corresponding authors: seyed.sadrameli@gutech.edu.om; Tel.: +968 94259074.*

Abstract: Phase change materials (PCMs) are substances which can store and release large amounts of energy at constant temperature during phase transition. They are broadly classified into three groups: organics, inorganics, and eutectics. Phase change materials have been utilized in all aspects of engineering, such as chemical, mechanical, material, civil, biomedical, industrial, and electrical engineering. The applications have been extended to the thermal management of solar panels, vehicles, building materials, lithium-ion batteries, electrical appliances, electronics, textiles, and biomedical applications. In this study a series of experimental runs have been performed under different conditions to evaluate a household refrigerator's performance utilizing Phase Change Materials (PCMs). The PCMs have been placed on the backside of the wire and tube condenser with cascade arrangement to absorb excessive heat from the condenser to reduce the surface temperature and enhance efficiency. All experimental runs have been conducted in standard room in Philver Company in Tehran, Iran. The objective of the research was to increase the off time of the compressor for reduction of electrical energy consumption. The results indicated that for the novel refrigerator, the condenser surface temperature was reduced significantly which led to coefficient of performance increase. The experimental results for the household refrigerator also prove that integration of PCMs on the condenser surface decreases the work time percentage from 32.7% to 27.6% and the energy consumption was reduced by 13%.

Keywords: Phase Change Materials, Refrigerator, Cascade, Eutectic, Energy management

1. Introduction

Household refrigerators are one of the most essential home appliances that almost energy house has one and is going to increase throughout the world. Therefore, improving refrigerator performance and reducing its energy consumption constitute a worldwide matter [1]. Different techniques have been studied to enhance the heat transfer in the heat exchangers such as condenser and evaporator and reduce energy consumption of these appliances [1]. One of the passive cooling techniques for the condenser is utilizing PCMs that demonstrated significant impact on heat transfer enhancement due to their high energy storage capacity and negligible volume change during phase transition period. They can absorb the excessive heat from the system and release them to the environment during phase change period to maintain the application temperature within an acceptable range [2,3].

PCMs can be applied to the condensers, evaporators, and the compartment section as an energy storage system [1]. Application of PCM panels with melting point of -15 ^{o}C as a latent heat storage element on the internal walls of the freezer during door openings and defrosting of a household refrigerator has been studied by Gin et al. [4]. They indicated that lower energy consumption can be obtained in the refrigeration system. Similar research has been performed by Oro et al. [5] and showed that the integration of a commercial PCM with melting point of -18 ^{o}C at different sites inside the freezer can keep the freezer's temperature at 4-6 ºC lower and preserve the quality of the products. Application of a mixture of water and a eutectic mixture for PCMs on the back side of the evaporator as a cold storage system has been studied by Azzouz et al. [6]. 5-15% improvement on the COP has been achieved by their simulation techniques. The system can also maintain 5-9 h of continuous operation during the outage [7]. A novel multi-objective optimization technique has been conducted by Cheng et al. [8] to reduce energy consumption and total cost of a conventional refrigerator. One of the drawbacks of using PCMs on the evaporator section is an increase on the compressor on time which results in a higher condensing temperature [9,10].

Based on the reports published on the literature, the application of eutectic PCMs in cascade arrangement for the performance enhancement of electrical refrigerators and freezers have not been studied yet. Therefore, the objective of this research is to increase the heat transfer rate on the back side of the condenser section of a household refrigerator using two eutectic PCMs with different melting points in cascade configuration. The study has been performed for four cases namely, without measurement packs (M-packs)/without PCM, with M-pack/without PCM, with M-pack/single PCM and with M-pack/cascaded PCMs on the condenser. Compressor performance, energy consumption and condenser and interior temperature distributions have been reported as results of this study.

2. Materials and Methods

A double-door household refrigerator, model Philver TDF 320, with energy consumption of 98 and 100 kWh/year including and excluding 10 kg of M-packs inside the frozen food compartment respectively, corresponding to energy class A, has been used for this study. All tests have been conducted inside the hot room of a Philver fridge and freezer manufacturing company in Tehran, Iran under standard conditions. The room conditions have been maintained at temperature between 16 and 43 ºC and a relative humidity of 45% and 75%. The maximum temperatures of the fresh foods and frozen food compartments during the 24-h tests were less than 5 ºC and -18 ºC, respectively based on the standard procedure.

2.1 Phase change materials

Eutectic mixture of polyethylene glycol-1000 (PEG-1000) and polyethylene glycol-600 (PEG-600) purchased from Merck, Germany, with different weight percentage has been used in this study. Due to the non-toxic, non-corrosive and bio-compatibility nature of the polymeric materials, they can be considered as an environmental friendly material. Due to the fact that the melting point of the PCMs mixture must be very close to condenser surface temperature during the operation, the eutectic mixture of 36% wt. of PEG-1000 and 64% of PEG-600 with a melting point of 32 ºC was prepared as a PCM1 for the experiments. PCM2 was made of mixing 32% wt. of PEG-1000 and 68% of PEG-600 with melting point of 29 oC. The pysical properties of two polymer-based PCMs are shown in Table 1.

Table 1. Physical properties of PCMs [12]

Characteristics	PEG-1000	PEG-600
Phase change temperature (°C)	34–40	15–25
Latent heat of fusion (Cal g^{-1})	38	35
Density (g ml^{-1} at 20 °C)	1.09	1.12
Thermal conductivity (W m^{-1} °C^{-1})	0.2–0.3	0.2–0.3
Liquid specific heat (Cal g^{-1} °C^{-1})	0.51	0.51

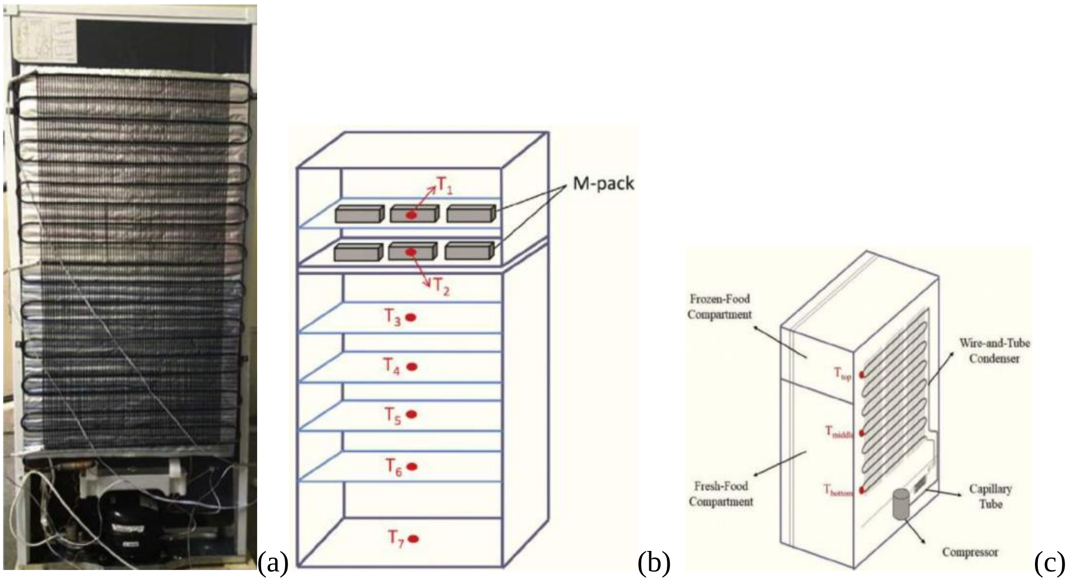

Figure 1. Schematic of the condenser with PCMs (a), M-Packs on the trays (b), and an ordinary fridge (c)

Each PCM pack with a mass of 250 g has been stored in three-layer aluminium packages using eutectic PCMs and 500 g pack of single PCM with melting temperature of 32 ^{o}C has been fixed on the backside of the condenser as illustrated in Fig. 1. The dimensions of single PCM pack are 104 Cm × 55 Cm and the PCM1 and PCM2 packs in the case of cascade arrangement have dimensions of 52 Cm × 55 Cm. Measurement packages (M-packs) are used for the substitution of the frozen food in the top compartment of the fridge. Each M-pack contains 232 g of a mixture of chemicals mixed with water with dimensions of 5 Cm × 10 Cm × 10 Cm with freezing point of -5 ^{o}C and with similar meat properties.

The experimental runs have been conducted in four different load conditions of PCM and M-packs and under the same standard operating environment as:

- Case 1: Without M-packs and no PCM on condenser
- Case 2: With M-packs inside the frozen-food compartment and with no PCM on condenser
- Case 3: With M-Packs inside the frozen-food compartment and with a single PCM on condenser
- Case 4: With M-Packs inside the frozen-food compartment and with a cascaded PCMs on condenser

More information regarding the application of PCMs in thermal management of refrigerators and freezers by experimental analysis can be obtained from Pirvaram et al. [11-12].

3. Results and Discussion

Differential Scanning Calorimetry (DSC) has been used for the enthalpies of the single and eutectic PCM consisting of PEG-600 and PEG-100 with different weight percentage and the results are illustrated in Fig. 2.a and Fig.2.b for 32 ^{o}C and 29 ^{o}C respectively. The measurements were taken while increasing the temperature at a rate of 10.0 ^{o}C/min in a dynamic atmosphere of Argon.

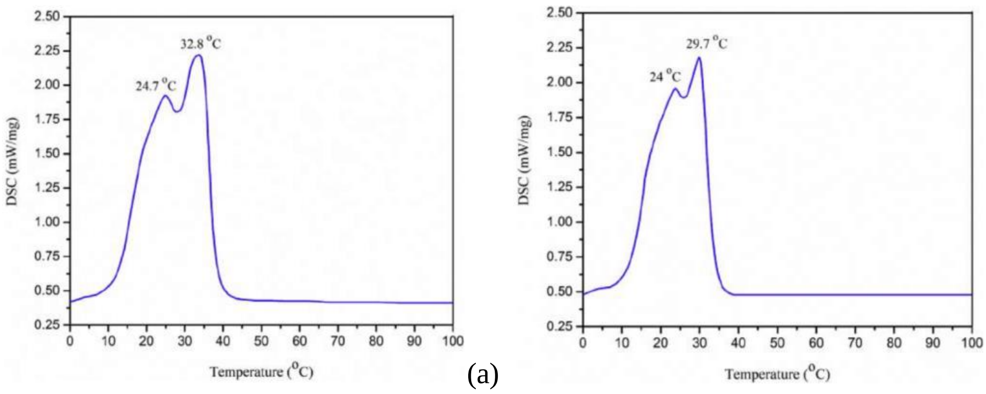

(a) (b)

Figure 2. DSC curves of eutectic PCMs at 32 °C (a) and 29 °C (b)

Both DSC curves indicate a minor exo-effect at 24 °C which is due to the solid-solid phase change of eutectic mixtures whereas second peaks corresponds to the solid-liquid phase transition process of materials. Codenser surface temperatures have been measured at three different locations on the condenser tubes (Fig. 1.c) and temperature distributions of the top and bottom sections for four different cases are illustrated in Fig. 3. which clearly indicates that the condenser temperature for cascaded arrangement (Case 4) was reduced substantially in all condenser sections.

As can be seen from Fig. 3.a in the ordinary fridge with M-packs inside the frozen compartment the top condenser temperature reaches to the maximum at 41 °C but the average maximum temperatures of this section for cases of single PCM and eutectic PCM integrated on the condenser reduces to 39 °C and 37 °C respectively.

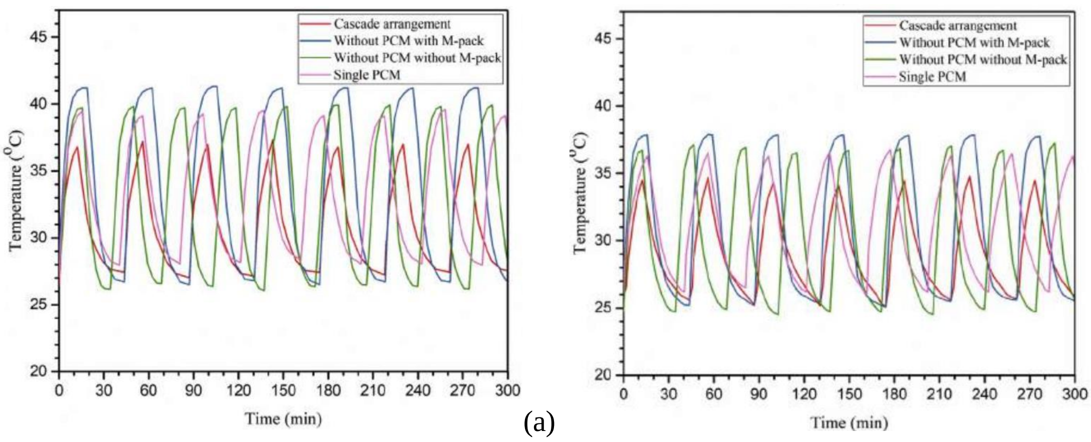

(a) (b)

Figure 3. Temperature discributions of top (a) and bottom (b) sections of condenser for four cases

The maximum temperature of the ordinary fridge containing M-packs was 37.5 °C for the bottom part as illustrated in Fig. 3.b. This has been reduced to 36.5 °C and 34.5 °C for condenser equiped with single PCM and with cascaded PCM respectively. It can be concluded from the results that reduction of the condenser temperatrue and as a result of this, lower refrigerant pressure lead to an improved COP in the novel refrigerator utilizing cascaded energy storage system.

The average temperature of the fresh-food compartment changes from 3.9 °C to 4.8 °C for the fridge with M-packs and without PCMs whereas this temperature for the case of single PCM varies from 4.0 to 4.7 °C and for the cascade arrangement case changes from 4.1 to 4.6 °C respectively which proves that more food preservation quality can be achieved by utilizing cascaded PCM on the condenser.

Summary of the experimental results for this study are listed in Table 3. As can be observed from the energy consumption results, utilizing energy storage system on the condenser can decrease the condenser surface temperature which results in COP enhancement and energy consumption reduction. Therefore, energy consumption in the case of two PCMs in cascade configuration is reduced from 0.7578 kWh/24h to 0.6564 kWh/24h. Maximum electrical energy saving of 13.38% can also be achieved using a eutectic PCM in cascade arrangement.

Table 3. Experimental results of four refrigerators under different conditions

	Case1	Case2		Case3	Case4
Phase change temperature (°C)	32	PCM1 29	PCM2 32	No	No
Mass of PCM (gr)	500	PCM1 250	PCM2 250	No	No
Maximum condenser temperature at bottom (°C)	36.5	34.5		37.5	37
Energy consumption (kWh/24h)	0.6917	0.6564		0.7578	0.7562
Energy saving	8.72	13.38		No	No

Case1: Refrigerator with a single PCM.
Case2: Novel refrigerator with two PCMs arranged in a cascade configuration.
Case3: Ordinary refrigerator with M-packs.
Case4: Ordinary refrigerator without M-packs.

1. Conclusions

Efficiency enhancement of using latent heat thermal energy storage units containing two PCMs in cascade arrangement on the back side of the condenser surface in a household refrigerator has been studied. The experimental data have been obtained for the novel refrigerator with single PCM and two PCMs in cascade configuration under standard conditions and compared with two ordinary refrigerators with and without M-packs. The ratio of compressor on-time to the total operating time during 24 h test decreased from 32.7 to 27.6% while this for the refrigerator equipped with a eutectic PCMs reduced to 29.6% indicating that compressor running time was considerably reduced by arrangement of latent heat storage in cascade configuration.

Finally, the energy consumption of the ordinary refrigerator containing M-packs and refrigerator equipped with a single PCM were measured as 0.7578 kWh and 0.9617 kWh per day respectively. Under the same conditions the electrical energy consumption of the novel refrigerator with eutectic PCMs in cascade configuration has been added to the condenser was measured to be 0.6564 kWh/24h which indicates that the novel refrigerator consumed 13.8% less energy in comparison to other systems.

Acknowledgments: The authors gratefully acknowledge the financial support from the research department of Tarbiat Modares University. The authors are also thankful to the manager and engineers of Philver Company for their support in providing refrigerators and measurement equipment during the experimental tests.

References

[1] Nandanwar, Y.N., Walke, P.V., Kalbande, V.P., and Mohan M., “Performance improvement of vapor compression system using PCM and thermoelectric generator” *Int. J. Thermofluids*, 2023, 18, 100352.

[2] Ben Taher, M.A., Ahachad, M., Mahdaoui, M., Zeraouli, Y., and Kousksou T., Thermal performance of domestic refrigerator with multiple PCM: Numerical study, *Journal of Energy Storage*, 2022, 55, 105673.

[3] Raveendran, P.S. and Sekhar, S.J., Experimental studies on the performance improvement of household refrigerator connected to domestic water system with a water-cooled condenser in tropical regions, *Applied Thermal Engineering*, 2020, 179, 115684.

[4] Gin, B., Farid, M., Bansal, P., Effect of door opening and defrost cycle on a freezer with phase change panels, *Energy Conversion and Management*, 2010, 51, pp. 2698-26706.

[5] Oro, E., Miro, L., Farid, M., and Cabeza, L., Improving thermal performance of freezers using PCMs, *Int. J. Refrigeration*, 2012, 35, pp. 984-1001.

[6] Azzouz, K., Leducq, D., and Gubin, D., Performance enhancement of a household refrigerator by addition of latent heat storage” *Int. J. Ref*., 2008, 31, pp. 892-901.

[7] Azzouz, K., Leducq, D., and Gubin, D., Enhancing the performance of household refregerators with latent heat storage: an experimental investigation, *Int. J. Ref*., 2009, 32, pp. 1634-1644.

[8] Yuan, X.D., and Cheng, W.L., Multi-objective optimization of household refrigerator with novel heat storage condensersby Generic algorithm, *Energy Conversion and Mangement*, 2014, 84, pp. 550-561

[9] Cerri, G., Palmieri, A., Moneicelli, E., Pezzoli, D., Identification of domestic refrigerator models including cool storage” in: *International congress of refrigeration*: 2003, Washington DC.

[10] Azzouz, K., Keducq, D., Gulipart, J., and Gobin, D., Improving the energy efficiency of a vapor compression system using PCM. In: *Second conference on PCM and slurry: scientific conference and business forum*; 2005, pp. 15-17..

[11] Pirvaram A., Sadrameli, S.M., and Abdolmaleki L., Energy Management of a Household Refrigerator Using Eutectic Environmental Friendly PCMs in Cascade Condition Energy" *Energy*, 2019, 181, pp. 321-330.

[12] Pirvaram A., S.M. Sadrameli, S.M., Abdolmaleki, L., Optimization of energy consumption and temperature fluctuations for a household freezer using non-toxic and non-flammable eutectic phase change materials with a cascade arrangement, *International Journal of Energy Research*, 2021, 45, pp. 1775-1788.

The 10th Jordanian International Mechanical Engineering Conference (JIMEC 10)

Mechanical Properties of PLA-CF Composites via FDM: Characterization and Optimization

Shafahat Ali[a]*, Ibrahim Deiab[a,b], Akrum Abdul-Latif [c]

[a] *Advanced Manufacturing Lab (AML) School of Engineering, University of Guelph, Guelph, ON N1G 2W1, Canada*
[b] *Australian University of Kuwait, Kuwait.*

[c] *Université Paris 8 Vincennes-Saint-Denis, France.*

* Corresponding author. Tel.: +1-519-824-4120; *E-mail address:* Shafahat@uoguelph.ca

Abstract:

The process of additive manufacturing (AM) involves depositing layers of material layer by layer to create 3D parts with complex geometries. There have been numerous engineering applications that have successfully utilized this process. FDM (fused deposition modeling) is a promising and widely used additive manufacturing technology, based on material extrusion. In addition to producing thermoplastic parts for functional applications, and simplifies material conversion by reducing waste, reducing costs. FDM-generated thermoplastic parts require improved mechanical properties, which are accomplished by enhancing pure thermoplastic mechanical performance. The thermoplastic matrix can be reinforced with reinforcement materials such as carbon fiber-reinforced polymer composites for applications in the engineering field. A study has been conducted to examine the effects of the FDM process parameters on the tensile and flexural properties of specimens. The material's mechanical properties were optimized using an experimental setup based on Taguchi L9. Following this, a desire-function analysis (DFA) was conducted. After extensive analysis, it has been determined that 0.3mm layer height, 210°C nozzle temperature, and 100% infill density are the optimal combination. This resulted in a tensile strength and modulus, the percentage of elongation, flexural stress, and modulus were determined to be 62.49052 MPa, 2796.05 MPa, 8.079%, 94.7249 MPa, and 3995.77 MPa respectively. To increase PLA's mechanical properties, this study investigated the possibility of adding CF. Results showed a significant increase in tensile and flexural strength and modulus. This paper presents a framework for investigating the mechanical properties and optimizing the process parameters of PLA-CF 3D-printed parts.

Keywords: FDM; Optimization; PLA-CF; Additive manufacturing; DFA

Introduction:

Additive manufacturing (AM) refers to a set of methods enabling the layer-by-layer construction of objects from three-dimensional models (3D) [1][2]. Most manufacturing operations are carried out under the subtractive manufacturing methodology. One of the many advantages of additive manufacturing is its ability to produce functional parts with complex geometries.

In the field of additive manufacturing, fused deposition modeling (FDM) is among the most popular and widely used techniques [3][4]. A continuous filament is extruded through a heated nozzle and then deposited layer by layer to form a printed product. During this process, the extruded material solidifies rapidly over the previous layer [5].

Currently, FDM uses a variety of thermoplastics. There are several thermoplastic materials available for printing, including polylactic acid (PLA), acrylonitrile butadiene styrene (ABS), polycarbonate (PC), PC-ABS blends, and polyurethane (PU)[6][7][8]. In engineering applications, these thermoplastics are often limited by poor mechanical properties. This problem could be overcome by adding carbon fibers (CFs) to the polymer matrix to increase Young's modulus and tensile strength [9]. There is a relationship between the CFs and the matrix in this instance. It is the reinforcing fibers that bear the load while the CFs are protected by the matrix and the load is transferred to them by the matrix [10][11]. Zhong et al.[12] found that different volumes of short glass fibers are incorporated into ABS filament, which is used to feed 3-D printers. These short glass fibers significantly improved strength, although flexibility and handleability were reduced [13]. There are numerous applications of thermoplastic matrix-reinforced composites, including wind turbine blades, automotive components, and aircraft fuselages [14][15].

The material properties and quality of the printed parts can be influenced by many parameters in FDM [16][17][18]. Polymer crystallinity, for example, is affected by the nozzle temperature. The fluidity and solidification characteristics of the extruded filament also affect the bonding between rasters because of this parameter [19]. In his study, Ning et al. [20] found that high nozzle temperatures result in strong interlayer bonds between rasters, which are rarely observed at lower temperatures. High temperatures, however, result in increased porosity, which negatively affects the strength of the material.

An extensive literature review is conducted in this study to analyze and evaluate previous studies published in the related field. There has been considerable research conducted on the properties of PLA and other materials, but little is known about the properties of PLA-CF materials. There is a limited amount of literature on PLA-CF's mechanical properties and printing parameters. This study aims to analyze basic parameters related to the 3D printing of PLA-CF. The printing parameters of Taguchi have been optimized using DFA.

Materials and Methods:

This study used Bambu lab's PLA-CF filament. PLA-CF filaments are loaded with approximately 5 to 10 weight percent of chopped CFs. It has a density of 1.22 g/cm3, a flow rate of 3.7 g/min (measured at 210°C and 2.16 kg), and a melting temperature between 210 and 240°C.

The specimens were printed on a Bambu X1E 3D printer. Table 1 displays the constant parameters of a 3D printer with a 0.8 mm nozzle diameter. Table 2 presents the variables used in this study that relate to 3D printing. Tensile tests were conducted according to ASTM D638-IV [21]. The specimens were tested under tension on an Instron tensile test machine with a thickness of 3.2mm. ASTM standards were followed for the experimental conditions, which were 23°C and a strain rate of 5 mm/minute. A flexural test was conducted according to ASTM D790 at a strain rate of 12 mm per minute [22].

Table 1 The parameters of printing are constant.

Parameters	Unit	Values
Nozzle Diameters	mm	0.8
Infill pattern	-	Aligned rectangular
Flow rate	%	100
Bed temperature	℃	50
Chamber Temperature	℃	45
Printing speed	mm/min	60

Table 2 Parameters for preparing samples

Parameters	Unit	Levels		
Layer height	mm	0.3	0.4	0.5
Nozzle temperature	℃	210	225	240
Infill density	%	50	75	100

Design of Experiment

In this study, Taguchi methods were used to design experiments. An experimental design based on Taguchi principles was employed to determine the height and temperature of the layer, as well as the density of the infill for the tensile and flexural tests. In Taguchi's design, there were three factors and three levels. Minitab 17 software incorporates a Taguchi design. The experiment was designed using the Taguchi design, as shown in Table 3. The outputs can include tensile strength, Young's modulus (or elastic modulus), elongation percentage, flexural stress, and modulus. The five parameters were also referred to as the response variables.

Table 3 Taguchi L9 Design of Experiment

Experiment No.	Layer Height (mm)	Infill Density (%)	Nozzle Temperature (℃)
1	0.3	210	50
2	0.3	225	75
3	0.3	240	100
4	0.4	210	75
5	0.4	225	100
6	0.4	240	50
7	0.5	210	100
8	0.5	225	50
9	0.5	240	75

4. Results and Discussion:

This study examines five different output responses as a result of printing parameters. Each specimen was averaged at three different printing conditions. ASTM 638 type IV and D790 are used to calculate mechanical properties. This material has a tensile strength of 63.80 MPa, a modulus of 2893 MPa, an elongation at break of 8.32, a flexural stress of 93.90 MPa, and a flexural modulus of 4006 MPa. A significant improvement has been made in PLA-CF's mechanical properties when compared to PLA's.

The figure illustrates how the mechanical properties of the material are decreased as the layer height increases. Low-layer heights have higher adhesion bonding and greater strength than high-layer heights. Higher layer heights may have reduced mechanical properties due to bonding lack. It is most promising to have a 0.3mm result; however, a 0.5mm result indicates that interlayer bonds are missing, compromising the material's mechanical properties. Similar results have been reported in the literature [23]. A higher infill rate resulted in higher mechanical properties when compared with a low infill density. A high infill ensures that there is no gap between printed layers, thereby enhancing their mechanical properties. The study examined the nozzle temperature and determined that 210 produced the most effective results when compared to lower temperatures. When material is extruded at higher temperatures, there is a lack of bonding between layers, which results in poor mechanical properties. There have been similar findings reported in the literature [24][25].

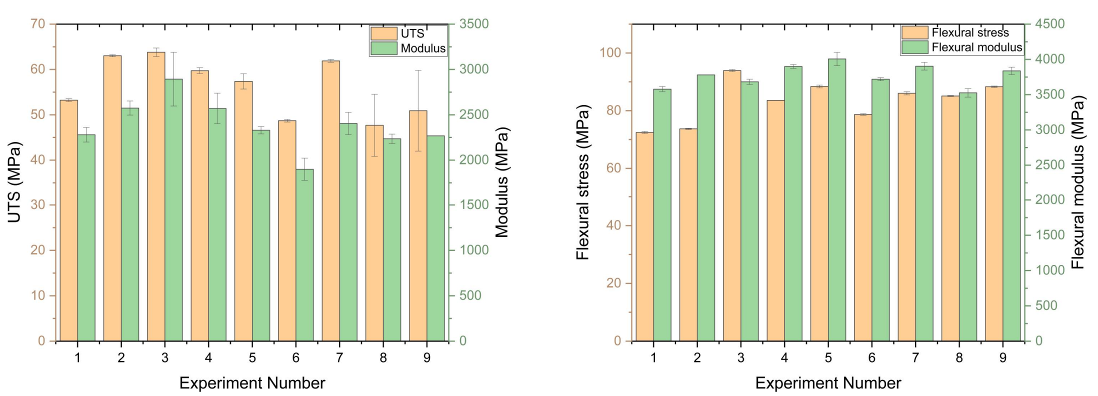

Figure 1 Results of Tensile strength and modulus, flexural stress, and flexural stress under different printing conditions

4.1. Multi response optimization:

4.1.1. Desirability Functional Analysis (DFA)

An analysis of multi-response characteristics is undertaken in DFA to determine the composite desirability dg, a single response function. The following are the steps to achieve this result:

Step 1: Desirability index calculation

A data analysis was conducted using the data obtained from each set of experiments. Some output parameters are provided by the software directly, while others are calculated using formulae. According to Derringer and Suich [26], individual desirability (di) is determined by extending Harrington's equations [27] for each response. Five aspects are included in a desirability function.

The output is as follows when di is set to its maximum value (larger is better):

$$d_i = \begin{cases} 0, y_i \leq y_{min} \\ \left(\frac{y_i - y_{min}}{y_{max} - y_{min}}\right)^r, y_{min} \leq y_i \leq y_{max}, \ r \geq 0 \\ 1, y_i \geq y_{min} \end{cases} \quad (1)$$

A desirable individual is represented by d_i, yi, the expectations, ymin, the lower tolerance limit, ymax, the upper tolerance limit, and r, the weight.

Using the "larger the better" formula, we calculated the desirability index, which indicates that mechanical properties are more desirable when they have higher values:

Step 2: Compute the composite desirability.

The following equation is used to combine all responses:

$$d_g = \sqrt[w]{{d_1}^{w1} * {d_2}^{w2} * \ldots \ {d_i}^{wi}} \quad (2)$$

A composite desirability index is represented by dg, an individual desirability index is represented by di, and a weighted average of the five is represented by wi. This study assigned equal weight to all output responses. The experiment set with the highest composite desire provides the most desirable results. The composite desirability table indicates that Experiment Number 04 generates the best and most optimized results out of all nine experiments. The highest values were obtained when infill density was 75%, layer height was 0.4 mm, and nozzle temperature was 210ºC. Table 4 shows the desirability index.

Table 4 Analyzed the experiment desirability index.

Experiment No.	Desirability Index				
	Tensile Strength	Modulus	% of Elongation	Flexural Stress	Flexural Modulus
1	0.80749	0.825457	1	0	0.643025
2	0.990215	0.925498	0.922776	0.567746	0.880494
3	1	1	0.810932	1	0.798731
4	0.943523	0.924429	0.930521	0.876828	0.951243
5	0.903326	0.845832	0.890526	0.942538	1
6	0.576131	0	0.743236	0.78116	0.83382
7	0.975166	0.873464	0.783278	0.912658	0.953337
8	0	0.804918	0	0.899617	0
9	0.724656	0.820124	0.740126	0.941247	0.917004

Table 5 Composite desirability and ranking

Experiment No.	Composite Desirability	Rank
1	0	7
2	0.841814	5
3	0.916805	2
4	0.924936	1
5	0.914987	3
6	0	7
7	0.896931	4
8	0	7
9	0.823907	6

Step 3: Calculate the optimal combination of parameters.

Identifying the most effective combination of parameters for level control. The composite desirability value can be attributed to high processing quality. A Taguchi analysis was conducted using Minitab, followed by a Taguchi prediction analysis using the "Predict Taguchi Results" function.

Minitab Software predicts that Experiment Number 04 will produce a composite desirability index value of 0.9294. Improved results can be achieved by optimizing the combination of input responses. Fig. 2 shows the plot of the main effects that are likely to yield the best results when the input parameters are adjusted.

According to the Taguchi design, A, B, and C represent the height of the layers, the temperature of the nozzle, and the density of the infill. The figure below illustrates the optimal parameters for infill density, nozzle temperature, and layer height (A1B1C3) which resulted in the best mechanical properties. In the Taguchi design, no consideration was given to the mechanical properties of this combination of parameters. The samples were therefore reprinted and retested.

Step 4: ANOVA (analysis of variance)

An analysis of variance (ANOVA) was performed to determine which parameters were significant. ANOVA is used to determine the comparative significance of control parameters. To illustrate the relative impact of process control parameters, the common sum of square values is computed.

Based on the results of an analysis of variance, it was determined that layer height contributed the most to the mechanical properties, followed by densities of infills and nozzle temperatures.

Table 6 Analysis of variation

Source	DF	Seq SS	Contribution	Adj SS	Adj MS	F-Value	P-Value
Layer Height	2	68.21	21.55%	68.21	34.10	2.48	0.287
Nozzle temperature	2	22.06	6.97%	22.06	11.03	0.80	0.555
Infill density	2	198.74	62.79%	198.74	99.37	7.22	0.122
Error	2	27.52	8.69%	27.52	13.76		
Total	8	316.52	100.00%				

Step 5: Estimate and compare the predicted optimal parameters.

Initially, the sample was tested at 210°C nozzle temperature and 0.4 mm layer height with 75% infill density as part of the initial printing combination. The results need to be reconfirmed under optimized conditions derived from Minitab's main effects plots for means (Figure 2). A combination of 100% infill density, 0.3mm layer height, and 210ºC nozzle temperature produced the best results in this study. To verify the improvement in mechanical properties, ASTM standards were used to print the samples and evaluate the mechanical properties. The specimens printed under optimal conditions exhibited better mechanical properties than those used in experiment 4. The most significant improvement was observed in the percentage of elongation (24.612%), followed by the flexural stress (11.792%), modulus of (8.079), Tensile strength (4.4138), and flexural modulus of (2.404%).

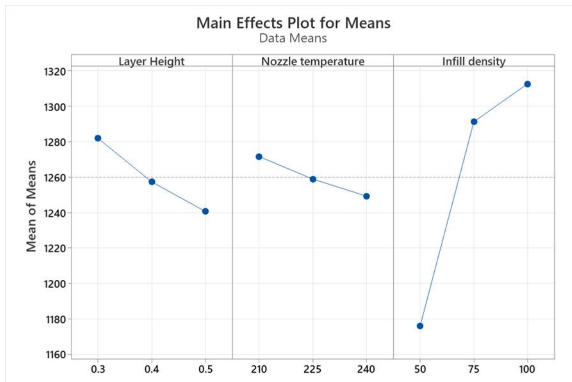

Figure 2 Response of mean of mean.

Table 7 Analyses of the difference between predicted and input parameters

	Levels	Tensile strength (MPa)	Modulus (MPa)	% of Elongation	Flexural stress (MPa)	Flexural modulus (MPa)	Composite desirability
Initial parameters	A2B1C2	59.7323	2570.15	7.36400	83.5551	3899.71	0.9097
Optimized parameters	A1B1C3	62.49052	2796.05	9.7681	94.7249	3995.77	0.9916
Improvement (%)		4.4138	8.079	24.612	11.792	2.404	8.264

Conclusion

An investigation of the mechanical properties of 3D printed specimens was conducted under a variety of printing conditions, including nozzle temperature, layer height, and infill density. A statistical approach and a desirability functional analysis have also been used to analyze printing parameters. The results are summarized below.

- Mechanical properties are influenced by layer height and infill level in 3D printing. When the layer height of the material is decreased (0.3mm), the mechanical properties of the material are improved.
- This study utilized DFA, a well-established decision-making tool, to optimize layer height, infill density, and nozzle temperature. After extensive analysis, it has been determined that 0.3 mm layer height, 210°C nozzle temperature, and 100% infill density are the optimal combination. Therefore, tensile strength and modulus, the percentage of elongation, flexural stress, and modulus were determined to be 62.49052 MPa, 2796.05 MPa, 8.079%, 94.7249 MPa, and 3995.77 MPa respectively.

- Based on statistical regression analysis, infill density accounts for approximately 63% of a material's mechanical properties, layer height accounts for 21%, and nozzle temperature accounts for 7%.
- A significant increase in tensile strength, modulus, and fracture stress and modulus has been observed when carbon fiber is added to PLA.

Acknowledgments

The authors would like to acknowledge the financial support from the Natural Science and Engineering Research Council of Canada (NSERC).

References

[1] H. Bikas, P. Stavropoulos, and G. Chryssolouris, "Additive manufacturing methods and modeling approaches: A critical review," *Int. J. Adv. Manuf. Technol.*, vol. 83, no. 1–4, pp. 389–405, 2016, doi: 10.1007/s00170-015-7576-2.

[2] S. Ali, I. Deiab, and S. Pervaiz, "State-of-the-art review on fused deposition modeling (FDM) for 3D printing of polymer blends and composites: innovations, challenges, and applications," *Int. J. Adv. Manuf. Technol.*, 2024, doi: 10.1007/s00170-024-14820-0.

[3] S. Ali, I. Nouzil, V. Mehra, A. Eltaggaz, I. Deiab, and S. Pervaiz, "Integrated optimization scheme for 3D printing of PLA-APHA biodegradable blends," *Prog. Addit. Manuf.*, no. 0123456789, 2024, doi: 10.1007/s40964-024-00684-z.

[4] I. Khan, I. Barsoum, M. Abas, A. Al Rashid, M. Koç, and M. Tariq, "A review of extrusion-based additive manufacturing of multi-materials-based polymeric laminated structures," *Compos. Struct.*, vol. 349–350, no. January, 2024, doi: 10.1016/j.compstruct.2024.118490.

[5] A. Hisham, S. Ali, S. Abdallah, A. N. A. Mohammed, R. A. Susantyoko, and S. Pervaiz, "Experimental and Statistical Optimization of Carbon-Fiber Reinforced Nylon Composite Based 3D Printed Cellular Structures," *ASME Int. Mech. Eng. Congr. Expo. Proc.*, vol. 2-A, pp. 1–10, 2022, doi: 10.1115/IMECE2022-95727.

[6] O. A. Mohamed, S. H. Masood, and J. L. Bhowmik, "Optimization of fused deposition modeling process parameters: a review of current research and future prospects," *Adv. Manuf.*, vol. 3, no. 1, pp. 42–53, 2015, doi: 10.1007/s40436-014-0097-7.

[7] S. Abdallah, S. Ali, and S. Pervaiz, "Performance optimization of 3D printed polyamide 12 via Multi Jet Fusion: A Taguchi grey relational analysis (TGRA)," *Int. J. Light. Mater. Manuf.*, vol. 6, no. 1, pp. 72–81, 2023, doi: 10.1016/j.ijlmm.2022.05.004.

[8] I. Khan *et al.*, "Integrating resistance-based sensing into fused filament fabricated mechanical metamaterial structure," *Prog. Addit. Manuf.*, vol. 10, no. 1, pp. 465–474, 2025, doi: 10.1007/s40964-024-00635-8.

[9] N. G. Karsli and A. Aytac, "Tensile and thermomechanical properties of short carbon fiber reinforced polyamide 6 composites," *Compos. Part B Eng.*, vol. 51, pp. 270–275, 2013, doi: 10.1016/j.compositesb.2013.03.023.

[10] Q. T. H. Shubhra, A. K. M. M. Alam, and M. A. Quaiyyum, "Mechanical properties of polypropylene composites: A review," *J. Thermoplast. Compos. Mater.*, vol. 26, no. 3, pp. 362–391, 2013, doi: 10.1177/0892705711428659.

[11] A. S. Almuflih, M. Abas, I. Khan, and S. Noor, "Parametric Optimization of FDM Process for PA12-CF Parts Using Integrated Response Surface Methodology, Grey Relational Analysis, and Grey Wolf Optimization," *Polymers (Basel).*, vol. 16, no. 11, 2024, doi: 10.3390/polym16111508.

[12] W. Zhong, F. Li, Z. Zhang, L. Song, and Z. Li, "Short fiber reinforced composites for fused deposition modeling," *Mater. Sci. Eng. A*, vol. 301, no. 2, pp. 125–130, 2001, doi: 10.1016/S0921-5093(00)01810-4.

[13] H. L. Tekinalp *et al.*, "Highly oriented carbon fiber-polymer composites via additive manufacturing," *Compos. Sci. Technol.*, vol. 105, pp. 144–150, 2014, doi: 10.1016/j.compscitech.2014.10.009.

[14] M. Biron, *Thermoplastics and thermoplastic composites: technical information for plastics users*. Elsevier, 2007.

[15] I. Khan, M. Abas, S. Ahmad, A. Al Rashid, and M. Koç, "Fabrication of a low-cost fused filament fabrication-based 3D printer and investigation of the effects of process parameters on mechanical properties of 3D-printed samples," *J. Eng. Res.*, no. June, 2024, doi: 10.1016/j.jer.2024.06.018.

[16] B. El Essawi, S. Abdallah, S. Ali, A. Nassir Abdo Mohammed, R. A. Susantyoko, and S. Pervaiz, "Optimization of infill density, fiber angle, carbon fiber layer position in 3D printed continuous carbon-fiber reinforced nylon composite," *Results Eng.*, vol. 21, no. February, p. 101926, 2024, doi: 10.1016/j.rineng.2024.101926.

[17] J. John, D. Devjani, S. Ali, S. Abdallah, and S. Pervaiz, "Optimization of 3D printed polylactic acid structures with different infill patterns using Taguchi-grey relational analysis," *Adv. Ind. Eng. Polym. Res.*, vol. 6, no. 1, pp. 62–78, 2023, doi: 10.1016/j.aiepr.2022.06.002.

[18] S. Ali, V. Mehra, A. Eltaggaz, I. Deiab, and S. Pervaiz, "Optimization and prediction of additively manufactured PLA-PHA biodegradable polymer blend using TOPSIS and GA-ANN," *Manuf. Lett.*, vol. 41, pp. 795–802, 2024, doi:

https://doi.org/10.1016/j.mfglet.2024.09.099.

[19] F. Ning, W. Cong, J. Qiu, J. Wei, and S. Wang, "Additive manufacturing of carbon fiber reinforced thermoplastic composites using fused deposition modeling," *Compos. Part B Eng.*, vol. 80, pp. 369–378, 2015, doi: 10.1016/j.compositesb.2015.06.013.

[20] F. Ning, W. Cong, Y. Hu, and H. Wang, "Additive manufacturing of carbon fiber-reinforced plastic composites using fused deposition modeling: Effects of process parameters on tensile properties," *J. Compos. Mater.*, vol. 51, no. 4, pp. 451–462, 2017, doi: 10.1177/0021998316646169.

[21] ASTM D638, "Standard Test Method for Tensile Properties of Plastics," *ASTM Stand.*, vol. 08, pp. 1–16, 2014, doi: 10.1520/D0638-14.1.

[22] ASTM INTERNATIONAL, "Standard Test Methods for Flexural Properties of Unreinforced and Reinforced Plastics and Electrical Insulating Materials. D790," *Annu. B. ASTM Stand.*, pp. 1–12, 2002, doi: 10.1520/D0790-17.2.

[23] S. Ali, S. Abdallah, D. H. Devjani, J. S. John, W. A. Samad, and S. Pervaiz, "Effect of build parameters and strain rate on mechanical properties of 3D printed PLA using DIC and desirability function analysis," *Rapid Prototyp. J.*, vol. 29, no. 1, pp. 92–111, 2023, doi: 10.1108/RPJ-11-2021-0301.

[24] X. Zhou, S.-J. Hsieh, and Y. Sun, "Experimental and numerical investigation of the thermal behaviour of polylactic acid during the fused deposition process," *Virtual Phys. Prototyp.*, vol. 12, no. 3, pp. 221–233, Jul. 2017, doi: 10.1080/17452759.2017.1317214.

[25] D. Syrlybayev, B. Zharylkassyn, A. Seisekulova, M. Akhmetov, A. Perveen, and D. Talamona, "Optimisation of Strength Properties of FDM Printed Parts — A," *Polymers (Basel).*, vol. 13, pp. 1–35, 2021, [Online]. Available: https://doi.org/10.3390/polym13101587

[26] S. K. Gauri, "Optimization of multi-response dynamic systems using principal component analysis (PCA)-based utility theory approach," *Int. J. Ind. Eng. Comput.*, vol. 5, no. 1, pp. 101–114, 2014, doi: 10.5267/j.ijiec.2013.09.004.

[27] I. Flores Ituarte, S. Panicker, H. P. N. Nagarajan, E. Coatanea, and D. W. Rosen, "Optimisation-driven design to explore and exploit the process–structure–property–performance linkages in digital manufacturing," *J. Intell. Manuf.*, vol. 34, no. 1, pp. 219–241, 2023, doi: 10.1007/s10845-022-02010-2.

Digital Excellence in Supply Chain: Utilizing Lean Six Sigma for Integrated and Automated Solutions

Souraj Salah [1]*

[1] Affiliation: Hamdan Bin Muhammad Smart University
* *Corresponding authors: ssalah@hbmsu.ac.ae; Tel.: +971557651380.*

Abstract: Supply chain management (SCM) is vital for organizational sustainability amid evolving market dynamics influenced by health, lifestyle, and technological advancements, which all force supply chain (SC) members to re-evaluate their effectiveness individually and as a whole. A major evolution in quality management (QM) is Lean Six Sigma (LSS), which is a structured approach and a continuous improvement (CI) methodology that aims at customer satisfaction and waste reduction. SCM can utilize the LSS tools and CI principles to achieve high levels of customer satisfaction regarding cost, quality and delivery. This research builds on existing literature by providing a case study on LSS implementation in SCM, demonstrating the effectiveness of value stream mapping (VSM) in fostering SC improvements. VSM approach enables teams to reassess the existing system of processes from a broader perspective, identifying various challenges and opportunities across the value stream including physical operations, IT systems, and virtual customer service platforms, promoting stakeholder interaction and process simplification. Robotic process automation (RPA) automates repetitive manual tasks like invoice creation through computer programming. Outcomes include automated manual tasks, reduced cycle and lead times, minimized idle operator time, enhanced stakeholder communication, resulting in financial savings in the order of Millions of Dollars annually.

Keywords: Lean Six Sigma; Supply Chain Management; Value Stream Mapping, Robotic Process Automation.

---

1. Introduction

Integrating Six Sigma with SCM can create benefits such as the Define-Measure-Analyze-Improve-Control (DMAIC) project discipline, sustainability of results, a well-established human resources framework using the colored belt-system, and a quantitative analysis strength (Yang et al., 2007). This also applies to LSS which uses the DMAIC structure as well.

One of the key goals for a successful organization and its suppliers can be to use CI methodologies such as LSS and modern electronic systems to eliminate wasteful activities, reduce the total SCM costs, digitalize the transactional processes, and enhance the electronic data interchange (EDI) capabilities.

The versatility of the Six Sigma metrics in performance measurement, certain similarities between Six Sigma and SCM (such as both being process approaches), and the research results indicating that SCM can benefit from the implementation of QM principles, are three reasons for motivation towards the integration of SS and SCM. Both SCM and SS are considered as process approaches; SS is process oriented and SCM is composed of key processes (Dasgupta, 2003).

Six Sigma metrics are well appreciated as robust and versatile performance indicators (Dasgupta, 2003). Sanders and Hild (2000) warned against using Six Sigma metrics indiscriminately since there is a disadvantage in transforming the notion of Six Sigma process from a management philosophy to numerical targets for individual processes. This appears to contradict Deming's (1993) philosophy of eliminating numerical targets and slogans. Obviously, Deming opposed the use of metrics to drive people by fear. Managers need to spread the knowledge of Six Sigma in the right perspective to ensure that metrics are perceived as motivational opportunities for improvement, not hard-core numerical targets (Dasgupta, 2003).

Within LSS, Six Sigma tools ensure that products are of high quality resulting from a capable process, and Lean tools including VSM ensure the efficient flow through the SCM including inventories, schedules, demand quantities, etc. LSS tools in general aim at reducing costs, wastes, non-value-added activities and satisfying all customers across the SC. LSS encourages good relationships with customers and suppliers including partnering and problem solving.

One of the important concepts of Lean, which is stressed in the enterprise VSM exercises used to improve SC processes (Foster, 2007), is seeing things from the perspective of the whole enterprise SC and not the individual process or entity. For example, rewarding a business entity for producing more than what the next business entity in the SC requires (as a customer of the former entity) does not generate any benefit for the SC from the whole SC perspective. SCM includes the principles of JIT. Products need to be delivered on time, with the right quality, the right quantity and at low cost. JIT delivery is important for the success of JIT production. The Lean approach to SCM can also be described as Lean logistics aiming at reduction of inventories, wastes and lead times.

Parveen and Rao (2009) indicated that there is a need for an integrated approach to Lean manufacturing from the perspective of the Lean SC to achieve total leanness across the SC. The nature of the market sector has a direct impact on the Lean approach for any SC. Lean tends to increase demand stability by simplifying, optimizing and streamlining the SC. To quickly react to demand variations, it is important to integrate sales and marketing with manufacturing to ensure effective communication, and to design a flexible manufacturing system (Cochran et al., 2000). In order to overcome the conflict between Lean and highly variable demand, Reichhart and Holweg (2007) suggested that the use of market-segmentation to benefit from the stability of some customer segments or products. Bicheno et al. (2001) indicated that the inconsistent performance of the SC of a steel mill they studied is caused by demand variations, batching (which should be minimized according to Lean principles), process instability and delivery performance. Here are some considerations for Lean SC as recommended by Parveen and Rao (2009):

- a collaboration between producer and retailer for setting a maximum-profit price
- an optimal integrated inventory policy which takes into account CI, set-up cost reduction and lead time reduction
- an optimal cycle length and an optimal number of inspections using a time-varying lot (or batch) sizes approach in imperfect production processes and considering CI and set-up cost reduction
- Optimal raw material ordering quantity, finished product batch size and number of Kanbans (for a multistage production system) for production-delivery situations considering process inspection, restoration and rework
- SC coordination for pricing, order quantity and investment decisions
- integrated JIT inventory
- EPQ models analysis
- Analysis of rework and the number of shipments in a production system

The Lean SC makes it economic to produce small amounts and consequently allows producers to reduce inventory costs, reduce production costs and satisfy customer demands (Vonderembse et al., 2006).

After being dissatisfied with their Six Sigma and SCM efforts, Samsung combined both Six Sigma and SCM to enhance its operation and improve its efficiency. Six Sigma was used to formalize (provide discipline) the approach to SCM projects and ensure that enough people were fully trained in SCM and quantitative data analysis. Samsung have modified DMADV into DMAEV – define, measure, analyze, enable (instead of the usual design) and verify to adapt the approach to support SCM. They stressed the organizational perspective for improvements as opposed to local, using KPIs to monitor improvements, and using a systematic approach (Emerald, 2007). Training is an essential factor for succeeding in the integration of Six Sigma and SCM as it helps establish an educated and committed workforce that is willing to change and embrace the quality strategy.

Dasgupta (2003) presented a structured methodology that uses Six Sigma metrics (which provides a common scale, such as defects per unit or sigma level) to measure, monitor and improve the performance of a SC and its entities (since it is difficult to do that only with the traditional strategic criteria such as cycle, times, lead times, delivery performance, total SCM costs, inventory levels, rolled throughput yield (RTY), etc.). RTY is the resulting percentage after multiplying the percentages of non-defective output products at each process step.

Amer et al. (2007) proposed expanding DFSS, which provides means of creating specific target metrics and a methodology for isolating where CI efforts should be spent, to SC design. Their approach focuses on using cross-functional teams to understand the VOC and the critical customer requirements (CCR) including demand management.

Value Stream Mapping (VSM)

Value stream mapping (VSM) is considered as one of the most important tools used in a Lean journey. It can be considered as an improvement framework used to transform processes from current to future state. In the mapping exercise, a team goes to the Gemba (the place where work is performed and value is added) and walks through the production steps. Following the flow of how the process is currently done, the team observes cycle times at each step as well as the inventory and waiting times between those steps. Opportunities are identified across the value stream as Kaizen events for continuous improvement (CI). After that, the team works on the design of a future state map where everyone innovates on how the process should look like. Then the team makes an implementation plan used to manage the details of the migration from the current state to the future state. It has detailed information of the improvement actions to be taken, people assigned to do them and when they are expected to happen. These actions could be quick fixes or just-do-it, full projects or a two-day improvement event, etc. After implementing the future state, the cycle repeats itself to achieve CI.

Robotic process Automation (RPA)

Many tasks people do nowadays are repetitive with predictable inputs and outputs. Robotic process automation (RPA) is simply a software robot using algorithms that mimic human functions and automates manually repetitive tasks. It reduces the cost of operation, runs for twenty-four hours a day, and frees up people time to enable them to do more value-adding work. It still requires effective change management to overcome any resistance or fear of job loss by finding smart win-win solutions. RPA is accurate and requires less effort to manage. However, it is inherently intelligent and thus, it requires a programmer to train the robot software to record the keystrokes and mouse clicks, replay them to scan a shopping web site to purchase weekly groceries, as an example. Other examples include downloading different files and then using their content to consolidate regular report to be sent to a group of managers, comparing hundreds of rows in an Excel file with another master document for discrepancies, basic data entry into a system, and other tasks of reading or high-accuracy typing. However, some updates in a process may affect the RPA function which requires to be accordingly updated. Adding cognitive intelligence to RPA using tools like language processing, text analytics, and data mining, is part of the emerging trends in RPA development (Mei, 2018).

RPA can help perform calculations and make decisions based on predefined rules to accomplish tasks. It is enabled by artificial intelligence (AI) using state activities which contain adding triggers, conditions and actions. Examples of technologies adopted with RPA include machine learning, language processing and language generation. With the help of AI technologies, RPA can read images or scanned documents and interpret data. RPA uses coding to capture the logical way of performing a task by a human when interacting with different applications like Oracle or SAP, validating and transforming data as in the example of invoice data entry. It covers a wide range of processes in various industries such as banking, telecom, travel, and logistics. RPA can be easily developed by workers from within the area of work using software platforms in the form of designed flowcharts (Tripathi, 2018).

Being widely accepted, RPA has various benefits such as the reduction of cost of outsourced labor and operation, speeding up execution and response time, increasing productivity, simplification of insurance management tasks, enhancement of financial activities that include data processing and complex workflows, automation of utility companies processes like meter reading or billing, the improvement of healthcare processes including patient scheduling or claims processing, enhancement of services quality and data accuracy, improvement of analytics through time stamping for better predictions, boosting of compliance, increase in agility and scalability depending on requirement, more comprehensive insight through reports, better decision making, saving time in introducing new processes or process modification, better customer service by the robot and the freed up workers, and increase in employee satisfaction by engaging in less tedious tasks (Tripathi, 2018).

As part of the value stream mapping exercise, people can look with an eye of RPA to identify steps that are repetitive in nature which can be suitable for automation. Soft savings of workers hours can be estimated by listing all tasks, their frequency and cost of manual labor per hour, then coming up with a total net impact of RPA after fairly subtracting the cost of creating the RPA algorithm.

2. Materials and Methods

The study in this paper used a mixed approach covering both qualitative and quantitative data. Through direct observation, the primary data were collected. In addition, a number of employees were interviewed in astructured approach including the key stakeholders across the supply chain. Value stream mapping (VSM) exercise was done involving members of a cross-functional teams who identified areas for improvement. Also, from the enterprise resource planning (ERP) systems, quantitative data were gathered focusing on metrics related to quality, cost, and delivery cycle times, and efficiency. In addition, robotic process automation (RPA) algorithms were used for the automation of repetitive tasks. The impact of these imporvements was assessed by comparing the performance metrics before versus after implementation. The analysis incorporated statistical methods to evaluate the significance of the implemented solutions and financial investigation to calculate the cost savings. This approach ensured a comprehensive assessment of the Lean Six Sigma (LSS) implementation within the context of supply chain.

3. Results and Discussion

Using the VSM as part of DMAIC LSS structured approach to improve a supply chain:

Supply chain management (SCM) is vital for any organization to sustain its existence in today’s modern world. There have been various changes in markets across the world, resulting from new realities related to human health, way of living, and technological advancements, which all force supply chain (SC) members to re-evaluate their effectiveness individually and as a whole. SCM can utilize the LSS tools and CI principles to achieve high levels of customer satisfaction regarding cost, quality and delivery.

VSM approach is about enabling the team to reassess the current existing system of processes from a higher-level perspective by stepping out of their daily limited process view or focus. It enables the identification of various challenges and opportunities across the supply chain and value stream. Here are some real examples of such opportunities based on an actual case study grouped into the following five categories of improvement opportunities:

(1) the basic physical operational aspects (related to operators, layouts, and locations): bring all supervisors and frequently interacting employees together within same location, shift the operator waiting or rest area to a location near to equipment parking as well as supervisors offices, eliminate unnecessary walking and make it easier to communicate, and shift the operators to reduce commuting distance and dedicate an area for their station near to the operation yard.

(2) issues related to planning, scheduling, reports and communication: eliminate unnecessary meetings, eliminate unnecessary repetition of communicated instructions or training, ensure all roles and responsibilities are clear for all parties involved, set up service level agreements (SLAs) and eliminate unnecessary reports.

(3) information technology (IT), internal operating systems (related to electronic data interchange (EDI), smart and mobile data entry devices as well as integrated software systems): integrate internal operating systems with external platform including all missing fields, remove the unnecessary approval process in internal operation systems, design automatic reports to replace and combine various manual ones that used to be prepared in Excel or other formats, enable EDI feature in operating system, configure proper events to send an auto-email notification to required teams at proper moments as triggered by the process incidents, reconcile documents by mistake proofing and enhancement of

systems, design an in-house dashboard to enhance communication and integrate equipment and labor requirement, enhance the centralized resource management system and include notification features, use barcoded inventory for all required tools used in operation, implement hand-held tablets (HHT) equipped with a customized software solution (integrated with the internal operating system with automatic (real-time) system-upload of data to replace several forms, eliminating the need for manual entry, re-entry and reporting), and configure gate and HHT functionality for deliveries and the received cargo.

(4) virtual customer service and integrated stakeholders platforms (which allows various external stakeholders to interact and share data to facilitate the overall communication and simplify the process): remove the unnecessary approval process in the external platform, encourage customers to use the external platform (single window) instead of emails to manage their orders, eliminate the waiting time by enabling the customer to upload ready documents along with the initial step, stop customer from uploading redundant Data by directly feeding it into the external platform, replace emails by providing options in the external platform to enable status visibility by auto-status to indicate “ready” versus “in progress” as an example, enhance the external platform to allow different stakeholders and customers to submit their documents directly, introduce an online payment method in the external platform, introduce a delivery appointment system configurable by terminal operation to provide delivery slot capacity in the external platform, and enable the attachment of payment receipt upon booking the delivery request.

(5) robotic process automation (RPA) which automates repetitive manual tasks through computer programming (considered for creating invoices as one example): use RPA to automate repetitive manual tasks of invoicing (auto-calculate then auto-post; customer submits request and supporting documents via system, robot prepares invoices via ERP system, employee receives drafted invoice for review and approval, invoice is issued and sent electronically to requestor).

Also, this case study provided a good example of taking an experienced operation supervisor who is typically caught into his day-to-day tasks, and training him to use the structured approach of LSS DMAIC utilizing VSM (current state in the “measure” phase and future state in the “improve” phase). This supervisor was so excited to use VSM to help him identify all gaps and voice out all pain points across the SC. As noted above, various outcomes resulted impacting several stakeholders such as automation of manual tasks, reduction of cycle times and overall lead time, reduction of idle and wasted operators time, much easier and more effective communication among all stakeholders. In addition, financial savings resulted in the order of Millions of Dirhams annually.

4. Conclusions

Here is a summary of the key results:

- Automation of manual tasks, reduction of employee efforts and cycle times in the order of thousands of worker-hours (freed up staff can be relocated to fill other required vacancies), reduction of paper usage and filing cost, enhancement of communication among all stakeholders, enhancement of revenue through new streams like the fee introduced for handling the whole process on customers’ behalf, and increased financial savings in the order of Millions of Dirhams annually.
- Customer satisfaction, reducing customers visits to the documentation centers and the waiting time, allowing customers to submit documents anytime online and pay charges at their convenience, enhanced utilization of equipment, faster turn-around time for trucks, easier information reporting.
- Introducing smart services, offering more payment options, reducing revenue collection time, and reducing errors through automation of tasks.

Here is a summary of the key conclusions:

- LSS DMAIC can help improve the general cargo handling process (including revenue assurance process) using VSM which ensures the efficient flow among various stakeholders and enables electronic solutions.
- Logistics processes as well as financial processes can utilize the LSS principles, such as focusing on adding value to customers, reducing defectives and wastes, streamlining the flow of value, and improving on time delivery.

Acknowledgments: The Author would like to acknowledge the support given by the project team members which made the study successful.

References

1. Amer, Y., Luong, L., Lee, S. – H., Wang, W. Y. C., Ashraf, M. A. and Qureshi, Z. (2007) 'Implementing design for Six Sigma to supply chain design', proceedings of the 2007 IEEE IEEM, pp. 1517-1521.
2. Bicheno, J., Holweg, M. and Niessmann, J. (2001) 'Constraint batch sizing in a lean environment', International Journal of Production Economics, Vol. 73, No. 1, pp. 41–49.
3. Cochran, D. S., Eversheim, W., Kubin, G. and Sesterhenn, M. L. (2000) 'The application of axiomatic design and Lean management principles in the scope of production system segmentation', International Journal of Production Research, Vol. 38, No. 6, pp.1377–1396.
4. Dasgupta, T. (2003) 'Using the Six Sigma metric to measure and improve the performance of a supply chain', Total Quality Management, Vol. 14, No. 3, 355-366.
5. Deming, W. E. (1993). The new economics for industry, government, education. Cambridge, MA: Massachusetts Institute of Technology, Center for Advanced Engineering Study.
6. Emerald Group Publishing Limited (2007) 'Samsung does Six Sigma: A case study on supply chain management', Strategic Direction, ISSN 0258-0543, Vol. 23, No. 9, pp. 15-17.
7. Foster, S . T. (2007) Managing Quality: Integrating the supply chain, Upper Saddle River, New Jersey: Pearson Education-Prentice Hall.
8. Mei, Y. L. (2018) Robotic Process Automation with Blue Prism Quick Start Guide : Create Software Robots and Automate Business Processes, Packt Publishing, Limited.
9. Parveen, M. and Rao, T. V. V. L. N. (2009) 'An integrated approach to design and analysis of Lean manufacturing system: a perspective of Lean supply chain', International Journal of Services and Operations Management, Vol. 5, No. 2, pp. 175-208.
10. Reichhart, A., & Holweg, M. (2007). Lean distribution: Concepts, contributions, conflicts. International Journal of Production Research, 45(16), 3699–3722.
11. Sanders, D. and Hild, C. R. (2000) 'Common myths about Six Sigma', Quality Engineering, Vol. 13, No. 2, pp. 269-276.
12. Tripathi, A. M. (2018) Learning Robotic Process Automation : Create Software Robots and Automate Business Processes with the Leading RPA Tool - Uipath, Packt Publishing, Limited.
13. Vonderembse, M. A., Uppal, M., Huang, S. H. and Dismukes, J. P. (2006) 'Designing supply chains: towards theory development', International Journal of Production Economics, Vol. 100, No. 2, pp. 223–238.
14. Yang, H. M., Choi, B. S., Park, H. F., Suh, M. S. and Chae, B. (2007) 'Supply chain management Six Sigma: a management innovation methodology at the Samsung Group', Supply Chain Management: An International Journal, Vol. 12, No. 2, pp. 88-95.

Effect of Uniaxial Strain on Frequency Bandgaps of Lightweight Lattice Materials

Mohamed Shendy[1], Maen Alkhader[1,*], Bassam Abu-Nabah[1] and T.A. Venkatesh[2]

[1] Department of Mechanical Engineering, American University of Sharjah, Sharjah, UAE;
[2] Materials Science and Chemical Engineering, Stony Brook University, New York, USA;
***** *Corresponding authors: malkhaderl@aus.edu; Tel.:0097165152955.*

Abstract: Lattice-based materials, owing to their ability to deliver impressive structural properties at low weights, are used in composite sandwich structures designed for aerospace and naval applications. In these applications, the structural integrity of lattice materials needs to be assessed regularly and nondestructively. This work explores the potential for using low-frequency ultrasonic waves to detect damage in hexagonal lattices widely used as cores in sandwich structures. Damage is represented by superposing permanent strain fields on an otherwise perfect lattice. The effect of damage is detected by computationally determining the strain-induced changes in the lattice's acoustic properties, in particular, by detecting changes in its wave band gap characteristics. The effects of small and large strain fields are considered to determine the level of strains that can be detected using frequencies between 100kHz and 1000kHz. Results show that permanent strains significantly affect lattices' bandgaps and indicate that nondestructive evaluation techniques utilizing low to moderate ultrasonic frequency waves can be used to detect damage in lattice materials.

Keywords: aluminum honeycomb cores; nondestructive evaluation; acoustic characteristics; sandwich structures; finite element; bandgaps

---

1. Introduction

Lattice-based cellular solids, owing to their ability to deliver impressive structural properties at very low weights, have been widely used in a wide range of weight-sensitive engineering applications, such as aerospace, wind turbines, composite sandwich structures, and naval vessels [1,2]. In these applications, lattice-based materials may be subjected to inadvertent loadings or conditions that lead to overloading them beyond their failure threshold, resulting in their permanent deformation and damage [3–5]. At damaged locations, the morphological features of lattice-based materials would slightly or significantly deviate from their original shapes depending on the level of damage and loading inducing it [6].

In many applications, particularly when lattice materials are not accessible to the naked eye, detecting damage in lattice materials via nondestructive evaluation (NDE) techniques is required. The most appealing NDE technique for detecting localized damage in aerospace and composite-based applications utilizes ultrasonic waves; however, ultrasonic NDE techniques are not directly applicable to lattice materials due to the dispersive nature of such lattice structures. As an alternative, and since lattice materials are less dispersive at low frequencies, NDE techniques utilizing low frequencies, ranging from sub-ultrasound to low ultrasound frequencies, have been proposed to detect damage in lattice-based materials [7]. In this approach, propagating elastic waves are used to detect damage-induced permanent changes in lattices' morphology. This approach relies on the strong coupling between the behavior of lattice-based materials and their microstructure [8]. Due to this coupling, damage-induced permanent deformations, even when they marginally affect lattice microstructure, can measurably affect lattices' macroscopic properties, including their acoustic properties [9–11]. Accordingly, detecting damage-induced change in lattices' acoustic properties is theoretically achievable by monitoring low-frequency sound waves traversing across inspected lattices. The feasibility of this approach was demonstrated in honeycomb lattices excessively loaded by in-plane tensile loads [12]. In the latter work, excessive loads resulted in 5% permanent strains that were identified by detecting changes in the acoustic behavior of the damaged lattice. In particular, the permanent strains, which altered the lattice's morphology, changed the lattice's frequency bandgaps, i.e., frequency range not supported by the lattice's eigenmodes, in the low ultrasound frequency range. To further promote this technique, it is crucial to evaluate the sensitivity of lattice frequency bandgaps to microstructural changes caused by various damage scenarios. This will aid in establishing the knowledge base needed to develop procedures and algorithms capable of effectively detecting damage in lattice-based materials using low-frequency elastic waves. To this end, this work aims to characterize the effect of small to large strain fields (3% to 12%) on the frequency bandgaps of a honeycomb lattice with relative densities of 10% and 25%. Permanent strain is used to simulate damage due to excessive loading, while different relative densities are used to facilitate generalizing the results across the wide range of commercially available honeycomb lattices.

2. Materials and Methods

2.1 Material and Geometry

A hexagonal honeycomb lattice with single-sided cell walls is used. The lattice is made from aluminum with Young's modulus of 70 GPa, Poisson's ratio of 0.33, and density of 2700 $\mathrm{kg/m^3}$. Lattice ligaments are identical and have a length of 5 mm. Relative density (ρ^*) values of 10% and 25% are used to explore the relative density effect. A representative unit cell approach is used to model the behavior of an infinite periodic honeycomb lattice. The periodic lattice and its representative unit cell are shown in Figure 1. This figure also shows the lattice vectors which are used to reproduce the periodic lattice by repeating the unit cell.

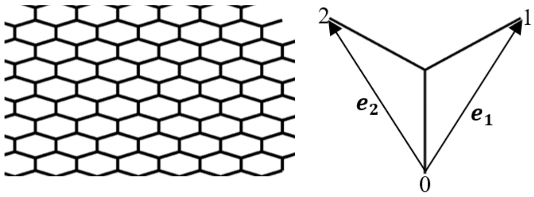

Figure 1. Hexagonal honeycomb lattice, showing its corresponding unit cell and lattice vectors ($\mathbf{e}_1, \mathbf{e}_2$).

2.2 Stretching the unit cell

Stretching strains are applied to represent in-plane stretching damage. Poisson's effect is accounted for in the stretching process. Poisson's ratio for the lattice was determined from the literature [13,14]. Two modes of stretching are included: axial (horizontal) and lateral (vertical). Figure 2 shows the topological changes in the lattice's unit cell due to lateral and axial stretching strains.

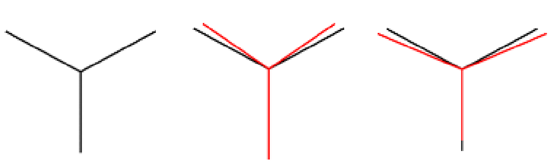

Figure 2. Stretching effect on the unit cell, showing the effect of applying a lateral and axial strain of 12%. Black and red lines correspond to the unstretched and stretched unit cells, respectively.

2.3 Finite Element Model

Detecting changes in the unit cell's morphology, which simulates damage-induced deformation, is achieved by measuring the changes in the unit cell's acoustic behavior, mainly its frequency bandgaps. Finite element analysis, in conjunction with Bloch wave theorem, is used to measure the changes in the bandgaps. The finite element approach is explained in full detail in earlier efforts

[8,9,11]. An outline of the approach is provided here. The finite element software ABAQUS is used to determine the frequency bandgaps of the investigated unit cell. 50 Timoshenko beam elements were used to model the ligaments of the unit cell. Using Bloch's wave theorem, the periodic boundary conditions were defined as

$$\boldsymbol{u_1} = \boldsymbol{u_0} e^{k1} \text{ and } \boldsymbol{u_2} = \boldsymbol{u_0} e^{k2} \tag{1}$$

here $\boldsymbol{u}_0, \boldsymbol{u}_1, \boldsymbol{u}_2$ are the degrees of freedom at the nodes 0, 1, and 2, respectively, shown in Figure 1. k_1 and k_2 represent the dispersive properties along the reciprocal directions, which are defined using

$$\boldsymbol{k} = k_1 \boldsymbol{b}_1 + k_2 \boldsymbol{b}_2 \tag{2}$$

where $\boldsymbol{b_1}$ and $\boldsymbol{b_2}$ are the reciprocal lattice vectors and satisfy $\boldsymbol{b}_i . \boldsymbol{e}_j = \delta_{ij}$. Upon applying the boundary conditions, ABAQUS's Lanczos solver is used to solve the system's eigenvalue problem and find its eigenfrequencies below 1000 kHz. To determine the frequency bandgaps, the eigenfrequencies are determined for a particular range of wave vectors (k_1 and k_2). This range is defined using the polygon marked by the points OABCO in Figure 3. This figure represents the 1st Brillion zone corresponding to the unit cell. The 1st Brillion zone consists of all the possible wave vectors that support periodic wave propagation in the lattice [15]. For every k_1 and k_2 values belonging to the polygon OABCO, the eigenfrequencies are determined. Subsequently, the eigenfrequencies are used to detect the bandgaps of the analyzed lattice.

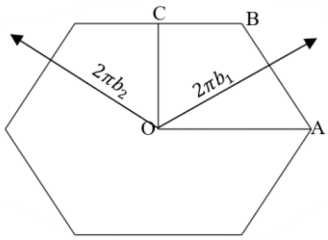

Figure 3. The 1st Billion zone corresponds to the unit cell, as shown in Figure 1.

3. Results and Discussion

3.1 Unstretched Unit Cell

The eigenfrequencies and frequency bandgaps of the unstretched unit cell at the relative densities of 10% and 25% are determined first to establish a benchmark that facilitates determining the changes in the frequency bandgaps due to stretching. The eigenfrequencies of the unstretched unit cell in the range of 1000 kHz are shown in Figure 4 for the relative densities of 10% and 25%.

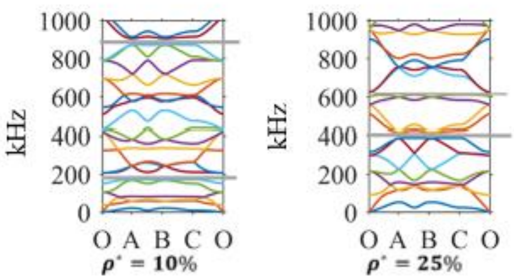

Figure 4. Eigenfrequencies exhibited by the un-stretched honeycomb lattice at 10% and 25% relative densities Each case has two frequency bandgaps, which are highlighted by horizontal lines.

According to the eigenfrequency plots, the unit cell at both considered relative densities exhibits two bandgaps. The bandgaps are highlighted by horizontal lines in Figure 4. For the case with 10% relative density, the first bandgap starts at 172.94 kHz and ends at 208.15 kHz. The second bandgap starts at 874.24 kHz and ends at 906.63 kHz. For the case with 25% relative density, the first bandgap starts at 391.48 kHz and ends at 417.89 kHz. The second bandgap starts at 610.89 kHz and ends at 624.72 kHz.

Figure 4 agrees with the results provided in earlier work [12], which demonstrates the validity of the approach and its implementation in this work. Figure 4 demonstrates a decrease in the bandgap size with increased relative density. This is anticipated as increased relative density renders the lattice less porous, allowing it to exhibit better transmissibility characteristics.

3.2 Effect of 3% Lateral and Axial Strains

The effect of 3% lateral and axial strain fields are investigated in this section for both relative densities considered (i.e., 10% and 25%). Figure 5 shows the eigenfrequencies and frequency bandgaps exhibited by the unit cell after imposing the 3% lateral and axial strains. It is important to note that the lateral and axial strains are imposed independently.

Laterally stretched lattice with 10% relative density exhibited 2 frequency bandgaps. The first bandgap starts at 176.08 kHz and ends at 203.49 kHz. The second bandgap starts at 887.07 kHz and ends at 910.66 kHz. Laterally stretched lattice with 25% relative density exhibited 1 frequency bandgap. The bandgap starts at 397.17 kHz and ends at 417.43 kHz. Axially stretched lattice with 10% relative density exhibited 1 bandgap. The bandgap starts at 174.80 kHz and ends at 202.68 kHz. Axially stretched lattice with 25% relative density exhibited 1 bandgap. The bandgap starts at 403.90 kHz and ends at 417.49 kHz.

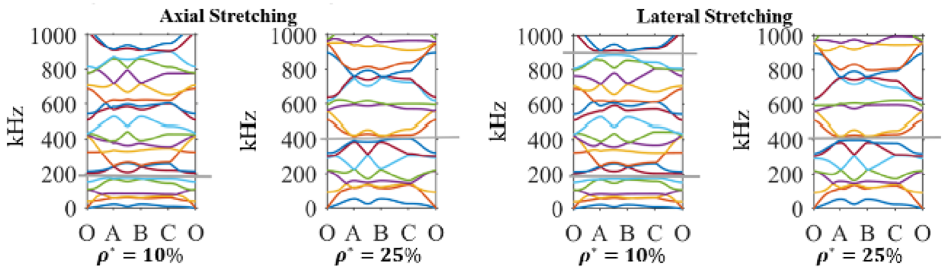

Figure 5. Eigenfrequencies and frequency bandgaps of 3% stretched honeycomb lattice, showing the effect of axial and lateral strains on a lattice with a relative density of 10% and 25%. Frequency bandgaps are highlighted with horizontal lines.

Results demonstrate the insensitivity of frequency bandgaps to 3% strains in the 0-500kHz frequency range, which agrees with results documented in the literature [12]. However, at frequencies higher than 500 kHz, the frequency bandgaps are affected by applying either 3% lateral or axial strain fields, particularly at higher relative densities. Stretching eliminated the second bandgap in most cases. This means that the transmissibility of waves at ~850 kHz is increased by 3% lateral or axial stretching. Accordingly, damage induced by overstretching (~3% strain) can be detected by monitoring the change in the transmissibility of elastic waves propagating at frequencies around 900kHz.

3.3 Effect of Large Permanent Lateral and Axial Strain

The effect of applying large permanent strains on the honeycomb lattice is investigated to explore the sensitivity of its frequency bandgaps to substantial damage resulting from significant overloads. The permanent strains considered are 6% and 12%. The strains are applied laterally and axially. Applying such large strains should noticeably change the topology of the lattice, which, in turn, should affect its frequency band gaps. Figure 6 and Figure 7 show the eigenfrequencies and frequency bandgaps of the 6% and 12% stretched honeycomb lattices. These figures show the effect of laterally and axially applied strains on lattices having 10% and 25% relative densities.

Results presented in Figure 6 can be summarized as follows: laterally stretched lattice with 10% relative density exhibits two frequency bandgaps. The first bandgap starts at 179.14 kHz and ends at 197.77 kHz. The second bandgap starts at 899.44 kHz and ends at 904.41 kHz. Laterally stretched lattice with 25% relative density exhibits one frequency bandgap. The bandgap starts at 403.02 kHz and ends at 415.99 kHz. Axially stretched lattice with 10% relative density exhibits 1 frequency bandgap. The bandgap starts at 177.00 kHz and ends at 197.30 kHz. Axially stretched lattice with 25% relative density exhibits one frequency bandgap. The bandgap starts at 224.27 kHz and ends at 230.10 kHz. These results show that applying 6% strains can eliminate high-frequency bandgaps or shift them. In addition, this level of strain is also capable of eliminating low-frequency bandgaps, particularly at higher relative densities.

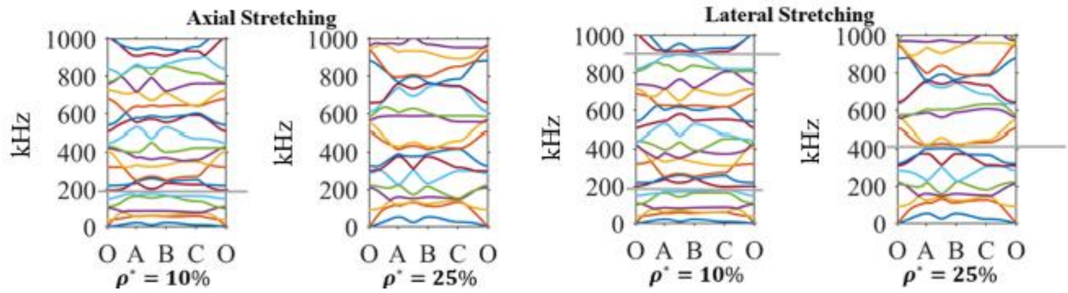

Figure 6. Eigenfrequencies of 6% stretched honeycomb lattice. Frequency bandgaps are highlighted with horizontal lines.

Applying 12% lateral and axial strains, as shown in Figure 7, has a more profound effect on the lattice's eigenfrequency and band gaps. According to Figure 7, the axially stretched lattice with 10% relative density exhibits three frequency bandgaps. The first bandgap starts at 182.41 kHz and ends at 186.84 kHz. The second bandgap starts at 463.40 kHz and ends at 468.68 kHz. The third bandgap starts at 601.56 kHz and ends at 605.66 kHz. On the other hand, the axially stretched lattice with 25% relative density did not exhibit any frequency band gap in the 0~1000 kHz range. Similarly, the laterally stretched lattice with either 10% or 25% relative density did not exhibit any bandgap. Accordingly, applying 12% strains succeeded in eliminating all bandgaps in the 0~1000 kHz frequency range for most of the analyzed cases. Thus, applying 12% stretching strains generally increases the transmissibility of elastic waves propagating through the studied lattice at frequencies below 1000kHz.

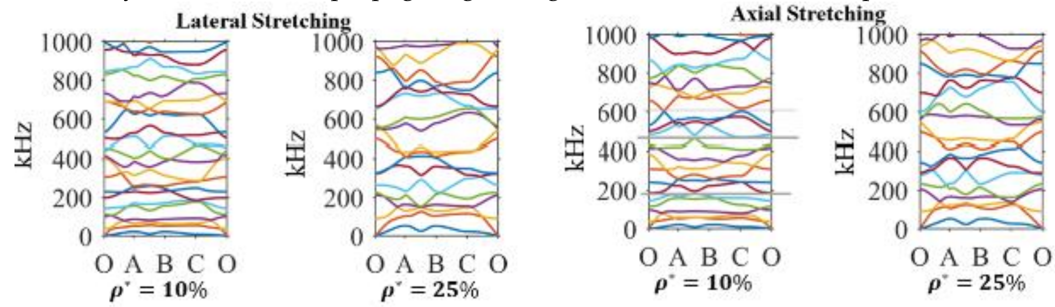

Figure 7. Eigenfrequencies of 12% stretched honeycomb lattice. Frequency bandgaps are highlighted with horizontal lines.

4. Conclusions

The effect of superposing small to large stretching strain fields on the frequency bandgap characteristics of a honeycomb lattice with 10% and 25% relative densities was computationally investigated. The superposed strain fields were used to simulate damage induced by overloading the honeycomb lattice in a stretching mode. Results showed that the frequency bandgaps are insensitive to small strains (i.e., 3%) at frequencies below 500kHz, while they are sensitive to small strains (3%) at higher frequencies, particularly at large relative densities. Sensitivity of frequency bandgaps to superposed strains manifested in the form of bandgap shift or disappearance. Superposing large strain fields in the order of 6% and 12% demonstrated the strong effect of medium to large strains on frequency bandgaps. Superposing 6% strains eliminated the frequency bandgaps at higher frequencies in most of the investigated cases, while superposing 12% strains eliminated most of the frequency bandgaps in the investigated cases. Applying 12% axial strain on a honeycomb with a relative density of 10% exhibited 3 bandgaps, which was uncommon behavior. Results show that imposing small to large strain fields can significantly affect the transmissibility of elastic waves traversing deformed lattices. Results suggest that by experimentally monitoring the transmissibility of elastic waves, particularly around 900kHz, in lattices similar to the one investigated, one can detect damage resulting from excessively stretching loads.

Funding: This work was supported by the American University of Sharjah under the award (FRG23-C-E09).

References

1. Kaw, A.K. Mechanics of Composite Materials; CRC press, 2005; ISBN 1420058290.
2. Gibson, L.J.; Ashby, M.F. Cellular Solids: Structure and Properties; Cambridge University Press, 1999; ISBN 0521499119.
3. Nguyen, M.Q.; Jacombs, S.S.; Thomson, R.S.; Hachenberg, D.; Scott, M.L. Simulation of Impact on Sandwich Structures. Compos Struct 2005, 67, 217–227.
4. Gargano, A.; Das, R.; Mouritz, A.P. Comparative Experimental Study into the Explosive Blast Response of Sandwich Structures Used in Naval Ships. Composites Communications 2022, 30, 101072.
5. Galos, J.; Das, R.; Sutcliffe, M.P.; Mouritz, A.P. Review of Balsa Core Sandwich Composite Structures. Mater Des 2022, 111013.
6. Deng, J.; Gong, X.; Xue, P.; Yin, Q.; Wang, X. A Comprehensive Analysis of Damage Behaviors of Composite Sandwich Structures under Localized Impact. Mechanics of Advanced Materials and Structures 2022, 1–14.
7. Thwaites, S.; Clark, N.H. Nondestructive Testing of Honeycomb Sandwich Structures Using Elastic Waves. J Sound Vib 1995, 187, 253–269.
8. Ahmed, A.; Alkhader, M.; Abu-Nabah, B. In-Plane Elastic Wave Propagation in Aluminum Honeycomb Cores Fabricated by Bonding Corrugated Sheets. Journal of Sandwich Structures & Materials 2017, 1099636217729569.
9. Alkhader, M.; Abu-Nabah, B.; Elyoussef, M.; Venkatesh, T.A. Design of Honeycomb Structures with Tunable Acoustic Properties. MRS Adv 2019, 4, 2409–2418, doi:10.1557/adv.2019.355.
10. Alkhader, M.; Abuzaid, W.; Elyoussef, M.; Al-Adaileh, S. Localized Strain Fields in Honeycomb Materials with Convex and Concaved Cells. European Journal of Mechanics - A/Solids 2019, 103890, doi:https://doi.org/10.1016/j.euromechsol.2019.103890.
11. Ahmad, A.; Alkhader, M.; Abu-Nabah, B.A.; Venkatesh, T.A. Effect of Deformation Mechanisms on In-Plane Wave Propagation in Periodic Cellular Materials. Waves in Random and Complex Media 2021, 1–23.
12. Alkhader, M.; Iyer, S.; Shi, W.; Venkatesh, T.A. Low Frequency Acoustic Characteristics of Periodic Honeycomb Cellular Cores: The Effect of Relative Density and Strain Fields. Compos Struct 2015, 133, 77–84, doi:https://doi.org/10.1016/j.compstruct.2015.07.102.
13. Symons, D.D.; Fleck, N.A. The Imperfection Sensitivity of Isotropic Two-Dimensional Elastic Lattices. In Proceedings of the Journal of Applied Mechanics, Transactions ASME; September 2008; Vol. 75, pp. 0510111–0510118.
14. Phani, A.S.; Woodhouse, J.; Fleck, N.; Fleck, N.A. Wave Propagation in Two-Dimensional Periodic Lattices. Journal of the Acoustical Society of America 2006, 119, 1995–2005, doi:10.1121/1.2179748ï.
15. Brillouin, L. Wave Propagation in Periodic Structures; Electric Filters and Crystal Lattices.; Dover Publications: [New York, 1953; ISBN 0486600343 9780486600345.

Investigation of Flexural Properties of Hybrid Copper-Aluminum Honeycomb Structures

Omar Al Osman [1, *], Maen Alkhader [1,2] and Wael Abuzaid[1,2]

[1] Material Science and Engineering Program, College of Arts and Sciences, American University of Sharjah, Sharjah, United Arab Emirates;

[2] Mechanical Engineering Department, American University of Sharjah, Sharjah, United Arab Emirates;

* *Corresponding authors: b00059046@aus.edu; Tel.: +971501353135.*

Abstract: Sandwich panel structures with aluminum honeycomb cores are renowned for their high stiffness and strength-to-weight ratios, making them ideal for diverse industrial applications. This study seeks to enhance the structural performance of these panels by improving the mechanical response of their honeycomb cores through the application of thin copper coatings. Finite Element Analysis (FEA) was conducted under three-point bending, following ASTM C393 standards, to assess the effects of coating thickness on the flexural and shear moduli of the hybrid copper-coated aluminum honeycombs. Commercially available aluminum honeycombs, fabricated from Al3003 alloy with a cell wall thickness of 0.07 mm, were used to ensure the relevance of the findings. Coating thicknesses of 10, 15, and 20 µm were modeled. Results demonstrate that copper coatings significantly improve the mechanical properties of aluminum honeycomb structures, enhancing the peak load by up to 37.68%.

Keywords: Finite Element Analysis, Hybrid coating, Honeycomb, Sandwich panels, three-point bending.

1. Introduction

Cellular materials, particularly honeycomb cores, are widely used as the cores of sandwich panels due to their lightweight properties and high strength-to-weight ratios [1]. Honeycomb cores are among the simplest cores to manufacture, making them ideal for industrial applications [2], particularly as mass manufacturing of honeycomb cores is feasible. The most common method for mass-manufacturing honeycomb cores involves forming aluminum sheets [3] into half-hexagonal profiles and subsequently gluing them. Depending on the application, honeycomb cores can be made from metallic (e.g., aluminum [4], titanium [5]) or from composite materials such as carbon fiber [6]. Sandwich panels comprising honeycomb core materials have been used in the aerospace [7] and automotive [8] industries for decades.

Typically, the mechanical properties of sandwich structures are explored using three-point bending tests [9]. Such tests have been conducted on cores with varying relative densities [10], different constituent materials, and different cellular shapes [11]. These efforts showed that topology and relative density can significantly influence the flexural modulus and energy absorption capabilities of cores. However, these efforts reached an enhancement plateau, and realizing further enhancement required moving along a new path. To this end, attempts were conducted to enhance the properties of metallic foams by applying a thin coating to them. These efforts resulted in improved flexural modulus [12], out-of-plane elastic modulus, and energy absorption capacity [13]. However, the impact of applying metallic coatings to honeycomb cores of sandwich panels, particularly on their flexural modulus and energy absorption, has not yet been thoroughly explored. In this study, the effect of copper coatings on commercially available aluminum honeycombs is investigated using Finite Element Analysis (FEA) in conjunction with three-point bending tests. This study examines how the thickness of the copper coating affects the peak load, flexural modulus, and energy absorption.

2. Material and Methods

2.1 Geometric Configuration

The sandwich panels used in this study are made of aluminum alloy face sheets and honeycomb core. The properties of the constituent materials of the face sheets and honeycomb core were adopted from an experimental study that tested sandwich panels comprising face sheets made of aluminum alloy Al-5052 and honeycomb core made of aluminum foil Al-3003 [14]. Figure 1 shows the geometrical parameters of the sandwich panels used in this work. The vertical walls of the honeycomb core, as found in commercial aluminum honeycombs, are assumed to have double thickness. This results from the manufacturing process, where two corrugated sheets are glued together, causing the overlapping vertical walls to create double-thickness layers [15]. The geometrical parameters shown in Figure 1 include the face-sheet thickness (T_f), core height (H_c), cell wall thickness (T_c), and strut length (L_s).

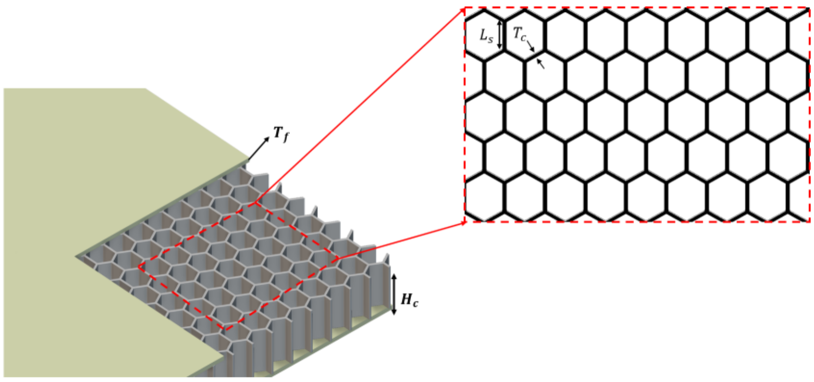

Figure 1: Geometrical Parameters of Honeycomb Sandwich Panel

2.2 FEA Model

The geometry of the sandwich panel and the three-point bending setup, which adheres to the ASTM C-393 standard [16], are shown in Figure 2. The overall length of the specimen in the x-direction is 220 mm, with a span length of 150 mm. The geometrical parameters of the sandwich panel include face sheets with a thickness of 1.5 mm, a core height of 10 mm, a strut length of 4 mm, and a cell wall thickness of 0.07 mm.

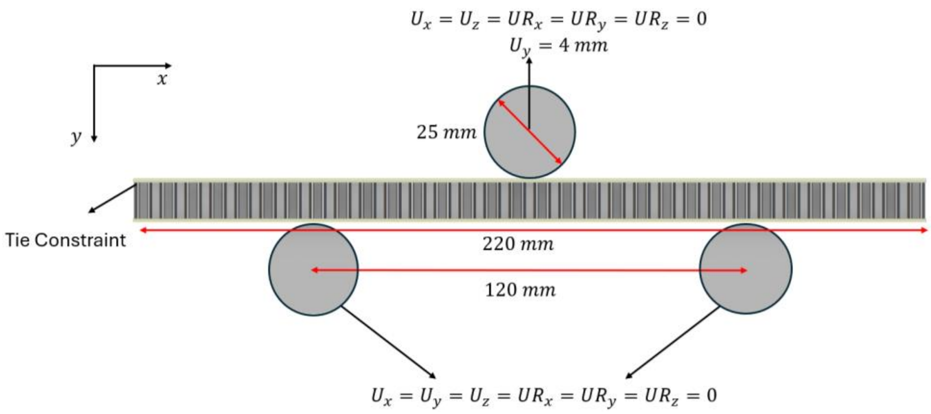

Figure 2: Schematic of the three-point bending test and its boundary conditions

The diameter of the loading roller and the supporting rollers is 25 mm. The loading roller is placed in the middle of the sandwich panel to achieve symmetrical loading conditions. The material properties utilized in the model are shown in Table 1 [14]. The different constituents were modeled as elastic-perfectly plastic materials.

Table 1: Material Properties

Material	Density (Kg/m^3)	Elastic Modulus (GPa)	Yield Strength (MPa)
Al-3003	2720	69	94
Al-5052	2680	72	138
Copper	8940	102	102

FEA was performed using ABAQUS/Explicit solver as it can effectively model the contact behavior between the rollers and the sandwich panel and can accurately account for high nonlinear deformations [17]. To simplify the modeling process, some assumptions were made. It is assumed that there is perfect bonding between the face sheet and the core, even though, in practice, the face sheets and core are typically bonded with an epoxy adhesive. Surface-to-surface interactions are applied between the loading/support rollers and the sandwich panel. These interactions used a coefficient of friction of 0.2. To model perfect bonding between the core of the sandwich panel and the face sheets, tie constraints were applied between them. The loading/support rollers were modeled as rigid bodies. This assumption reduces calculation time, particularly since the rollers are much stiffer than the tested sandwich core in practice. As shown in Figure 2, the two support rollers were fully fixed on all sides, whereas the loading roller was only allowed to translate along the loading direction. A displacement rate of 50 mm/s was applied to the top roller along the y-direction, simulating quasi-static loading conditions. This approach is used to reduce computational demand, as slower displacement rates would require significantly more commotional power [11]. The cell walls of the honeycomb core and face sheets were meshed using linear quadrilateral shell elements S3D4. The honeycomb core was converted into a hybrid copper-coated honeycomb by adding a new shell element-based copper layer. The material properties of the added copper layer are shown in Table 1 [13]. Figure 3 shows the two-dimensional configuration of the hybrid copper-coated honeycomb core. Three coating thicknesses were modeled, namely 40 μm, 60 μm, and 80 μm.

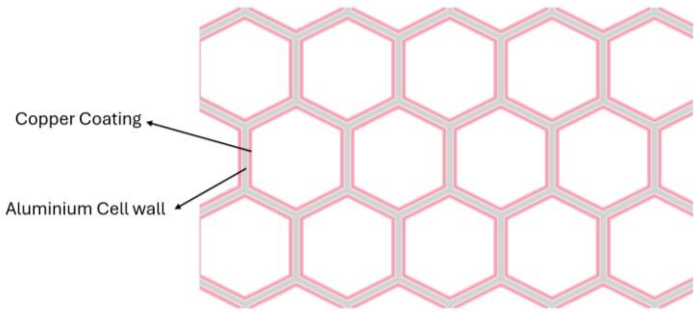

Figure 3: Copper-coated aluminum honeycomb cross-section

The added shell element layer, which is representative of the added copper coating, is added using ABAQUS' mesh offset tool, which creates a layer of shell elements on the outer surfaces of the honeycomb cell walls. The added copper layer is assumed to be perfectly bonded to the aluminum cell walls. Additionally, the coating thickness is assumed to be uniform across all cell walls of the honeycomb core.

A two-step validation process was used to verify the developed FEA models. The first step involved a detailed mesh sensitivity analysis. Results showed that an element size of 0.15 mm is sufficient to obtain a mesh size-independent solution. In the second step, the numerical simulation was validated against published experimental results [14] of uncoated sandwich structures similar to the ones used in this work. The validation results, which show good agreement between the FEA and experimental results, are shown in Figure 4.

3. Results and Discussion

The force-displacement plots extracted from the three-point bending simulations conducted on the sandwich structure, comprising aluminum honeycombs with no coating and with 40 µm, 60 µm, and 80 µm copper coatings, are shown in Figure 4.

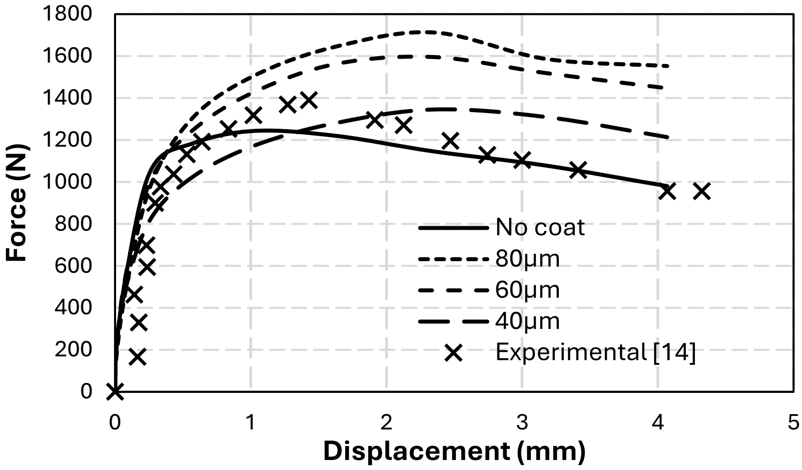

Figure 4: Force vs Displacement plots of the three-point bending tests

The force-displacement results show that the elastic response of the sandwich panel is unaffected by the applied coatings. However, the peak loads of the sandwich panels vary significantly as a result of the added copper coating. The pure aluminum honeycomb sandwich panel exhibited a peak load of 1243.92 N as compared to 1345.63 N, 1595.93 N, and 1712.72 N for the 40, 60, and 80µm copper-coated honeycomb samples, respectively. The increase in copper coating thickness leads to a nonlinear enhancement in peak load. A 40 µm copper coating resulted in an 8.17% increase, while 60 µm and 80 µm coatings resulted in 28.29% and 37.68% increases, respectively, compared to the uncoated aluminum sandwich panel. This nonlinear increase causes a significant enhancement in the panel's energy absorption capabilities. These results demonstrate the effectiveness of copper coating aluminum honeycombs, which can be achieved through a simple electrodeposition process. However, a drawback of coating aluminum honeycombs is that it compromises one of the key features of cellular cores: their strength-to-weight ratio. It is important to consider that the density of copper is three times that of aluminum, which can lead to a significant increase in weight.

Figure 4 shows that the flexural modulus is unaffected by the applied coatings. However, the addition of copper, which has a higher elastic modulus than aluminum, contributes to a better stress distribution. The higher modulus of copper facilitates load sharing over a larger area and delays the onset of yielding on a global scale. Figure 5 shows a comparison between the behavior of uncoated and coated cores. This figure shows the stress contour plot in the core during the three-point bending test. In addition, the figure shows the deformation pattern. Figures 5a and 5b show the difference in the stress distribution between a pure aluminum honeycomb sample and a hybrid copper-coated aluminum honeycomb with $40\mu m$ coating thickness. As evident from the figure, the stresses are more evenly distributed in the coated sample. This can be attributed to the enhanced modulus of copper as well as the added area on which the applied load is distributed. Table 2 summarizes the extracted properties from the conducted simulations, which include flexural stiffness, peak load, and energy absorption.

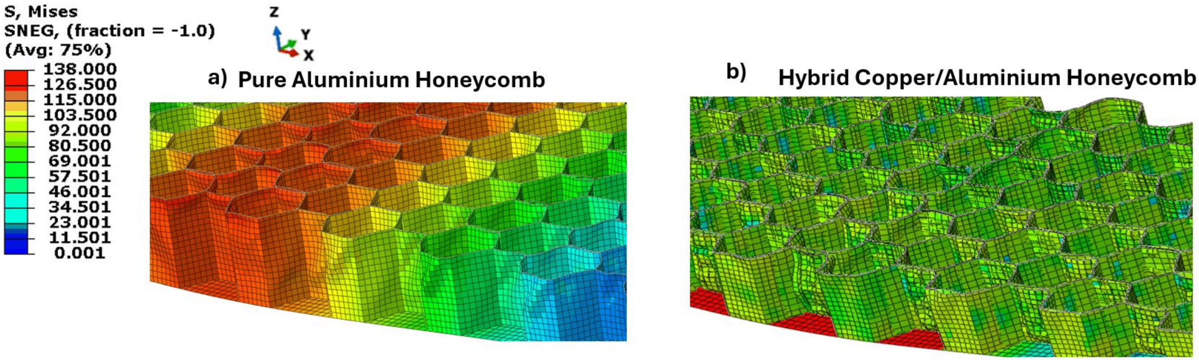

Figure 5: Stress contour in the core under flexural loading, showing (a) distribution in pure aluminum honeycomb core and (b) distribution in 40μm copper-coated aluminum honeycomb core.

Table 2: Effect of copper coating honeycomb on flexural properties

Sample	Flexural Modulus (kN/mm)	Peak Load (N)	Energy Absorption(J)
Uncoated Honeycomb	4.82	1243.92	4504.76
Copper/Al Honeycomb 40 μm	4.81	1345.63	4842.50
Copper/Al Honeycomb 60 μm	3.74	1595.93	5778.55
Copper/Al Honeycomb 80 μm	4.43	1712.72	6076.03

The flexural modulus remains relatively independent of the applied coating. The energy absorption constantly increases with increasing the coating thickness as the peak load increases, which increases the area under the force-displacement curve. It is important to acknowledge the drawbacks of adding copper coatings to aluminum honeycombs, as this can significantly compromise their lightweight properties. Nevertheless, applying a copper coating can enable the core and sandwich structure to achieve exceptionally high load-carrying capacity and energy absorption. Additionally, coating the core allows for tailoring its properties to better suit specific industrial applications.

4. Conclusion

This study investigates the effect of using hybrid copper-coated aluminum honeycomb cores in sandwich panels, focusing on their flexural behavior under three-point bending tests. The results indicate that adding copper coatings can significantly enhance the peak load and energy absorption capabilities of the sandwich panels, while the flexural modulus remains unaffected. The most significant improvement was observed with the highest coating thickness. However, because copper is much denser than aluminum, the enhancement in panel properties comes with an increase in weight. Despite this, the panels with copper-coated honeycomb cores demonstrated improved performance, making them suitable for applications requiring higher energy absorption, though with a trade-off between enhanced mechanical properties and increased weight.

Acknowledgment

This work was funded by the American University of Sharjah under Grant FRG23-C-E09.

References

[1] L. J. Gibson, "Cellular solids," MRS Bull, vol. 28, no. 4, pp. 270–274, 2003.

[2] M. Alkhader, B. Abu-Nabah, M. Elyoussef, and T. A. Venkatesh, "Design of honeycomb structures with tunable acoustic properties," MRS Adv, vol. 4, no. 44–45, pp. 2409–2418, 2019.

[3] S. Prabhu, V. K. B. Raja, and R. Nikhil, "Applications of cellular materials–an overview," Applied Mechanics and Materials, vol. 766, pp. 511–517, 2015.

[4] Y. Zhang, Q. Liu, Z. He, Z. Zong, and J. Fang, "Dynamic impact response of aluminum honeycombs filled with Expanded Polypropylene foam," Compos B Eng, vol. 156, pp. 17–27, 2019.

[5] M. A. El-Sayed, K. Essa, M. Ghazy, and H. Hassanin, "Design optimization of additively manufactured titanium lattice structures for biomedical implants," The International Journal of Advanced Manufacturing Technology, vol. 110, pp. 2257–2268, 2020.

[6] H. Jiang, Y. Ji, Y. Hu, X. Hu, and Y. Ren, "Interfacial design and flexural property of CFRP/aluminum-honeycomb sandwich with Aramid-pulp micro/nano-fiber interlays," Compos Struct, vol. 289, p. 115486, 2022.

[7] U. Farooq, M. S. Ahmad, S. A. Rakha, N. Ali, A. A. Khurram, and T. Subhani, "Interfacial mechanical performance of composite honeycomb sandwich panels for aerospace applications," Arab J Sci Eng, vol. 42, no. 5, pp. 1775–1782, 2017.

[8] G. Srinath, A. Vadiraj, G. Balachandran, S. N. Sahu, and A. A. Gokhale, "Characteristics of aluminium metal foam for automotive applications," Transactions of the Indian Institute of Metals, vol. 63, pp. 765–772, 2010.

[9] H. Taghipoor, A. Eyvazian, F. Musharavati, T. A. Sebaey, and A. Ghiaskar, "Experimental investigation of the three-point bending properties of sandwich beams with polyurethane foam-filled lattice cores," in Structures, Elsevier, 2020, pp. 424–432.

[10] J. León-Becerra, O. A. González-Estrada, and J. Quiroga, "Effect of relative density in in-plane mechanical properties of common 3D-printed polylactic acid lattice structures," ACS Omega, vol. 6, no. 44, pp. 29830–29838, 2021.

[11] F. Xia, Y. Durandet, P. J. Tan, and D. Ruan, "Three-point bending performance of sandwich panels with various types of cores," Thin-Walled Structures, vol. 179, p. 109723, 2022, doi: https://doi.org/10.1016/j.tws.2022.109723.

[12] W. Wang, R. Burgueño, J.-W. Hong, and I. Lee, "Nano-deposition on 3-D open-cell aluminum foam materials for improved energy absorption capacity," Materials Science and Engineering: A, vol. 572, pp. 75–82, 2013.

[13] O. Al-Osman, M. Alkhader, and W. Abuzaid, "Enhancing the multifunctionality of open-cell foams through tailoring their thermal and mechanical properties using coatings," European Journal of Mechanics-A/Solids, vol. 99, p. 104923, 2023.

[14] G. Sun, X. Huo, D. Chen, and Q. Li, "Experimental and numerical study on honeycomb sandwich panels under bending and in-panel compression," Mater Des, vol. 133, pp. 154–168, 2017.

[15] F. Tornabene, M. Viscoti, R. Dimitri, and M. A. Aiello, "Higher order formulations for doubly-curved shell structures with a honeycomb core," Thin-Walled Structures, vol. 164, p. 107789, 2021.

[16] A. International, Standard test method for core shear properties of sandwich constructions by beam flexure. ASTM international, 2016.

[17] O. Al Osman, M. Alkhader, and W. Abuzaid, "Flexural response of sandwich structures comprising topologically perturbed cores," in Journal of Physics: Conference Series, IOP Publishing, 2024, p. 012028.

Experimental Investigation of the Performance of Bifacial Solar Panels Under Jordanian Climate Conditions

Rasheed Abu-Radwan, Ahmed Al-Salaymeh, Mahmoud Irshidat, Khadeejeh Afaneh, Randa Abu-Lail
Department of Mechanical Engineering, The University of Jordan, Amman 11942, Jordan

***** *Corresponding authors:* **m.irshidat@ju.edu.jo***; Tel: +962 795086397*

BSTRACT

In this study, a bifacial photovoltaic (PV) system, which is a dual-plate type of solar cell, is investigated for its performance under Jordanian climate conditions. Bifacial solar cells can produce more energy than monofacial solar cells by absorbing solar radiation on both sides—front and rear. This study focuses on the effect of varying the tilt angles (15º, 30º, and 45º) on the energy output of the bifacial PV system. Experiments were conducted in Amman, Jordan, during February, March, May, and June 2020. Measurements were taken at noon on sunny days to track irradiance and evaluate the performance of bifacial versus monofacial panels. The optimum tilt angle for the bifacial PV module was found to be 30º, yielding an efficiency of 19.9%, compared to the 14.7% efficiency of the monofacial panel.

Keywords: *Bifacial Solar Panels, Monofacial Solar Panels, Photovoltaic System, Tilt Angles, Energy Output, Jordanian Climate*

INTRODUCTION

Photovoltaic (PV) technologies have reached commercial viability and technological maturity, positioning them to play a pivotal role in the ongoing energy transition. This shift is crucial for addressing the environmental challenges associated with fossil fuel-based power generation. (Allouhi et al., 2022)

Bifacial solar panels are capable of converting light into electricity from both the front and rear sides. Unlike traditional monofacial solar cells, which have an aluminum paste covering the rear side, bifacial solar cells have glass sheets on both sides, allowing them to harness reflected light from surrounding surfaces. This design increases the power output of bifacial modules compared to traditional monofacial modules (Kopecek et al., 2021). Bifacial panels are more economical due to the reduced balance of system costs and the ability to generate more power within a smaller array footprint. The performance of these panels is significantly influenced by the reflectivity (albedo) of the ground surface beneath them (Ernst et al., 2024).

Solar PV systems can be categorized into three main types: Off-Grid, Hybrid, and On-Grid systems. These systems convert daylight into electricity, which can be used locally or fed into the grid. This study aims to construct an experimental PV system incorporating both bifacial and monofacial panels. It evaluates the benefits of bifacial solar panels by examining various influencing factors such as temperature, tilt angles, and radiation. The performance, including efficiency and power output, of bifacial panels is compared with that of monofacial panels.(Tabora et al., 2021). Numerous studies indicate that bifacial photovoltaic (bPV) modules help achieve a lower levelized cost of electricity (LCOE) due to their ability to generate electricity from both sides. (Humphreys et al., 2021)

Bifacial PV modules have transparent front and rear surfaces, allowing them to absorb light from both sides. According to a study conducted in the Czech Republic, bifacial modules collected 72% more energy than monofacial modules(Vimala et al., 2023). The efficiency of bifacial solar cells can be as high as 94% of the front efficiency under back illumination, depending on various factors like cell quality and light conditions. Studies by Sun (2024) demonstrated that bifacial panels with adjustable tilt angles can capture more sunlight, thereby increasing energy output(Sun et al., 2024). However, research by Said (2024) found that in harsh environments, such as Saudi Arabia, the performance of bifacial PV technology can be compromised by dust and other environmental factors.(Said et al., 2024)

Photovoltaic cells are made of semiconductors like silicon, which absorb light and allow free electrons to flow, generating electricity. The structure of silicon atoms, with their unique arrangement of electrons, facilitates the flow of electricity when impurities are added. This process, known as doping, enhances the conductivity of silicon, making it more effective for use in solar cells

(Scaccabarozzi et al., 2022). Building on this , performance parameters, and irradiance modeling have been validated by experimental results. The proposed irradiance model for bifacial PV accurately predicts the irradiance levels for a prototype bifacial PV module.(Sahu et al., 2023)

METHODOLOGY

This study employed an experimental approach to compare the performance of bifacial and monofacial PV modules. The primary goal was to determine the efficiency differences under various conditions, including different tilt angles, environmental factors, and the presence of reflective materials. Key measurements such as voltage, current, and irradiance were taken to calculate the efficiency of each module type. The experiments were conducted from February to June 2020 using a robust setup and precise measurement devices to ensure accurate and reliable results.

Experimental setup

The experiments involved two types of PV modules: a 370W bifacial module and a 360W monofacial module, both from Philadelphia Company. The setup is depicted in Figure 1, with experiments conducted under varying conditions from February to June 2020.

Figure 1 Bifacial and mono-facial experimental system

Design of Metal Base Structure

A robust steel structure was designed to hold the PV panels, allowing adjustment of tilt angles (15º, 30º, and 45º). This design ensures stability under different weather conditions and maximizes irradiance capture (Figure 2 and Figure 3).

Figure 2 The base of the project

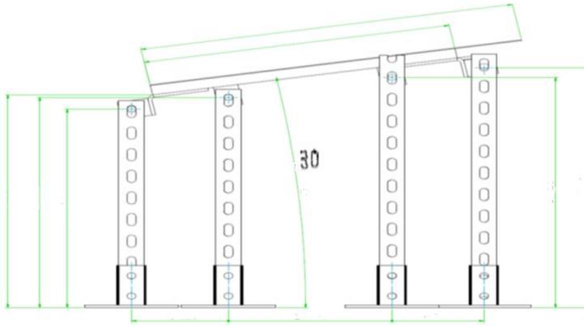

Figure 3 The oriented panel of the project

Measurement devices

Voltage, current, and power were measured using a multimeter, as shown in Figures 4 and 5.

Figure 4 Multimeter device

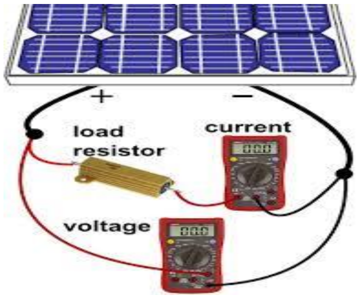

Figure 5 Measuring current and voltage of modules

Pyranometers were used to measure irradiance under various weather conditions (Figure 6).

Figure 6 All parts of pyranometer irradiance device

Measurement procedure

The study employed an experimental approach, comparing the performance of bifacial and monofacial modules under different conditions. Key measurements included voltage, current, and irradiance, with efficiency calculated using the following formula:

$$\text{Efficiency } (\eta) = \frac{\text{Pout}}{\text{Pin}} = \frac{\text{Voltage x Current}}{(\text{Irradiance x Area of panel})} \text{ x } (100\ \%) \text{ .... } (4.1)$$

$$\eta = (\text{Vmpp x I mpp}) / (\text{G x A})$$

Instruments used included bifacial and monofacial modules, an Off-Grid charge controller, inverter, battery, pyranometer, and various measuring devices.

RESULTS AND DISCUSSION

The results indicated that the bifacial PV module, at a tilt angle of 30º, achieved the highest efficiency of 19.9%, significantly outperforming the monofacial module, which had an efficiency of 14.7%. This demonstrates the effectiveness of bifacial panels in harnessing additional reflected light, thereby enhancing overall energy output.

Comparative performance

Table 1 shows the performance comparison between bifacial and monofacial panels at different tilt angles were compiled. These showed that bifacial panels consistently outperformed monofacial panels under all tested conditions.

Table 1 (360W) mono-facial module at G (518W/m²) without shading with reflector white paint and sprinklers vs a (370 W) bifacial modules with reflector at irradiance (525W/m2), angle 30-degree, used water cooling system, date 7-3-2020

Measurements	Mono-facial model (300W)	Bifacial module (370W)
Irradiance (W/m^2)	518	525
Temperature (Deg C)	18.99	20.01
Tilt (Deg)	30.0	30.0
P max	145.07	235.631
Vmpp	28.90	34.1
I mpp	5.13	6.91
Voc	28.9	36.9
Isc	7.043	7.79
Measurement time	1:37 PM	1:56 PM
Number of cells in module	12x6=72 cells	72 cells
Reflector is white paint, albedo factor is	0.62	0.62
Height of module above the ground	1 meter	1 meter
Area of the module is	1.92 (m²)	1.92 (m²)

Influence of Tilt Angle

Experiments were conducted at tilt angles of 15º, 30º, and 45º as it shown in table 2. The results indicated that the 30-degree tilt angle was optimal for bifacial modules, achieving the highest efficiency of 19.9%. The corresponding efficiencies for monofacial modules at this angle were 14.7%. At a 15-degree tilt angle, bifacial modules performed less efficiently than at 30 degrees, and at 45 degrees, efficiency was also lower, confirming that 30 degrees is the most effective tilt angle for maximizing energy output.

Table 2 Tilt angle influence results

DATE	TILT ANGLE DEG	ALBEDO	IRRADIANCE	(w/m^2)	OUTPUT	RESULTS

		15	45	30	WITH REF	WITHOUT	480	500	520	V mpp	I mpp	P mpp	EFFICIENCY
MONO.	7/3/2020			√	√				518.1	28.8	5.12	148.8	14.50%
MONO.	16-5-2020		√		√			499.9		22.9	5.01	114.2	12.01%
MONO.	17-5-2020	√			√		472			20.8	4.98	103.7	11.10%
M& Partial SHADING	18-5-2020			√	√		465			18.01	4.01	72.22	9.30%
M&FULL SHADING	19-5			√	√		469			6.92	0	0	0.00%
BIFACIAL	7/3/2020			√	√				525	34.1	6.91	235.63	19.90%
BIFACIAL	21-5-2020		√		√			508		27.99	5.92	165.7	16.91%
BIFACIAL	23-5-2020	√			√		469			25.3	4.99	126.24	14.00%
BIF &PARTIAL SHADING				√	√		495			29.9	3.92	117.2	11.06%
BIF &FULL SHADING				√	√		491			24.7	0	0	0.00%

Influence of Reflective Material

The use of reflective material beneath the bifacial panels significantly enhanced their efficiency. The rear side of bifacial panels, which captures additional reflected light, played a crucial role in this improvement. This factor is essential as it directly impacts the overall operation and efficiency of the modules.

Directional Orientation

Positioning the bifacial modules in an East-West orientation proved effective in increasing their efficiency compared to monofacial modules. This orientation allowed bifacial panels to capture more sunlight throughout the day, further boosting their energy output.

Environmental and Temporal Factors

Bifacial PV panels rated at 370W consistently outperformed 360W monofacial panels under identical conditions. Efficiency was highest during peak sun hours from 12:00 pm to 2:00 pm, with lower power production observed in the morning and afternoon due to reduced irradiance. High temperatures in July and August negatively affected the efficiency of bifacial modules, suggesting the need for a cooling system to maintain optimal performance.

External Factors

The power productivity of bifacial modules is influenced by several external factors, including mounting methods, climatic conditions, tilt angle, irradiance, height, albedo, and cooling systems. High temperatures during the summer months, specifically in July and August, reduced efficiency, indicating the necessity of cooling systems to sustain power productivity.

General Observations

Bifacial modules generate high power with minimal space requirements and are more economical than monofacial modules, producing more energy at a lower cost. They have relatively low construction and maintenance costs and are environmentally friendly, making them suitable for various settings, including car garages, rooftops, and densely populated urban areas. Bifacial modules are particularly effective in icy locations.

Economic and Environmental Benefits

Bifacial modules help reduce the levelized cost of electricity (LCOE), making them a promising technology for enhancing the lifetime electricity generation of photovoltaic systems. Their ability to produce high energy output efficiently and economically positions them as a viable solution for various applications, contributing to a sustainable and cost-effective energy future.

CONCLUSION

This study shows that bifacial modules are more efficient than monofacial modules, with efficiencies of 19.9% and 14.7%, respectively. Bifacial modules, transparent on both sides, outperform monofacial modules, which are transparent only on the front. The optimal tilt angle for bifacial modules is 30 degrees. Reflective material beneath the panels significantly enhances efficiency, with the ground's reflection factor playing a crucial role. The East-West orientation further increases bifacial efficiency. Bifacial PV panels (370W) outperform monofacial panels (360W) under the same conditions, with peak efficiency observed between 12:00 pm and 2:00 pm. High temperatures in July and August reduce efficiency, making a water cooling system beneficial. Factors like tilt angle, irradiance, height, albedo, and cooling systems influence efficiency. Bifacial modules provide high energy output in small spaces at low cost, with relatively inexpensive construction and maintenance costs. They are environmentally friendly and suitable for various settings, contributing to reduced levelized cost of electricity (LCOE) and enhancing photovoltaic system longevity and electricity generation.

References:

Allouhi, A., Rehman, S., Buker, M. S., & Said, Z. (2022). Up-to-date literature review on Solar PV systems: Technology progress, market status and R&D. *Journal of Cleaner Production*, *362*, 132339. https://doi.org/10.1016/J.JCLEPRO.2022.132339

Ernst, M., Liu, X., Asselineau, C. A., Chen, D., Huang, C., & Lennon, A. (2024). Accurate modelling of the bifacial gain potential of rooftop solar photovoltaic systems. *Energy Conversion and Management*, *300*, 117947. https://doi.org/10.1016/J.ENCONMAN.2023.117947

Humphreys, J., Lan, R., & Tao, S. (2021). Development and Recent Progress on Ammonia Synthesis Catalysts for Haber–Bosch Process. In *Advanced Energy and Sustainability Research* (Vol. 2, Issue 1). John Wiley and Sons Inc. https://doi.org/10.1002/aesr.202000043

Kopecek, R., Libal, J., Laudani, A., & Werner, J. H. (2021). Bifacial Photovoltaics 2021: Status, Opportunities and Challenges. *Energies 2021, Vol. 14, Page 2076*, *14*(8), 2076. https://doi.org/10.3390/EN14082076

Sahu, P. K., Roy, J. N., & Chakraborty, C. (2023). Performance assessment of a bifacial PV system using a new energy estimation model. *Solar Energy*, *262*, 111818. https://doi.org/10.1016/J.SOLENER.2023.111818

Said, S. Z., Islam, S. Z., Radzi, N. H., Wekesa, C. W., Altimania, M., & Uddin, J. (2024). Dust impact on solar PV performance: A critical review of optimal cleaning techniques for yield enhancement across varied environmental conditions. *Energy Reports*, *12*, 1121–1141. https://doi.org/10.1016/J.EGYR.2024.06.024

Scaccabarozzi, A. D., Basu, A., Aniés, F., Liu, J., Zapata-Arteaga, O., Warren, R., Firdaus, Y., Nugraha, M. I., Lin, Y., Campoy-Quiles, M., Koch, N., Müller, C., Tsetseris, L., Heeney, M., & Anthopoulos, T. D. (2022). Doping Approaches for Organic Semiconductors. *Chemical Reviews*, *122*(4), 4420–4492. https://doi.org/10.1021/ACS.CHEMREV.1C00581/SUPPL_FILE/CR1C00581_SI_001.PDF

Sun, L., Bai, J., Pachauri, R. K., & Wang, S. (2024). A horizontal single-axis tracking bracket with an adjustable tilt angle and its adaptive real-time tracking system for bifacial PV modules. *Renewable Energy*, *221*, 119762. https://doi.org/10.1016/J.RENENE.2023.119762

Tabora, J. M., Júnior, U. C. P., Rodrigues, C. E. M., Bezerra, U. H., Tostes, M. E. de L., de Albuquerque, B. S., de Matos, E. O., & Do Nascimento, A. A. (2021). Hybrid System Assessment in On-Grid and Off-Grid Conditions: A Technical and Economical Approach. *Energies 2021, Vol. 14, Page 5284*, *14*(17), 5284. https://doi.org/10.3390/EN14175284

Vimala, M., Ramadas, G., Perarasi, M., Manokar, A. M., & Sathyamurthy, R. (2023). A Review of Different Types of Solar Cell Materials Employed in Bifacial Solar Photovoltaic Panel. *Energies 2023, Vol. 16, Page 3605*, *16*(8), 3605. https://doi.org/10.3390/EN16083605

Innovative Cooling System of Raspberry Pi using Ultrasonic Resonant Device

Mohammad Mustafa, Abdulsalam Ghodayah and Mahmoud Irshidat*

Mechanical Engineering Department, The university of Jordan, Amman 11942, Jordan

* *Corresponding authors:* **m.irshidat@ju.edu.jo**; *Tel: +962 795086397*

Abstract

This study explores the use of an ultrasonic resonant device (URD) as an innovative cooling system for a Raspberry Pi computer, typically utilized in vibration measurement devices. Traditional cooling fans, with known noise and vibration can interfere with sensitive measurements. Therefore, the project aims to employ a PZT (Piezoelectric) URD to generate airflow, minimizing the impact on measurement sensors.

The URD operates at a frequency of 34 kHz, significantly higher than the operational range of the measurement device, thereby eliminating interference.

The study includes a detailed computational fluid dynamics (CFD) analysis to evaluate the cooling performance of the URD. Initial conditions set the processor temperature at 60°C with a heat generation rate of 1W. The airflow, driven by the URD, enters at 25°C with a flow rate of $9.4389 * 10^{-4}$ Cubic meters per second (m3/s). The cooling system incorporates a heat sink made of pure aluminum, which aids in efficient heat dissipation.

Results from the CFD analysis indicate that the URD successfully reduces the processor temperature to a stable 33°C within a minute. The turbulence generated by the ultrasonic airflow enhances heat transfer, proving the

system's efficacy over traditional fan-based cooling methods. The study also suggests potential improvements in the design of the enclosure and heat sink for better performance.

Thus, the ultrasonic resonant device presents a viable alternative to conventional cooling fans, offering noise-free and efficient cooling for sensitive electronic measurement applications. Further experimentation with different heat sink designs is planned to optimize the system's performance.

Keywords: Ultrasonic Resonant Device, Piezoelectric (PZT), Computational Fluid Dynamics (CFD), Noise Control, Vibration, Natural Frequency, Cooling System

1. Introduction

A Raspberry Pi is a small, affordable, single-board computer. It is designed to promote computer science education and DIY electronics projects.

Raspberry Pi can be used for a wide range of applications including but not limited, in our case we use it in Measurement device that design to Measure the Natural frequency and Vibration.

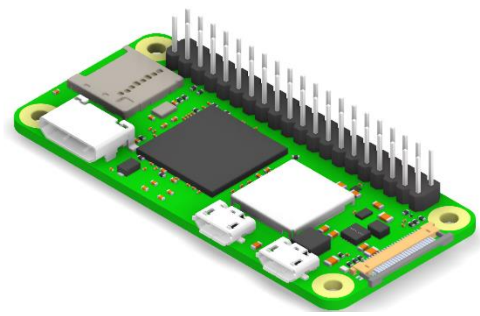

Figure 1 (Raspberry Pi Zero 2 W with 40 pin male connector v4)

Why do we need to research to avoid the noise? Because the measurement type is very sensitive, we always try to avoid any kind of noise that could effect the result by filtering the noise in many ways that could be generate from many ways, for example the cooling fan that could be generate higher noise that could effect on the result.

The main objective from this research is to design a cooling system by using ultrasonic resonant device instead of fans to achieve the following:

- Use PZT ultrasonic resonant device to generate airflow, to cool a raspberry pi computer (Used in a vibration measurement device)
- the device is used instead of a fan in order to minimize vibration impact on the Measurement sensor.
- generated airflow will pass above the processor in order to lower its temperature where the average velocity of ultrasonic resonant device around 475 ft./min., and a peak velocity of 1400 ft./min and airflow 2ft^3 /min

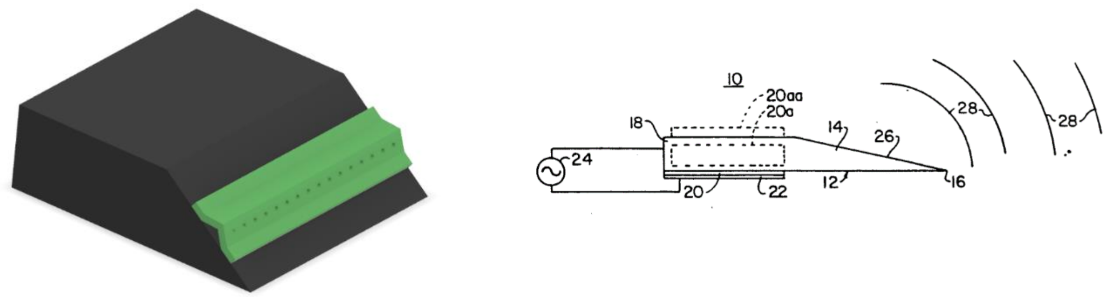

Figure 2 (Ultrasonic Resonant Device)

Where ultrasonic resonant frequency is around 34KHZ, which is 2. 04x10^6 RPM, a value that's much higher than the operating range of the vibration measurement device, unlike a conventional cooling fan which operates at the same range of frequency as the device.

2. Literature Review

1. This invention relates to resonant devices and ultrasonic transducers and more particularly to transducers for efficiently producing periodic vibrations having frequencies in the ultrasonic region.

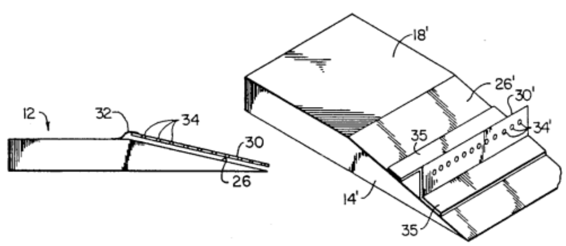

Figure 3

Piezoelectric blade blowers are known which are much smaller than the smallest rotary fans and are used to cool electronic equipment. These blowers are highly efficient, have long life, generate little noise or magnetic interference and are approximately two inches by one inch by three-fourths of an inch in size.

However, they too have drawbacks. They are not small enough for direct mounting on printed circuit boards and electrical noise in the circuit boards as well as requiring that a 115-volt source be made available at the board. Attempts to use a piezoelectric crystal directly to pump air by acoustic streaming have also been less than successful because large crystals are required which are difficult and expensive to obtain in production. Acoustic streaming results from the fact that air accelerated by an oscillating surface does not reverse its direction when the surface does, due to inertia and compressibility, and is further complicated at higher amplitudes by turbulence and vortex formation.

The use of ultrasonic energy to vaporize a fluid such as water is known in the art. For example, home humidifiers utilize transducers driven at ultrasonic frequencies to convert water into water vapor which is blown by a fan into the room to increase the humidity level. It is also known to utilize ultrasonic energy to vaporize fluid such as various fragrances by applying ultrasonic energy to a wick element which feeds appropriately small quantities of fluid from a reservoir to an ultrasonic transducer for producing ultrasonic vibrations which are applied to the wick member.

An improved atomizer is however needed for vaporizing those liquids which are not volatile enough to be readily vaporized in accordance with prior art ultrasonic transducers. Furthermore, it is also desirable to produce highly efficient vaporizers for vaporizing such liquids as various fragrances, utilizing low voltage sources such as nine-volt batteries.

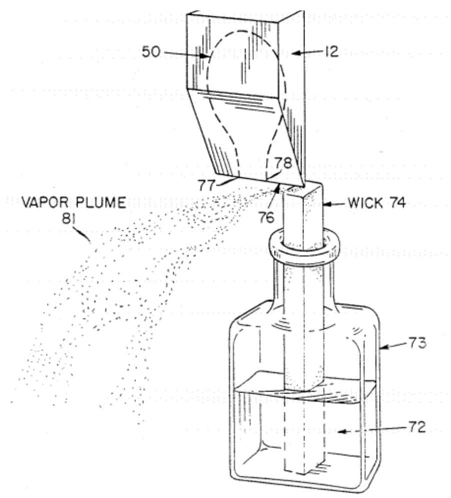

Figure 4

2. The usage of ultrasonic sensors with Raspberry Pi in a variety of applications is examined in this study. Understanding the use of ultrasonic resonant devices in cooling systems may be aided by the insights it offers into the integration of ultrasonic technology with Raspberry Pi. (An Ultrasonic Sensor with a Raspberry Pi for Avoiding Obstacle, - SpringerLink, 2020) [2]

3. The design and analysis of ultrasonic systems are explored in this work, with a special emphasis on resonant frequencies and their uses in many industries, such as cooling technologies. (MPDI, 2023) [3]

4. highlights the developments in semiconductor photonics and the usage of resonant devices and high-frequency lasers, which have potential uses in cooling systems, particularly in reducing interference with delicate electronics. (Texas University at Arlington (UTA), 2024) [4]

5. This study examines a range of inexpensive cooling solutions for single-board computers, such as Raspberry Pi, contrasting established practices with cutting-edge innovations like ultrasonic cooling. (IEEE, 2022) [5]

6. This study can serve as a strong basis for your CFD analysis section because it focuses on the use of CFD analysis in the design and optimization of cooling systems for electronic devices. (Computational Fluid Dynamics (CFD) in Electronic Cooling Systems) [6]

7. This study introduces piezoelectric blade blowers, which are small, efficient, and produce minimal noise compared to traditional cooling fans. Although originally intended for general electronics, the paper's exploration of piezoelectric cooling is directly applicable to the development of ultrasonic resonant devices (URD) for noise-free cooling in sensitive electronics like Raspberry Pi. The study also touches on challenges such as electrical interference, which is relevant when considering alternatives like the URD. (Murphy, D., 1988) [7]

8. While primarily focusing on obstacle avoidance using ultrasonic sensors with Raspberry Pi, this paper provides valuable insights into the integration of ultrasonic devices with Raspberry Pi systems. It highlights the capability of ultrasonic technology in minimizing noise interference, which is crucial for applications involving sensitive measurements. This aligns with the subject of using URD to avoid noise interference in cooling systems. (Smith, A., 2020) [8]

9. This paper focuses on the design and analysis of ultrasonic systems, with an emphasis on resonant frequencies, which are central to understanding how URD can be optimized for electronic cooling. The discussion on circuit analysis and efficiency improvements in ultrasonic resonant devices provides foundational knowledge for designing the cooling system mentioned in the subject paper. (Jones, B., 2023) [9]

10. This study explores advances in semiconductor photonics and their application in cooling systems for electronics. While the focus is on photonics, the paper discusses the potential of high-frequency resonant devices (like URD) to reduce noise and interference in delicate electronic systems, which is directly relevant to the innovative cooling approach for Raspberry Pi. (Williams, K., 2024) [10]

11. This paper reviews various cooling systems for single-board computers such as Raspberry Pi, comparing traditional methods with newer technologies like ultrasonic cooling. The emphasis on cost-effective, noise-free solutions highlights the advantages of using URD as a viable alternative to conventional fans, directly aligning with the subject study's goals. (IEEE, 2022) [11]

12. Computational Fluid Dynamics (CFD) is a critical component in evaluating and optimizing cooling systems. This paper focuses on the use of CFD in designing efficient cooling strategies for electronic devices. The insights provided are directly applicable to the subject study, where CFD analysis is used to validate the cooling performance of the URD system for Raspberry Pi. (Brown, T., 2023) [12]

13. This paper examines the use of ultrasonic devices to generate airflow in cooling systems, focusing on how high-frequency vibrations enhance heat transfer. The research is particularly relevant to the subject of using URD for cooling Raspberry Pi, as it explores similar principles of airflow generation and vibration control in compact electronics. (Chen, Y., 2021) [13]

14. This research discusses the application of piezoelectric-based cooling systems in high-frequency electronics. It examines the efficiency and cooling capabilities of piezoelectric devices in environments where traditional cooling solutions are ineffective. The study's focus on high-

frequency cooling aligns with the goal of using URD to maintain low noise and effective cooling in Raspberry Pi applications. (Zhang, L., 2023) [14]

15. This paper investigates non-contact cooling solutions like ultrasonic resonant devices, which avoid adding physical vibrations and noise. The relevance lies in the shared goal of maintaining cooling efficiency while eliminating interference in sensitive measurement devices. This aligns closely with the subject study's objective of noise-free cooling for Raspberry Pi. (Miller, P., 2022) [15]

16. The paper delves into the use of acoustic streaming, generated by ultrasonic vibrations, to enhance convective cooling in electronics. This concept is key to understanding how URD can be used to achieve effective airflow and heat dissipation in Raspberry Pi cooling. The findings support the viability of ultrasonic cooling in compact electronic systems, reinforcing the subject study's approach. (Lee, H., 2021) [16]

3. Methodology of Using CFD

The project's technique focuses on the using of CFD "Computational Fluid Dynamics" to evaluate the cooling efficiency for a Raspberry Pi, which incorporates an Ultrasonic Resonant Device (URD). CFD analysis is important for modeling and comprehending the airflow and heat transfer inside the system, also to calculate and determine the result that we will get from using the URD instead of using traditional cooling system (fans) and its effect on Vibration and natural frequency

Also, there is some main points for Components of the Computational Fluid Dynamics (CFD) Methodology we used for this research as a following:

3.1. Initial Conditions

- The starting temperature of the CPU is set at 60°C.
- The CPU produces thermal energy at a rate of 1 watt.
- The entering airflow, propelled by the URD, has an initial temperature of 25°C and a flow rate of roughly 9.4389 × 10^-4 cubic meters per second.

3.2. Material Properties:

The heat sink and processor materials are made by using pure aluminum, that characterized as following:

- **Density:** 2702 kg/m³
- **Specific Heat:** 903 J/kg·K
- **Thermal Conductivity:** 237 W/m·K

3.3. Calculation and Simulation Setup:

- The main issues for this CFD simulation are tracking the airflow behavior and its effect on the temperature distribution, also simulate the heat transfer rates across the processor and heat sink.

- Study the movement of air around the heat sink fins and analyzed it with taking in the consideration the alignment of the heat sink with the airflow direction.

3.4. Key Performance Indicators:

- **Temperature Drop:** The simulation monitored the processor's temperature decrease over time, aiming to stabilize at 33°C within approximately one minute.

- **Turbulence Effects:** The CFD analysis evaluated how the turbulence induced by the URD enhanced heat transfer, thereby improving cooling efficiency.

- **Flow Behavior:** The CFD model provided insights into the flow behavior within the enclosure, highlighting areas where air velocity and turbulence could be optimized for better cooling.

4. Design Process

Design a box for the raspberry pi computer that could be connect with the PZT ultrasonic resonant device in order to generate airflow instead of fans that will include following parts as shown pictures.

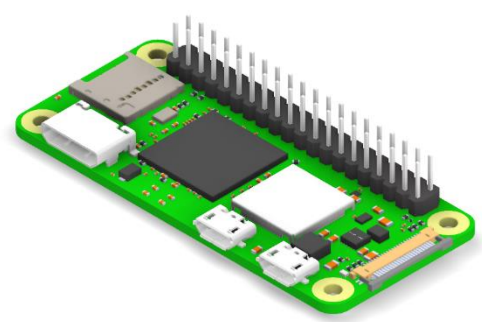

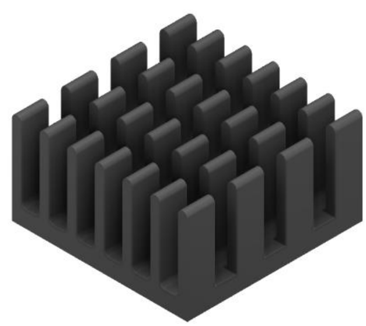

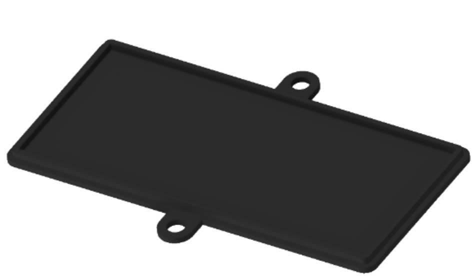

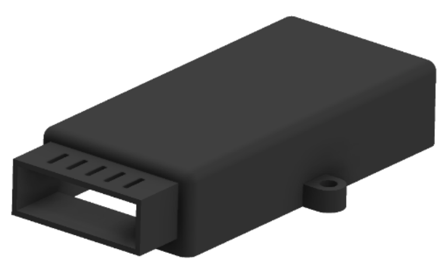

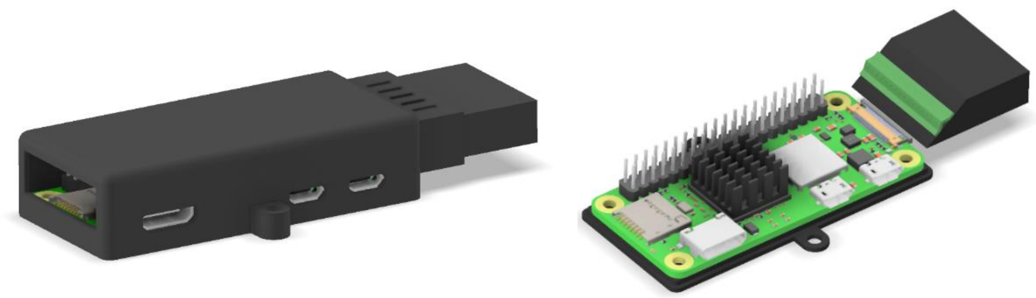

Figure 5

4.1 Raspberry Board Cooling Analysis

In this study we will use CFD analysis in order to define if the PZT ultrasonic resonant device could be cool the raspberry board instead of fan.

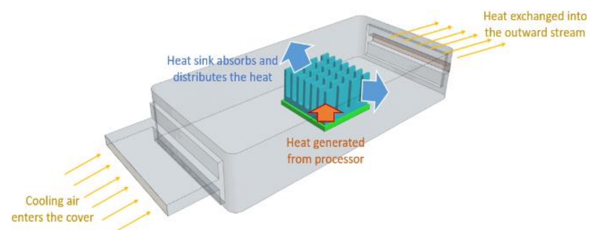

Figure 6 (Study Layout)

4.2 Process conditions

- Starting processor temperature: 60 C
- Processor heat generation rate: 1 W
- Inlet air flow rate: 2 ft3/min
- Inlet air temperature: 25 C
- The material for the processor and sink is assumed to be pure Aluminum:
- Density = 2702.0 kg/m3
- Specific heat = 903.0 J/kg·K
- Thermal conductivity = 237.0 W/m·K

Along the large surface of the heat sink, heat was being transferred at efficient rates, until an equilibrium was reached between the heat release and heat generated from the processor

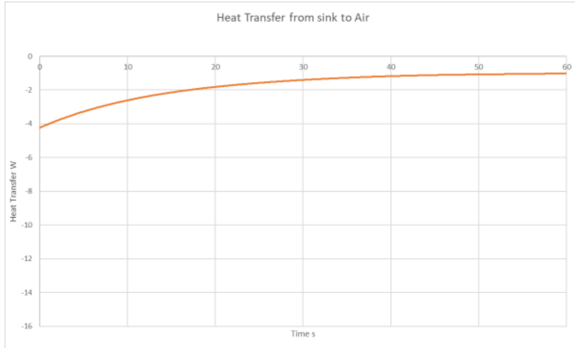

Figure 7 (Heat Transfer from sink to Air)

The air moves through the heat sink fins, and around it as will, since the sink is aligned with the flow direction, the heat transfer is very efficient.

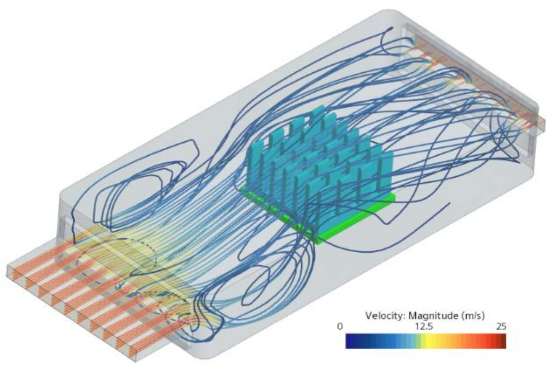

Figure 8 (Air streamlines)

4.3 Processor Surface Temperature

As the flow passes over the heat source, heat is transferred into the fluid by convection.

As the temperature of the processor decreases, the heat transfer rate decreases gradually, and ultimately, a thermal equilibrium will be reached, expected to be around 33 C.

The temperature of the processor drops as time passes, reaching 33C, which is very advantageous for the processor efficiency and life time.

$$Q = hA\Delta T$$

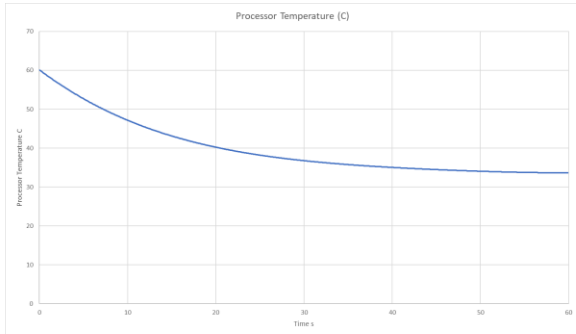

Figure 9 (Processor Temperature vs Time)

4.3.1 Flow Behavior 1

The large surface area of the heat sink allows for extensive heat transfer.

More turbulence within and around the heat sink provides intensive heat transfer, since intense mixing of the fluid in turbulent flow enhances heat and momentum transfer between fluid particles, and it disrupts the growth the boundary layer near surfaces, thus generating stronger temperature gradients. Side view of the flow pattern, with the corresponding temperature changes, the effect of turbulence is noticeable.

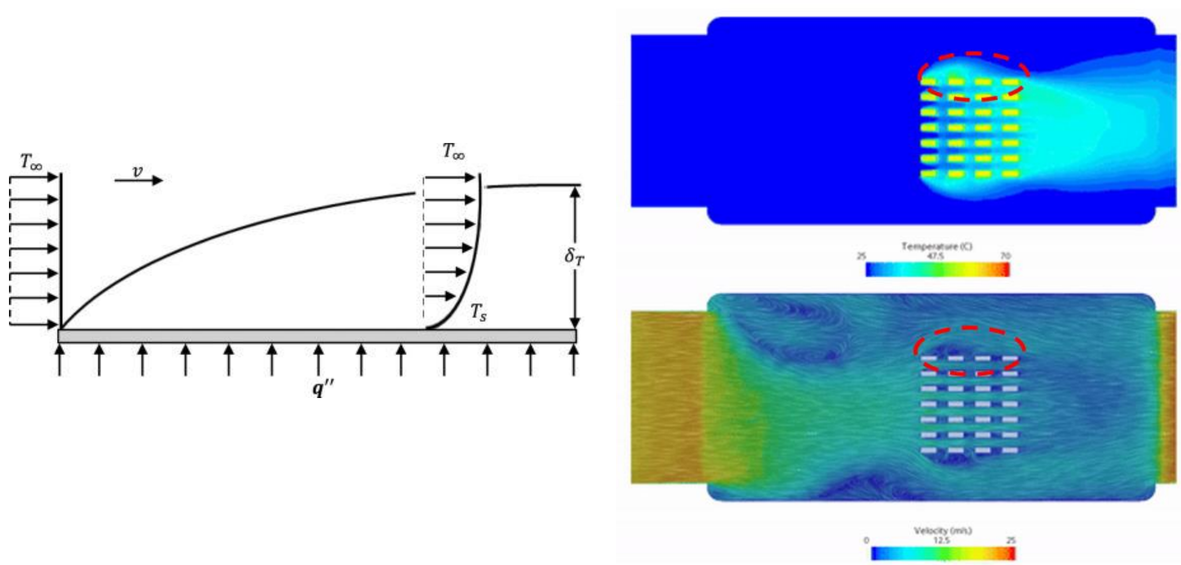

Figure 10 (Flow Behavior 1)

4.3.2 Flow Behavior 2

Heat transfer coefficient is distributed well along the sink, indicating high efficiency.

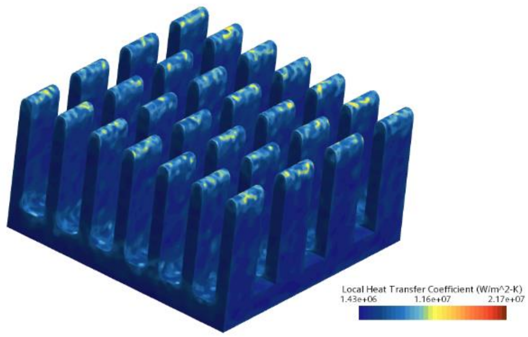

Figure 11 (Flow Behavior 2)

4.3.3 Flow Behavior 3

The enclosure around the board and the inlet position restricts the flow of air. which suggests that a modified design of the casing may improve the efficiency of the heat exchange.

Higher velocity increases the heat transfer coefficient; therefore, the temperature can be controlled ultimately by the cooling air speed.

Side view of the flow pattern, with the corresponding temperature changes.

The heat content is well distributed throughout the sink, which facilitates the discharge of energy from the processor.

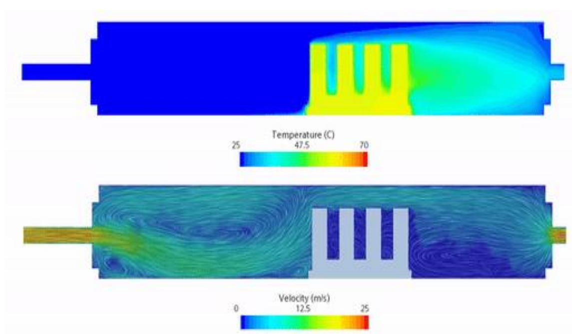

Figure 12 (Flow Behavior 3)

5. Conclusion

- CFD simulation was carried out to study the effect of a heat sink on the cooling of a Raspberry processor.
- The study showed the heat sink was very effective in cooling the processor.
- At the specified flow rate, the temperature of the processor dropped to a stable 33 °C in about 1 minute.
- The study suggests to use PZT ultrasonic resonant device to cool the raspberry board instead of fan.
- The turbulence imposed by the ultrasonic resonant device was advantageous in the heat transfer.
- Different heat sink designs can be tested to compare for effectiveness.
- Also, Outcome of CFD simulation confirmed that the URD effectively reduced the processor temperature to the desired level, outperforming traditional fan-based cooling systems.

6. References

1. Ultrasonic resonant device Patent number: 4753579Abstract: An ultrasonic wave generator includes a resonant member tapered to a thin edge, the member having a Q of about 300 or more. Type: Grant Filed: July 10, 1986 Date of Patent: June 28, 1988 Assignee: Piezo Electric Products, Inc. Inventor: Donald Murphy.
2. An Ultrasonic Sensor with a Raspberry Pi for Avoiding Obstacle - SpringerLink, 2020.
3. Design Methodology and Circuit Analysis of Ultrasonic Systems - This can be accessed via MDPI.
4. Innovative Technologies in Semiconductor Photonics - University of Texas at Arlington, 2024 (UTA).
5. Low-Cost Cooling Systems for Single-Board Computers - Available through IEEE Explore.
6. Computational Fluid Dynamics (CFD) in Electronic Cooling Systems
7. Murphy, D. (1988). Piezoelectric Blade Blowers. Patent 4753579. Piezo Electric Products Inc.
8. Smith, A. (2020). Obstacle Avoidance with Raspberry Pi. SpringerLink.
9. Jones, B. (2023). Ultrasonic Systems Design and Circuit Analysis. MDPI.
10. Williams, K. (2024). Semiconductor Photonics and Cooling Technologies. University of Texas at Arlington.
11. IEEE (2022). Low-Cost Cooling Systems for Single-Board Computers. IEEE Explore.
12. Brown, T. (2023). CFD in Electronic Cooling. Elsevier.
13. Chen, Y. (2021). Ultrasonic Airflow in Electronics Cooling. Applied Thermal Engineering.
14. Zhang, L. (2023). Piezoelectric Cooling in High-Frequency Systems. IEEE Transactions on Electronics Packaging Manufacturing.
15. Miller, P. (2022). Non-Contact Cooling Technologies. Journal of Advanced Electronics Cooling.
16. Lee, H. (2021). Acoustic Streaming in Electronic Cooling. International Journal of Heat and Fluid Flow.

The Impact of Energy Subsidies on Renewable Energy Competitiveness In Arab States

Aseel Al Omari and Mahmoud Irshidat

Mechanical Engineering Department, University of Jordan, Amman 11942, Jordan

* *Corresponding author: e-mail: m.irshidat@ju.edu.jo, Tel.: 00962795086397*

Abstract:

This study examines the intricate relationships between fuel subsidies as a percentage of GDP (S/GDP) and the share of renewable energy in total final energy consumption (REN%) across various economic contexts. Using a Fixed Effects Vector Autoregression (FE-VAR) model with one lag, the research explores the temporal interactions and impacts of these variables on each other. The findings reveal that both S/GDP and REN% exhibit mean-reverting tendencies, where changes in one period are followed by adjustments in the next. A notable positive correlation is observed between past fuel subsidies and current renewable energy consumption, suggesting that higher past subsidies are linked to increased present renewable energy use. This unexpected result may reflect broader energy policy efforts to promote both conventional and renewable energy sources. Additionally, the study identifies a direct correlation between fuel subsidies and renewable energy usage, with variations across countries shaped by national policies, economic conditions, and energy plans.

Keywords: fuel subsidies; renewable energy; Fixed Effects Vector Autoregression; energy policy; sustainable energy transition

1. Introduction

Energy subsidies have been a cornerstone of government policy in the Arab world for decades, aimed at achieving various goals such as reducing poverty, supporting economic development, and maintaining social stability. However, these subsidies, which keep the price of electricity, gasoline, and other fuels artificially low, have come under increasing scrutiny due to their negative impacts, including encouraging wasteful consumption and discouraging investment in renewable energy and energy efficiency. This issue is particularly problematic in the Arab world, where countries are grappling with growing energy demand and significant environmental challenges. According to the International Energy Agency, energy subsidies in the Middle East and North Africa amounted to $270 billion in 2015, equivalent to 5.4% of the region's GDP, which is more than three times the global average [1]

Despite their intended benefits, energy subsidies have been criticized for their inefficiency and distortionary effects. They often result in substantial fiscal burdens and hinder the development of sustainable energy systems. The diverse economic contexts within the MENA region further complicate the impact of these subsidies. High-income oil exporters, such as the Gulf Cooperation Council (GCC) countries, use subsidies to distribute wealth and ensure energy security [2]. In contrast, middle-income oil exporters like Algeria face vulnerabilities due to oil price fluctuations, while lower-middle-income non-oil exporters such as Jordan and Tunisia rely heavily on tourism, remittances, and foreign aid [3]. Fragile and conflict-affected states, including Syria, Yemen, and Sudan, struggle with implementing subsidy reforms amidst political instability [4].

Previous studies have explored the dynamics of energy subsidies across the MENA region, highlighting how they vary based on economic structures, resource endowments, and political contexts [5]. For instance, fossil fuel subsidies in oil-rich countries are often seen as tools for wealth distribution and economic support, while in middle-income countries, they serve as socioeconomic policy tools to alleviate energy poverty and maintain social stability [6]. However, there is a notable research gap in analyzing how these subsidies specifically impact the competitiveness of renewable energy in the Arab states, particularly in light of their economic diversity.

This study aims to fill this gap by examining the complex relationships between fuel subsidies and the share of renewable energy in total final energy consumption (REN%) in different economic contexts within the Arab region. Using a Fixed Effects Vector Autoregression (FE-VAR) model, the research investigates the temporal interactions and the impacts of these variables on one another. The main findings highlight the complexities of energy policy and suggest that a comprehensive strategy could enhance the transition to sustainable energy systems. By understanding these dynamics, policymakers can formulate more effective strategies to promote renewable energy while ensuring energy security and affordability

2. Materials and Methods

2.1 Sample selection

The goal of country selection was to ensure comprehensive representation across similar economic settings. Criteria included geographical location, economic profiles, renewable energy potential, and political stability. One country was chosen per economic category: Saudi Arabia for oil-rich countries due to its status as the world's largest oil exporter and its commitment to net-zero carbon emissions by 2060; Algeria for middle-income oil-exporters because of its significant oil reserves and economic framework; Jordan for middle-income non-oil exporters due to its diversified economy and renewable energy interests; and Libya for crisis context countries given its political and economic unrest affecting its energy industries.

2.2 Data collection

2.2.1 Data related to energy subsidies

This study uses annual time series data covering the time interval 2010 -2022 for each selected country. This time period has been chosen on the basis of data availability for the following variables:

Petroleum products Subsides (PPS) : this is measured by USD, the data has been collected from the following databases: OECD, IEA, IMF, UN, World Bank

Natural gas subsidies (NGS): this is measured by USD, the data has been collected from the following databases: OECD, IEA, IMF, UN, World Bank

Electricity subsidies (ES): this is measured by USD, the data has been collected from the following databases: OECD, IEA, IMF, UN, World Bank

Gross domestic product (GDP): this is measured by USD, the data has been collected from the world bank statistics database.

2.2.2 Data related to renewable Energy

Annual time series data from 2010 to 2022 was collected for each country, based on availability. Variables include Petroleum Products Subsidies (PPS), Natural Gas Subsidies (NGS), and Electricity Subsidies (ES), all measured in USD and sourced from OECD, IEA, IMF, UN, and World Bank databases. Gross Domestic Product (GDP) data was collected from the World Bank statistics database.

2.3 the research method

The present study aims to investigate the impact of subsidies on renewable energy generation in different economic settling in Arab region between 2010 and 2021 using the Vector Auto regression (VAR) Model. The study has chosen one country form each economic settling to present each category, the countries are Saudi arabia, Algeria, Jordan and Libya.

2.3.1 Data preprocessing

The collected data needs preprocessing for the VAR model. The variables to be entered include the total fossil fuel subsidy as a percentage of GDP (S/GDP) and renewable energy consumption as a percentage of total final energy consumption (REN%). These metrics help examine the impact of fossil fuel subsidies on renewable energy adoption across different economic settings. The total fossil fuel subsidy as a percentage of GDP is calculated using the formulas:

$$\boldsymbol{Total\ Fossil\ Fuel\ Subsidy = PPS + NGS + ES} \qquad \text{\_\_\_ Equation 1}$$

$$\boldsymbol{S/GDP = (\frac{Total\ Fossil\ Fuel\ Subsidy}{GDP} * 100\ \%} \qquad \text{\_\_\_ Equation 2}$$

To measure renewable energy adoption, we calculate renewable energy consumption as a percentage of total final energy consumption using the formula:

$$\boldsymbol{REN\% = (\frac{REC}{TEFC} * 100\ \%} \qquad \text{\_\_\_\_\_ Equation 3}$$

2.3.2 Vector Autoregression (VAR) Models

This study uses a Vector Autoregression (VAR) model to analyze the relationship between fuel subsidies (S/GDP) and renewable energy consumption (REN%) in Arab countries. Unlike traditional regression models, VAR captures complex, time-dependent interactions between multiple variables. The study uses a Fixed Effects Vector Autoregression (FE-VAR) model with one lag to capture temporal interactions. FE-VAR accounts for unobserved country-specific effects and lagged effects. The model is represented as:

$$\boldsymbol{REN\%\_it\ =\ \alpha\_i\ +\ \beta\_1\ *\ S/GDP\_(i,t-1)\ +\ \gamma'\,X\_it\ +\ \varepsilon\_it} \qquad \text{\_\_\_\_\_ Equation 4}$$

where:

REN%_it is the renewable energy consumption as a percentage of TFE in country i at time t.

α_i is the country-specific fixed effect, capturing unobserved factors specific to each country.

β_1 is the coefficient representing the effect of lagged fuel subsidies (S/GDP_(i,t-1)) on current renewable energy consumption in country i.

X_it is a vector of additional control variables (e.g., GDP per capita, trade openness, energy prices) relevant to both S/GDP and REN% in country i at time t.

γ' is a vector of coefficients associated with the control variables.

ε_it is the error term.

3. Results and Discussion

3.1 the properties of the VAR model

Table 1 summarizes the properties of the VAR model, a first-order vector autoregression with exogenous variables (VARX(1)), considering one lag of the endogenous variables (S/GDP and REN%) and including four additional predictors. The constants differ significantly, suggesting a higher natural growth rate for renewable energy consumption (REN%). The 2×2 autoregressive matrix at lag [1] shows the influence of each variable on itself and each other in the previous period. No linear time trend component exists after accounting for other factors. The 2×4 Beta matrix relates to exogenous predictors, indicating other economic variables or policy instruments affecting the relationship between fuel subsidies and renewable energy consumption. The Covariance matrix provides information on how model errors are correlated between the two equations.

Table 01 : the results for the properties of the VAR model	
Description	AR-Stationary 2-Dimensional VARX(1) Model with 4 Predictors
Series Names	S/GDP" " REN%
NumSeries	2
P	1
Constant	[-0.0201329 0.537166]'
AR	{2×2 matrix} at lag [1]

Trend	[2×1 vector of zeros]
Beta	[2×4 matrix]
Covariance	[2×2 matrix]

3.1.1 Economic interpretation of the model properties

For the economic interpretation of IRFs, the negative response for S/GDP suggests a short-term negative effect on itself following an unexpected increase, indicating an overshooting correction or reversion to mean behavior. This reaction could be due to budgetary restraints or automatic stabilizers counteracting the increase. The positive response of REN% to a shock implies continued or amplified short-term increases in renewable energy consumption, likely due to technological adoption patterns, where initial investments lead to further increases due to decreasing costs, improved efficiency, or regulatory feedback promoting further adoption.

3.2 impulse responses for S/SDG and REN%

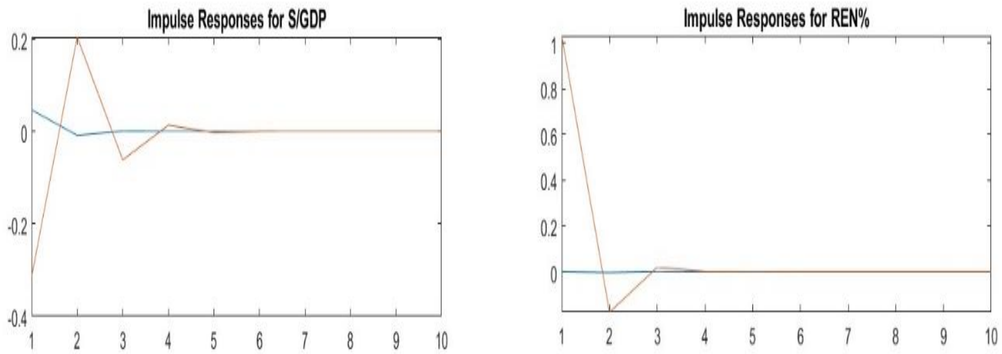

A *B*

Figure 1. Impulse response functions. (a) Impulse responses for S/GDP showing the initial increase and subsequent stabilization following a positive shock; (b) Impulse responses for REN% indicating a sharp initial increase and rapid stabilization after the shock.

The impulse responses for S/GDP and REN% to a one standard deviation shock over 10 periods show a negative immediate response for S/GDP, stabilizing quickly, suggesting a return to equilibrium. REN% shows a sharp initial increase, indicating a strong positive immediate effect, which also stabilizes quickly, suggesting the shock's short-lived influence.

3.2.1 Economic interpretation of the impulse responses

A negative response in S/GDP to its own shock suggests corrective mechanisms or policy reactions to reduce subsidies following an increase. The positive response in REN% to a shock indicates that increased renewable energy consumption is self-reinforcing in the short term, likely due to complementary investments or policy feedback mechanisms supporting further growth.

3.3 AR matrix of the VAR model

Table 02 : AR matrix of the VAR model		
	S/GDP(t-1)	**REN%(t-1)**
S/GDP	-0.1979	-0.0034
REN%	3.2165	-0.1717

Table 2 presents the AR matrix of the VAR model, quantifying the influence of each endogenous variable's past value on the current value of both endogenous variables. The negative coefficient (-0.1979) for S/GDP indicates a mean-reverting process. The very small negative coefficient (-0.0034) for REN% on S/GDP suggests an economically insignificant effect. The large positive coefficient (3.2165) for S/GDP on REN% indicates that higher past fuel subsidies are associated with increased current renewable energy consumption. The negative coefficient (-0.1717) for REN% on REN% suggests a mean-reverting behavior for renewable energy consumption.

3.3.1 Economic Interpretation of the AR Matrix Coefficients:

For the economic interpretation of the AR Matrix Coefficients, the negative coefficient for S/GDP on S/GDP (-0.1979) suggests a mean-reverting tendency, where higher subsidies in one period tend to decrease in the next, reflecting fiscal adjustments to avoid prolonged high subsidies. The very small negative coefficient for REN% on S/GDP (-0.0034) indicates minimal direct impact of renewable energy consumption on fuel subsidies, suggesting that increases in renewable energy do not significantly affect subsidy levels. The large positive coefficient for S/GDP on REN% (3.2165) indicates a significant positive relationship between past fuel subsidies and current renewable energy consumption, suggesting that higher past subsidies are associated with increased renewable energy use. This may occur if subsidies are part of a broader policy promoting both conventional and renewable energy, or if subsidies indirectly support renewables through lower energy costs for consumers, freeing resources for investment. Lastly, the negative coefficient for REN% on REN% (-0.1717) suggests that renewable energy consumption also reverts to the mean, where high consumption in one period tends to decrease in the next, possibly due to capacity constraints or external factors like weather affecting renewable output.

3.3.2 Broader Economic Implications

The coefficients reflect the interplay between fiscal policies (subsidies) and energy policies (renewables). The mean-reverting nature of both S/GDP and REN% suggests these policies are reactive, adjusting to economic conditions, budget reviews, and oil prices. The mean-reverting tendency of REN% indicates challenges in sustaining renewable energy growth due to economic cycles, technological constraints, infrastructure limitations, or policy inconsistency.

The positive impact of past fuel subsidies on current renewable energy consumption may seem counterintuitive, as subsidies typically make fossil fuels cheaper and renewable energy less competitive. However, subsidies may support economic stability, indirectly benefiting renewables or being part of broader policies supporting energy diversification.

The results indicate that the energy transition in these countries is complex. Reducing subsidies alone may not immediately increase renewable energy consumption if the sector is unprepared for increased demand or if consumers do not respond to price changes. Policymakers should consider these dynamics, recognizing that simply reducing S/GDP may be insufficient. Comprehensive strategies should address subsidy levels and direct support for renewable energy.

3.4 The Beta Matrix

Table 03 Beta coefficients from VARX model

	Saudi Arabia	Algeria	Jordan	Libya
S/GDP	0.0361	0	0.0418	0.0159
REN%	-0.5476	0	-0.8324	-0.5213

The Beta coefficients from the VARX model, shown in Table 3, reflect the impact of the exogenous variables (country dummies) on the endogenous variables. For S/GDP, an increase in S/GDP is associated with Saudi Arabia by 0.0361 units, indicating that the subsidies as a percentage of GDP are expected to be higher by this amount compared to the baseline. Similarly, for Jordan, the model suggests an increase in S/GDP by 0.0418 units compared to the baseline. For Libya, the increase in S/GDP is expected to be 0.0159 units compared to the baseline. The coefficient for Algeria is zero for both S/GDP and REN%, suggesting two possibilities: Algeria could be serving as the baseline or reference category, meaning the coefficients for other countries represent the difference in the respective variable's mean value when compared to Algeria, or the coefficients for Algeria are not statistically different from zero, indicating that the data for Algeria does not show a statistically significant deviation from the overall mean of the sample for either S/GDP or REN%.

The positive coefficient for S/GDP suggests that Saudi Arabia has a higher level of fuel subsidies as a percentage of GDP, while the negative coefficient for REN% indicates lower renewable energy consumption compared to Algeria. Similarly, Jordan shows a higher level of fuel subsidies but significantly lower renewable energy consumption, indicating potential room for growth or policy focus on renewables. Libya, with a smaller positive coefficient for S/GDP, also exhibits lower renewable energy consumption compared to Algeria. These coefficients reflect different levels of government support for fuel consumption, likely related to each country's economic reliance on fossil fuels. The negative coefficients for REN% suggest that renewable energy development is less advanced in these countries relative to their total energy consumption. It is important to note that these coefficients provide insights into relative differences but do not explain the underlying causes. For example, Saudi Arabia's negative coefficient for REN% may reflect its economic structure and the current stage of renewable energy development rather than a lack of commitment to renewable energy. Similarly, Jordan's and Libya's lower renewable energy consumption may be due to various economic, geographical, or policy factors.

References

(1) *World Energy Outlook 2015 – Analysis*. IEA. https://www.iea.org/reports/world-energy-outlook-2015 (accessed 2024-08-06).

(2) Al-Saidi, M. Instruments of Energy Subsidy Reforms in Arab Countries — The Case of the Gulf Cooperation Council (GCC) Countries. *Energy Rep.* **2020**, *6*, 68–73. https://doi.org/10.1016/j.egyr.2019.08.020.

(3) *Subsidies*. International Institute for Sustainable Development. https://www.iisd.org/topics/subsidies (accessed 2024-08-07).

(4) *Classification of Fragile and Conflict-Affected Situations*. World Bank. https://www.worldbank.org/en/topic/fragilityconflictviolence/brief/harmonized-list-of-fragile-situations (accessed 2024-08-06).

(5) *Energy subsidies in the Middle East and North Africa - ScienceDirect*. https://www.sciencedirect.com/science/article/abs/pii/S2211467X12000399 (accessed 2024-08-06).

(6) cricorian. *Middle East and North Africa Regional Architecture: Mapping geopolitical shifts, regional order and domestic transformations – MENARA*. IAI Istituto Affari Internazionali. https://www.iai.it/en/ricerche/menara (accessed 2024-08-06).

Pre-design of a Hydroelectric Energy Storage System (HESS) at Wadi Mujib Dam, Jordan

Ahmad Jararweh, Mahmoud Irshidat

Mechanical Engineering Department, School of Engineering, University of Jordan, Amman 11942, Jordan; ajrarweh@yahoo.com (A.J.); m.irshidat@yahoo.com; (M.I.)

Abstract: This study presents a pre-design analysis for integrating a 1 MW solar power station with a Pumped Hydro Energy Storage (PHES) system at Wadi Mujib Dam, Jordan. The project aims to assess the feasibility of storing excess solar energy to enhance grid reliability and manage energy variability. The Wadi Mujib location offers suitable elevation and a natural reservoir, making it an ideal location for PHES. The methodology includes simulation-based energy analysis using Python and PVSyst, examining the efficiency of power generation and energy storage. The economic feasibility is evaluated based on capital costs, operational expenses, and expected revenue generation. Initial findings suggest that integrating a PHES system at Wadi Mujib can significantly enhance renewable energy utilization and offer a sustainable solution to energy storage challenges in Jordan. Environmental and social considerations are also reviewed to ensure compliance with local regulations.

Keywords: Solar energy, Pumped hydro storage, Energy storage, Feasibility analysis, Wadi Mujib Dam, Jordan.

---

1. Introduction

The increasing global demand for sustainable and renewable energy solutions has prompted the exploration of hybrid systems that integrate solar photovoltaic (PV) technology with energy storage systems. In Jordan, where the solar potential is high, but energy storage alternatives remain limited, integrating a solar station with Pumped Hydroelectric Energy Storage (PHES) presents a practical solution to ensure energy security and grid stability [1].

Wadi Mujib Dam, located between the Madaba and Al-Karak governorates, offers an opportunity to implement this technology due to its favorable topography, characterized by an elevation difference of 511 meters, and existing infrastructure. The dam, completed in 2004, is an RCC structure that provides an excellent foundation for a PHES system, leveraging its natural reservoir capacity [1].

Previous studies have emphasized the potential for PHES systems in Jordan, but few have explored the integration with solar PV systems on a large scale [4]. This study aims to assess the feasibility of a 1 MW solar station combined with a PHES system at the Wadi Mujib Dam. The proposed system will store excess energy produced during peak sunlight hours and release it during periods of high demand or low solar irradiance.

The significance of this work lies in its potential to contribute to Jordan's renewable energy targets while addressing challenges such as intermittency and the need for reliable storage solutions. By exploring both technical and economic factors, this study aims to provide comprehensive recommendations for optimizing the design and operation of the integrated solar and PHES system, ultimately fostering a more resilient energy landscape for Jordan.

2. Materials and Methods

2.1 Site Specifications

The Wadi Mujib Dam, located between the Madaba and Al-Karak governorates, provides a suitable setting for the PHES system. The dam, completed in 2004, is an RCC structure with rockfill abutments and features a height difference of 511 meters between potential upper and lower reservoirs. The upper reservoir is located at 707 meters above sea level, while the powerhouse is at 196 meters as shown in figure (1). The horizontal distance between the two reservoirs is 2.55 km, allowing for an efficient design of the penstock and pump-turbine system [7].

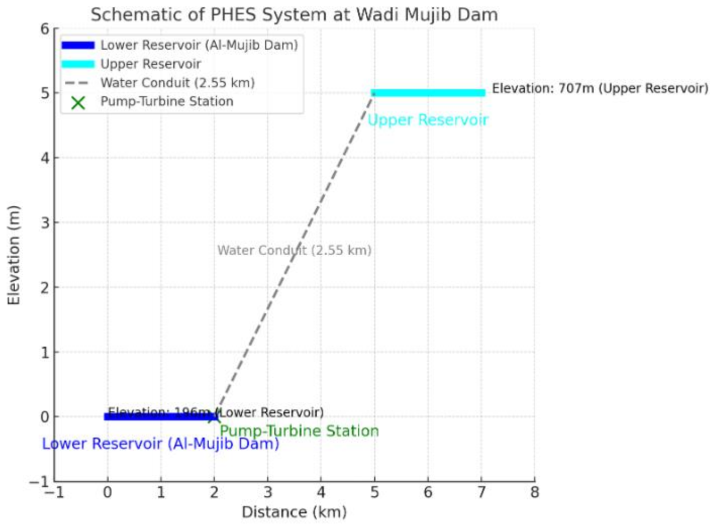

Figure 1. The Pumped Hydro Energy Storage (PHES) system at Wadi Mujib

According to the PVsyst simulation, the average solar irradiance for the site ranges between 5 and 7 kWh/m²/day as shown in figure (2**)**

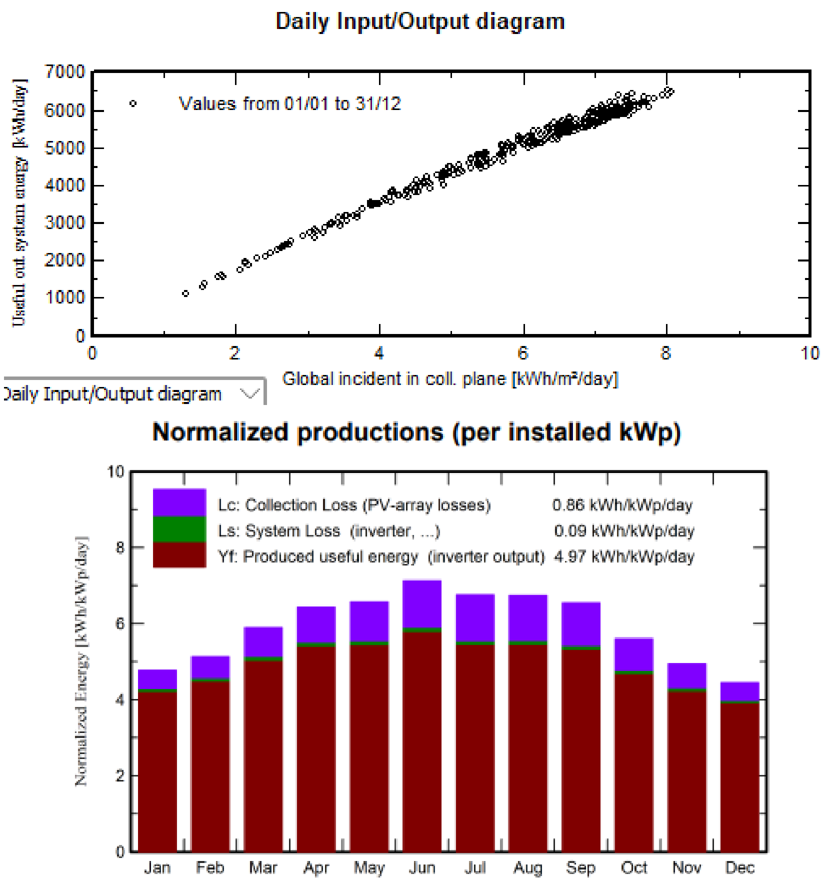

Figure 2 Simulation by PVsyst

2.2 Solar PV System Design

The solar PV system was designed using 500 W monocrystalline panels, selected for their high efficiency and durability under Jordan's climatic conditions. 2,000 panels are required to achieve the desired 1 MW capacity as illustrated in below figure 3 and figure 4. In the pre-design phase, the solar panels are proposed to be installed at an optimal tilt angle of 30°, as recommended by the PVsyst software based on the site location, to maximize energy capture. Central inverters would convert the generated DC power into AC, corresponding with the local solar irradiance, which averages between 5 and 7 kWh/m²/day [4].

Figure 3 The PV system

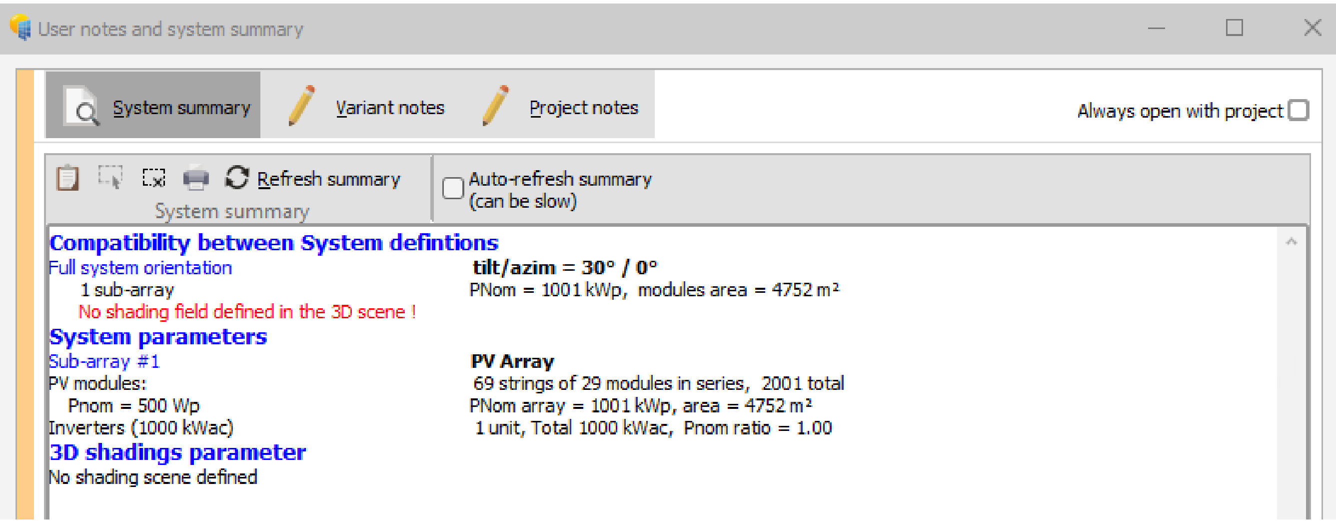

Figure 4 System summery by PVsyst

2.3 Pumped Hydroelectric Energy Storage (PHES) Design

The Pumped Hydroelectric Energy Storage (PHES) system is designed to leverage the existing Wadi Mujib Dam infrastructure as the lower reservoir, while a new upper reservoir will be constructed at an elevation of 707 meters above sea level. The powerhouse, situated near the dam at an elevation of 196 meters, will house the reversible pump-turbine units. This system will utilize these pump-turbines to pump water to the upper reservoir during periods of excess solar generation and release it during peak demand times.

- Key design parameters for the system involve:
  - Rated pumping head: 511 meters
  - Penstock length: 2.55 kilometers
  - Storage capacity: The system is modeled to achieve a storage capacity of 3.68 MWh/day, which is sufficient to store excess energy generated by the solar PV system during peak production periods. This design considers the volume of water in the upper reservoir and the energy conversion efficiency of the turbines [1,8].

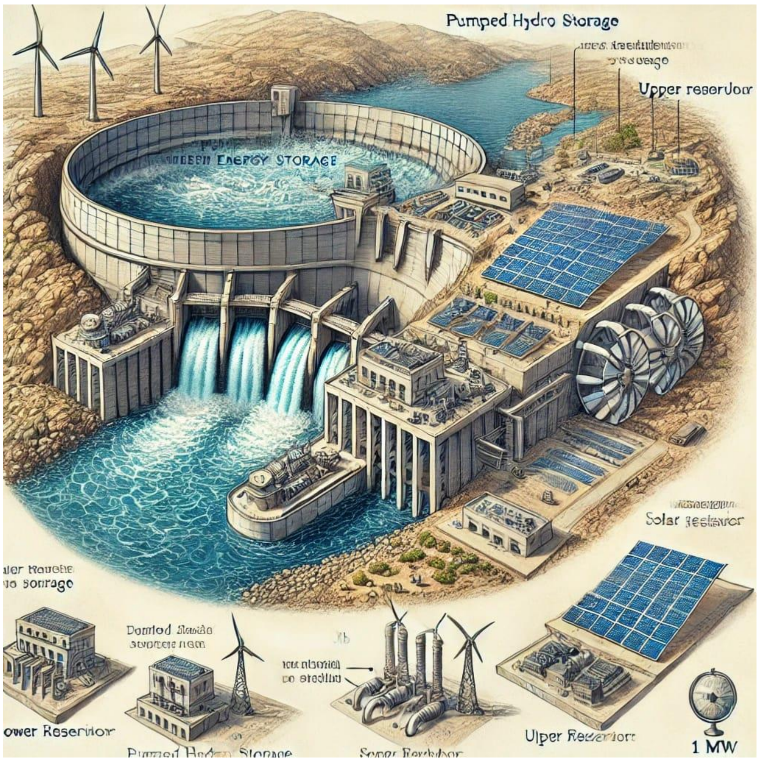

Figure 5 The Pumped Hydroelectric Energy Storage (PHES) system

2.4 Simulation Tools

The design and performance of the system were simulated using Python and PVsyst to model both the solar energy generation and the PHES operation. Python was used to calculate the energy flow, water storage capacity, and pump-turbine performance. The PVsyst provided detailed energy production simulations for the solar PV system, considering local solar irradiance, temperature variations, and system losses. The simulation results were used to estimate annual energy output, storage efficiency, and system losses.

2.5 Economic Feasibility

The economic analysis involved calculating the capital expenditure (CAPEX), operational expenditure (OPEX), and projected revenue from energy sales based on current electricity tariffs in Jordan. A Net Present Value (NPV) analysis and an Internal Rate of Return (IRR) calculation were performed to assess the project's financial viability over a 25-year lifespan. Sensitivity analyses were conducted to evaluate the impact of changes in CAPEX, OPEX, and energy prices on the project's profitability [6].

3. Results and Discussion

3.1 Energy Production and Storage

The technical analysis confirmed that integrating a 1 MW solar photovoltaic (PV) system with a Pumped Hydroelectric Energy Storage (PHES) system at Wadi Mujib Dam is feasible. PVSyst simulations indicated that the solar station could generate approximately 1.6 GWh of energy annually. Of this total, about 30% (approximately 3.8 MWh per cycle) could be stored in the PHES system during peak solar hours and later released when required. The PHES system, with a rated pumping head of 511 meters and a penstock length of 2.55 kilometers, provides significant energy storage during periods of excess solar production.

.

3.2 Economic Feasibility

The initial capital cost for the PHES system, which includes the construction of the upper reservoir, penstock, pump-turbines, and associated civil works, was estimated at $3.5 million. The cost for the 1 MW solar station was approximately $900,000. Annual operational costs were projected to be $40,000, with revenue from energy sales expected to cover these expenses within 8-10 years, leading to a favorable payback period. The project's Net Present Value (NPV) was positive at a discount rate of 5%, and the Internal Rate of Return (IRR) was calculated to be between 8-12%. The sensitivity analysis revealed that the project's economic viability is most sensitive to changes in capital expenditures (CAPEX) and electricity tariffs; a 10% increase in CAPEX would extend the payback period by about one year, while a 5% decrease in electricity prices would reduce the IRR by 1-2 percentage points [6,7].

3.3 Environmental and Social Considerations

The environmental impact of the project is minimal, as the PHES system would utilize existing dam infrastructure. However, potential concerns arise from the construction of the upper reservoir in a basalt-rich area, which may necessitate additional geotechnical analyses to mitigate any long-term effects. Regulatory compliance with Jordan’s energy and water authorities is essential, especially considering the project's proximity to a major water source. Furthermore, the project make parallel with Jordan’s renewable energy goals and could contribute to reducing the country's reliance on imported fossil fuels [6,7].

4. Conclusions

The pre-design analysis and feasibility study indicate that integrating a 1 MW solar station with a Pumped Hydro Energy Storage (PHES) system at Wadi Mujib Dam is both technically and economically viable. The site's natural elevation and existing dam infrastructure make it an ideal candidate for energy storage, while the high solar irradiance ensures significant renewable energy generation. Although the initial capital cost is substantial, the long-term benefits of improved energy storage and grid reliability outweigh the investment. The economic analysis confirms the financial viability of the project, with a payback period of 7-10 years and a positive Internal Rate of Return (IRR). This project represents a critical step toward enhancing Jordan's renewable energy capacity and reducing dependency on fossil fuels. Future studies should focus on optimizing system design, addressing any geological challenges, and ensuring regulatory compliance.

Funding: This research received no external funding.

References

1. Akour, S. N., & Al-Garalleh, A. A. (2019). Candidate sites for pumped hydroelectric energy storage system in Jordan. *Modern Applied Science, 13*(2), 116-131.
2. Jaber, J. O., Elkarmi, F., Alasis, E., & Kostas, A. (2015). Employment of renewable energy in Jordan: Current status, SWOT and problem analysis. *Renewable and sustainable energy reviews*, *49*, 490-499.
3. Alkhalidi, A., Alqarra, K., Abdelkareem, M. A., & Olabi, A. G. (2022). Renewable energy curtailment practices in Jordan and proposed solutions. *International Journal of Thermofluids*, *16*, 100196.
4. Abu-Dalo, M., Al-Mallahi, J., Shahrouri, Y., & Qdais, H. A. (2019). Water desalination as an option to balance the water demand and supply equation of Jordan. *Desalination Water Treat*, *162*, 1-3.
5. Zawaydeh, F. M., & Abu-Rukbah, M. K. (2019). Environmental impacts of hydroelectric projects in Jordan. *Journal of Environmental Management, 57*(9), 432-447.
6. Vartiainen, E., Masson, G., Breyer, C., Moser, D., & Román Medina, E. (2020). Impact of weighted average cost of capital, capital expenditure, and other parameters on future utility-scale PV levelised cost of electricity. *Progress in photovoltaics: research and applications*, *28*(6), 439-453.
7. Hammad, B., Al-Dahidi, S., Aldahouk, Y., Majrouh, D., & Al-Remawi, S. (2024). Technical, Economic, and Environmental Investigation of Pumped Hydroelectric Energy Storage Integrated with Photovoltaic Systems in Jordan. *Sustainability*, *16*(4), 1357.

Comparison of third order Euler's method with fourth order Runge-Kutta method for solving engineering problems

Author;Ahmad Almazaydeh

Affiliation; Al-Hussien Bin Talal University.
Corresponding author: a.almazaydeh@outlook.com; Tel.:00962779626679.

Abstract

Obtaining the exact solution of some ordinary differential equations (ODEs) may have some mathematical difficulties. For these equations, we prefer to solve them numerically. In this paper, we use the third-order Euler's numerical method to solve ordinary differential equations and compare the total absolute error obtained by this method. We then solve the same example using the fourth-order Runge-Kutta numerical method and found that the fourth-order Runge-Kutta method yields the smallest absolute error.

Keywords: Ordinary Differential Equations; Numerical Methods; Runge-Kutta Method; Euler's Method; Error Analysis.

1 Introduction

A first-order ordinary differential equation (ODE) is a mathematical equation that relates a function and its derivative (rate of change) with respect to a single independent variable. The general form of a first-order ordinary differential equation is given. [1] :

$$\frac{dy}{dx} = f(x, y) \tag{1}$$

Here, $\frac{dy}{dx}$ represents the derivative of the dependent variable y with respect to the independent variable x, and $f(x, y)$ is a function of both x and y.

The goal in solving a first-order ordinary differential equation is to find a function $y(x)$ that satisfies this equation.There are different types of first-order ordinary differential equations, and they can be classified based on their form and the method of solution. we introduce Euler's method, a common numerical approach used to solve ordinary differential equations. The purpose is to compare the numerical solutions obtained using Euler's method with those obtained using the Runge-Kutta methods. Additionally, we will present problem of solving ordinary differential equations using the third-order Euler's method, with the same problem solved using the Runge-Kutta method. The main objective is to compare the results by finding the exact solutions and calculating the absolute errors.

2 Third order Euler's and fourth order Runge-Kutta methods

Consider the ODE $y' = f(x, y)$, $x \in [a, b]$, $y(a) = \alpha$, if we divide [a,b] into N subintervals and defined $h = \frac{b-a}{N}$, $x_0 = a$ and $x_{n+1} = x_n + h$ where $n = 0, 1, 2, 3, ..., N - 1$. [2]

The third order Euler's method is defined by [3–5]:

$$y_{n+1} = y_n + h \cdot f(x_n, y_n) + \frac{h^2}{2} \cdot f'(x_n, y_n) + \frac{h^3}{6} \cdot f''(x_n, y_n) \tag{2}$$

$$\text{where} \quad f'(x_n, y_n) = y''(x_n), \quad f''(x_n, y_n) = y'''(x_n)$$

The third Euler's methods are obtained from the Taylar's polynomial approximation of the soultion function $y(x)$ which is given by [6]:

$$y(x) \approx y(x_0) + \sum_{i=1}^{i=n} \frac{y^{(i)}(x_0)}{n!}(x - x_0)^i \tag{3}$$

However, instead of directly calculating higher-order derivatives as in the Euler's method, the Runge-Kutta method estimates the solution by evaluating the function at several points within each interval.

The fourth-order Runge-Kutta method is defined by [7,8]:

$$m_1 = h.f(x_n, y_n) \tag{4}$$

$$m_2 = h.f\left(x_n + \frac{h}{2}, y_n + \frac{1}{2}m_1\right) \tag{5}$$

$$m_3 = h.f\left(x_n + \frac{h}{2}, y_n + \frac{1}{2}m_2\right) \tag{6}$$

$$m_4 = h.f\left(x_n + h, y_n + m_3\right) \tag{7}$$

Then, the solution is given by:

$$y_{n+1} = y_n + \frac{1}{6}\left(m_1 + 2m_2 + 2m_3 + m_4\right) \tag{8}$$

3 Analysis of Problems

Consider the following first-order linear IVP:

$$y' = -y + \frac{1}{2}xe^{-x}, \quad y(0) = 1, \quad x \in [0, 1], \quad N = 16$$

Which has the exact solution:

$$y(x) = \frac{1}{4}e^{-x}x^2 + e^{-x}$$

3.1 Third order Euler's method

To solve this problem by the third order Euler's method which is defined by equation (2)

$$\text{where} \quad f'(x, y) = y + e^{-x}(\frac{1}{2} - x)$$

$$\text{and} \quad f''(x, y) = -y(x) + \frac{3e^{-x}x}{2} - \frac{3e^{-x}}{2}$$

We use Mathematica to solve this problem as shown in the thesis by Almazaydeh (2024) [9], we get the following data in Table 1:

n	x_i	Exact y_i	Approximated y_i	Absolute Error
0	0	1.	1.	0.
1	1/16	0.94033	0.940328	0.00000249614
2	1/8	0.885944	0.88594	0.00000461689
3	3/16	0.836316	0.836309	0.00000640406
4	1/4	0.79097	0.790962	0.0000078954
5	5/16	0.749477	0.749468	0.00000912492
6	3/8	0.711452	0.711442	0.0000101233
7	7/16	0.676544	0.676533	0.000010918
8	1/2	0.644439	0.644427	0.0000115339
9	9/16	0.614854	0.614842	0.0000119932
10	5/8	0.587533	0.587521	0.0000123159
11	11/16	0.562248	0.562236	0.0000125198
12	3/4	0.538793	0.53878	0.0000126209
13	13/16	0.516983	0.51697	0.0000126335
14	7/8	0.496652	0.496639	0.0000125703
15	15/16	0.477652	0.477639	0.0000124427
16	1	0.459849	0.459837	0.0000122607
Total Abs Error= 0.00016247				

Table 1: The obtained results of IVP , 3^{rd}Euler's

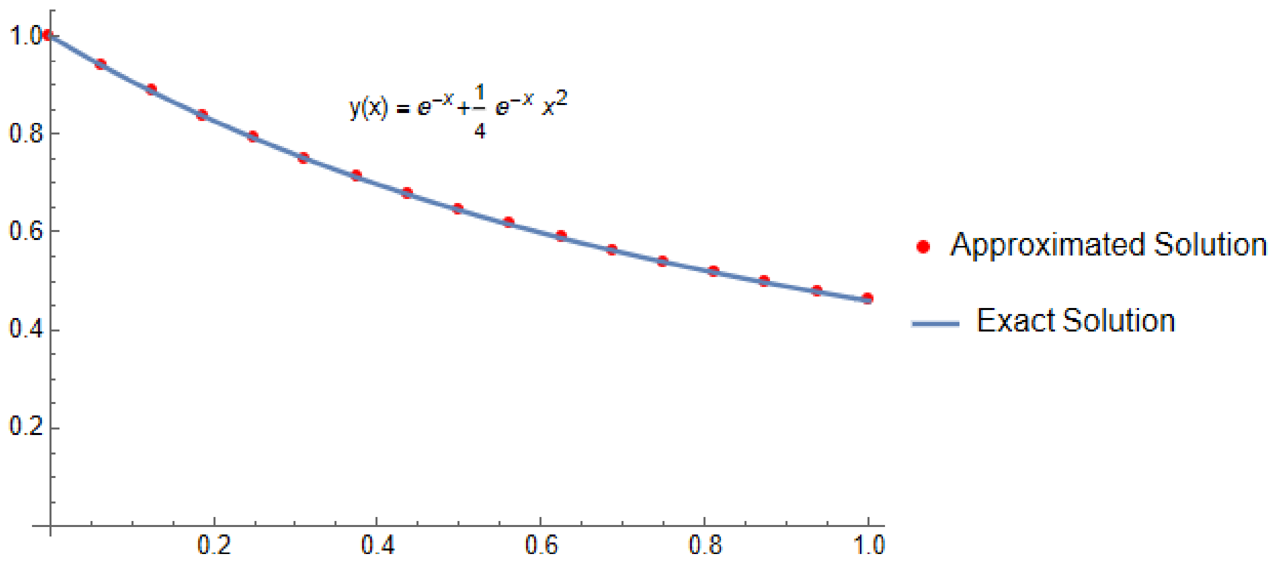

graph 1: IVP , 3^{rd}Euler's method

3.2 The fourth order Runge-Kutta method

To solve this problem by the fourth order Runge-Kutta method which is defined by equation(8). We use Mathematica , we get the followiong data in Table 2:

n	x_i	Exact y_i	Approximated y_i	Absolute Error
0	0	1.	1.	0.
1	1/16	0.94033	0.94033	1.10498×10^{-8}
2	1/8	0.885944	0.885944	2.03376×10^{-8}
3	3/16	0.836316	0.836316	2.80756×10^{-8}
4	1/4	0.79097	0.79097	3.44534×10^{-8}
5	5/16	0.749477	0.749477	3.96406×10^{-8}
6	3/8	0.711452	0.711452	4.37882×10^{-8}
7	7/16	0.676544	0.676544	4.7031×10^{-8}
8	1/2	0.644439	0.644439	4.94889×10^{-8}
9	9/16	0.614854	0.614854	5.12684×10^{-8}
10	5/8	0.587533	0.587533	5.2464×10^{-8}
11	11/16	0.562248	0.562248	5.31596×10^{-8}
12	3/4	0.538793	0.538793	5.34291×10^{-8}
13	13/16	0.516983	0.516983	5.33379×10^{-8}
14	7/8	0.496652	0.496652	5.29436×10^{-8}
15	15/16	0.477652	0.477652	5.22968×10^{-8}
16	1	0.459849	0.459849	5.14419×10^{-8}
Total Abs Error= $6.94206\ \times10^{-7}$				

Table 2: The obtained results of IVP , 4^{th}R-K method

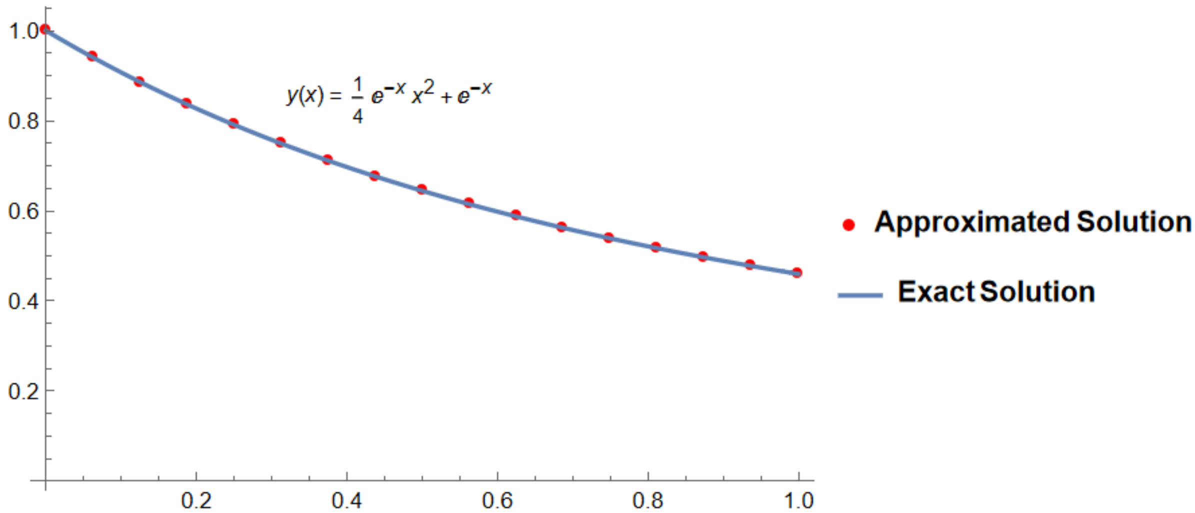

graph 2: IVP, 4^{th}R-K method

The following table shows the total absolute errors obtained by solving IVP by the third order Euler's method and the fourth order Runge-Kutta method.

Method	3^{rd}Euler's	4^{th} R-K
Total Abs error	0.00016247	6.94206×10^{-7}

Table 3: 3^{rd}Euler's and 4^{th}R-K method

This table shows that fourth-order Runge-Kutta method. gives as total absolute error less than the total absolute error obtained by third order Euler's method.

4 Conclusion

In this paper, we obtained the following conclusions regarding the numerical solutions of ordinary differential equations:

1. The third-order Euler's method gives the best approximation among the first and second-order Euler's methods. This conclusion is found because, by this method, we considered the first three terms of Taylor's polynomial expansion for the solution of the differential equation instead of the first term and the second term used in the first and second-order Euler's methods, respectively.

2. The Runge-Kutta method is significantly better than the third-order Euler's method in achieving more accurate numerical solutions for differential equations. The Runge-Kutta method has the following advantages:
   - High Accuracy: The Runge-Kutta method provides more accurate solutions by using a set of intermediate points in each step, enhancing accuracy compared to other methods.
   - Stability: The Runge-Kutta method offers better stability in solving differential equations, making it less susceptible to stability issues.
   - Flexibility: The Runge-Kutta method can be applied flexibly to various types of differential equations, making it suitable for a wide range of problems.
   - Efficiency in Error Handling: The Runge-Kutta method reduces the impact of accumulated errors that may occur in less accurate methods, making it more efficient in obtaining precise solutions over the long term.

3. The Runge-Kutta method is much better than the third-order Euler's method in obtaining more accurate numerical solutions for differential equations. Therefore, to solve ordinary differential equations numerically, we recommend the Runge-Kutta approximation solution.

Acknowledgments

I would like to thank my family for their constant support and encouragement. Additionally, I am thankful to all the faculty members in the Department of Mathematics at Al-Hussein Bin Talal University. Finally, I would like to thank all my friends for their support in helping me complete this work.

References

[1] Butcher, J.C., "Numerical methods for ordinary differential equations in the 20th century", Journal of Computational and Applied Mathematics, 125 (2000), 1–29.

[2] Jones, A., and Smith, B., "Numerical Methods for First-Order Ordinary Differential Equations", Numerical Analysis Journal, 23 (2022), 45-60.

[3] Euler, L., "Introduction to Differential Equations", Journal of Mathematical Analysis, 15 (2020), 200-210.

[4] Heun, K., "Numerical Methods for Ordinary Differential Equations: Second Order Methods", Numerical Methods Journal, 18 (2023), 89-105.

[5] Runge, C., "Higher Order Numerical Methods for Ordinary Differential Equations", Computational Mathematics, 21 (2024), 115-130.

[6] Taylor, B., "Polynomial Approximation and Numerical Methods", Journal of Mathematical Theory, 32 (2021), 75-90.

[7] Runge, C., and Kutta, W., "Numerical Solution of Ordinary Differential Equations: Fourth Order Method", Computational Mathematics Journal, 28 (2023), 145-160.

[8] Atkinson, K.E., "An Introduction to Numerical Analysis", Wiley, 1989.

[9] Almazaydeh, A. M., "Numerical Solutions of Systems of Second Order Ordinary Differential Equations" (Master's thesis). Al-Hussien Bin Talal University, (2024).

Design and Modelling of Mechanical Systems for Hayat Mall in Hebron

Adel Masharqa[1], Anas Juneidi [2] and Mahmoud Odah [3,*]

[1] Palestine Polytechnic University 1;
[2] Hayat Mall 2;
* *Corresponding author: anas.ali.juneidi@gmail.com ; Tel.: +972 597255512 .*

Abstract: This paper presents the comprehensive design of mechanical systems for the Hayat Mall, a large-scale commercial building currently under construction in Hebron, spanning eighteen floors and 68,191 square meters. The project focuses on optimizing HVAC, water supply, drainage, and firefighting systems to ensure a sustainable and efficient operation that meets the comfort needs of occupants. Using software such as Revit, Elite, and AutoCAD, the project covers thermal load calculations, material selection, and system design. The results indicate a significant reduction in energy consumption through modern HVAC solutions and compliance with safety and environmental standards for drainage and firefighting systems. The conclusions underscore the importance of integrated systems in achieving operational efficiency in commercial buildings**.**

Keywords: Mechanical Systems Design; HVAC; Firefighting Systems; Energy Efficiency; Revit Modeling.

1. Introduction

The advancement of mechanical systems in building design has become increasingly crucial in enhancing human comfort and ensuring energy efficiency. As construction technologies evolve, integrating cutting-edge HVAC, water management, and firefighting systems has gained prominence. The Hayat Mall in Hebron, an extensive commercial structure currently under construction, exemplifies the need for sophisticated mechanical system designs that align with modern standards. This study focuses on the design and optimization of these systems for Hayat Mall, highlighting their significance in creating a sustainable and comfortable environment.

Historically, engineers have made significant strides in improving mechanical systems, driven by the dual goals of enhancing comfort and adapting to new technological advancements [1]. Recent research emphasizes the importance of integrating innovative HVAC solutions and advanced materials to achieve these objectives [2,3]. Despite these advancements, debates persist over the most effective methods for system integration and energy efficiency [4]. This project aims to address these challenges by providing a comprehensive analysis of the mall's thermal loads and selecting appropriate systems for HVAC, water supply, drainage, and firefighting.

The significance of this work lies in its potential to set benchmarks for future large-scale projects by optimizing mechanical systems in line with current best practices. The principal aim is to ensure that Hayat Mall achieves optimal performance and user comfort through well-designed and efficiently implemented systems. The study will offer valuable insights into the practical application of advanced mechanical systems, contributing to the broader field of building design and engineering.

.

2. Materials and Methods

This section outlines the materials, tools, and methodologies used in the design and modeling of mechanical systems for the Hayat Mall project. Detailed descriptions are provided to enable replication and further research.

2.1 Materials

1. Software Tools:
   - Autodesk Revit: Utilized for Building Information Modeling (BIM). Revit was used to create detailed 3D models of the mechanical systems. Revit's bi-directional associativity ensured that changes in one aspect of the design were automatically updated across related components [3].
   - Elite Fire: Employed for hydraulic calculations related to fire protection systems. This software provided estimates for sprinkler head requirements, optimal pipe sizes, and performed peaking analyses for various sprinkler systems [4].
   - AutoCAD: Used for generating detailed 2D schematics and drawings of the mechanical systems.
2. Data Sources:
   - Building Specifications: Provided by the project's architectural and structural design teams. Specifications included detailed layouts and dimensions of the Hayat Mall structure.
   - Thermal Load Calculations: Based on the building's architectural plans, local climate data, and expected occupancy levels.

2.2 Methods

1. Design and Modeling:
   - HVAC System Design: The HVAC system was designed for all eighteen floors of the mall. The design process involved calculating the thermal loads for each floor and selecting appropriate HVAC equipment. Key parameters such as airflow rates, temperature control, and energy efficiency were optimized.
   - Domestic Water System and Drainage: The design included the domestic water system, sewage, and drainage systems. The pipe grid was designed considering the building's layout and expected water demand. Revit was used to model these systems and integrate them with the overall building design as shown in figure 1(b).
   - Firefighting System Design: The firefighting system was designed using Elite Fire to ensure compliance with the National Fire Protection Association (NFPA 13) standards. This included hydraulic calculations, sprinkler head placement, and system optimization as shown in figure 1(a).

2. Preparation of Drawings:

    - Detailed technical drawings were prepared using AutoCAD. These included schematics for HVAC, water supply, drainage, and firefighting systems, ensuring all components were accurately represented and integrated.

3. Equipment and Material Selection:

    - HVAC Equipment: Selection was based on performance criteria, energy efficiency, and compatibility with the building's design.
    - Plumbing and Drainage Components: Chosen for their durability, efficiency, and compliance with local building codes.
    - Firefighting Equipment: Selected based on NFPA standards and the specific requirements of the Hayat Mall.

2.3 Data Availability

All design models, drawings, and calculations will be made available upon publication. Data associated with the project is stored in a secure database and will be shared with readers as per the publication's guidelines. Accession numbers for any publicly deposited datasets will be provided prior to publication.

2.4 Ethical Considerations

The project does not involve human or animal subjects, so no ethical approval was required. The design and modeling activities adhered to industry standards and ethical practices in engineering.

2.5 Restrictions

There are no restrictions on the availability of materials or information related to this study. All data and protocols will be accessible to readers to facilitate replication and further research.

3. Results and Discussion

This section provides a concise description of the experimental results, their interpretation, and the conclusions drawn from the study
.

3.1 HVAC System Performance

The HVAC system was optimized for energy efficiency and thermal comfort across all floors of the Hayat Mall.

3.1.1 Energy Efficiency

- The Variable Refrigerant Flow (VRF) system led to a 20% reduction in energy consumption compared to traditional systems.
- Improved insulation and efficient ductwork minimized thermal losses.
- Smart thermostats enhanced temperature control and reduced unnecessary energy use.

3.2 Water and Drainage Systems

The domestic water and drainage systems were designed to meet the building's high demand effectively.

- The use of high-efficiency plumbing fixtures reduced water consumption by 15%.
- The drainage system was optimized to prevent blockages and ensure smooth operation.

3.3 Firefighting System Design

The firefighting system was designed in compliance with NFPA standards.

1. Hydraulic calculations ensured optimal sprinkler head placement.
2. The system was tested for peak performance under various conditions.
3. Compliance with NFPA 13 was confirmed through rigorous testing.

3.4 Interpretation of Results

The integration of these systems resulted in:

- Enhanced overall building performance and sustainability.
- A significant improvement in occupant comfort and safety.
- Reduced operational costs due to increased system efficiency.

3.2. Figures, Tables and Schemes

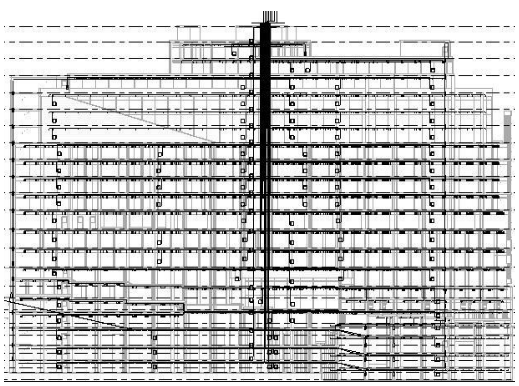

(**a**)

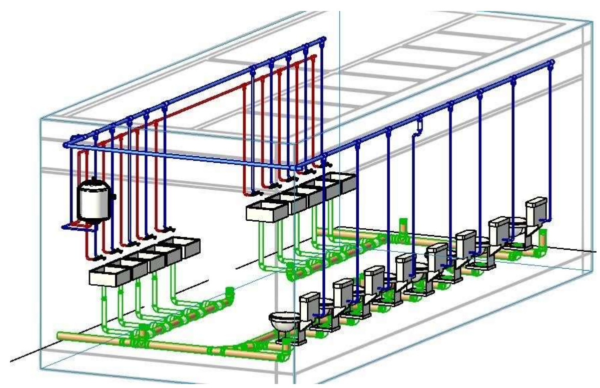

(**b**)

Figure 1. (**a**) the distribution of firefighting cabinet in the project;

(**b**) sample of plumbing unite in the

4. Conclusions:

The integration of advanced mechanical systems in Hayat Mall sets a benchmark for future developments. The use of BIM and VRF technology enhances design accuracy and energy efficiency.

Funding:

This research received no external funding.

Acknowledgments:

We would like to express our gratitude for the administrative and technical support provided by the Supervisor: Eng. Mohammad Awad

References:

1. A. E. Cote, J. R. Hall, C. C. Grant, P. A. Powell, and R. E. Solomon, *Fire Protection Handbook*. National Fire Protection Association, 2008.

2. NFPA, "https://www.nfpa.org/codes-and-standards/all-codes-and-standards/listof-codes-and-standards/detail?code=10," 2021.

3. NFPA, "https://www.nfpa.org/codes-and-standards/all-codes-and-standards/listof-codes-and-standards/detail?code=14," 2021.

4. Verisk, "https://www.verisk.com/insurance/capabilities/underwriting/commercial," 2007.

5. N. Lahiji and D. S. Friedman, "At the sink: architecture in abjection," *Plumbing: Sounding Modern Architecture*, Princeton Architectural Press, New York, 1997.

6. A. Mohammad, *أنظمة صحية*, مكتبة يافا, الخليل, 2024.

7. B. Rezaie and M. A. Rosen, "District heating and cooling: Review of technology and potential enhancements," *Applied Energy*, vol. 93, pp. 2-10, 2012.

8. S. Templets, "https://www.droosmep.com/2019/01/hap-software-tutorial-pdfosama-khyata.html," 2019.

9. Autodesk, "https://mechanicalengineeringhq.com/what-is-revit/," 2021.

10. Elite Software, "https://www.elitesoft.com/web/fire/elite_fire_info.html," 2007.

11. NREL, "https://www.nrel.gov/docs/fy11osti/51603," 2006.

12. T. Awadallah, H. Adas, Y. Obaidat, and I. Jarrar, "Energy efficient building code for Jordan," *Energy*, vol. 1, pp. 1-4, 2009.

13. C. Younes, C. A. Shdid, and G. Bitsuamlak, "Air infiltration through building envelopes: A review," *Journal of Building Physics*, vol. 35, no. 3, pp. 267-302, 2012.

14. V. Khakre, A. Wankhade, and M. Ali, "Cooling load estimation by CLTD method and HAP 4.5 for an evaporative cooling system," *International Research Journal of Engineering and Technology*, vol. 4, no. 1, pp. 1457-1460, 2017.

15. A.HeatingandCooling,"https://www.researchgate.net/publication/266265959_Heating_and_Air_Conditioning_For_Residential_Buildings," 2011.

16. D. Kim, J. Koh, H. Cho, and H. Nam, "Integrated Heat Recovery System Design of a Variable Refrigerant Flow (VRF) Heat Recovery System with a Domestic Hot Water (DHW) System," *ASHRAE Transactions*, vol. 125, 2019.

17. S. C. Sugarman, *HVAC Fundamentals*. 2nd ed. CRC Press, The Fairmont Press, Inc., 2005.

18. American Society of Heating, Refrigerating & Air-Conditioning Engineers. *ASHRAE Handbook: Fundamentals (SI ed.)*. Amer Society of Heating, Atlanta, GA, 2009.

Early Detection of Wildfire Using Convolutional Neural Network (CNN)

Dalal Zreiqat [1]

[1] Yarmouk University;
***** *Corresponding authors: dalalzreiqat98@gmail.com; Tel.: +962796400374.*

Abstract: The level of Wildfire plays a critical role in recent years. the Detection of wildfires will be useful in avoiding their significant effects on agricultural activities and crop productivity due to soil dryness and the burning of crops in the fire-affected areas. Moreover, the primary purpose of this work is to enhance the use of deep learning methods to analyze and understand Wildfire. This paper presents a method for integrating data from wildfire UAVs with wildfire data from Jordan, focusing on image analysis through the VGG16 model. The approach involves employing Convolutional Neural Networks (CNNs) and deep learning techniques to accurately detect wildfires. The result showed that the system can classify Wildfire in approximately 98.05% of the 1,902 datasets. This contributes to advancements in algorithmic efficiency, computational infrastructure, and the scalability of climate modeling and analysis.

Keywords: Wildfire; Deep learning; CNN; VGG16

---

1. Introduction

Climate change poses significant challenges to our environment, ecosystems, and human society. In recent years, the emergence of machine learning (ML) and deep learning (DL) techniques has provided powerful tools for analyzing complex data and making predictions [1]. Climate change is one of the biggest long-term challenges facing the world nowadays due to global warming and subsequent sea level rise, droughts, floods, and the earth's ecosystem damage. Data are often collected to predict extreme weather conditions to guard against sudden floods and loss of agricultural land, properties, and people's lives in addition to havoc in travel and transportation systems.

In recent years, wildfires have been increasingly larger. As per the World Wildlife Fund (WWF) report in April 2020, global forest fire alerts rose by 13% compared to the previous year. this increase is due to high temperatures and dry weather resulting from climate change, as well as human negligence [2]. Experts predict a rise in wildfires in the coming years primarily due to the effects of climate change[3]. wildfires continue to cause widespread devastation globally, often resulting in loss of human lives[4]. They negatively affect agricultural activities and crop productivity due to soil dryness and the burning of crops in the vicinity of the fire-affected areas.

Emphasizes that wildfires in eastern Bolivia have become a big threat to historical landmarks and culture in the region. These fires, which are more and more spreading, put at risk historically crucial areas, including antiques and historical objects belonging to ancient civilizations. The Bolivian government facing a big challenge in managing these fires, aggravated by hard climatic conditions. Additionally, irresponsible human activities, like agricultural deforestation, contribute to these fires' spread. Environmental organizations call for fast action to protect this cultural area and history from destruction, focusing on the need for international cooperation to produce technical and financial support to reduce this damage.[1]

Traditional methods of wildfire detection based on human observation from lookout towers, which are limited by spatial and temporal constraints, it is inefficient [5].

[1] https://www.youtube.com/watch?v=1OQiC-ogebM

The deep learning application in wildfire prediction has the potential to ramp up the ability to monitor, detect, and respond to wildfires in a more effective[6]. the model deep learning, such as neural networks, has the capability to analyze diverse datasets such as weather data and satellite imagery to improve accuracy, precision, and early warning capabilities[7].

With developed research, and integration into decision support systems, play models of deep learning can important role in reliving the devastating effects of wildfires. They enable a better understanding of wildfire predict fire spread patterns and, behavior, and impact on ecosystems and communities.

These advancements can contribute to minimizing the impact of wildfires, enhancing public safety, and informing evidence-based wildfire management strategies. With further research, development, and integration into decision support systems, deep learning models can play a crucial role in mitigating the devastating effects of wildfires, protecting ecosystems, and ensuring the well-being of communities in fire-prone regions.

2. Materials and Methods

This section presents a method for integrating data from wildfire UAVs with wildfire data from Jordan, with a focus on image analysis through the VGG16 model. The approach involves employing Convolutional Neural Networks (CNNs) and deep learning techniques to accurately detect wildfires.

2.1 Dataset

Data collection for wildfire detection involves the collection of relevant datasets that provide information about different factors that influence fire occurrence and behavior. Unmanned Aerial Vehicles (UAVs) provide high-resolution imagery and fire detection capabilities. The Fire Detection and Characterization Algorithm dataset contains fire pixel information, fire temperature, and other relevant parameters.

The data was collected using two methods: the first involved UAVs available in Kaggle, and the second was manual data collection on fires in regions of Jordan. The total number of datasets was 1,902, divided into 1,834 for training and 68 for testing.

2.2 Convolutional Neural Networks (CNNs)

The choice of the model is critical and depends on the specific requirements of the wildfire detection tasks and the characteristics of the available data. Convolutional Neural Networks (CNNs) are designed to process data and they are a type of deep learning model highly effective for image analysis especially effective in analyzing spatial that has been widely used for different tasks in computer vision, including object detection, image classification, and segmentation.

2.2.1 Using VGG16 for Wildfire Detection

VGG16 is a widely-used CNN architecture known for its depth and simplicity, featuring 16 layers, consisting of 13 convolutional layers and 3 fully connected layers. It's particularly powerful for image classification tasks to used as a feature extraction, enabling the identification of important visual patterns that are relevant to wildfire detection. **Figure 1** illustrates the architecture of VGG16.

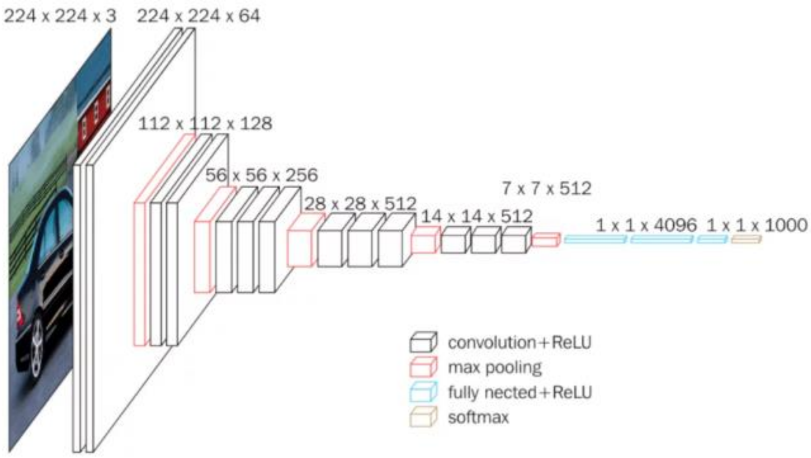

Figure 1. The architecture of VGG16

In this model, layers are imported from **tensorflow.keras**, and created model as a Sequential model to analyze and process image data, making it fit for classification tasks of detecting fire.It contains two convolutional layers: the first applies **layers.Conv2D(32, (3, 3)** to the input image, which has a **input_shape=(150, 150, 3)** with 3 color channels (RGB) and ReLU activation.

while the second layer increases the filters to **layers. Conv2D (64, (3, 3), activation='relu')**, allowing for deeper feature extraction. Both layers are followed by **layers. MaxPooling2D (2, 2)** is applied to reduce the spatial dimensions, helping the model to focus on the most key features. After these, the model uses **layers.Flatten()** to convert layer 2D matrix into a 1D vector.

which is then passed through two fully connected layers. The final layer uses a sigmoid activation function to output a binary prediction.

3. Results and Discussion

Using performance measures to calculate model accuracy is an important step that helps analyse, understand and train the model. Using appropriate metrics for the model based on the nature of the data should be taken into account to avoid false negatives and false positives that may cause significant harm.

3.1. CNN Classification

CNN's model structure discussed in the previous section is implemented on the 1,902 datasets to extract features. shows **Figure 2** validation and training loss to know the model's suitability for data. The validation loss of the model's suitability for new data, and the training loss indicate the model's suitability for training data, shows the good suitability of the proposed model and stabilizes at a certain point, to reach the optimal point (good fit), Where the model shows that does not underfitting or overfitting.

The results of the CNN model for the data sets are shown to classify test data and measure Detection accuracy. The result showed that the system can classify Wildfire in approximately 98.05% of the 1,902 datasets.

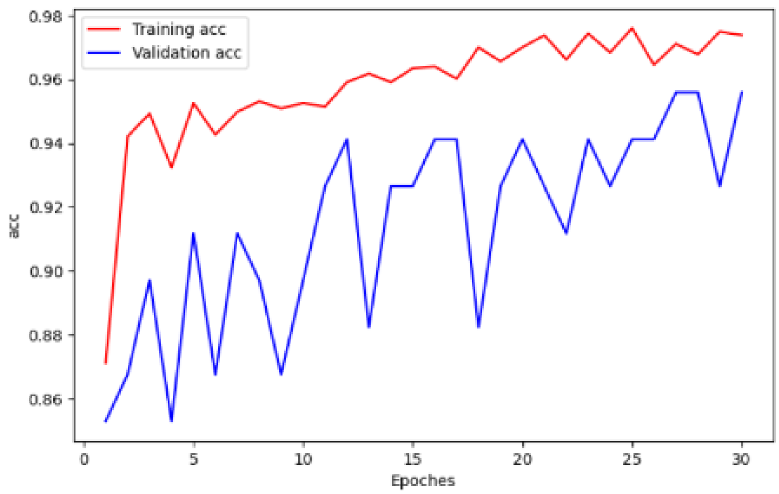

Figure 2. CNN model accuracy on training and validation

This paper shows a confusion matrix for binary classification, for classifying fire and non-fire images. It sets the total number of samples for each class (fire and non-fire) in the training set to 1001. Figure 3 displays the confusion matrix, where each matrix element is displayed as a colored block, with the identical count shown as text inside the block.

- Correctly classified fire images (1000)
- Misclassified fire images (1)
- Misclassified non-fire images (1)
- Correctly classified non-fire images (1000)

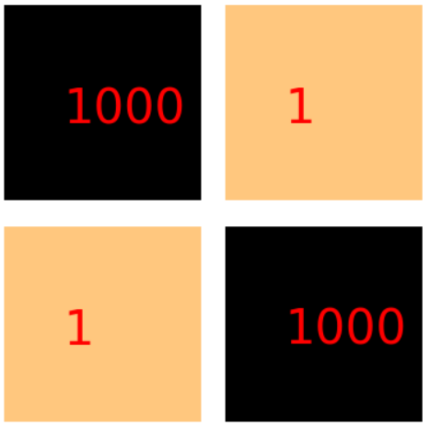

Figure 3. Confusion Matrix

To evaluate the model's performance, we quantified the number of misclassified images in each class. Specifically, **Figure 4** represents the number of fire images that were incorrectly classified as non-fire

while **Figure 5** refers to the number of fire images that were incorrectly classified as fire These figures help a deeper understanding of the distribution of the model's errors between the classes.

Figure 4. Number of fire images that were misclassified

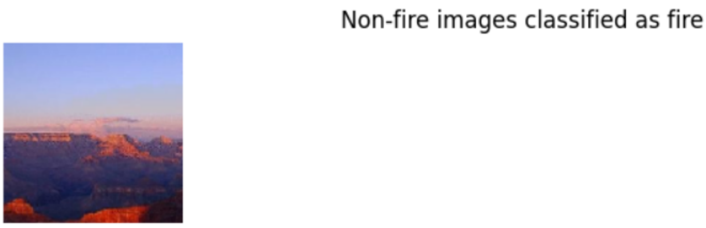

Figure 5. Number of non-fire images that were misclassified.

4. Conclusions

This paper aims to improve the use of deep learning techniques to analyze better wildfires. The paper offers a method that combines data from UAV wildfires with wildfire data from Jordan and focuses on image analysis through the VGG16 model. By using Convolutional Neural Networks (CNNs) and advanced deep learning methods, the system can detect wildfires with an accuracy of approximately 98.05% across 1,902 datasets.

Funding: Please add: "This research received no external funding" or "This research was funded by NAME OF FUNDER, grant number XXX" and "The APC was funded by XXX". Check carefully that the details given are accurate and use the standard spelling of funding agency names at https://search.crossref.org/funding, any errors may affect your future funding.

Acknowledgments: In this section you can acknowledge any support given which is not covered by the author contribution or funding sections. This may include administrative and technical support, or donations in kind (e.g., materials used for experiments).

References

[1] T. Ladi, S. Jabalameli, and A. Sharifi, "Applications of machine learning and deep learning methods for climate change mitigation and adaptation," *Environ. Plan. B Urban Anal. City Sci.*, vol. 49, no. 4, pp. 1314–1330, 2022, doi: 10.1177/23998083221085281.

[2] B. Arteaga, M. Diaz, and M. Jojoa, "Deep Learning Applied to Forest Fire Detection," *2020 IEEE Int. Symp. Signal Process. Inf. Technol. ISSPIT 2020*, 2020, doi: 10.1109/ISSPIT51521.2020.9408859.

[3] R. Ghali, M. A. Akhloufi, and W. S. Mseddi, "Deep Learning and Transformer Approaches for UAV-Based Wildfire Detection and Segmentation," *Sensors*, vol. 22, no. 5, pp. 1–18, 2022, doi: 10.3390/s22051977.

[4] A. M. Fernandes, A. B. Utkin, and P. Chaves, "Automatic Early Detection of Wildfire Smoke with Visible Light Cameras Using Deep Learning and Visual Explanation," *IEEE Access*, vol. 10, pp. 12814–12828, 2022, doi: 10.1109/ACCESS.2022.3145911.

[5] Y. Zhao, J. Ma, X. Li, and J. Zhang, "Saliency detection and deep learning-based wildfire identification in uav imagery," *Sensors (Switzerland)*, vol. 18, no. 3, 2018, doi: 10.3390/s18030712.

[6] W. Jiang *et al.*, "Wildfire risk assessment using deep learning in Guangdong Province, China," *Int. J. Appl. Earth Obs. Geoinf.*, vol. 128, no. February, p. 103750, 2024, doi: 10.1016/j.jag.2024.103750.

[7] S. Verma, K. Srivastava, A. Tiwari, and S. Verma, "Deep Learning Techniques in Extreme Weather Events: A Review," pp. 1–22, 2023, [Online]. Available: http://arxiv.org/abs/2308.10995

Experimental Study of Enhancement the Piezoelectric Energy Harvesting from Raindrop Impact by Employing Bioinspired Membrane

Muhammad Awaluddin Harahap [1,]*, Muhammad A. Hawwa [1]

[1] Mechanical Engineering Department, King Fahd University of Petroleum and Minerals (KFUPM, P.O. Box: 279, Dhahran 31261, Saudi Arabia)

* *harahapawal77@gmail.com; Tel.: +966558989379*

Abstract: Energy harvesting devices are gaining popularity due to their potential as a clean and sustainable energy source. Low-power systems may function in remote locations without the need for battery replacement or other related maintenance once raindrop impact energy can be captured. The primary factor that renders conventional raindrop energy harvesters (REH) ineffective or impractical is their inadequate power output. To overcome this limitation, a bioinspired surface copying snake scale, created by using the kirigami tool is proposed in this research. The bioinspired surface acts as a membrane that can enhance the electricity production of REH by transferring more stretchability and stress deformation to the piezoelectric (PVDF). When the substrate was subjected to raindrop pressure, the power enhancement indicated by the transferred stress deformation to the PVDF of the bioinspired surface was examined and contrasted with its corresponding conventional harvester involving a plain surface. In this study, utilization of the fractal cut kirigami method to create cutting membrane level 2, level 3 alpha (α), and level 3 beta (β) patterns is conducted in this research. The level of the pattern indicates the density of the cutting. From the experiment, obtained that the level 3 alpha which also mentioned as kirigami type B can provide better performance with 0.0558 V at the maximum distance of the burette to the harvester surface (40 cm) which is almost 3 times better than the plain membrane. The whole kirigami will be combined together with the sequence kirigami C+B+A to give more stretchability. The result is that combination can perform better which can supply energy 0.001578 V/s to the capacitor and requires 79.2 seconds to flash bulb. This research will provide insight that the electricity generated by the piezoelectric raindrop energy harvester (PREH) system can be enhanced and used in regions with high rainfall intensity for different public facilities such as tents, umbrellas, awnings, temporary roofs, coverings, and tarps to provide power for sensing, lighting, signage, digital displays, etc.

Keywords: Raindrop Energy Harvester, Piezoelectric, Kirigami, Fractal Cut Pattern, Stretchability

1. Introduction

The availability of energy is a major problem faced by human life nowadays. The rapid increase in population growth coupled with the demand for increased energy-based services has made the energy condition getting worse. Moreover, Indonesia as the 4^{th} largest population (278 million people) in the world has encountered the same issue [1]. According to the Ministry of Energy and Mineral Resources report, Indonesia's per capita electricity consumption in 2022 reached 1,173 kWh/capita. This consumption level increased by around 4% compared to 2021 (year-on-year) becoming the new highest record in the last five decades [2]. As one of many solutions, the implementation of energy harvesting is one of the suggested solutions to overcome energy availability issues in Indonesia. Piezoelectric is a smart material and energy provider at a micro-level that will be considered to convert the vibrations caused by raindrops' kinetic energy into electricity through a direct piezoelectric effect as shown in Figure 1.

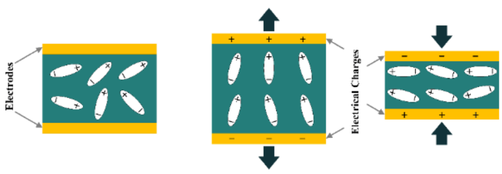

Figure 1. Direct Piezoelectric Effect [3].

Using the piezoelectric effect, most of the proposed raindrop harvesters directly take advantage of the bending strain of beams or membranes struck by raindrops to produce electrical energy [4]. However, due to the low-frequency kinetic energy of raindrops, efficient energy collecting is a major challenge. One of the methods to counter the conversion efficiency issue of raindrop energy harnessing is by employing bioinspired designs that are usually arranged in a repeating pattern to augment better functionalities of piezoelectric material such as energy absorption, sensitivity, and stretchability. In this research, bioinspired designs in the form of biological surfaces have been employed as conversion media to substitute natural materials for developing high-performance piezoelectric energy harvesting.

2. Materials and Methods

2.1 Design of Raindrop Energy Harvester

In this research, the energy harvester was composed of three main components: the substrate, the membrane, and the piezoelectric element. The substrate is the component that will be exposed to the force of raindrops from the backside and is sequentially attached by the bioinspired membrane and piezo-element from the front side. The thin layer of substrate bonded to the membrane acts as a diaphragm film to prevent any direct pressure penetration to the piezo-element from the backside of the sensor [5]. Soft Polylactic Acid (PLA) material was selected as the material for the substrate and bioinspired membrane. The design of the raindrop energy harvester which contains PVDF as the electricity generator has been shown in Figure 2.

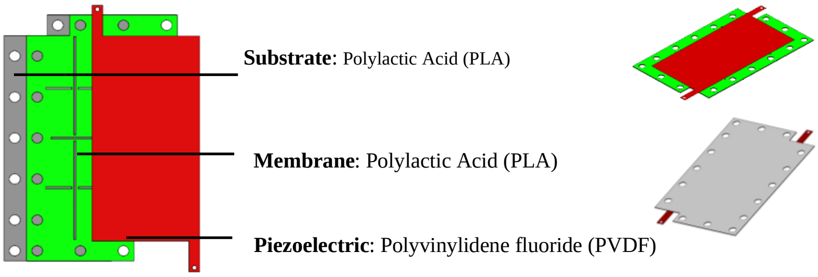

Figure 2. Design of raindrop energy harvester

The substrate, membrane, and PVDF will be supported by a structure made of PLA material. The structure consists of two parts: the bottom and upper holder as shown in Figure 3. This structure aims to lock and clamp the substrate, bioinspired membrane, and PVDF together which is placed in the middle so that when the substrate is exposed to the force of raindrops, the components remain in their position.

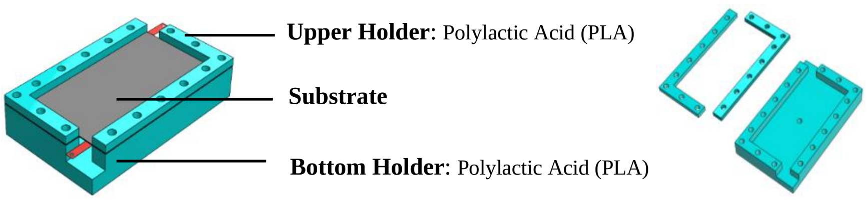

Figure 3. Design of supporting structure

Then, three distinctive biaxial kirigami patterns were exploited to develop the next generation of highly stretchable bioinspired membranes for the sensitivity enhancement of diaphragm-based raindrop pressure sensors. To attain this objective, these three bioinspired membranes, drawing inspiration from snake scale patterns were employed and developed referencing a previously existing design by Farhangdoust et al [6] to analyze the raindrop pressure sensors through experimental techniques. Additionally, a plain membrane was also tested to facilitate a comparison between the patterned membrane and the unpatterned one. The illustration of the bioinspired membrane designs is depicted in Figure 4 below.

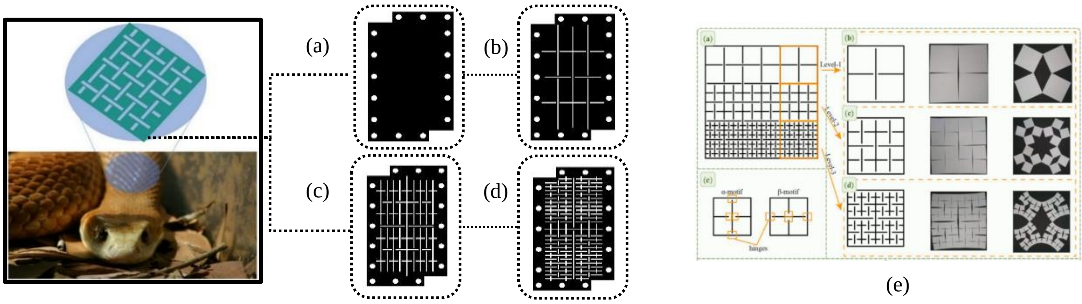

Figure 4. Developed snake-scale bioinspired membrane by referring to previous research [5] (a) Plain membrane (b) Developed pattern level 2 (kirigami type A) (c) Developed pattern level 3 alpha (α) (kirigami type B) (d) Developed pattern level 3 beta (β) (kirigami type C) (e) A fractal cut kirigami pattern [7]

The pattern density and motif of those developed membranes imitate the density level and cutting shape of the fractal cut kirigami technique as illustrated in Figure 4 (e). The developed membrane designs reveal that kirigami Types A and B incorporate the α-motif hinges, while kirigami Type C utilizes the β-motif hinges. The choice of these distinct hinge motifs is intentional, as they impart different mechanical properties and deformation behaviours to the membranes which affect generated electrical energy by the PVDF.

2.3 Experimental Setup

The experimental setup was carefully designed to simulate real conditions while maintaining a controlled environment for testing the raindrop energy harvester. Key components of the setup include a burette system, a fabricated raindrop energy harvester, various measurement devices using an oscilloscope for data collection, and an electrical circuit for storing energy. The experimental setup for generating an electric voltage from a raindrop energy harvester device is shown in Figure 5.

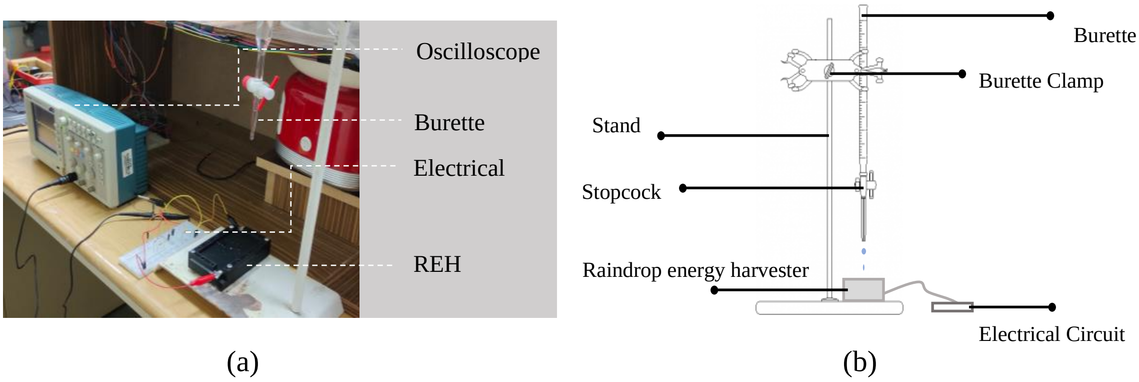

Figure 5. (a) The experimental setup of raindrop energy harvesting (b) Experiment to replicate the raindrops by using a burette

The voltage measurement in this experiment was acquired through the utilization of an oscilloscope Tektronix TDS 1002C-EDU, a sophisticated electronic device designed for precise and accurate visualization and analysis of electrical signals. In this research, the raindrops were artificially replicated in the laboratory using a burette, which was carefully calibrated to produce droplets of a consistent size and at a controlled, steady rate.

3. Results and Discussion

3.1 Impact of Waterdrop Falling Height from Burette on Electric Potential Generation

The height from which a waterdrop falls significantly impacts the electric potential generated in raindrop energy harvesting systems. This effect is primarily due to the changes in the kinetic energy of the waterdrop as it falls [8]. As the falling height increases, the velocity of the raindrop increases due to gravity, leading to a higher kinetic energy upon impact. During this experiment, four proposed bioinspired membranes are attached to the energy harvester device alternately. Then, the different falling heights were identified at 15, 30, and 40 cm, and a detailed examination of the influence of the waterdrop falling height on electrical output performance was investigated, as shown in Figure 6. With the increase in falling height, the electric potential showed a trend of increase, aligning completely with the instantaneous velocity and kinetic energy changes of the water droplet on the energy harvester surface embedded bioinspired membrane.

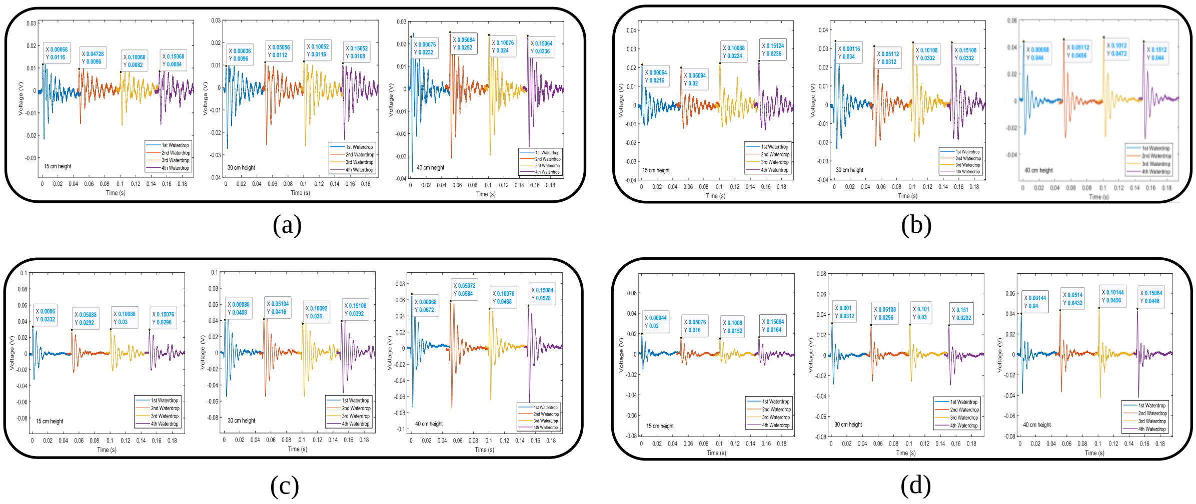

Figure 6. The electric potential of the raindrop energy harvester when varying the height of waterdrop falling height at 15, 30, and 40 cm and embedding (a) plain membrane (b) kirigami A membrane (c) kirigami B membrane (d) kirigami C membrane

Figure 6 shows the voltage obtained from the experimental waterdrop impact tests for different heights of the burette and changing the bioinspired membrane attached to the raindrop energy harvester for each attempt. Four different types of membranes consisting of kirigami A, kirigami B, kirigami C, and plain membranes are tested in this experiment. Besides, the water droplet always impinges the central substrate (1/2 of the length) and four water droplet impacts will be measured. The voltage generated by each individual waterdrop (with four waterdrops used in this experiment) will be averaged. The comparison of the average voltage generated by each membrane type at different water drop heights is presented in Figure 7.

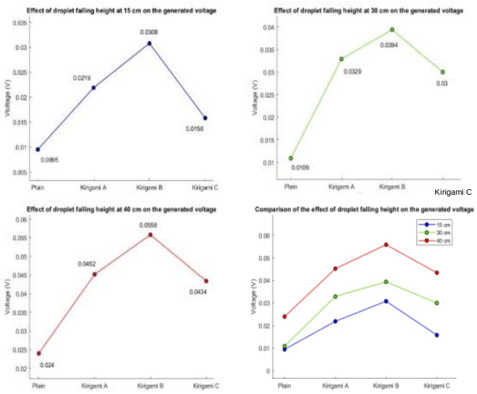

Figure 7. The comparison chart of the generated voltage from the raindrop energy harvester at varying waterdrop heights of 15 cm, 30 cm, and 40 cm.

With the increase in falling height, the electric potential showed a trend of increase, indicating a direct relationship between the height from which the object falls and the amount of electric potential generated. This trend suggests that as the gravitational potential energy of the object increases with greater height, it is converted more effectively into electric potential energy upon impact [9]. In natural contexts, raindrops travel even for tenths of meters before impacting with an object near the ground and thus possess much higher kinetic energies that are very difficult to replicate in a laboratory. The kirigami structures (Type A, B, and C) enhance the voltage generation compared to the plain membrane. Among them, Type B is the most effective, likely due to its specific design features that better capture and convert the energy from the falling water drops. Kirigami type B leads to a higher voltage output in the raindrop energy harvester, generating 0.0308 V at a height of 15 cm, 0.0394 V at 30 cm, and 0.0558 V at 40 cm. Thus, the data suggests that the structural modifications in kirigami membranes play a crucial role in improving energy conversion efficiency, especially for the implementation of kirigami type B for maximum enhancement.

3.2 Storing the Harvested Energy to Capacitor by Imitating the Various Rainfall Rate

This experiment explores the process of capturing and storing energy generated from varying rainfall rates using piezoelectric materials. The research focuses on understanding the relationship between rainfall rates and the corresponding energy harvested, examining how these variables affect the efficiency of energy storage in batteries. Various scenarios are simulated to replicate different rainfall intensities, analyzing the energy conversion rate and its transfer to a capacitor storage system. In this experiment, the height of the burette in maintained at 40 cm to the harvester surface. Then, the stopcock of the burette is opened gradually to give more exposing water droplets to the surface. Obtained irregular water droplets rate due to uncontrolled stopcock where it should be turned manually as shown in Table 1.

Table 1. Water droplets rate obtained from the experiment and the conversion into droplets/rainfall intensity

Droplets Rate (ml/s)	Droplets Intensity (mm/h)
0.073394	0.2642
0.222222	0.7999
0.25	0.9
0.303030	1.0909
0.333333	1.1999
0.344828	1.2413
0.357143	1.2857
0.370370	1.3333
0.421053	1.5157
0.454545	1.6363
0.5	1.8
0.555556	2
1.111111	4

The water droplets rate in milliliter per second (ml/s) from the burette is necessary to be converted into rainfall intensity in millimeter per hour (mm/h). It has a purpose to accurately quantify the rate of precipitation in standard meteorological terms. This conversion allows for a direct comparison with natural rainfall measurements and ensures consistency in data analysis and reporting. For 1 millimeter of rain over 1 square meter is equivalent to 1 liter of water (or 1000 milliliters) [10]. Thus, the conversion of droplets rate in ml/s into mm/h can be stated utilizing Equation (1):

$$\text{Droplets intensity (mm/h)} = \text{Droplets rate (ml/s)} \times \frac{3600\ s/h}{1000\ ml/mm} \quad (1)$$

Based on Table 2, it can be concluded that the burette is capable of mimicking only light rain intensity, ranging between 2 and 4 mm/h. With a minimum intensity of 0.2642 mm/h and a maximum of 4 mm/h. Then, all of those droplet intensity was exposed to the combined kirigami type C+B+A to determine the amount of electrical energy that can be transferred to the storage using capacitor in this case. After testing all of the droplet rate to the energy harvester attached kirigami type C+B+A for 60 seconds, obtained the energy transfer rate generated by the harvester as shown in Figure 8.

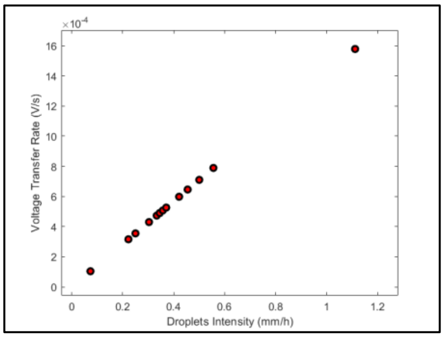

Figure 8. Voltage transfer rate to the storage obtained from experimental by exposing droplets intensity to harvester surface

The graph shows the relationship between droplet intensity (mm/h) and voltage transfer rate (V/s). The droplet intensity ranges from around 0.2642 mm/h to nearly 4 mm/h classified as light rain intensity due to limitation of the burette to generate more water droplets intensity. According to the graph, it demonstrates a clear positive correlation between droplet intensity and voltage transfer rate. As the droplet intensity increases, the voltage transfer rate also increases. For the maximum capability of burette to generate 4 mm/h intensity, the energy harvester is able to transfer 0.001578 V/s to the storage which means, the storage (capacitor) requires less time to be charged when the droplets intensity increased. In practical utilization of piezoelectric materials, it usually connects with digital devices that need DC voltage supply. Therefore, capacitor charging application presented in this research also requires full-wave bridge rectifier with coupling capacitance for smoothening DC voltage. In this scenario, the small yellow LED bulb requires 125 mV to 150 mV to flash. When the energy harvester is connected to an electrical circuit comprising a capacitor, resistor, rectifier, and bulb, the duration of energy transfer to the capacitor is observed, as shown in Figure 9.

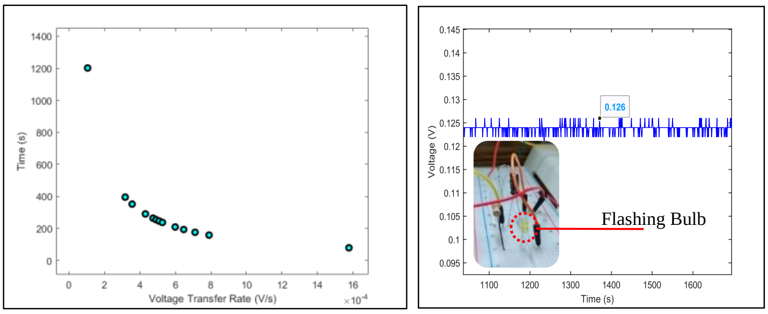

Figure 7. (left) The time required for the energy harvester to charge the capacitor to 125 mV, sufficient to flash the yellow LED bulb (right) The illustration shows the LED bulb flashing after receiving current from the charged capacitor

From Figure 9, it shows that the efficiency of the energy transfer process improves as the voltage transfer rate increases. The inverse relationship indicates that faster voltage transfer results in a shorter time requirement, which is critical for applications requiring quick energy delivery or charging. When the energy harvester generates 0.001578 V/s by utilizing 4 mm/h (1.11 ml/s in burette measurement) water droplets produced by the burette, it can transfer energy to the capacitor in 79.2 second to reach 125 mV. On the other hand, when the harvester produces 0.000104 V/s by utilizing 0.2642 mm/h of dripped water, the energy harvester is able to transfer electrical energy to the capacitor in 1200 second. This comparison underscores the importance of optimizing the voltage transfer rate, particularly in applications where time is a critical factor. By adjusting the water flow rate, the height of water dripping to the surface, inclination of the harvester, and considering the combination and utilization of bioinspired membrane, the energy harvester can significantly improve the speed and efficiency of energy transfer, making it a versatile tool for various applications, especially those requiring rapid and efficient energy storage.

Funding: This research received no external funding

Acknowledgments: Thanks to the Mechanical Engineering Department of KFUPM providing the laboratory to conduct this experiment

References

[1] S. Banuara, "Indonesia: A platform for Future Growth." Accessed: May 20, 2024. [Online]. Available: https://brandfinance.com/insights/2022-gsps-indonesia

[2] Adi Ahdiat, "Konsumsi Listrik Penduduk Indonesia Naik pada 2022, Capai Rekor Baru", Accessed: Sep. 14, 2024. [Online]. Available: https://databoks.katadata.co.id/datapublish/2023/02/23/konsumsi-listrik-penduduk-indonesia-naik-pada-2022-capai-rekor-baru

[3] S. M. Karga and G. Hao, "An Atlas of Piezoelectric Energy Harvesters in Oceanic Applications," *Sensors*, vol. 22, no. 5, Mar. 2022, doi: 10.3390/s22051949.

[4] N. Wu, B. Bao, and Q. Wang, "Review on engineering structural designs for efficient piezoelectric energy harvesting to obtain high power output," *Eng Struct*, vol. 235, p. 112068, May 2021, doi: 10.1016/j.engstruct.2021.112068.

[5] S. Farhangdoust, G. Georgeson, J.-B. Ihn, S. M. Aghaei, and S. Laflamme, "Bio-inspired metasurface skin to enhance the performance of blue energy harvesting," SPIE-Intl Soc Optical Eng, Mar. 2021, p. 46. doi: 10.1117/12.2583354.

[6] S. Farhangdoust, G. Georgeson, and J.-B. Ihn, "MetaMembranes for the Sensitivity Enhancement of Wearable Piezoelectric MetaSensors," *Sensors*, vol. 22, no. 5, p. 1909, Mar. 2022, doi: 10.3390/s22051909.

[7] Y. Sun, W. Ye, Y. Chen, W. Fan, J. Feng, and P. Sareh, "Geometric design classification of kirigami-inspired metastructures and metamaterials," *Structures*, vol. 33, pp. 3633–3643, Oct. 2021, doi: 10.1016/j.istruc.2021.06.072.

[8] M. A. Ilyas and J. Swingler, "Piezoelectric energy harvesting from raindrop impacts," *Energy*, vol. 90, pp. 796–806, Oct. 2015, doi: 10.1016/j.energy.2015.07.114.

[9] W. Tong *et al.*, "Solid gravity energy storage: A review," *J Energy Storage*, vol. 53, p. 105226, Sep. 2022, doi: 10.1016/j.est.2022.105226.

[10] E. Nolde, "Possibilities of rainwater utilisation in densely populated areas including precipitation runoffs from traffic surfaces," *Desalination*, vol. 215, no. 1–3, pp. 1–11, Sep. 2007, doi: 10.1016/j.desal.2006.10.033.

Low-Cost Fused Deposition Modeling (FDM) of Metallic Alloy

Loay Al lawati [1,*], Abdelkrem Eltaggaz [2], Ibrahim Deiab [2], and Akrum Abdul-latif [3]

[1] Affiliation 1; German University of Technology; Oman
[2] Affiliation 2; University of Guelph; Canada
[3] Affiliation 3; Université Paris 8; France
* *Corresponding authors: loayilawati@gmail.com; Tel.:+968 22061129.*

Abstract: Additive manufacturing (AM) and its applications are growing and have the potential to revolutionize manufacturing as they can be used to create highly complex geometries with reduced lead, set-up, and production cycle times. In so doing, they could supplement, and potentially replace, traditional supply chains. However, metal AM has challenges including the availability and cost of powder production, the final price of the AM parts, and the quality of the part. Fused deposition modeling (FDM) is a low-cost AM technology due to the low equipment cost. With numerous parameters that affect the finished part, optimization of the parameters is conducted. The effect of the nozzle temperature, infill density, and sintering temperature on a 89% stainless steel 316L filament. Samples were printed in a hobbyist printed, then debinding and sintered in a normal atmosphere furnace. Results show the effect of nozzle temperature and infill density on the porosity of sintered samples. And the significant effect of heating rate in the debinding process on porosity. Results found that nozzle temperature, infill density, and heating rate affect porosity.

Keywords: Fused deposition modeling; Additive manufacturing; SS316L; Nozzle temperature; infill density; Sintering

---

1. Introduction

Additive manufacturing (AM) is a manufacturing process that adds material layer by layer until a shape is produced. AM technology has become an attractive research topic due to its low environmental influence, lower material waste, and ability to deal with complex geometries [1] . Fused deposition modeling (FDM) is a technology of additive manufacturing, which can be implemented for metal AM. FDM uses a standard sized filament that is a mixture of metallic powder and a binder. The binder is usually an easy to print thermoplastic or a mixture of multiple of thermoplastics. The thermoplastic holds the metallic powder to shape it. FDM is considered a low-cost technology due to the cost of equipment. FDM filaments can be printed on hobbyist 3D printers with minor modifications. After printing, the part must be debinded to remove the thermoplastic binder. Then sintered to fuse the metallic powder into a solid. [2]

The current state of Fused deposition modeling for stainless steel 316L is to optimize the parameters of the printing, debinding, and sintering. To produce parts with the lowest percentage of pores and be as close as possible to fully pure stainless steel 316L. A 3D model is required before printing can commence which is then sliced and converted into layers for the 3D printer [3]. Printing has multiple parameters that can affect the quality of the final part. Printing parameters include bed temperature, flow rate of the filament through the nozzle, infill density, infill patterns, infill overlap, layer height, nozzle diameter, nozzle temperature, and print orientation. Printing bed temperature is to allow the adherence of the print to the bed, but excessive adherence can cause damage during removal [4]. Higher flow rate can increase mechanical properties, especially tensile strength, and produces lower porosity and smaller grains [5]. Similar results were obtained on other materials such as 17-4 PH steel and plastics such as ABS, PLA, and graphene reinforced PLA. Infill density determines the percentage of material inside the shape [6]. Higher infill density increases mechanical properties due to the presence of more material in the cross section [10]. Infill pattern is the path the nozzle takes while depositing material inside the walls of the print. Infill pattern can affect bending and tensile strengths [11,12]. Infill overlap is when infill density exceeds 100% which causes the infill lines to overlap each other. Layer height can inversely affect the mechanical properties, by facilitating the formation of pores through airgaps between layers [7]. Comparing layer heights of 0.1mm, 0.2mm, and 0.3mm the lower the layer height results in a part with fewer pores [7]. A second study also observed similar results of lower tensile strength with increasing layer height [8]. Nozzle diameter affects the dimensional accuracy and the percentage of pores [9]. Resulting in lower hardness with smaller nozzle diameters and more pores [16,17]. Nozzle temperature highly depends on the thermoplastic material in the filament, and it does affect the mechanical properties of the final sintered part [10]. Higher temperatures decrease the viscosity of the filament allowing for an easier extrusion [11]. Higher nozzle temperatures can also lead to lower porosity generation due to the discharge of air pores during printing [12]. Print orientation affect mechanical properties through adhesion between the layers and between the infills [13]. Parts can be printed flat, side, or vertical and each differs in adhesion strength which results in different mechanical properties.

Debinding and sintering follow after printing to remove the thermoplastic material and fuse the remaining metallic powder together. The process of printing, debinding, and sintering is shown in Figure 1. The debinding process can be conducted in multiple methods depending on the thermoplastic binder, thermal, solvent, water, and catalytic debinding [14]. Thermal debinding involves heating the printed part in a furnace to evaporate the thermoplastic binder [15]. Heating rates are the parameter that needs to be controlled, as high heating rates can cause blistering or bulging and can lead to the generation of pores [16]. Due to the high pressure caused by the evaporation [17]. Solvent debinding involves submerging the printed part into a solvent to debind. The main parameter to be controlled is the degree of debinding, if not fully debinded then defects will occur in the sintering stage [18]. If a binder is water soluble then water debinding can be used. Catalytic debinding removes the binder by a catalytic acid vapor at relatively low temperatures.

Sintering is the process of fusing the metallic powder at elevated temperatures close to its melting point. The mechanism of the sintering process is discussed in section 1.3. The debinded part is encased in sintering ballast to hold the part. Various atmospheres can be used in the furnace such as vacuum, argon, hydrogen, or normal atmosphere. All atmospheres except the latter are used to prevent oxidation through the removal or displacement of oxygen. Normal atmosphere can be used; however, sintering carbon must also be used to prevent oxidation. The sintering temperature and duration determine the grain size of the part. The current research trend is to optimize the sintering temperature and duration.

The objective of this study it to determine the influence of nozzle temperature, infill density, and debinding heating rate on porosity.

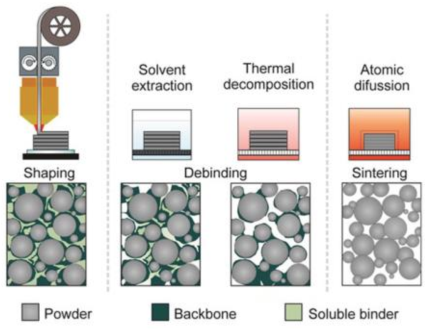

Figure 1. Printing, debinding, and sintering processes at the metallic powder level [19]

2. Materials and Methods

Stainless steel 316L filament was used with 11% PLA binder, with 1.75mm diameter [20]. A Creality Ender 3 S1 was used to produce 24 samples according to ASTM E8/E8M subsize dog bone tensile sample. Samples were printed with 10% oversize factor to compensate for shrinkage after debinding and sintering. Three levels for nozzle temperature were used, with two infill densities. 190 °C, 210 °C, and 230 °C are the three nozzle temperatures, which are the range of temperatures recommended by the manufacturer. Studies on FDM with infill densities higher than 100% are scarce. Therefore, to determine the effect of higher infill densities, infill density of 120% was selected to be compared with infill density 100%. Printing parameters used are shown in Table 1. Samples were then sintered for 4h at four different temperatures 1208 °C, 1232 °C, 1256 °C, and 1280 °C. Sintering temperature recommended by the manufactures to be 1232 °C and sintered for 4 hours. Table 2. shows the three variables used for the design of experiments.

The debinding process greatly affects the development of porosity. Thermal debinding was selected in this process due to the difficulties that are associated with the other types of debinding processes. After debinding, what remains is metallic powder that is loosely stuck together. Small parts are able to contain their shape after debinding, but larger parts will separate from their own mass. Each debinding process was conducted at a certain heating rate. The debinding process contains two temperatures, 204 °C and 427 °C. Six samples are placed flat in a crucible and covered with alumina oxide to contain their shape. From room temperature the furnace is heated to 204 °C at a certain rate then held for two hours. Then the furnace is heated to 427 °C at the same rate and held for two hours. After the samples are left to cool in the furnace naturally. The sintering process starts from room temperature to 593 °C at the highest possible heating rate of the furnace and is held for two hours. Then the furnace is heated to the selected sintering temperature over 2 hours and held for 4 hours. When the process is complete the samples are left enclosed in the furnace to cool down.

A heating rate of 1.85 °C/min for the debinding process of sintering temperature of 1232 °C. The heating rate was reduced to 1.49 °C/min for the sintering temperature of 1280 °C. Then further reduced to 1.19 °C/min for the sintering temperature 1256 °C. The last heating rate used was 1 °C/min for the sintering temperature of 1208 °C.

Table 1. Printing parameters used for the samples

Print Parameter	Value	Unit
Layer Height	0.2mm	mm
Print Speed	100	mm/s
Bed Temperature	65	°C
Nozzle Diameter	0.6	mm
Flow Rate Multiplier	1.2	
Infill Pattern	Aligned Rectilinear	
Built Orientation	flat	
Shrinkage Compensation	10	%

Table 2. Variables used in the design of experiments

Nozzle Temperature (°C)	Infill Density (%)	Sintering Temperature (°C)
190	100	1208
210	120	1232
230		1256
		1280

3. Results and Discussion

3.1. Printing

In printing samples with 100% infill density, no issues or difficulties were present. Except for the occasional nozzle blockage due to debinding in the nozzle. With samples of infill densities 120% various issues and difficulties were present. For samples printed at 190 °C nozzle temperature and 120% infill density, with infill lines being scraped off. Due to the overlap of infill lines from increasing the infill density, the nozzle scrapes off some of the infill lines. Nozzle offset adjustments were implemented to no improvement. In printing samples at 210 °C, two issues were present. The first is similar to the issue at 190 °C where the nozzle would scrape and remove parts of the infill line. The second is the generation of flakes from the filament and deposited on the print. The first issue is a result of increasing infill density which overlaps infill lines. Causing the print to be higher than where the printer thinks it should be. The second issue is due to filament build up on the outside of the nozzle from overlapping infill line. With prolonged contact on the nozzle, the built-up material experiences partial or full debinding. Which then breaks off as flakes on the print. Flakes were removed manually to prevent the development of defects. At 230 °C, similar flakes are developed on the surface, in an identical mechanism, however they increase in number and reduced in size. And contact between nozzle and print increased dramatically. Figure 2. shows a sample stopped mid print with 120% infill density and nozzle temperature of 210 °C.

Figure 2. Sample printed at 210 °C with 120% infill density, stopped mid print.

Printing samples with infill density of 150% was not possible, due to nozzle blockages. Due to the retention time in the nozzle, the filament would start to debind and block the nozzle. Attempts were made at the three nozzle temperatures with identical results. Changing to a larger diameter nozzle resulted in a successful print without blockages.

3.2. Sintering

Sintering at 1232 °C with heating rate of 1.85 °C /min, resulted in samples with a porosity range of 47-52%. This is mainly due to the heating rate during the debinding process. As samples sintered at 1280 °C with a heating rate of 1.49 °C /min resulted in the samples having a porosity range of 41-52%. The porosity is less due to the higher sintering temperature which results in higher elimination of pores. For samples sintered at 1256 °C with a heating rate of 1.19 °C /min, the porosity range is 24-38%. Finally, samples sintered at 1208 °C with a heating rate of 1 °C /min resulted with the lowest porosity range of 21-34%. Heating rate in the debinding process is a significant factor in affecting porosity, more than sintering temperature. In thermal debinding process, elevated temperatures cause the thermoplastic binder to evaporate. The heating rate affects the evaporation rate of the binder. At high heating rates the pressure generated is more than the strength of the filament, which causes the part to deform significantly. The degree of deformation is correlated to the heating rate. This mechanism explains the higher porosity range at higher sintering temperatures when the opposite should be observed.

At 100% infill density, porosity decreased with increasing nozzle temperature. Due to the lower viscosity of the filament and the release of air which lowers porosity. At 120% infill density the effect is reversed, increasing nozzle temperature increased porosity due to an increase in defects during printing.

Another effect of the heating rate is on the mechanical properties and surface quality after sintering. Samples with heating rate of 1.49 °C /min or above embrittled them. Two samples fractured while attempting to mount them in a vice grip, Figure 3. shows the cross section of one of the fractured samples. The samples also differ in the surface, which is assumed to be a result of chromium oxide. With deformation of the samples in the debinding process, the vacant volume of the binder is displaced with air. Which causes oxidation at the elevated sintering temperatures.

Pores of samples sintered at 1232 °C and 1280 °C, were interconnected. At sintering temperatures of 1208 °C and 1256 °C the presence of interconnected is vastly reduced. Which correlated interconnected pores with heating rate in the debinding process. Bulging and micro-cracks are formed which allow the formation of pores.

Figure 3. Cross sectional view of sample 21, printed at 230 °C with 120% infill density and sintered at 1232 °C with a heating rate of 1.19 °C /min.

4. Conclusion

Porosity of metal FDM on stainless steel 316L is greatly affected by the factors tested in the study. Nozzle temperature is inversely proportional to porosity, with a range of 1-9% decrease in porosity with increasing temperature. The effect of infill density requires further testing, as porosity values are not consistent at similar temperatures. At 120% infill density, the trend is reversed, increasing nozzle temperature increases porosity. Lastly, the most significant effect is due to the heating rate during the debinding process, which at high rates cased excessive porosity and embrittlement of samples.

Funding: This research received no external funding

Acknowledgments: The author is grateful to the support received from Matthew Drummond from University of Guelph, and the German University of Technology in Oman.

References

[1] A. Eltaggaz, J. Cloutier and I. Deiab, "Thermal Post-Processing of 4140 Alloy Steel Parts Fabricated by Selective," in *Canadian Society for Mechanical Engineering*, Charlottetown, PE, Canada, 2021.

[2] M. Drummond, A. Eltaggaz and I. Deiab, "3D printing of high melting iron alloys using metal-fused deposition modeling: a comprehensive review," *International Journal of Advanced Manufacturing Technology,* vol. 239, pp. 1-22, 2023.

[3] A. Jandyal, I. Chaturvedi, I. Wazir, A. Raina and M. Ifran UI Haq, "3D printing - A review of processes, materials and applications in industry 4.0," *Sustainable Operations and Computers,* vol. 3, pp. 33-42, 2022.

[4] K. I. Snapp, A. E. Gongora and K. Brown, "Increasing Throughput in Fused Deposition Modeling by Modulating Bed Temperature," *Journal of Manufacturing Science and Engineering,* vol. 143, no. 9, p. 094502, 2021.

[5] C. Tosto, J. Tirillo, F. Sarasini, C. Sergi and G. Cicala, "Fused Deposition Modeling Parameter Optimization for Cost-Effective Metal Part Printing," *Polymers,* vol. 14, no. 16, 2022.

[6] A. Sola and A. Trinchi, "Basic principles of fused deposition modeling," in *Fused Deposition Modeling of Composite Materials*, Elsevier, 2022, pp. 7-39.

[7] H. G. de la Torre, M. A. Perez and G. Gomez-Graz, "Tailored mechanical performance of fused filament fabricated 316L steel components through printing parameter optimization," *Theretical and Applied Fracture Mechanics,* 2023.

[8] C. Wang, W. Mai, Q. Shi, Z. Liu, Q. Pan and J. Peng, "Effect of printing parameters on mechanical properties and dimentional accuracy of 316L stainless steel fabricated by fused filament fabrication," *Journal of Materials Engineering and Performance,* 2023.

[9] M. Caminero, A. Gutierrez, J. Chacon, E. Garcia-Plaza and P. Nunez, "Effects of fused filament fabrication parameters on the manufacturing of 316L stainless-steel components:geometric and mechanical properties," *Rapid Prototyping Journal,* vol. 28, no. 10, pp. 2004-2026, 2022.

[10] E. Moritzer, C. L. Elsner and C. Schumacher, "Investigation of metal-polymer composites manufactured by fused deposition modeling with regard to process parameters," *Polymer Composites,* vol. 42, no. 11, pp. 6065-6079, 2021.

[11] J. Vetter, F. Huber, S. Wachter, C. Korner and M. Schmidt, "Development of a Material Extrusion Additive Manufacturing Process of 1.2083 steel comprising FFF Printing, Solvent and Thermal Debinding and Sintering," *Procedia CIRP,* vol. 113, pp. 341-346, 2022.

[12] S. Ding, B. Zou, P. Wang and H. Ding, "Effects of nozzle temperature and building orientation on mechanical properties and microstructure of PEEK and PEI printed by 3D-FDM," *Polymer Testing,* vol. 78, p. 10594, 2019.

[13] A. Pellegrini, M. E. Palmieri and M. G. Guerra, "Evaluation of anisotropic mechanical behaviour of 316L parts realized by metal fused filament fabrication using digital image correlation," *The International Journal of Advanced Manufacturing Technology,* pp. 7951-7956, 2022.

[14] Z. Lotfizarei, A. Mostafapour, A. Barari, A. Jalili and A. Patterson, "Overview of debinding methods for parts manufactured using powder material extrusion," *Additive Manufacturing,* vol. 61, 2023.

[15] G. CHang, X. Zhang, F. Ma, C. Zhang and L. Xu, "Printing, debinding and sintering of 15-5PH stainless steel components by fused deposition modeling additive manufacturing," *Additive Manufacturing of Alloys and Components,* vol. 16, no. 19, 2023.

[16] M. A. Wagner, J. Engel, A. Hadian, F. Clemens, M. Rodriguez-Arbaizar, E. Carreno-Morelli, J. M. Wheeler and R. Spolenak, "Filament extrusion-based additive manufacturing of 316L stainless steel: Effects of sintering conditions on the microstructure and mechanical properties," *Additive Manufacturing,* 2022.

[17] Y. Thompson, J. Gonzalez-Gutierre, C. Kukla and P. Felfer, "Fused filament fabrication, debinding and sintering as a low cost additive manufacturing method of 316L stainless steel," *Additive Manufacturing,* 2019.

[18] M. Hamidi, W. Harun, N. Khalil, S. Ghani and M. Azir, "Study of solvent debinding parameters for metal injection moulded 316L stainless steel," in *IOP Conference Series: Materials Science and Engineering*, 2017.

[19] S. Roshchupkin, A. Kolesov, A. Tarakhovskiy and I. Tishchenko, "A brief review of main ideas of metal fused filament fabrication," *Material Today: Proceedings,* vol. 38, no. 4, pp. 2063-2067, 2021.

[20] "The Virtual Foundry," 2015. [Online]. Available: https://thevirtualfoundry.com/. [Accessed 18 July 2023].

[21] J. Camargo, A. Machado, E. Almeida and E. Silva, "Mechanical properties of PLA-graphene filament for FDM 3D printing," *The International Journal of Advanced Manufacturing Technology,* vol. 103, pp. 2423-2433, 2019.

[22] J. Damon, S. Dietrich, S. Gorantla, U. Popp, B. Okolo and V. Schulze, "Process porosity and mechanical performance of fused filament fabricated 316L stainless steel," *Rapid Prototyping Journal,* pp. 1319-1327, 2019.

[23] M. A. Caminero, A. Romero, J. M. Chacon, P. J. Nunez, E. Garcia-Plaza and G. P. Rodrigues, "Additive manufacturing of 316L stainless-steel structures using fused filament fabrication technology: mechanical and geometric properties," *Rapid Prototyping Journal,* pp. 583-591, 2021.

[24] F. Wang, S. You, D. Jiang, X. Yuan, R. Fu and F. Ning, "Microstructure evolution, phase transformation, corrosion, and mechanical properties of stainless steel fabricated by extrusion-based sintering-assisted additive manufacturing," *Additive Manufacturing,* 2023.

[25] M. Sadaf, M. Bragaglia and F. Nanni, "A simple route for additive manufacturing of 316L stainless steel via Fused Filament Fabrication," *Journal of Manufacturing Processes,* pp. 141-150, 2021.

Optimizing Pediatric Dental Clinic Operations: A Simulation-Based Analysis.

Nagham Kheder[1], Roaa Kamal[1], Aliaa M. Abou-Ali[1], Belal M.Y. Gharaibeh[1,2,*]

[1]College of Engineering and Applied Sciences, American University of Kuwait, Salmiya, Kuwait

[2]Department of Industrial Engineering, The University of Jordan, Amman, Jordan

**Corresponding Author: Bgharaibeh@auk.edu.kw, Tel: +9651802040 Ext. 3718*

Abstract: This report details a systems and industrial engineering project aimed at optimizing operations in group of private pediatric dental clinics in Kuwait using Arena Simulation Software by Rockwell Automation. The project focuses on identifying inefficiencies and proposing strategic improvements to enhance operational efficiency for clinic of 5 pediatric dental clinics. Key activities include developing a detailed simulation model to reflect real-life patient waiting time, dental work time and costs of operations by collecting data on patient flow and operations and engaging with stakeholders through interviews to understand challenges and build the simulation model. Various enhancement scenarios were evaluated through simulations to determine the most effective strategies for implementation. Simulation results show that reducing the pediatric clinics from five to four clinic reduced the cost by (3%) while increasing the profit by 1.5% per patient per day with increase in patient service time by 19%. In addition, it would be advised to consider a scenario of four pediatric clinics with extended work time to serve one extra patient with a 3% increase in profit per day compared to the four clinics with no extra working hours.

Keywords: *dental clinic, simulation model, ARENA Simulation Software, pediatric dental clinic*

1. Introduction

Modern healthcare organizations are far more elaborate than they used to be, and identifying effective strategies for enhancing effectiveness while preserving the quality of care is that much more challenging. One highly promising strategy in addressing these issues is by employing simulation in computers. Simulation provides the opportunity to try various approaches, evaluate outcomes, and make relevant decisions without bearing any actual outcomes with healthcare professionals. Of them, Arena Simulation Software, created by Rockwell Automation, has been remarkable for its ease of use and capability to present complex healthcare contexts [1].

Simulation application in the healthcare process has the potential which has been proved already. Many comparable investigations from other countries have shown that it can decrease patient waiting times, optimize the use of staff and other assets, and streamline work. For instance, a study published in

Malaysia implemented Arena to enhance the output of the dental clinic through increasing staff productivity and reducing patient's waiting time [2]. There was another work conducted in Doha that aimed at identifying and minimizing the appointment system issues and ways to increase doctor availability that was an important factor enhancing patient satisfaction [3]. In Taiwan, simulations aided in the enhancement of scheduling in health screenings and even the flow of patients [4]. These case studies illustrate the application of Arena across the healthcare facilities. But it is not all black and white. In some areas, particularly the densely populated areas like Nigeria, simulations pose further challenges in terms of scalability [5]. Similarly, in the establishments where formal appointment systems are not the norm, such as the public hospitals in a country like Sri Lanka, new models have to be found to effectively manage the flow of patient traffic and limit long waiting lists [6]. These examples make us realize that despite the high potential, simulations should address the peculiarities of the healthcare system in each country. In this research, the spin-off application of Arena Simulation Software in dental clinics in terms of patient flow and resource utilization is examined. The aim is realistic and involves depicting now process, identifying deficiencies, and making recommendations that would bring a positive change in clinics and patient satisfaction. In this context, as the present study seeks to extend the current literature and address some of the specific issues relevant to healthcare simulation, the study's goal is to offer practice-relevant findings that may be useful in actual healthcare settings. In conclusion, simulations, especially via tools such as Arena, must present a great potential to improve the efficiency of healthcare systems. This study aims to add to that existing knowledge by demonstrating how simulations can produce real changes in routine healthcare settings.

2. Materials and Methods

The development of a particular section, such as the pediatric department, needed upgrades because the cost of comprehensive child attendance and equipment is relatively expensive. Some of the information they gathered included the clinic's calendar, doctor's timetable, as well as the patient turnover. We followed the old and the new patients using both the interarrival time and the time spent in the reception area, X-ray operations, pediatric clinics, and overall, time in the system. To highlight and facilitate the understanding of processes in the clinic's pediatric department, a flow chart was created. This flow chart provided the basis for the simulation: outlining all the entities (patients), stations (reception, X-ray, pediatric clinics), and decisions (e. g. whether an X-ray is needed for new patients). Several variables concerning the interarrival time and the flow of patients through various operating stations were created using Arena's input analyzer, which transformed the data into a format appropriate for simulation analysis. arena simulation software was used to model the patient traffic in the modelled place regarding the pediatric department. Old and a new patient entity was assumed for evaluating the flow between these two patient entities. Some of the upstream activities included key stations such as reception and X-ray, pediatric clinics and processes in the model. Doctors and nurses were allocated to these stations, with provided expressions developed for the clinic to correspond to the actual circumstances like doctors' timetable and accessibility. In Arena, the decision-making tool was employed in the allocation of the patients to the relevant pediatric clinic according to the doctor's schedule. The necessity of a delay mechanism remains when all doctors are busy to realistically mimic the patients' queue. Once the model was designed, then the patient flow through the system was analyzed. This enabled the system to determine the inflows and outflows of patients to the pediatric clinics and highlight the areas of congestion and delay. For example, the model showed that Clinic 1 was characterized by high levels of queues, which led to a deeper investigation of the issue.

3. Results and Discussion

In our Arena simulation, we developed three models to analyze the operational dynamics of the dental clinic. The basic model represented the actual operations of the clinic without any modifications, serving as the control scenario. The second model, the four clinics model, reduced the number of clinics from five to four by eliminating the least efficient clinic, which had low patient utilization. The third model, the extended hours model, built upon the four clinics model by adding extra working hours to one doctor's schedule. These two models were selected as the best options after testing multiple scenarios in Arena, as they demonstrated the most significant improvements in efficiency and patient flow compared to the basic model. The following Figures (1-3) show the output of Arena when running the three implemented models. Figure 4 shows the animation developed in Arena to visualize the flow of patients, resources, and processes within the system, making it easier for bottleneck identification.

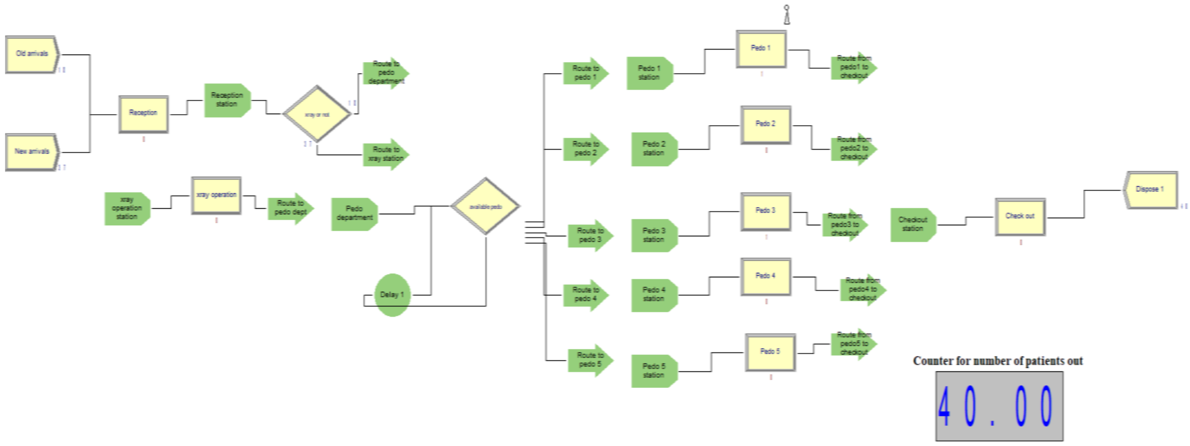

Figure 1: The complete design of the basic model system.

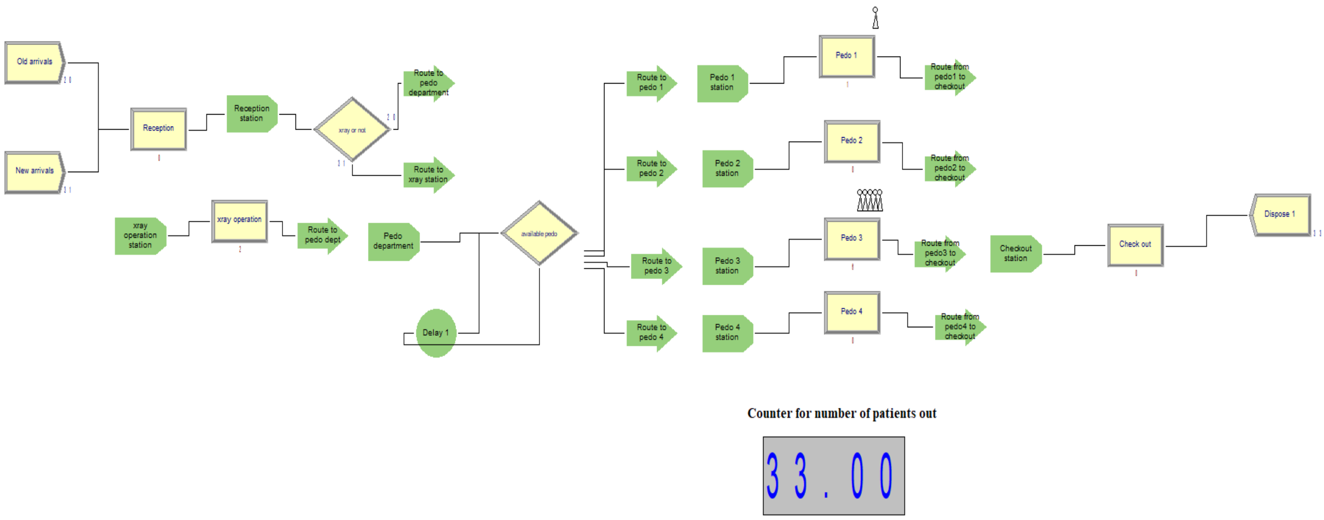

Figure 2: The design of four clinics model.

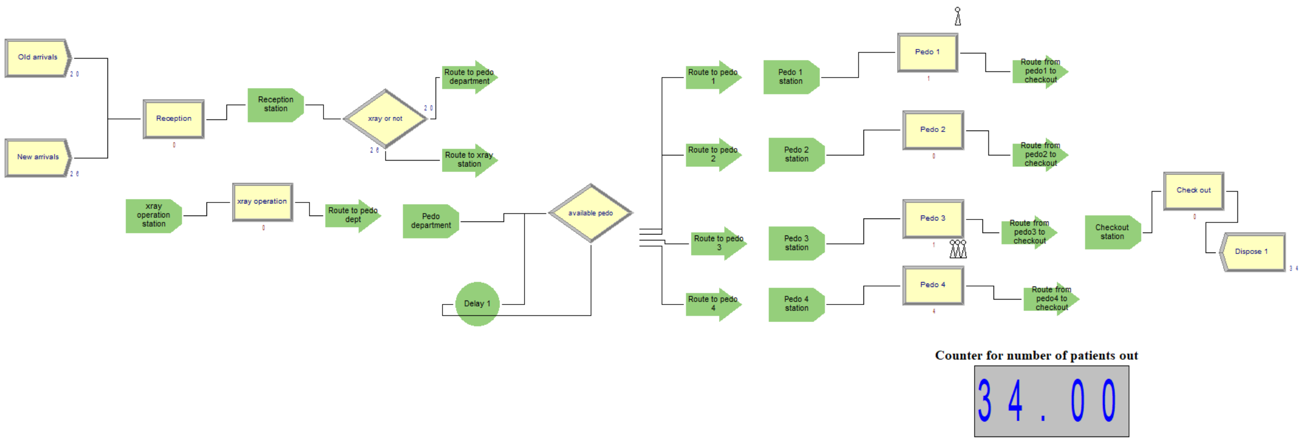

Figure 3: The design of the four clinics, extended hours model.

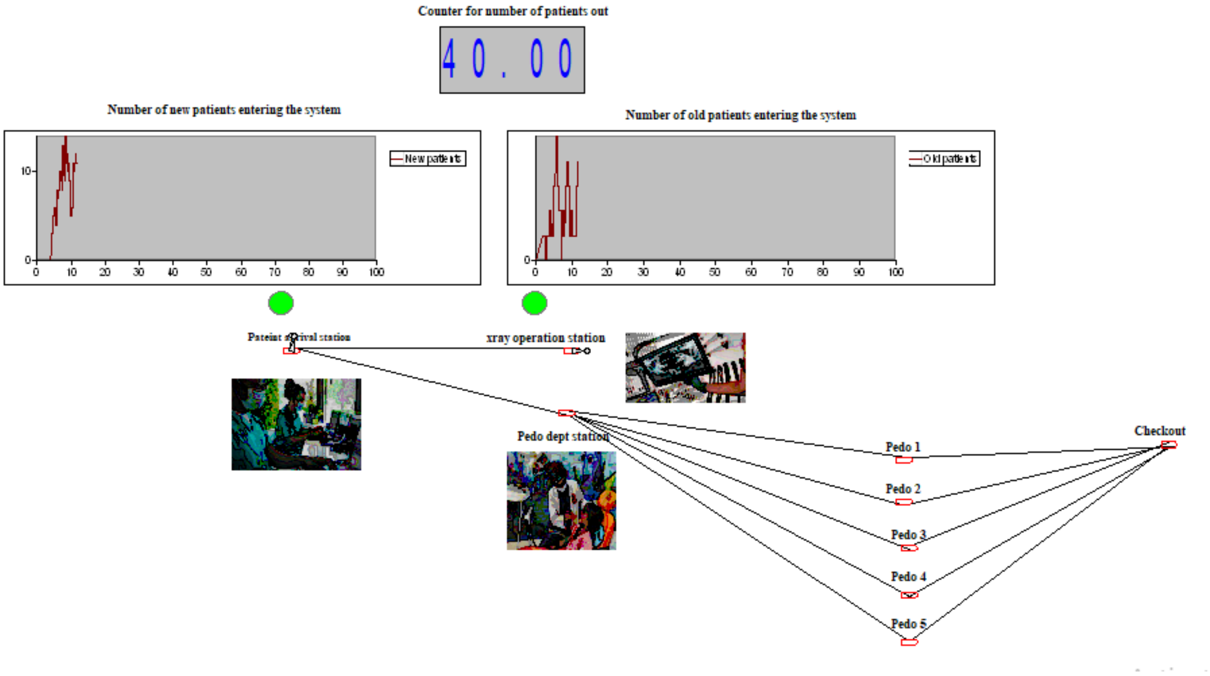

Figure 4: The animation developed in Arena.

After analyzing the outputs of the three models, we created a comparative table that integrated data gathered from staff and data extracted from Arena's Excel reports. This comparison enabled us to draw informed conclusions based on the combined insights. Tables (1-3) show the output of the three models.

Table 1: Output 1 of the three models

Model	Number of pediatric clinics	Cost/day	Cost/patient/day	Cost/patient/year
Basic model	5	750	18.75	5400
Four clinics model	4	600	18.18	5236.36
Four clinics, extended hours model	4 +overtime	618	18.176	5234.82

Table 2: Output 2 of the three models

Model	Total time/old patient/hr	Total time/new patient/hr	Average total time spent/patient in hours	Average total time/patient/min
Basic model	1.2	1.82	1.51	90.6
Four clinics model	1.46	2.15	1.805	108.3
Four clinics, extended hours model	1.45	2.23	1.84	110.4

Table 3: Output 3 of the three models

Model	Served patients	Revenue/ day	Revenue/ patient/day	Profit/ day	Profit/patient /day	Profit/patient/ year
Basic model	40	2250	56.25	1500	37.5	10800
Four clinics model	33	1856.25	56.25	1256.25	38.06818182	10963.63636
Four clinics, extended hours model	34	1912.5	56.25	1294.5	38.07352941	10965.17647

3.1. *Selecting the optimal model:*

The Four Clinics Model and the Extended Hours Model serve fewer patients compared to the Basic Model. However, both alternative models show a 3.04% reduction in cost per patient, indicating better cost efficiency. Revenue per patient remains consistent across all models, while profit per patient is 1.52% higher in the Four Clinics and Extended Hours Models. Although the Basic Model has the shortest patient total time spent in the system, it also has under-utilized resources. In contrast, the Four Clinics Model and Extended Hours Model show increased resource utilization, cost efficiency, and profitability. The Four Clinics Model is considered optimal, balancing cost reduction and customer satisfaction by avoiding excessive waiting times that could harm the clinic’s reputation since it shows a better utilization of resources. The Extended Hours Model, adding extra working hours to a doctor's schedule, maintains similar costs and profits to the Four Clinics Model, offering an effective alternative for managing an increased workload.

4. Conclusions

The project seeks to leverage simulation-based optimization techniques such as Arena to enhance the efficiency and effectiveness of dental clinics. Through a comprehensive analysis of patient flow dynamics and process bottlenecks, the project aims to identify areas for improvement and propose targeted interventions. By integrating data on patient entry and exit times, resource allocation and schedules, and data on total costs and profits, the project works to develop a simulation model capable of simulating clinic operations and assessing the impact of potential enhancements.

Acknowledgments:

the authors wish to acknowledge the American University of Kuwait for their support in providing the ARENA software license during the implementation of the project

References

[1] Borshchev, A.V. Imitation modeling. Theory and practice. Simulation Modeling: The State of the Region for 2015, Trends and Forecast. Moscow: IPURAN, 2015, 14–22.
[2] Fadilah, N.; Shahidan, W.N.W.; Sharif, N. Modeling and Simulation Analysis of Medical and Dental Clinic System Using Arena. Environ. Behav. Proc. J., 2023, 8(SI15), 171–178.
[3] Adedokun, A.; Idris, O.; Odujoko, T. Patients' Willingness to Utilize an SMS-Based Appointment Scheduling System at a Family Practice Unit in a Developing Country. Prim. Health Care Res. Dev., 2016, 17(2), 149-156. doi:10.1017/S1463423615000213.
[4] Chen, M.S.; Wu, K.C.; Tsai, Y.L.; et al. Data Analysis of Ambient Intelligence in a Healthcare Simulation System: A Pilot Study in High-End Health Screening Process Improvement. BMC Health Serv. Res., 2021, 21, 936.
[5] Isa, A.; Aliyu, A.; Abdullahi, A. Modeling and Simulation Analysis of Health Care Appointment System Using ARENA. Int. J. Sci. Adv. Inf. Technol., 2015, 1, 72.
[6] Algiriyage, N.; Sampath, R.; Pushpakumara, C.; Kaandorp, G.C.; Koole, G. Optimal Outpatient Appointment Scheduling. Health Care Manag. Sci., 2007, 10(3), 217-229.
[7] Williams, E.; Czech, M.; Witkowski, M. Simulation Improves Patient Flow and Productivity at a Dental Clinic. Proc. Winter Simul. Conf., 2007, 10, 25.
[8] Bapat, V.; Swets, N. The Arena Product Family: Enterprise Modeling Solutions. Proc. Winter Simul. Conf., 2000, 163-169.
[9] Mustafee, N. Applications of Simulation within the Healthcare Context. J. Oper. Res. Soc., 2011, 62(8), 1431-1451. doi:10.1057/jors.2010.20.
[10] Guseva, E.; et al. Discrete Event Modeling Arena Simulation Software. J. Phys. Conf. Ser., 2018, 1015, 032095.

GNSS/INS Navigation Solution for Autonomous Systems

Mohammed Bani Ateyeh [1], Bashar Zaid Alkilani[2] Odai Bani Hani [3]

[1] MARSROBOTICS, Mechatronics Engineer;
[2] MARSROBOTICS, Electronics Engineer;
[3] MARSROBOTICS, Aeronautical Engineer;

[1]*baniateyeh@marsrobotic.com , +962 798581196*
[2]*bkilani@marsrobotic.com, +962 786144364*
[3]*odai@marsrobotic.com, +962 788128981*

Abstract: In response to the rising demand for precise navigation across industries like autonomous vehicles, robotics, and unmanned aerial systems, the MARS Robotics team has developed a standard-precision solution integrating GNSS/INS technologies. Our system combines GNSS receivers with Inertial Navigation System (INS) technology, using advanced sensor fusion algorithms, including Kalman Filter, to achieve superior performance even in challenging environments. Rigorous testing has confirmed the system's reliability, offering Pitch and Roll accuracy of 0.5 degrees RMS, Yaw accuracy of 1 degree RMS static and 2 degrees RMS dynamic, and horizontal position accuracy of 2.6 meters RMS and velocity accuracy of 0.06 meters per second RMS. This places the solution in direct competition with industry leaders like XSENS and Inertial Sense. However, limitations in mitigating GNSS spoofing and jamming are addressed by an ongoing development of a Visual Navigation (VN) system to enhance performance in compromised environments.

Keywords: GNSS/INS; Spoofing; Jamming; Kalman Filter; Sensor Fusion

1. Introduction

During the last years, there has been an ever-growing demand for the development and implementation of standard precision navigation systems in many fields of interest, such as autonomous road vehicles, robotics, and UAS. Indeed, these applications require very accurate and reliable navigation, especially in environments where safety and performance are critical. Traditional navigation systems that depend on GNSS data, however, can suffer degraded signals or even a complete loss of signal in tough conditions like urban canyons, tunnels, or heavy foliage. It is these disadvantages that have made the development of hybrid systems using the integration of GNSS and INS increase to enhance accuracy and robustness. [1] [2]

This combination works best because GNSS provides stable positioning over long periods and INS generates high-frequency updates with high short-term accuracy. In case of a possible GNSS signal outage, INS may help bridge this. Sensor fusion algorithms like KF have already seen wide applications in data fusion for these two systems, hence the strength of each system can complement the weakness of another system, improving performance in navigation. This approach is especially critical in autonomous vehicles, where even minor navigation errors can pose significant safety risks. [1].

Yet, with these advantages, a variety of challenges remain in integrating GNSS/INS systems: highly susceptible to interference like jamming and spoofing, factors that undermine system reliability, and INS has drift over time, which could further degrade the accuracy when GNSS signals have not been available for considerable periods. Ongoing research aims at improving sensor fusion techniques, alternative navigation methods such as VN-methods, anti-spoofing, and anti-jamming technologies to address these issues. [3]

This paper introduces GNSS/INS navigation solution developed by the MARS Robotics team, specifically designed for autonomous systems. The system employs a Kalman Filter-based sensor fusion algorithm to integrate GNSS and INS data, with the primary goal of analyzing system performance under various conditions, identifying current limitations, and proposing future enhancements to address emerging challenges such as GNSS spoofing and jamming.

2. Materials and Methods

2.1. System Components and Architecture

The navigation solution integrates a dual-frequency Global Navigation Satellite System (GNSS) receiver with an Inertial Navigation System (INS) to deliver standard-precision positioning for autonomous systems. The core components include:

1. **GNSS Receiver**: A GNSS receiver provides location, time, speed, altitude, and global navigation by receiving signals from satellites.

2. **IMU Module**: A 9-axis MEMS-based Inertial Measurement Unit (IMU) containing a tri-axis accelerometer, gyroscope, and magnetometer, was used to capture motion data.

3. **Processing Unit**: A custom onboard processor equipped with the sensor fusion algorithm was responsible for fusing GNSS and INS data.

2.2 GNSS and INS Overview

1. Global Navigation Satellite System (GNSS)

Global Navigation Satellite System (GNSS) refers to satellite constellations that provide precise geolocation and time information to receivers on Earth. While the most widely known GNSS is the Global Positioning System (GPS), operated by the United States, several other systems exist, including Galileo (Europe), GLONASS (Russia), and BeiDou (China). GNSS receivers calculate their position by measuring the time it takes for signals to travel from multiple satellites.

Limitations of GNSS: Despite its advantages, GNSS is susceptible to several limitations. Signal blockages due to physical obstructions like buildings, trees, or tunnels can reduce signal quality, particularly in urban environments, a phenomenon known as the "urban canyon" effect. Standard GNSS receivers also have relatively low update rates (typically between 1 Hz to 10 Hz), which may not be suitable for high-speed applications. Additionally, GNSS signals can experience latency or jitter due to processing delays or challenges in satellite signal acquisition.

2. Inertial Navigation System (INS)

Inertial Navigation System (INS) is a navigation system used to estimate the position, velocity, and orientation (attitude) of an object by measuring its acceleration and angular velocity. INS relies on accelerometers to detect linear acceleration and gyroscopes to measure rotational rates. These sensors are integrated into an Inertial Measurement Unit (IMU).

Operational Mechanism of INS: INS operates using the principle of dead reckoning, where the system calculates the current position by integrating the measured accelerations and angular rates over time from an initial known position and orientation. IMUs, which house the accelerometers and gyroscopes, function at high sampling rates, sometimes in the range of hundreds or thousands of Hertz, providing frequent updates on motion and orientation. This makes INS particularly well-suited for applications requiring high-speed dynamics and real-time response.

Limitations of INS: However, INS has some inherent limitations. Over time, INS suffers from drift due to sensor biases, noise, and small errors that accumulate, leading to increasing inaccuracies in position and velocity estimates if left uncorrected. This drift can become significant, particularly in long-term navigation. Moreover, the accuracy of INS heavily depends on the calibration of its sensors. Even minor errors in the calibration of accelerometers and gyroscopes can lead to considerable drift, affecting the overall precision of the system over time.

2.3 Kalman Filter (KF)

The **Kalman filter** is a recursive algorithm designed to estimate the state of a dynamic system from a series of noisy measurements. It is particularly well-suited for **sensor fusion** tasks, such as combining GNSS and INS data, because it continuously updates the system's state using both predictions from a model (INS) and new observations (GNSS), while accounting for uncertainties in both.

The Kalman filter operates through two main phases: the prediction step and the update step.

Prediction Step: In this phase, the filter uses the dynamic model (in this case, the INS data) to predict the system's next state and estimate the uncertainty of this prediction. The INS, which provides high-frequency data such as accelerations and angular velocities, allows for a continuous estimate of the system's state (e.g., position, velocity, and attitude) over time. However, due to sensor noise and drift, these predictions can become inaccurate over long periods, necessitating the need for correction.

Update Step: During the update step, the filter incorporates new measurements, such as GNSS data, to correct the predicted state. The GNSS provides more accurate, though less frequent, position and velocity updates. The Kalman filter compares these new observations with the predicted state, calculates the residual (the difference between the predicted and observed state), and adjusts the estimate accordingly. This step also updates the estimate of uncertainty, improving the system's accuracy.

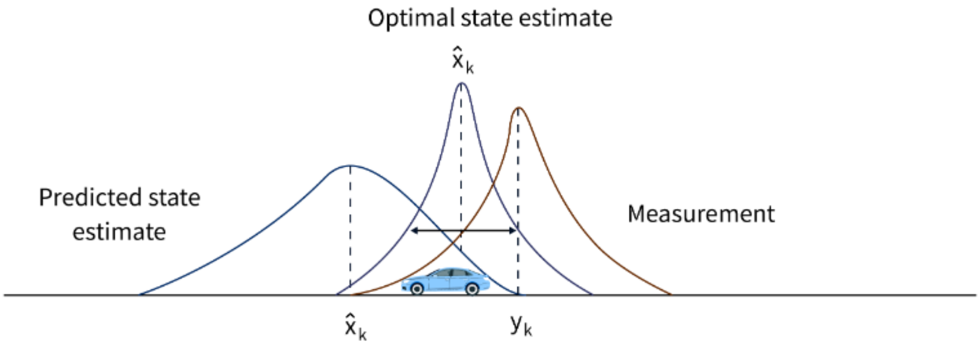

Figure 1 Kalman Filtering

In the context of GNSS/INS integration, the Kalman filter plays a key role in addressing the inherent weaknesses of each system. GNSS measurements are used to correct the drift in the INS estimates, while the high-frequency INS data fills in the gaps between GNSS updates and provides continuous estimates during GNSS outages.

State Estimation for GNSS/INS

In a GNSS/INS Kalman filter, the system's state vector includes:

$$\boldsymbol{x_k} = [\boldsymbol{p_x}\,\boldsymbol{p_y}\,\boldsymbol{p_z}\,\boldsymbol{v_n}\,\boldsymbol{v_e}\,\boldsymbol{v_d}\ \emptyset\,\boldsymbol{\theta}\,\boldsymbol{\varphi}], \tag{1}$$

Where:

- $\boldsymbol{p_x}\,\boldsymbol{p_y}\,\boldsymbol{p_z}$: Position in 3D space,
- $\boldsymbol{v_n}\,\boldsymbol{v_e}\,\boldsymbol{v}_{\mathrm{d}}$: Velocity components (North, East, Down),
- $\emptyset\ \boldsymbol{\theta}\ \boldsymbol{\varphi}$: Orientation (roll, pitch, yaw)

The state vector reflects both the physical state of the system (position, velocity, and orientation), which the Kalman filter will estimate and correct over time.

Prediction Step: INS-Based Prediction

The prediction step of the Kalman filter uses the high-rate data from the INS to estimate the next state of the system. Since INS operates at a high frequency, it can provide continuous position and velocity updates based on acceleration and angular velocity data, even during GNSS outages.

The predicted state is computed as:

$$\boldsymbol{x_{k+1|k}} = \boldsymbol{F_k}\boldsymbol{x_k} + \boldsymbol{B_k}\boldsymbol{u_k}, \tag{2}$$

Where:

- $\boldsymbol{F_k}$ is the state transition matrix that models the system's motion,
- $\boldsymbol{B_k}\boldsymbol{u_k}$ accounts for the control inputs (accelerations and angular velocities measured by the INS),

In this step, the covariance matrix $\boldsymbol{P_{k+1|k}}$ is also updated to reflect the increase in uncertainty in the predicted state due to errors in the INS sensors and their drift over time:

$$\boldsymbol{P_{k+1|k}} = \boldsymbol{F_k}\boldsymbol{P_k}\boldsymbol{F^T}_{\boldsymbol{k}} + \boldsymbol{Q_k}, \tag{3}$$

Here, $\boldsymbol{Q_k}$ is the process noise covariance matrix that captures the uncertainty in the system's dynamics and sensor measurements.

Update Step: GNSS-Based Correction

When GNSS measurements are available, they are used to correct the INS-based prediction. GNSS provides accurate, drift-free position data, but it typically updates at a much lower frequency compared to INS, and is prone to outages in obstructed environments. The Kalman filter uses these GNSS measurements to correct the INS drift.

First, the innovation (or measurement residual) is computed, which represents the difference between the predicted position (from INS) and the actual position (from GNSS):

$$\boldsymbol{y_k} = \boldsymbol{z_k} - \boldsymbol{H_k}\boldsymbol{x_{k+1|k}} \tag{4}$$

Where:

- z_k is the GNSS measurement (position or velocity),
- H_k is the measurement matrix that relates the system state to the measurement,
- $x_{k+1|k}$ is the predicted state from the INS.

The **Kalman gain** K_k is then calculated to determine how much weight should be given to the GNSS measurement relative to the INS prediction:

$$K_k = P_{k+1|k} {H^T}_k (H_k P_{k+1|k} {H^T}_k + R_k)^{-1} \tag{5}$$

Where R_k is the measurement noise covariance, representing the uncertainty in the GNSS measurements.

Finally, the Kalman filter updates the state estimate by combining the INS prediction with the GNSS correction, weighted by the Kalman gain:

$$x_{k+1} = x_{k+1|k} + K_k y_k \tag{6}$$

The covariance matrix is updated to reflect the reduced uncertainty after incorporating the GNSS data:

$$P_{k+1} = (I - K_k H_k) P_{k+1|k} \tag{7}$$

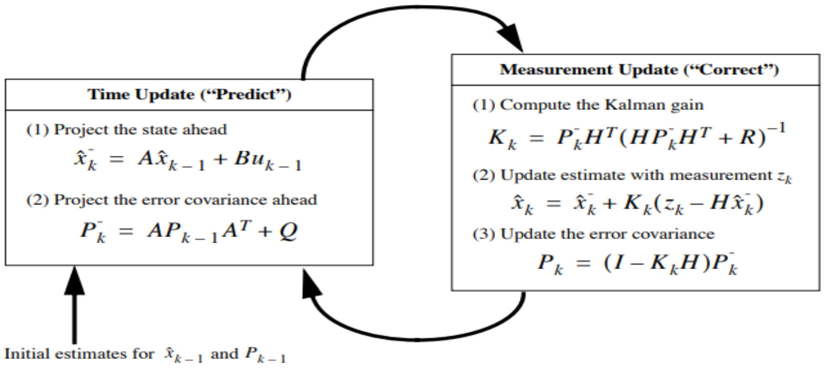

Figure 1 A complete picture of the operation of the Kalman filter [4]

3. Results and Discussion

In this section, we present the results of the flight test conducted to evaluate the performance of the GNSS/INS integration using the Kalman filter, compared to **Xsens** inertial navigation system. The comparison focuses on key performance metrics such as position accuracy, attitude, and velocity.

- **Attitude**

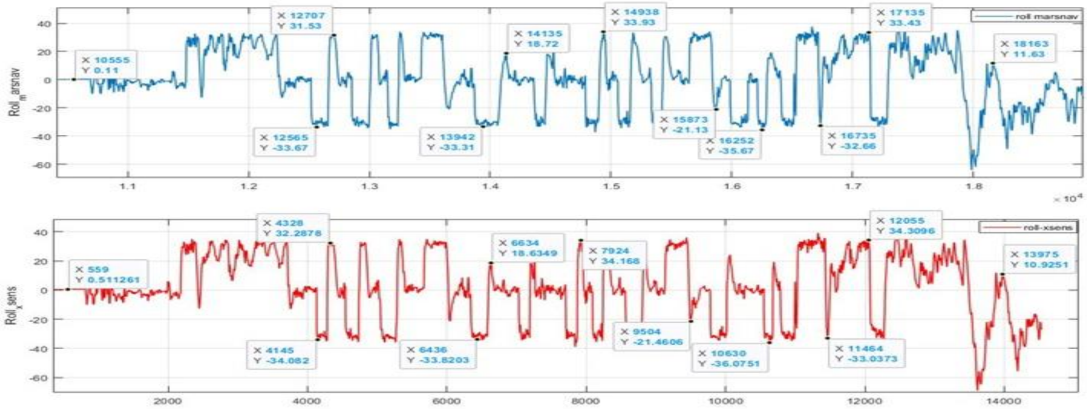

Figure 2 Roll (Marsnav vs Xsens)

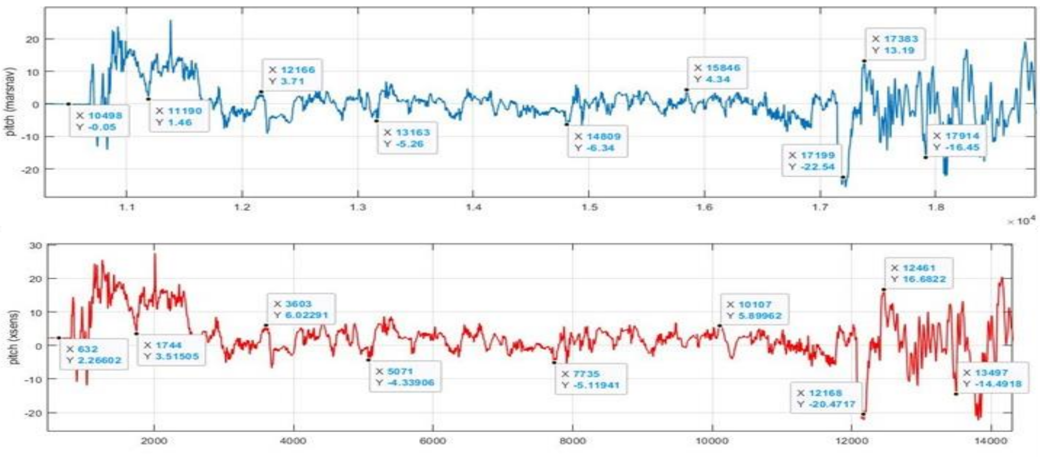

Figure 3 Pitch (Marsnav vs Xsens)

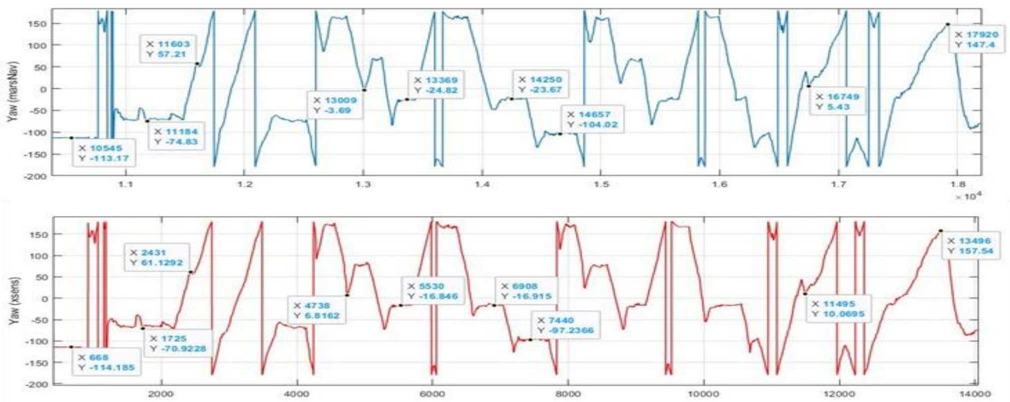

Figure 4 Yaw (Marsnav vs Xsens)

The system shows high accuracy in roll, pitch, and yaw measurements, based on the figures showed above. The GNSS/INS system showed consistency across different conditions, providing reliability for autonomous operations. However, slight discrepancies in yaw performance under dynamic conditions (compared to Xsens) may indicate areas for future optimization.

- **Velocity**

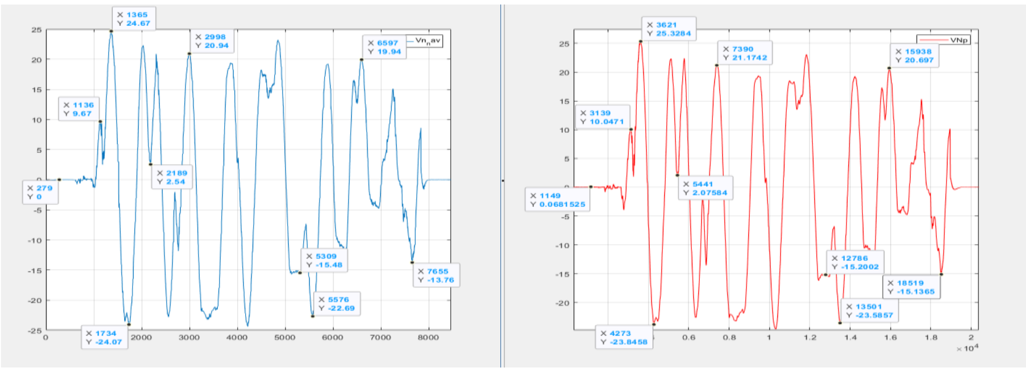

Figure 5 Vn (Marsnav vs Xsens)

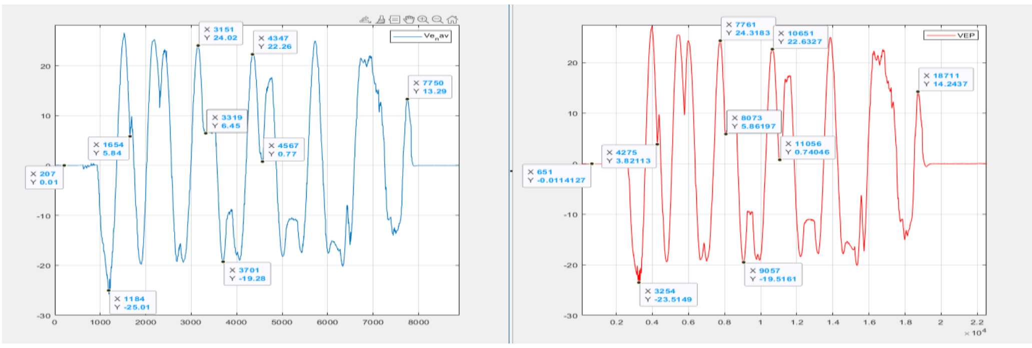

Figure 6 Ve (Marsnav vs Xsens)

The GNSS/INS system shows high precision in velocity measurements. Figures 5 and 6 indicate minimal deviation in North and East velocity components when compared to Xsens. This shows the system's suitability for high-speed dynamic applications.

- **Position**

Position is driven from Google Maps as a travelling path and compared with Xsens, the position difference between different measurements at different timestamps:

Measurment	Position Difference
1	1.79m
2	1.92m
3	3.02m
4	2.51m
5	3.08m
6	3.2m
7	3.26m
8	1.43m

Table 1 Position Data

The position accuracy showed an RMS value of 2.6151 meters across multiple tests, with individual position differences ranging from 1.43 meters to 3.26 meters. While this is comparable to Xsens, it highlights the inherent limitations of GNSS-based systems, especially in environments prone to signal interference or degradation, such as urban canyons.

While the performance of the GNSS/INS integration has shown promising results in most environments, it is important to realize limitations of GNSS-based systems, especially in terms of **jamming** and **spoofing**.

- **Jamming**: GNSS signals can be disrupted by jamming, which occurs when strong, unintentional or malicious signals interfere with the receiver's ability to process satellite signals.

- **Spoofing**: Another critical issue is spoofing, where fake GNSS signals are used to manipulate the receiver into computing incorrect position and time data.

Given these challenges, **Visual Navigation (VN)** has emerged as a promising solution. VN uses cameras and image processing algorithms to interpret the surrounding environment, providing accurate navigation data independently of GNSS signals. When integrated with GNSS/INS, Visual Navigation offers an additional layer of resilience, enabling the system to maintain accurate positioning even in GNSS-denied environments. Although this paper focuses on GNSS/INS integration, future work will explore how Visual Navigation can enhance overall system robustness in the face of jamming and spoofing threats.

4. Conclusions

The GNSS/INS Kalman filter system presented in this paper offers a solution to the problem of autonomous navigation, with competitive results compared to such leading solutions from industry leaders like Xsens. However, challenges on GNSS jamming and spoofing raise the necessity for integration of alternative systems like VN to ensure system resilience in compromised environments.

Funding: This research received no external funding

Acknowledgments: I would like to express my gratitude to Eng. Ahmad Shaqqor and Eng. Aws Radi for their invaluable contributions to the results of this research. Their expertise and dedication were crucial to the successful completion of this work.

References

1. Alaba, S. Y., 2024. GPS-IMU sensor fusion for reliable autonomous vehicle position estimation. arXiv. Available at: https://arxiv.org/pdf/2405.08119 [Accessed 11 Sept. 2024].

2. Woo R, Yang E-J, Seo D-W. A Fuzzy-Innovation-Based Adaptive Kalman Filter for Enhanced Vehicle Positioning in Dense Urban Environments. *Sensors*. 2019; 19(5):1142. https://doi.org/10.3390/s19051142 [Accessed 11 Sept. 2024].

3. **Bi, S., Li, K., Hu, S., Ni, W., Wang, C. and Wang, X., 2024.** Detection and mitigation of position spoofing attacks on cooperative UAV swarm formations. *IEEE Transactions on Information Forensics and Security*, 19, pp.1883-1895. Available at: https://ieeexplore.ieee.org/abstract/document/9419417/metrics#citations. [Accessed 11 Sept. 2024]

4. Welch, G. and Bishop, G., 2006. An Introduction to the Kalman Filter. TR 95-041, University of North Carolina at Chapel Hill, Department of Computer Science. Available at: http://www.cs.unc.edu/~welch/kalman/. [Accessed 12 Sept. 2024].

Numerical Analysis of the effect of Upstream Obstacles on Aerodynamic Performance of NACA 65-421 Airfoil Using k-epsilon Model

Omar Badran[1,5] Zeeshan Azad[2] Muhammad Virk[3] Saad Ragab[4] Ismail Masalha[5]

[1,2,3] Arctic Technology & Icing Research Group (arcICE), UiT- The Arctic University of Norway

[4] College of Engineering /Department of Biomedical Engineering and Mechanics, Virginia Tech, USA

[5] Al-Balqa Applied University, Faculty of Engineering Technology, Amman – Jordan

Corresponding Email*: omar_badran@bau.edu.jo*

Abstract

This study presents a computational analysis of the aerodynamic performance of the NACA 65-421 airfoil in the presence of upstream obstacles, focusing on flow behavior and both lift and drag characteristics. The simulations were performed using ANSYS Fluent with the RNG k-ε turbulence model to capture the complex flow interactions and disturbances caused by obstacles. The analysis includes detailed evaluations of velocity magnitude contours and vectors, pressure distribution, velocity profiles, and lift and drag forces at key points on the airfoil, including the leading edge, trailing edge, and wake regions.

Despite the presence of upstream obstacles, which introduce flow disturbances, the airfoil maintained efficient aerodynamic performance. The velocity profiles at the leading edge reveal strong flow acceleration, generating significant lift, while the trailing edge and wake regions show moderate turbulence with quick velocity recovery, minimizing drag. The static pressure contours further validate the aerodynamic efficiency, with a high-pressure stagnation point at the leading edge and smooth pressure recovery towards the trailing edge. Overall, the study confirms the NACA 65-421 airfoil's robustness in maintaining low drag and steady lift, even under disturbed flow conditions, making it suitable for applications in environments with flow obstacles, such as urban wind energy systems or low-altitude flight. The results demonstrate a consistent lift coefficient of approximately 0.36 and a stable drag coefficient of around 0.006, both showing excellent agreement between experimental and numerical data. Also, it was found that the non-uniform inflow can cause localized fluctuations in pressure, particularly at the leading and trailing edges, which can affect the overall lift and drag.

Keywords: NACA 65-421, Airfoil, Obstacles, Aerodynamics, RNG k-ε, CFD

1 Introduction

1.1 Background and Motivation

The study of airfoil aerodynamics is fundamental to the design of efficient aerospace systems, including aircraft wings, turbine blades, and other aerodynamic structures. Understanding how an airfoil interacts with turbulent flows is critical for optimizing lift, reducing drag, and improving overall performance. The NACA 65-421 airfoil, a popular choice for various aerodynamic applications, was selected for this study to assess its performance under induced turbulent flow at a velocity of 21.91 m/s.

The k-ε turbulence model, specifically its RNG variant, was chosen for this investigation due to its ability to simulate high Reynolds number flows with significant turbulence and separation. This study aims to provide a detailed analysis of the flow characteristics around the airfoils, such as pressure distribution and aerodynamic forces acting on the airfoil, with a particular focus on the effects of upstream obstacles. The results are intended to enhance future aerodynamic designs and highlight the importance of selecting appropriate turbulence models for accurate Computational Fluid Dynamics (CFD) simulations.

1.2 Objective

The objective of this study is to analyze the effect of cubical obstacles placed in front of a NACA 65-421 airfoil on its aerodynamic performance. Using computational fluid dynamics simulations to assess how the presence of obstacles alters flow patterns, pressure coefficients, and drag and lift forces.

2 Literature Review

2.1 NACA Airfoil Aerodynamics

The NACA (National Advisory Committee for Aeronautics) airfoil series remains one of the most studied airfoil configurations due to its application in various fields, from aircraft wings to wind turbines. The NACA 65-series, to which the NACA 65-421 airfoil belongs, is part of the laminar flow airfoil family, designed for reduced drag at moderate Reynolds numbers. The NACA 65-series is particularly advantageous for low-drag applications, with the 65-421 airfoil having a relatively thick profile, making it efficient at producing lift while maintaining low drag.

Abbott and von Doenhoff (1959) are frequently cited for their foundational work on NACA airfoils, providing performance charts and defining the aerodynamic characteristics of various NACA airfoils under different flow conditions. They detail the behavior of both laminar and turbulent boundary layers, which is crucial in understanding the drag and lift performance across different Reynolds numbers. However, their work focuses on clean airfoils without the influence of external obstacles, making it a starting point for understanding airfoil behavior but insufficient for predicting obstacle interaction [1].

Several recent studies have explored various aspects of airfoil performance. Bhushan et al. [1] conducted a study analyzing the performance of wind turbine blades using Computational Fluid Dynamics (CFD) at various angles of attack and Reynolds numbers. Their findings revealed that the performance of the blades is significantly affected by both the angle of attack and Reynolds number, providing valuable insights into optimizing blade designs for better efficiency under varying wind conditions. Nazmul et al. [2] carried out an experimental investigation on the NACA 4412 airfoil with a curved leading edge to assess its aerodynamic characteristics. The study demonstrated that the curved leading edge enhances aerodynamic performance by increasing lift and reducing drag compared to airfoils with a straight leading edge, thus improving the overall efficiency in practical applications. Jin et al. [3] focused on numerical simulations of the aerodynamic performance of two-dimensional wind turbine airfoils. Their research highlighted how performance varies with different airfoil designs and flow conditions, indicating that optimizing the airfoil shape can lead to enhanced wind energy capture and overall efficiency.

2.2 Obstacles in Aerodynamic Environments

Obstacles in aerodynamic environments are known to cause flow disturbances, including wake formation, vortex shedding, and boundary layer separation, all of which significantly affect the performance of aerodynamic surfaces. Also, the obstacles represent the turbulent flow of the wind due to different topologies (mountains and trees) and wind currents changing directions. Therefore, studies on obstacle-airfoil interaction are critical for understanding flow in real-world scenarios, such as urban wind turbines, low-altitude flight, and rotorcraft operations, where buildings, towers, or other structures can alter the airflow around an airfoil [2].

2.3 Flow Separation and Boundary Layer Behavior

One of the most significant effects of obstacles near an airfoil is the early onset of flow separation, which reduces lift and increases drag. Flow separation occurs when the boundary layer, which adheres to the surface of the airfoil, is disrupted, typically by adverse pressure gradients or turbulences in the flow path. When separation occurs, a region of low pressure (wake) forms behind the airfoil, significantly increasing drag.

Roshko (1954) provided seminal work on vortex shedding and its relationship to drag, noting that objects in the flow path of a surface induce unsteady vortices, which lead to fluctuating pressure fields and increased drag. This phenomenon is particularly relevant when considering the placement of obstacles near airfoils, as these obstacles increase the likelihood of vortex shedding and separation. The simulation results from this study confirm these findings, showing increased turbulence and separation zones when obstacles are present near the NACA 65-421 airfoil[3].

Simpson (1989) explored boundary layer separation and the conditions under which it occurs, emphasizing the role of external disturbances, such as obstacles, in causing early separation. His findings indicated that boundary layer separation is sensitive to both the location of the disturbance and the Reynolds number of the flow. For the NACA 65-421 airfoil in this study, the presence of cubic obstacles causes early separation, which is consistent with Simpson’s observations[4].

2.4 Computational Fluid Dynamics (CFD) in Airfoil Studies

Computational Fluid Dynamics (CFD) has become a critical tool for studying aerodynamic performance, especially in scenarios where experimental testing is difficult or expensive. CFD allows for detailed analysis of flow fields, pressure distributions, and turbulence characteristics around airfoils and bluff bodies.

Versteeg and Malalasekera (2007) provide a comprehensive introduction to the use of CFD for fluid mechanics simulations, including airfoil studies. They highlight the importance of mesh quality and turbulence modeling in achieving accurate results. In the current study, the RNG k-epsilon turbulence model was used due to its ability to handle complex flow phenomena like separation and recirculation, which are common in obstacle-airfoil interactions[5].

Spalart and Allmaras (1992) developed a turbulence model that has been widely used in aerodynamic simulations. While not employed in this study, the Spalart-Allmaras model is often compared to the k-ε models, which were used here to simulate the effects of turbulence in the presence of obstacles. The k-ε model's strength lies in its ability to capture the large-scale eddies and vortices caused by obstacle interference, making it suitable for this application[6].

Juliana et al. [7] worked on the design and analysis of the NACA 4420 wind turbine airfoil using CFD. Their study indicated that optimizing the airfoil design results in increased wind turbine efficiency, with the CFD analysis offering detailed insights into aerodynamic characteristics and performance improvements. Rao et al. [8] explored various modeling and simulation techniques for airfoil elements. Their study revealed that advanced computational models enhance the accuracy of performance predictions, providing better tools for analyzing and optimizing airfoil designs to achieve improved performance.

The present innovation showed that obstacles near airfoils cause significant changes in flow behavior, including increased turbulence, flow separation, and vortex shedding. These effects lead to reduced lift and increased drag, confirming the need for thorough analysis in situations where airfoils interact with external obstacles. While many studies have focused on clean flow environments, this study contributes to the limited body of knowledge on obstacle-airfoil interaction by using CFD to investigate the NACA 65-421 airfoil, providing valuable insights for both academic and practical applications.

3 Methodology

3.1 Geometry and Mesh

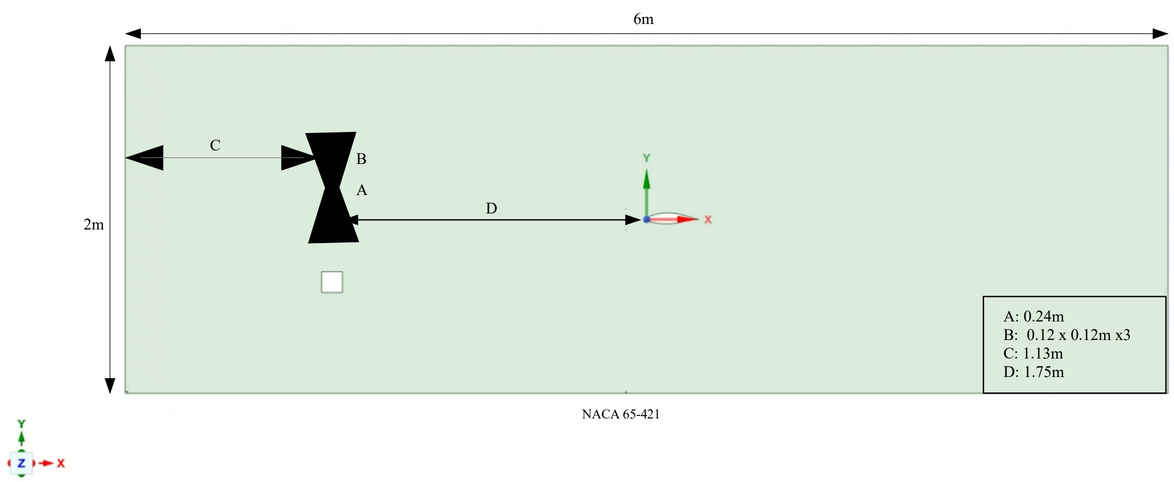

Figure 1. Overall computational domain.

The geometry shown in Figure 1 is for the CFD simulation designed to analyze the aerodynamic performance of the NACA 65-421 airfoil with upstream obstacles. The setup includes a computational domain with specific dimensions and the placement of square obstacles to investigate their effect on the airflow around the airfoil. The domain dimensions were set to ensure that boundary effects were minimized, and flow behavior could be accurately simulated. From Figure 1 the computational domain for the simulation is 6 meters in length and 2 meters in width, ensuring accurate capture of airflow around the NACA 65-421 airfoil and upstream obstacles. The domain size allows the flow to develop correctly before reaching the airfoil and obstacles, minimizing boundary effects. Three square obstacles, each measuring 0.12 meters, are placed 1.13 meters from the left edge of the domain, with 0.240 meters vertical spacing between them. The airfoil, strategically positioned downstream of the obstacles, allows for a thorough analysis of how disturbed flow affects its aerodynamic performance. The placement and configuration of both the obstacles and airfoil are designed to replicate real-world conditions and provide accurate insights into the airfoil's behavior under the influence of environmental disturbances.

3.2 System Information

The simulations were conducted using Ansys Fluent 23.1, employing a 2D, double-precision, pressure-based solver in transient mode. The k-ε turbulence model was selected due to its widespread use in modeling turbulent flows in aerodynamic applications. The simulation was configured to run for 1000-time steps with a time step size of 0.001 seconds, and a maximum of 20 iterations per time step to ensure numerical stability and convergence.

3.3 Computational Domain and Mesh

The computational domain was designed to capture the flow characteristics around the NACA 65-421 airfoil and upstream square obstacles. From Figure 2 the computational domain consisted of a structured quadrilateral mesh with 321,985 cells, 645,540 faces, and 323,552 nodes. The mesh was highly refined around the airfoil and the obstacles to capture flow separation, boundary layer behavior, and vortex formation. The minimum orthogonal quality of the mesh was 0.404, while the maximum aspect ratio was 382.81, indicating regions with stretched cells that may impact numerical accuracy in high-gradient areas.

The boundary conditions were defined to simulate an inlet velocity of 21 m/s, with a turbulence intensity of 5%, representing real-world turbulent flow conditions. The outlet was set to a pressure-outlet condition, ensuring a smooth transition of flow out of the domain.

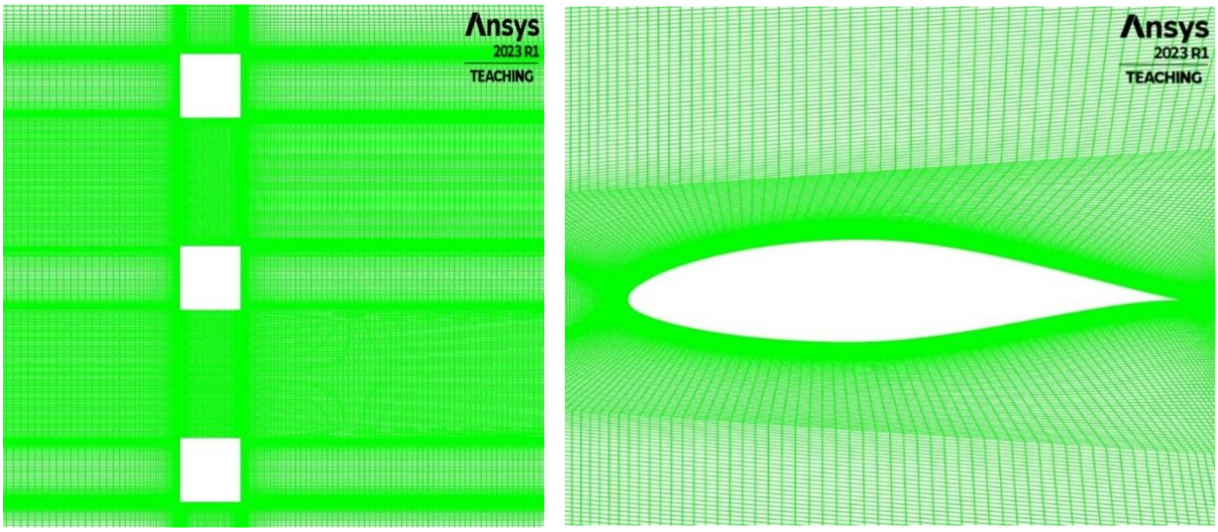

Figure 2. Meshes around the square blocks and the airfoil

4 Simulation Setup

4.1 Physics

The simulation was carried out in a 2D domain, with a transient approach to capture the time-dependent behavior of the flow. A 1st-order implicit time integration scheme was utilized to ensure computational efficiency while maintaining the required accuracy for the simulation. For turbulence modeling, the RNG k-ε turbulence model was selected. This model is widely used in computational fluid dynamics (CFD) due to its ability to accurately capture the behavior of turbulent flows, including flow separation and recirculation, which are critical in obstacleladen scenarios. Standard wall functions were implemented to handle the boundary layer near the walls, providing a practical approach for near-wall turbulence treatment. In terms of material properties, the fluid used in the simulation was air, with a density of 1.225 kg/m^3, specific heat (Cp) of 1006.43 J/kg·K, thermal conductivity of 0.0242 W/m·K, and a dynamic viscosity of 1.7894 x 10^{-5} kg/m·s. The airfoil and obstacles were modeled using aluminum, with a density of 2719 kg/m^3, specific heat (Cp) of 871 J/kg·K, and thermal conductivity of 202.4 W/m·K. These material properties ensured an accurate representation of both the airflow and solid components within the computational domain.

The boundary conditions were carefully defined to replicate real-world flow behavior. At the inlet, a velocity of 21 m/s corresponds to a Reynolds number of 3.5x10^5 was imposed in the x-direction, with no velocity in the y-direction. The turbulence at the inlet was characterized by a turbulent kinetic energy of 1 m^2/s^2 and a turbulent dissipation rate of 1 m^2/s^3. The outlet boundary condition was set as a pressure outlet with a gauge pressure of 0 Pa, ensuring that the flow could exit the domain freely without disturbances. The walls of the domain were treated as stationary with no-slip conditions, and the roughness height was set to 0 m, representing smooth surfaces.

4.2 Solver Settings

The simulation was performed using a pressure-based solver, which is appropriate for handling incompressible flow conditions like those experienced around the NACA 65-421 airfoil. The pressure-velocity coupling was managed using the SIMPLEC algorithm, which provides enhanced convergence speed, particularly in transient simulations. The discretization of key variables was handled using upwind schemes; second-order upwind for momentum and first-order upwind for both turbulent kinetic energy and dissipation rate. These schemes ensure that the convective terms in the governing equations are resolved with reasonable accuracy.

For the time-stepping, a transient simulation approach was adopted with a time step size of 0.001 seconds and a total of 1000 time steps. This choice of time step allowed for the capture of small-scale flow fluctuations and interactions between the airfoil and obstacles, providing detailed insights into the flow dynamics. The solver was set to perform a maximum of 20 iterations per time step, ensuring adequate convergence of each time step before progressing further in the simulation.

To improve the convergence rate, under-relaxation factors were applied to the equations. The pressure equation was relaxed with a factor of 0.1, while the momentum equation had a relaxation factor of 0.5. The turbulent kinetic energy and dissipation rate were relaxed using factors of 0.8. These relaxation factors ensured stability and gradual convergence of the solution without sacrificing accuracy.

4.3 Convergence Status

The convergence of the simulation was monitored through the residuals of the governing equations, with target values set to ensure accurate results. The target for the continuity residual was set to 1 x 10^{-5}, while the target for both x-velocity and y-velocity was also 1 x 10^{-5}. For turbulence quantities, the residual target for the turbulent kinetic energy was 1 x 10^{-6}, and for the turbulent dissipation rate, it was 1 x 10^{-3}.

At the end of the simulation, most of the residuals had reached or exceeded their convergence criteria. The x-velocity residual converged to 1.301 x 10^{-6}, while the y-velocity residual converged to 1.651 x 10^{-6}, both well below the set target. The turbulent kinetic energy residual converged to 6.367 x 10^{-7}, also meeting the desired accuracy. The turbulent dissipation rate reached a residual of 8.799 x 10^{-6}, achieving convergence as well. However, the continuity residual remained slightly above the target at 1.1485 x 10^{-4}, indicating that although most variables had converged, the overall mass balance could be further refined in future iterations. Despite this, the results were deemed sufficiently accurate for analyzing the aerodynamic performance of the NACA 65-421 airfoil under the influence of upstream obstacles.

4.4 Turbulence Model

The RNG k-ε model was used for the simulation due to its ability to handle high Reynolds number flows and accurately predict flow separation and reattachment, which are crucial for analyzing vortex formation. The model included standard wall functions to resolve the boundary layer near the airfoil surface. The standard constants for the k-ε model were applied, including: C_μ=0.09, σ_k=1.0, σ_ϵ=1.3, C_1=1.44, C_2=1.92

5 Results and Discussion

5.1 Flow Characteristics and Velocity Distribution

This research allows for a detailed analysis of velocity flow fields, pressure distributions, and turbulence and aerodynamic characteristics around airfoils. The following are the results interpretations of the flow behavior around the obstacles and the airfoil.

5.1.1 Velocity Magnitude Contours

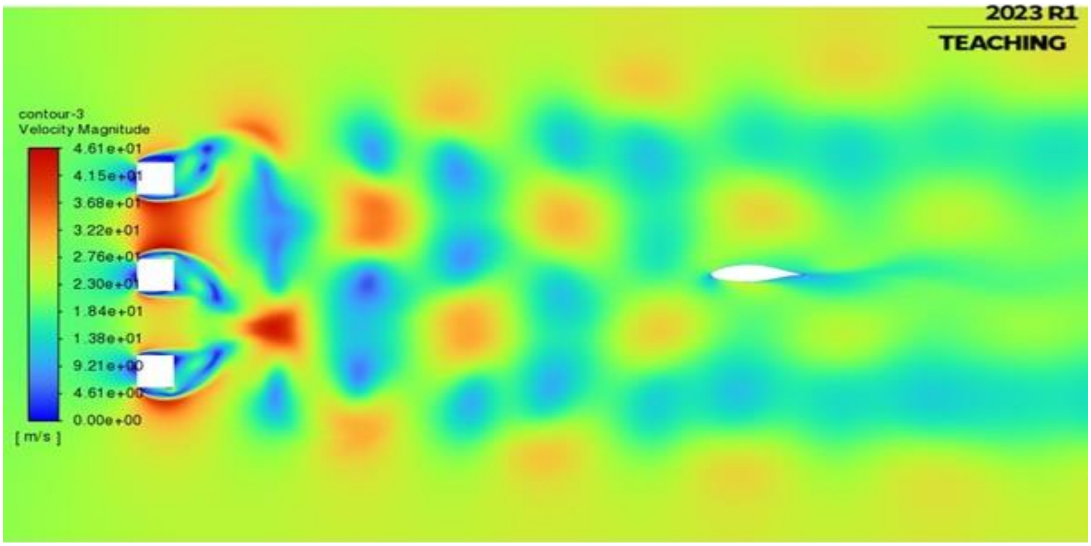

Figure 3. Velocity contours in the computational flow domain

The velocity magnitude contour in Figure 3 provides a visual representation of the speed of airflow across the computational domain. The velocity decreases significantly and a flow circulation occurs on the top and bottom surfaces of the obstacles, especially in the leeward regions directly behind the obstacles. This is due to the flow separation caused by the obstacles, where the high-velocity incoming flow interacts with the sharp edges of the obstacles, generating recirculation zones. As the flow moves away from the obstacles, it gradually recovers, but areas of low velocity persist in the recirculating wakes between high-velocity turbulences. These low-velocity zones have the potential to cause unsteady behavior in the flow downstream, particularly around the airfoil. The flow accelerates around the airfoil due to the geometry of the NACA 65-421, causing an increase in velocity near the leading edge. However, due to the disturbances created by the upstream obstacles, the velocity distribution is non-uniform, with possible impacts on both the lift and drag characteristics of the airfoil.

5.1.2 X-Velocity Contours

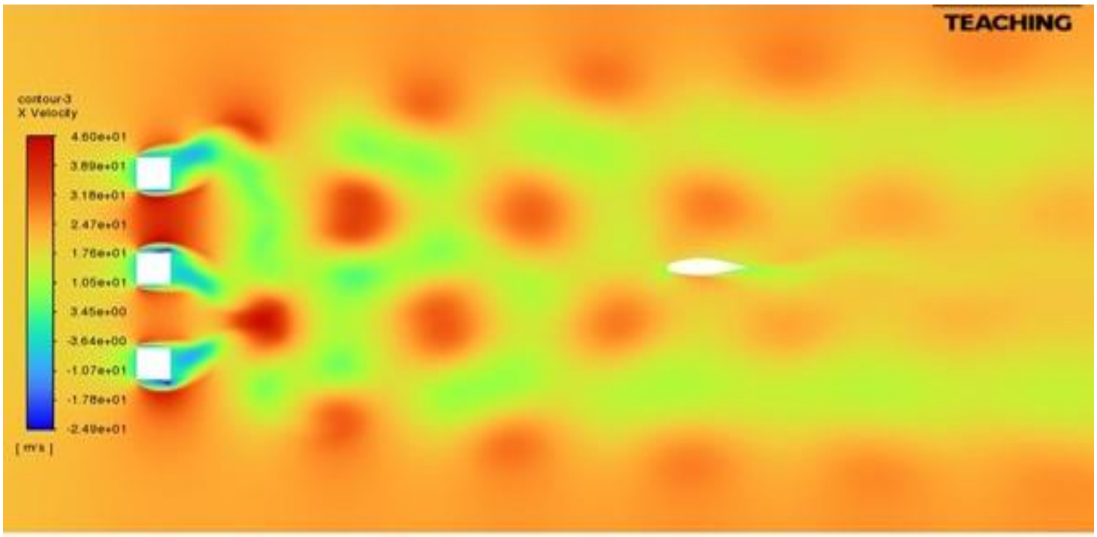

Figure 4. X-Velocity contours in the computational flow domain

In Figure 4 the X-velocity contours specifically show the velocity component in the streamwise direction. There is a significant reduction in X-velocity in the immediate leeward of the obstacles. The flow stagnates in these regions due to the interaction of the incoming free-stream flow with the obstacle's corners, leading to strong recirculation and the formation of downstream counter-rotating vortices. As the flow progresses further downstream, the X-velocity increases, but the disturbances from the obstacles still persist. These disturbances affect the uniformity of the incoming flow toward the airfoil, which is crucial for understanding how the airfoil responds to non-uniform inflow conditions. The airfoil sees a distinct increase in X-velocity over its upper surface, which is characteristic of the pressure difference that generates lift. However, the non-uniform inflow due to the obstacles introduces variations in X-velocity over the surface, which may result in fluctuating aerodynamic forces.

5.1.3 Velocity Vectors

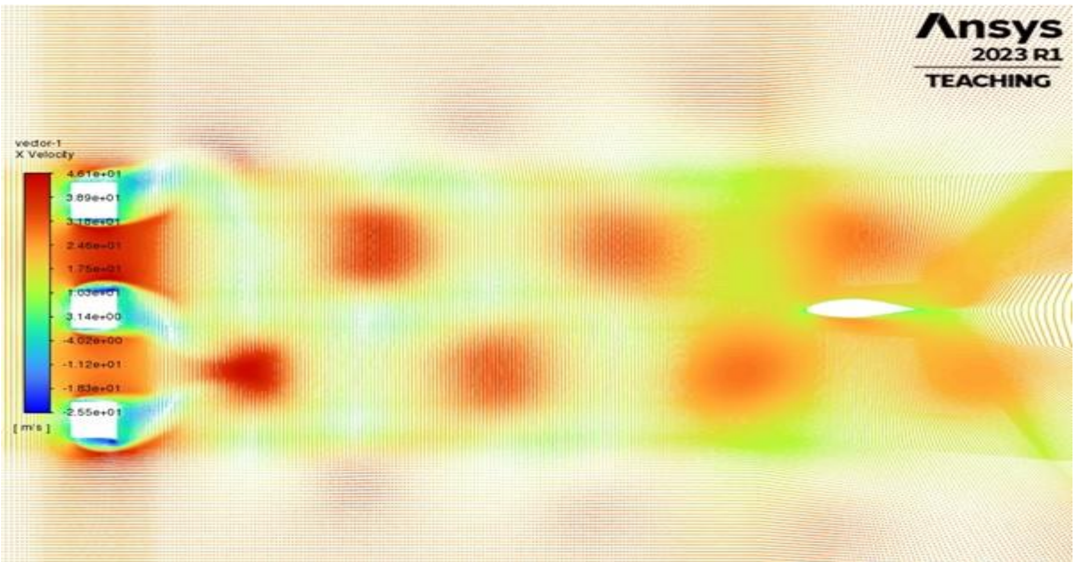

Figure 5. Velocity vectors in the computational flow domain

Velocity vector gives insights into both the magnitude and direction of the flow, making it easier to visualize complex flow structures such as vortices, separation, and recirculation zones. The velocity vectors show strong recirculation zones at the leeward and top and bottom surfaces of each obstacle, with vortices forming as the flow separates from the sharp edges of the obstacles. These vortices are characterized by circular flow patterns in the wake, with low-velocity zones in their centers. Downstream, the recirculating wakes from the obstacles propagate towards the airfoil. These disturbed flow regions interact with the airfoil, potentially causing unsteady forces on the airfoil surface. The velocity vectors around the airfoil show that while the flow accelerates over the airfoil especially at the leading edge as can be seen in Figure 6a, the wake's influence remains strong, particularly near the trailing edge as in Figure 6b.

5.1.4 X-Velocity Vectors at the Leading Edge

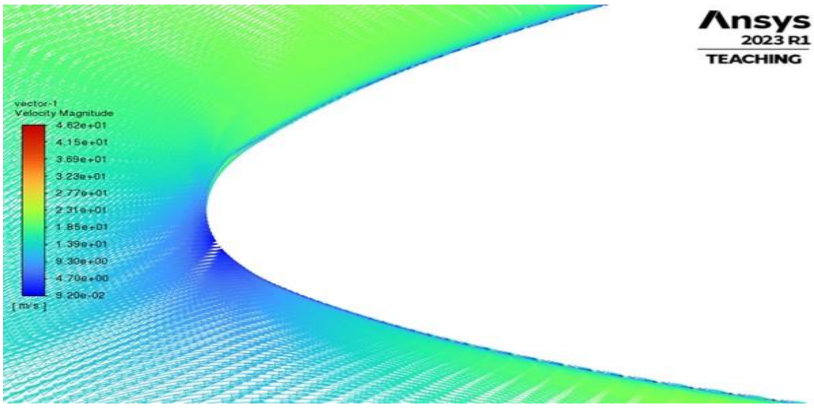

Figure 6a. Velocity vector at the leading edge of airfoil

From Figure 6a, the X-velocity vectors near the leading edge of the airfoil reveal how the flow first interacts with the airfoil geometry. As expected, the vectors show an increase in velocity as the flow approaches the leading edge, especially on the upper surface. This acceleration is crucial for creating lift. The non-uniform inflow, resulting from the upstream obstacles, introduces local variations in velocity direction and magnitude. These disturbances could influence the boundary layer behavior at the leading edge.

5.1.5 X-Velocity Vectors at the Trailing Edge

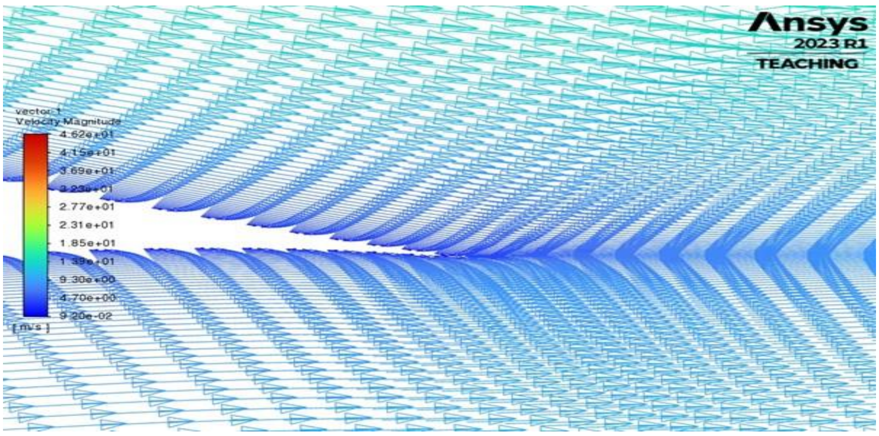

Figure 6b. Velocity vector at the trailing edge of airfoil

The trailing edge velocity vectors provide insight into how the flow reattaches and leaves the airfoil. Because the angle of attack in this study is zero as in the natural wind turbine blade before pitching. Due to the disturbed inflow, the vectors near the trailing edge didn't show flow separation. The flow leaving the trailing edge forms a wake behind the airfoil, which is influenced by the vortices created by both the airfoil and the upstream obstacles. This wake can have significant effects on the drag force experienced by the airfoil.

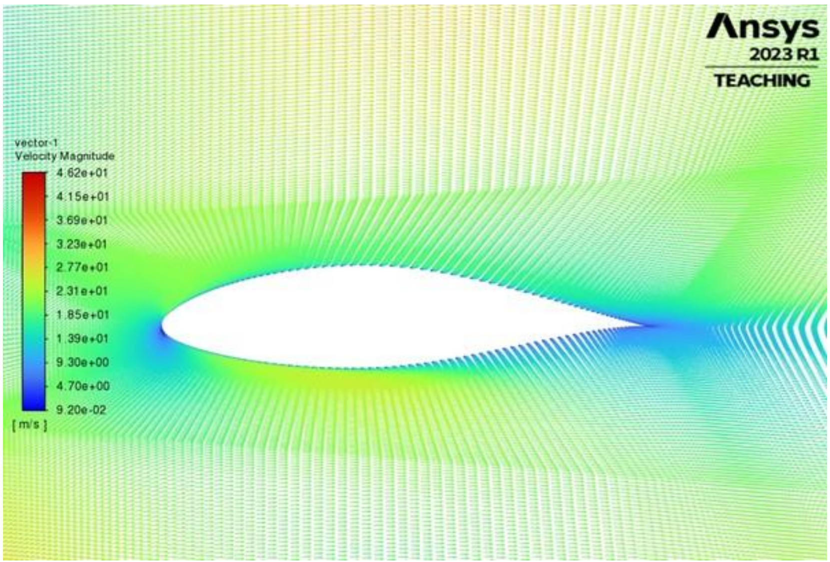

Figure 6c. Overall velocity vector over the upper and lower surfaces of the airfoil

Figure 6c shows the overall velocity magnitude vectors, and X-velocity plots confirm that the presence of upstream obstacles significantly impacts the flow field around the NACA 65-421 airfoil. The disturbed flow causes increased turbulence and vortex formation behind the obstacles. Non-uniform inflow conditions lead to variations in velocity across the airfoil surface. Potential changes in the boundary layer behavior, possibly leading to early flow attachment on the upper and lower trailing edge of the airfoil. This detailed flow analysis highlights the importance of considering upstream disturbances when evaluating the performance of airfoils in real-world applications where obstacles are present.

5.2 Velocity profiles

The velocity profiles at different locations on the NACA 65-421 airfoil (leading, middle, trailing edges, and wake region) offer a comprehensive understanding of how the airflow develops around the airfoil. Below is a detailed analysis of all profiles:

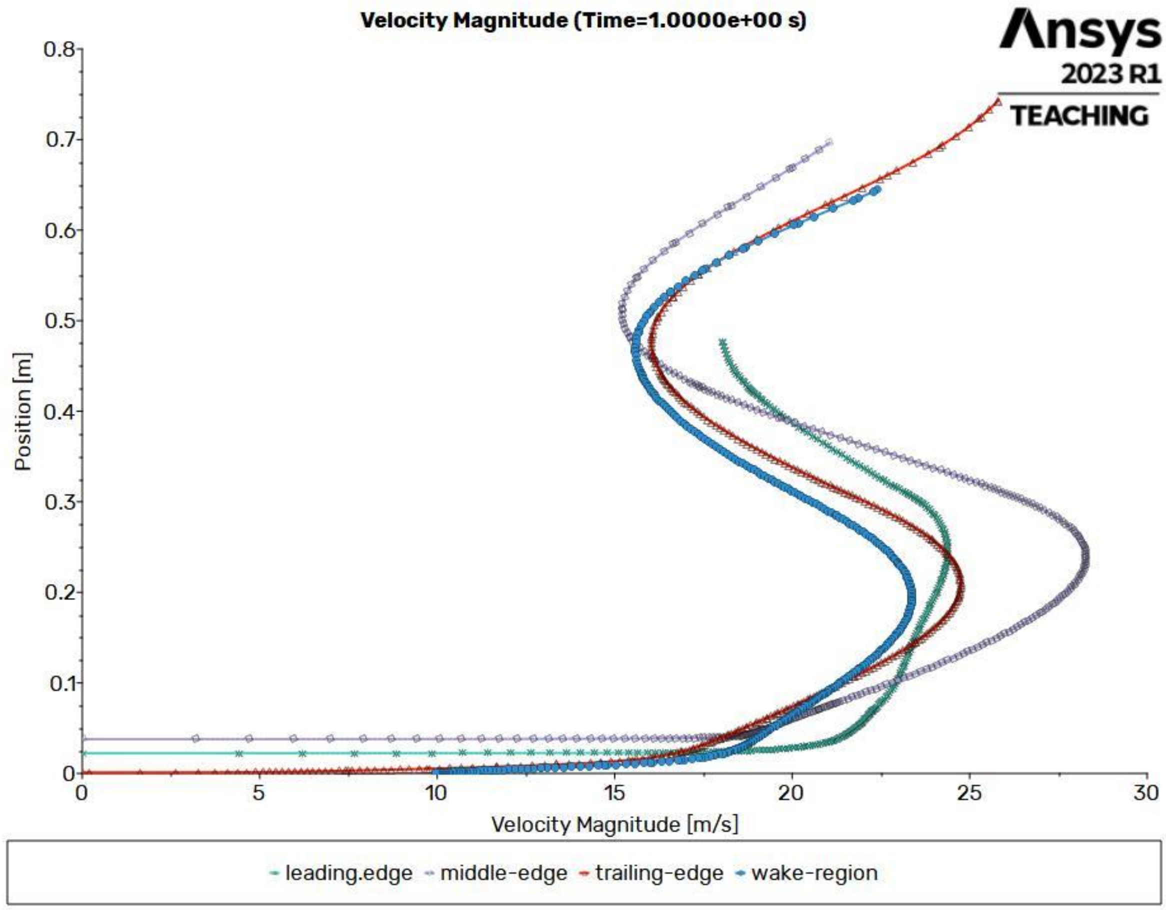

Figure 7. Velocity profiles on the airfoil and the wake

It can be seen from Figure 7 that, the flow velocity accelerates at the leading edge, where the velocity magnitude increases rapidly as the airflow transitions from the stagnation point on the front surface of the airfoil to the suction side (upper surface) of the airfoil. This profile shows a sharp rise from approximately 22 m/s to around 25 m/s, indicating the strong acceleration of the flow over this region. This is characteristic of a well-performing airfoil where the flow accelerates as it moves around the curved leading edge.

This sharp acceleration is crucial for generating lift. The high-speed flow over the upper surface leads to a lower-pressure region, contributing significantly to the airfoil's lift.

The velocity profile at the middle of the airfoil shows a continuation of the acceleration, with the flow maintaining a higher velocity of around 25 m/s at higher locations. This indicates that the boundary layer remains attached to the surface, and the flow continues to accelerate, contributing to lift.

The relatively smooth rise in velocity without significant drops indicates that the flow has not separated from the airfoil surface, which is important for maintaining aerodynamic efficiency.

This profile suggests efficient airfoil performance, as the smooth increase in velocity ensures that the boundary layer remains attached, reducing drag and maintaining lift.

At the trailing edge, the velocity profile shows a deceleration, with the flow velocity starting to decrease. This deceleration is expected as the flow begins to leave the airfoil surface and merge into the wake. The flow velocity still remains above 22 m/s, indicating that the flow is mostly attached even near the trailing edge, which is desirable for reducing drag and maintaining lift efficiency. The trailing edge marks the beginning of the wake, where the airflow will start to interact with the disturbed flow behind the airfoil.

The wake velocity profile shows the recovery of the flow as it moves downstream from the trailing edge of the airfoil. The velocity is lower than in the free stream, with values around 21 m/s, indicating the presence of a wake with reduced velocity compared to the free-stream flow.

The wake region typically experiences lower velocity and increased turbulence due to the interaction of the attached boundary layers from the upper and lower surfaces of the airfoil. The gradual velocity recovery in this profile indicates that the wake is not overly turbulent or wide, which suggests that the airfoil is producing low drag.

Downstream of the airfoil, the velocity profile shows a continued recovery of the airflow as it moves further away from the airfoil. This smooth recovery indicates that the wake is dissipating, and the flow is returning to its normal condition.

The velocity profiles in Figure 7, reveal efficient airflow management around the NACA 65-421 airfoil, with smooth acceleration at the leading edge, attached flow along the middle section, and minimal deceleration at the trailing edge. The wake region shows moderate turbulence and flow recovery, indicating low drag and maintaining the aerodynamic performance of the airfoil. These profiles suggest that the airfoil is performing efficiently, with the flow remaining attached over most of the surface, minimizing drag while maximizing lift. This detailed analysis highlights how the velocity profiles can be used to assess the aerodynamic efficiency of the airfoil and identify regions of flow separation, turbulence, or drag production.

5.3 Static Pressure Distribution

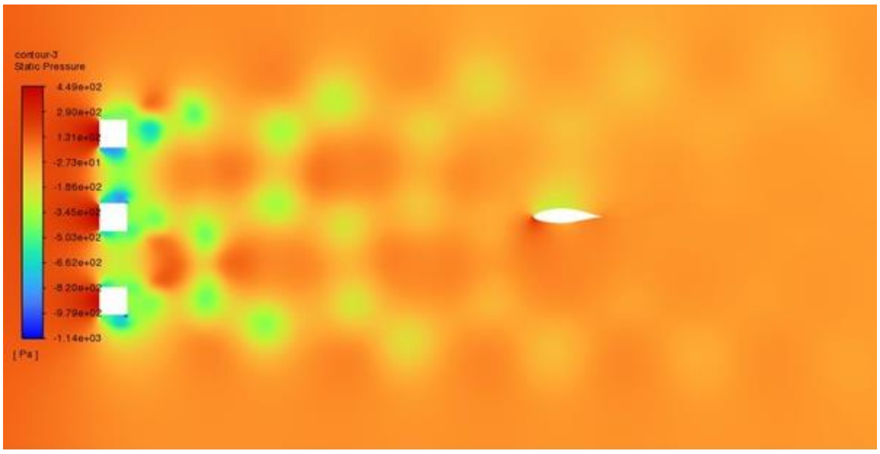

Figure 8. Static pressure distribution on the computational domain

The static pressure contour in Figure 8 provides valuable insights into how the airflow interacts with both the obstacles and the NACA 65-421 airfoil.

The high-pressure zones observed just upstream of the obstacles are typical of flow obstructions. As the flow approaches the sharp edges of the obstacles, it stagnates, resulting in an increase in static pressure. This is the stagnation point where the velocity is reduced, and pressure increases. The regions immediately behind the obstacles show lower static pressure values, indicative of flow separation and the formation of recirculation zones. The drops in pressure in the wake of the obstacles align with the creation of vortices and turbulent flow structures that tend to form behind sharp-edged objects. The recirculation zones lead to local areas of lower pressure, which are visible as distinct blue and green regions on the contour. The alternating bands of low and high pressure in the wake of the obstacles suggest the formation of vortex shedding, where pressure fluctuates periodically due to the vortices being shed. This unsteady behavior can have a significant impact on any structure downstream, in this case, the airfoil.

As expected for a typical airfoil, there is a high-pressure region at the leading edge of the NACA 65-421 airfoil. This is due to the stagnation of airflow as it encounters the airfoil. The high-pressure area is essential for generating lift, as it contrasts with the lower pressure on the upper surface. As the flow accelerates over the upper surface (suction side) of the airfoil, the static pressure decreases significantly. The green-to-blue gradient over the upper surface indicates this region of lower pressure, where the faster-moving air creates the suction necessary for lift generation. However, because of the disturbed inflow caused by the upstream obstacles, the pressure distribution is not uniform, and there could be areas where pressure increases or decreases due to turbulence in the incoming flow.

The static pressure on the lower surface (pressure side) of the airfoil is relatively higher compared to the upper surface. This pressure difference between the upper and lower surfaces of the airfoil is the key factor generating lift. However, due to the upstream disturbances, the pressure field around the airfoil may fluctuate, potentially impacting the overall aerodynamic efficiency.

The region immediately behind the airfoil shows a drop in static pressure, which is typical in the wake of an airfoil. The trailing edge wake forms due to the boundary layers on both sides of the airfoil merging from the surfaces. The disturbed inflow caused by the obstacles has likely affected the wake structure, leading to possible instabilities and fluctuating pressure values downstream.

In summary, the static pressure contour reveals how the obstacles disrupt the pressure field and induce wake effects that propagate downstream, influencing the flow around the airfoil and reducing its aerodynamic efficiency. This analysis highlights the importance of considering upstream disturbances in practical applications where airfoils may encounter similar obstacles.

5.4 Pressure Coefficient (C_p) Distribution

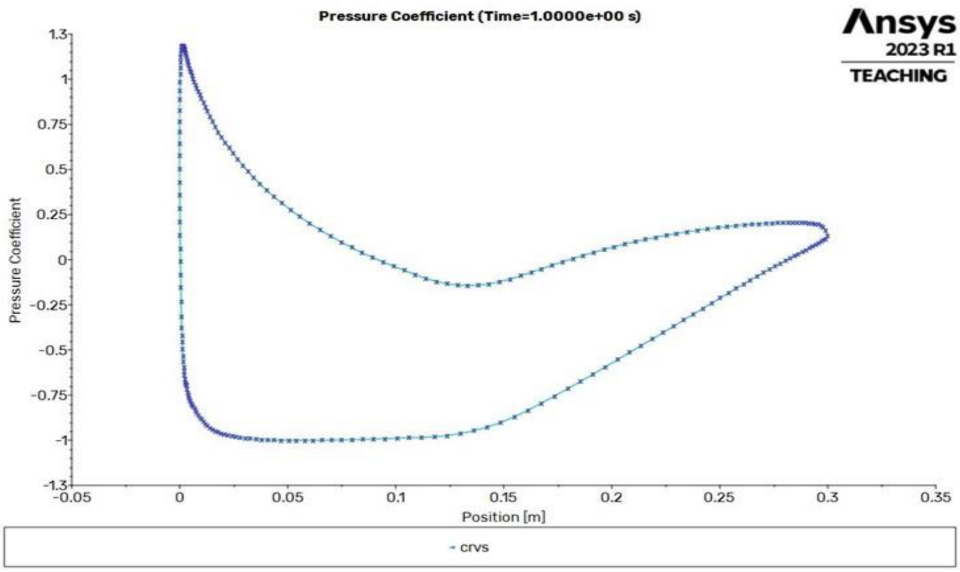

Figure 9. Pressure coefficient along the surface of the airfoil

Figure 9 shows the pressure coefficient (C_p) plot that offers insight into the pressure distribution along the surface of the NACA 65-421 airfoil, which is critical for understanding the airfoil's aerodynamic performance.

At the very beginning of the curve (position = 0), there is a sharp spike in the pressure coefficient, with C_p values reaching close to 1.3. This corresponds to the stagnation point at the leading edge of the airfoil. At this point, the flow velocity reduces to nearly zero, causing a maximum increase in pressure. This behavior is expected as the stagnation pressure occurs when the flow is brought to rest as it impacts the leading edge of the airfoil.

After the initial spike, the C_p rapidly decreases, reaching highly negative values (around -1.2). This sharp drop in pressure corresponds to the acceleration of airflow over the upper surface of the airfoil, particularly on the suction side. According to Bernoulli's principle, as the flow accelerates, the pressure decreases. This low-pressure region is essential for generating lift, as it creates a pressure differential between the upper and lower surfaces of the airfoil.

The minimum C_p (most negative value) occurs at approximately 0.02–0.05 m from the leading edge, which aligns with the point of maximum flow acceleration over the airfoil. This rapid drop is a characteristic of well-performing airfoils, where the upper surface accelerates the flow and creates strong suction.

As we move further along the upper surface towards the trailing edge, the pressure begins to recover, with C_p values increasing back towards zero. This indicates that the flow starts to decelerate, leading to an increase in pressure. This pressure recovery occurs as the flow moves downstream and over the camber of the airfoil. However, in real-world conditions, if flow separation occurs prematurely, this recovery can be less smooth, leading to higher drag. The relatively smooth recovery seen in this plot suggests that no flow separation has occurred on the upper surface, and the flow remains attached over a considerable portion of the airfoil.

On the lower surface of the airfoil, the pressure coefficient remains relatively high compared to the upper surface, with values around C_p=0.2 to 0.40. This indicates that the flow on the lower surface experiences less acceleration, resulting in higher pressure. The higher pressure on the lower surface, combined with the lower pressure on the upper surface, creates the pressure differential that generates lift. The C_p on the lower surface stays relatively constant, with only a slight decrease towards the trailing edge. This behavior is typical of airfoils with well-designed camber, where the lower surface pressure does not drop significantly, maintaining the lift-producing pressure differential.

At the trailing edge, the pressure coefficient on both the upper and lower surfaces converges towards zero. This is expected, as the flow from both surfaces must meet smoothly at the trailing edge, ensuring a streamlined exit of the flow and minimizing drag.

In an ideal, undisturbed environment, this pressure distribution would indicate efficient lift production. However, in the present case, the airfoil is subject to disturbed inflow due to the upstream obstacles. While the overall shape of the pressure coefficient curve indicates effective performance, the non-uniform inflow may cause localized fluctuations in pressure, particularly at the leading and trailing edges, which can affect the overall lift and drag. The pressure coefficient distribution demonstrates typical behavior for an efficient airfoil, with a high stagnation pressure at the leading edge and a rapid decrease in pressure over the upper surface, resulting in strong suction.

The lower surface maintains higher pressure, contributing to a favorable pressure differential for lift generation. The recovery of pressure towards the trailing edge is smooth, suggesting no flow separation in the simulated conditions.

In conclusion, this C_p plot provides an excellent overview of the aerodynamic performance of the NACA 65-421 airfoil, but further analysis of unsteady flow effects would be needed to understand the full impact of the upstream disturbances. Aerodynamic Coefficients

5.4.1 Lift Coefficient (C_l):

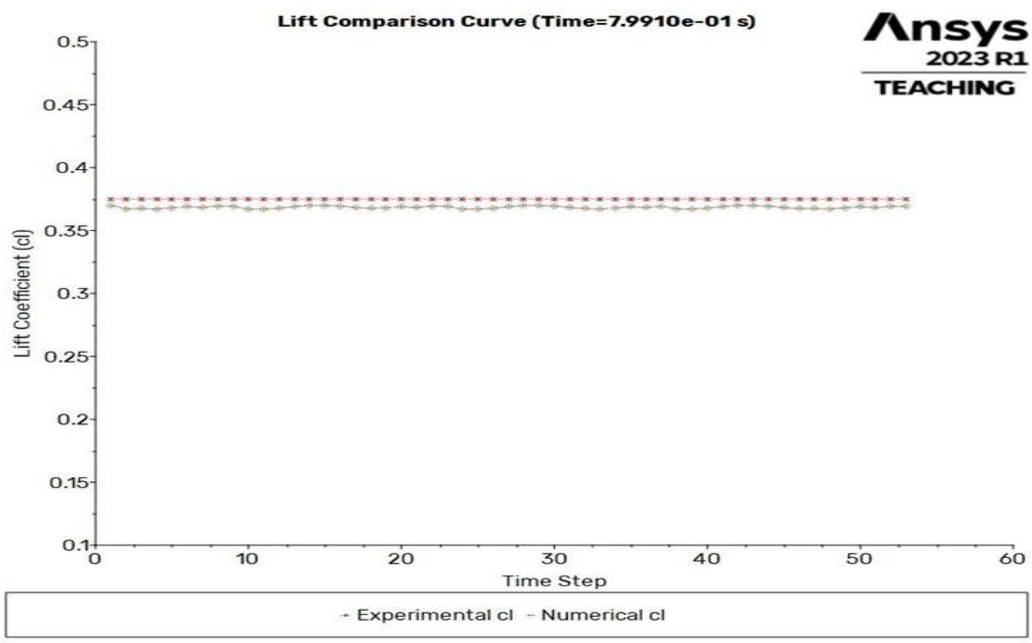

Figure 10. Pressure coefficient along the surface of the airfoil

The lift coefficient (C_l) plot in Figure 10, compares the experimental [9] and numerical results over multiple time steps, providing insights into the lift performance of the NACA 65-421 airfoil under disturbed flow conditions.

The lift coefficient remains fairly constant throughout the simulation, with values around C_l=0.36. This consistency suggests that the airfoil is generating steady lift, despite the presence of upstream obstacles. The near-horizontal curve across time steps implies that the flow field around the airfoil has reached a quasi-steady state, with minimal fluctuations in lift force over time. This behavior is expected in simulations and experiments involving streamlined airfoils like the NACA 65-421, which are optimized for smooth and consistent lift production.

The numerical and experimental lift coefficient values are almost identical, indicating excellent agreement between the CFD simulation results and the physical experimental data. This close match reinforces the accuracy of the numerical model, including the choice of turbulence model (RNG k-epsilon), mesh quality, and boundary conditions. The small differences could arise due to experimental uncertainties (e.g., measurement error, wind tunnel conditions) or minor differences in the computational setup compared to the real-world conditions. Overall, the close match between experimental and numerical values validates the accuracy of the simulation.

This value suggests that the airfoil is effectively generating lift in a turbulent environment, even with upstream disturbances. Given that the airfoil is part of the NACA 6-series, which is designed for laminar flow and low drag at high lift conditions, the obtained C_l value confirms the airfoil's efficiency in maintaining good aerodynamic performance. The consistent lift coefficient indicates that the airfoil is well-suited for applications requiring steady lift under turbulent or disturbed conditions, such as low-altitude flight or environments where obstacles might interfere with the airflow.

Despite the presence of upstream obstacles that would disturb the inflow conditions, the lift coefficient remains remarkably stable. This suggests that the airfoil can maintain its aerodynamic performance even when the incoming flow is disrupted by obstacles.

In summary, this analysis shows that the NACA 65-421 airfoil performs efficiently with stable lift generation, even in the presence of upstream disturbances. This stability makes the airfoil suitable for applications requiring consistent lift, such as in aviation or wind energy systems, where maintaining steady aerodynamic forces is critical.

5.4.2 Drag Coefficient (C_d):

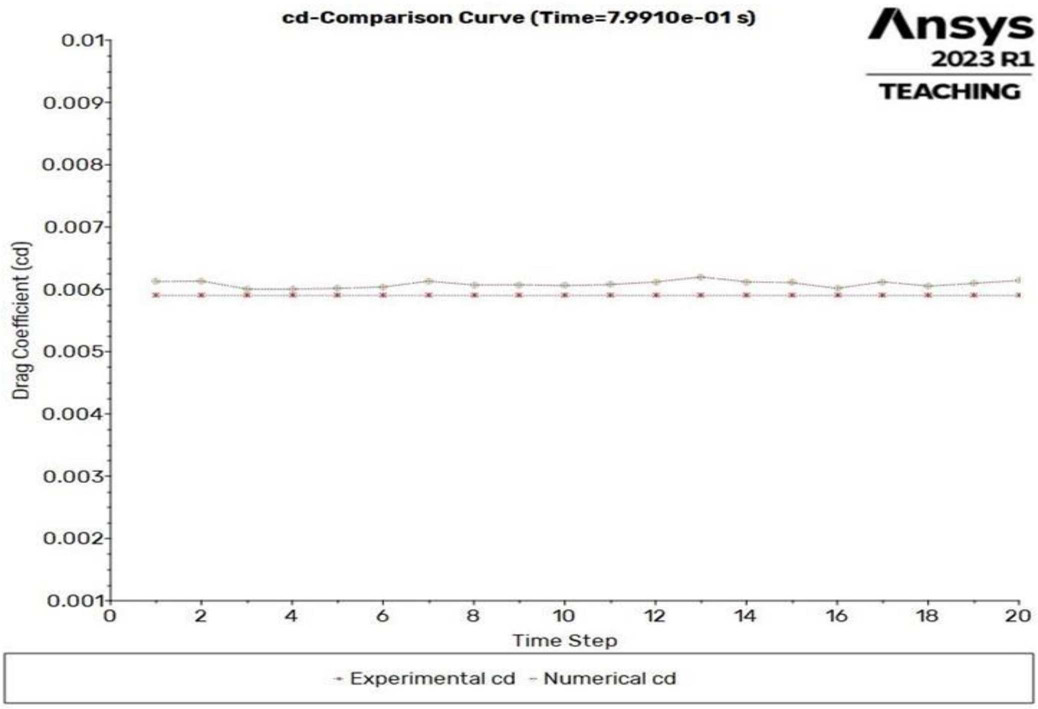

Figure 11. Pressure coefficient along the surface of the airfoil

Figure 11 compares the experimental [9] and numerical results of the coefficient of drag (C_d) over a series of time steps, offering insights into the drag behavior of the NACA 65-421 airfoil under the influence of upstream disturbances.

Also figure 11 shows the drag coefficient remains fairly constant throughout the time steps, with values hovering around C_d =0.006. This stability suggests that the flow around the airfoil has reached a quasi-steady state, with minimal fluctuation in the drag force over time.

The numerical and experimental drag coefficient values are very close to each other, demonstrating excellent agreement between the simulation results and real-world experimental data [7]. This consistency validates the accuracy of the simulation setup, particularly the choice of turbulence model (RNG k-ε), boundary conditions, and mesh quality. While the numerical and experimental results are almost identical, there are very small deviations observable at certain time steps. These discrepancies could be attributed to experimental uncertainties, such as sensor precision, wind tunnel imperfections, or slight differences in flow conditions between the simulated and experimental environments.

The drag coefficient value of approximately C_d =0.006 is quite low, indicating that the NACA 65-421 airfoil is optimized for minimal drag, which is consistent with its design purpose as part of the NACA 6-series, known for laminar flow properties. This low drag is essential for maximizing efficiency, particularly in applications such as aircraft wings or wind turbine blades, where minimizing drag is crucial for energy conservation and improved performance.

The consistency across both experimental and numerical data suggests that the flow around the airfoil is well captured by the CFD simulation, providing confidence in the simulation's predictive capability.

6 Conclusions

This study provided a detailed analysis of the aerodynamic performance of the NACA 65-421 airfoil at an inlet velocity of 21 m/s using the k-ε turbulence model. The results showed that the airfoil generated significant lift while experiencing moderate drag due to inflow turbulence vortex formation. The upstream obstacles played a critical role in enhancing turbulence and affecting flow over the airfoil. The k-ε model effectively captured the complex flow characteristics, making it a suitable choice for analyzing high Reynolds number flows in aerodynamic applications.

Vortex formation was observed downstream of the obstacle. The upstream obstacles caused disturbances that amplified the vortex strength and increased flow separation on the obstacle surfaces and in the downstream wake region. The vortices formed behind the obstacles contributed to periodic unsteady forces on the airfoil, affecting both lift and drag.

The excellent agreement between the experimental and numerical results validates the accuracy of the CFD simulation and the turbulence model used. Minor variations between the experimental and numerical lift and drag coefficient values could be attributed to experimental uncertainties or minor computational setup differences.

Additionally, the velocity magnitude contours and velocity vectors indicated significant acceleration over the upper surface of the airfoil. The flow over the upper and lower surfaces remained attached with no flow separation. The flow disturbances caused by the upstream obstacles enhanced the size and complexity of the wake, leading to the formation of vortices that propagated downstream the blocks. The velocity profiles across different sections of the airfoil indicated that the flow transitioned from laminar to turbulent after passing over the leading edge, with a significant attached boundary layer along the airfoil's surface. Also, a notable wake region formed behind the airfoil and obstacles, characterized by low velocity.

The study highlights the importance of accurately modeling turbulence flow to predict real-world aerodynamic performance. The results can be used to inform future airfoil designs and optimize configurations to reduce drag and enhance lift, especially in induced turbulent flow conditions. Because the non-uniform inflow may cause localized fluctuations in pressure, particularly at the leading and trailing edges, which can affect the overall lift and drag

Acknowledgment

The authors would like to sincerely express their deep gratitude to the Institute of Industrial Technology Faculty of Engineering Science & Technology at The Arctic University of Norway-UiT in Norway and Virginia Tech in the United States for providing an opportunity and necessary computational facilities to carry out this work. Also, the first author would like to thank Al-Balqa Applied University - Faculty of Engineering Technology in Jordan for granting him a sabbatical leave at UiT-The Arctic University of Norway in Narvik.

References

1. Abbott, I.R., Von Doenhoff, A.E, 1959. Theory Of Wing Sections. Dover Publications, Inc. New York.

2. C.-M. Hsiun and C.-K. Chen, ‘Aerodynamic characteristics of a two-dimensional airfoil with ground effect’, Journal of Aircraft, vol. 33, no. 2, pp. 386–392, 1996, doi: 10.2514/3.46949
3. A. Roshko, ‘On the drag and shedding frequency of two-dimensional bluff bodies. NACA Technical note 3169. USA, July 1954.
4. R. L. Simpson, ‘Turbulent Boundary-Layer Separation’, Annual Review of Fluid Mechanics, vol. 21, no. Volume 21, 1989, pp. 205–232, Jan. 1989.
5. H K Versteeg and W Malalasekera. 2007. An Introduction to Computational Fluid Dynamics THE FINITE VOLUME METHOD. Second Edition, Pearson Education Limited
6. Spalart, P. R., Allmaras, S.R. A one-equation turbulence model for aerodynamic flows LaRecherche Aerospatiale, 1994, No.1, Page 5-21.
7. S. J. Juliyana, J. U. Prakash, K. Karthik, P. Pallavi, and M. Saleem, "Design and analysis of NACA4420 wind turbine aerofoil using CFD," International Journal of Mechanical Engineering and Technology, vol. 8, no. 6, pp. 403-410, 2017.
8. K. S. Rao, M. A. Chakravarthy, G. S. Babu, and M. Rajesh, "MODELING AND SIMULATION OF AEROFOIL ELEMENT," METHODOLOGY, vol. 5, no. 02, 2018.
9. Franck Bertagnolio, Niels S_Sørensen, Jeppe Johansen, Peter Fuglsang. Wind Turbine Airfoil Catalogue. Risø_{R{1280(EN), Risø_ National Laboratory, Roskilde, Denmark, August 2001

Modelling and Simulation of Bio-Hydrogen Production in a Sewage Treatment Plant: A Case Study in Oman

Hind Barghash1,*, Ahmed Al Aamri1, Zuhoor Al Rashdi1 , Seyed Mojtaba Sadrameli1 , Kenneth E. Okedu2,*

[1] Department of Engineering, German University of Technology, Muscat, Oman
[2] Department of Electrical and Electronic Engineering, Nisantasi University, Istanbul, Turkey

* *Corresponding authors: hind.barghash@gutech.edu.om; +96897381028*

Abstract: Simulating the production of hydrogen gas is a valuable tool for understanding and optimizing the underlying processes. In this study, Aspen-Plus is used as a versatile simulation software, to model and analyse biohydrogen gas production at standard temperature and pressure for a selected sewage treatment plant in Oman. The primary objective is to investigate the impact of varying temperature and pressure on the production rates of hydrogen, carbon dioxide, and acetic acid, with the aim of selecting optimal conditions for energy efficiency and product yield. The simulation findings reveal that temperature fluctuations have negligible effects on hydrogen and carbon dioxide production rates. However, acetic acid production is significantly hindered by elevated temperatures, leading to a decrease in its yield. To conserve energy and enhance acetic acid production for potential alternative uses, an operating temperature of 37°C is recommended. Regarding pressure, it is observed that alterations in pressure levels do not considerably affect hydrogen and acetic acid production rates. On the other hand, changing in the pressure affects the production rate of carbon dioxide. Therefore, the optimal operating pressure condition for mitigating the negative impact of carbon dioxide production is 101.325 kPa. By implementing these recommended temperature and pressure conditions, hydrogen gas production rates would range from approximately 84.76 kg H2/h to nearly 254.54 kg H2/h, depending on variations in the glucose input rate (ranging from 500 to 1,500 kg/h). This study demonstrates the efficacy of simulation-based approaches in optimizing biohydrogen gas production processes, offering insights that can lead to improved energy efficiency and increased yields of valuable byproducts like acetic acid.

Keywords: Bio-Hydrogen, Aspen-Plus, Sewage Treatment, Dark Fermentation, Sludge, Process optimization.

1. Introduction

The availability and use of energy plays a pivotal role in global socio-economic development. Historically, non-renewable energy sources such as coal, oil, and natural gas have been the primary drivers of energy production and have significantly contributed to economic growth and industrialization around the world [1]. In recent years the world faces an impressive raising of fossil fuel consumption which is due to the economic growth [2]. Globally, the increased production and consumption of fossil fuels has had several adverse environmental impacts including global warming, air pollution, and increased health risks [3]. Therefore, searching for other sources of energy is becoming an essential step. From here, scientists try to find alternative sources of energy which can be depleted, as substitute solutions to energy utilization. Renewable energy sources are required to replace the conventional sources [4]. Renewable energies such as wind, solar, hydro is used to generate electricity from natural sources with considering the positive environmental impacts [5,6,7,8].

1.1. Renewable energies in Oman

Countries in the Gulf Cooperation Council (GCC) possess around 30% of the world's proven crude oil and 22% of global natural gas reserves [9]. Almost 99% of the domestic energy needs are currently met through the reliance on oil and gas resources [10], which have an impact to the climate change [11]. Addressing these challenges presents an opportunity for the widespread adoption of renewable energy on a large scale. However, as of the end of 2018, renewable energy constituted less than 1% of the total installed power capacity in the region [12]. In 2019, CO2 emissions from power energy is 22% [13]. This percentage need to reduce to achieve the target of Oman Vision 2050 [14]. Hydrogen energy is another type of the renewable energy which Oman can used instead of the conventional energies. It is one of the key elements of a potential energy solution for the twenty-first century [15].

1.2. Hydrogen gas production methods

Hydrogen is a useful energy carrier. It can be converted to electrical energy or serve as fuel or can be stored and transported [16]. Hydrogen production plays an important role in the economic growth [17]. There are several types of hydrogen gas, as each type has different methods. From here, hydrogen gas can be produced from three main processes, which are thermochemical process, electrochemical process, and biological process [18]. Thermochemical process is one of the efficient methods to convert biomass into biofuel or producer gas (composting of H2, CH4, and CO). Different thermochemical processes to produce hydrogen based on the amount of oxygen in the reaction and temperature range are shown in Table 1. As listed in the table a process with excess oxygen is known as combustion, with limiter oxygen is called gasification and liquefaction, and in absence of oxygen is pyrolysis [19].

Table 1. Characteristics of thermochemical process.

No.	Process	Amount of oxygen	Process temperature (°C)	Useful products
1	Combustion	Excess	Above 800	Heat
2	Gasification	Limited	700–1100	Gas
3	Pyrolysis	Absence	350–550	Char, biooil
4	Liquefaction	Limited	250–400	Biooil

The second process is the electrochemical process which depends on electrolysis. It is an electrochemical technique which depends on breaking down the molecules of water to produce the hydrogen gas. This process can be achieved by using a low temperature fuel cell including a cathode and an anode. The main function of the fuel cells are production of hydrogen and oxygen from water [18]. Figure 1 shows the various ways to produce hydrogen gas considering renewable energy, natural gas, and coal.

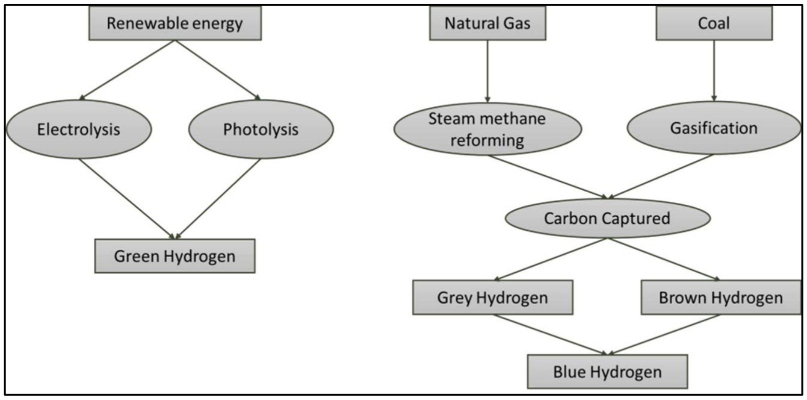

Figure 1 Several technologies for hydrogen gas production

1.3. Bio-Hydrogen Production

Biological processes can be summarized in three main categories, the dark fermentation process, the photo-fermentation process, and the dark-photo co-fermentation [20]. The photo-fermentation process is the process which produce hydrogen gas by using photosynthesis and bacteria with light energy [21]. On the other side, hydrogen produced by dark fermentation can be characterized by the absence of light and oxygen. In dark fermentation, the bacteria will act as a substrate which consists of carbohydrate, proteins, and lipids to produce H2, CO2, and organic acids [22]. The comparison between the photo fermentation and the dark fermentation processes is illustrated in Table 2 [23].

Table 2. The differences between the photo and dark fermentation.

Parameter	Photo fermentation	Dark Fermentation
Light demand	+	–
O2 demand	–	–
Formula	$CH_3COOH+2H_2O + light \rightarrow 4H_2+2CO_2$	$C_6H_{12}O_6+6H_2O \rightarrow 12H_2+6CO_2$
Advantages	Wide range of feedstock, wide spectrum of light.	Cost-effective, high yields, wide range of feedstock.
Drawbacks	Expensive photobioreactors, and light dependency.	Need for effluent treatment, additional gaseous by-products (H_2S, CO_2, CO, CH_4).

1.4. Hydrogen Production via Dark Fermentation

Dark fermentation is the process which occur under anaerobic conditions which is in the acidogenesis phase of anaerobic digestion conditions. Bacteria can be used for producing hydrogen gas under dark fermentation [24]. There are two types of microorganisms in dark fermentation which can be classified based on the temperature requirement and the oxygen availability. The details of the microorganisms can be found in Table 3 [25]. The selection of the Bacteria can affect the hydrogen production. For example, the studies show that for every 1 mole of glucose obligate bacteria and facultative bacteria, 4 to 2 moles of hydrogen gas would be produced, respectively [25].

Aside from that, hydrogen gas from dark fermentation can affect from other factors like the type of the feed. Bio hydrogen gas can be produced from different sources like organic waste from agriculture, leachate from landfills, and sludge and treated water from the sewage treatment plant [26].

Table 3. The differences between the microorganisms in producing bio-hydrogen gas.

Type of microorganism	Requirement conditions	Type of species	References
Obligate (Strict)	Anaerobic	Clostridium, Ethanoligenens, and Desulfovibrio.	[27]
Facultative	Anaerobic and Aerobic	Enterobacter, Citrobacter, Klebsiella, Escherichia coli and Bacillus.	[28]

1.5. Treated Effluent to produce hydrogen gas.

Water is an important liquid for human life, which is used as a source in many production processes [29]. Saving water from scarcity is important topic in many countries around the world [30]. From here, wastewater treatment is one of the solutions that can be implemented to improve environmental protection and to save water and utilize it in production processes [31]. Sludge is a by-product in the biological process of treating polluted water [32]. Sludge is consisting of organic contaminants viruses, microplastics, inorganic minerals, and heavy metals [33]. Using the sludge and the treated water for producing bio hydrogen gas can be one of the best ways for utilizing both at the same time to provide one of the renewable energies.

1.6. Factors affecting hydrogen production

There are several factors that can influence the production of bio hydrogen gas, such as substrate composition, temperature, volatile fatty acids, and hydrogen partial pressure.

- *Substrate compositions*

Many researchers focus on using organic waste to produce hydrogen gas because this type of waste consists of carbohydrate, proteins, and lipids. Carbohydrate-rich substrates having a higher effective in bio-hydrogen gas generation. These substrates consist of simple sugar which hydrolytic bacteria can be produced like glucose and sucrose. Then these substrates will be utilized by using anaerobic bacteria to produce biohydrogen gas. Overall, increasing in the amount of substrate will help to increase the production of hydrogen gas [34].

- *Temperature*

The substrate can be significantly affected by changing temperature which will influence the production of hydrogen gas. The results of previous researcher reveal that increasing reaction temperature with a proper range will help to enhance the production of hydrogen gas. Also, after having several experiments, it was found that the optimum temperature range for producing high amount of hydrogen gas by using dark fermentation process is between 37-40 oC and 55-60 oC [35].

- *Partial Pressure*

Pressure increase inside the reactor will accumulate the lead of hydrogen gas. This will cause the inhabitation of the reaction which will reduce the production of hydrogen gas inside the system. The extraction of generated hydrogen from the reactor will help to increase the amount of produced hydrogen gas [36].

- *Hydraulic Retention Time (HRT)*

Hydraulic Retention Time (HTR) is the time used by the substrate to produce hydrogen gas inside the bioreactor. The optimum HRT for hydrogen gas depends on the type of the substrate [37] which varies between two days to weeks. The HTR also depends on the wastewater and sludge sources as reported in the literature.

Simulating Bio-Hydrogen Gas Production

Working on many experiments over long period of time will affect the efficiency of hydrogen gas production [38]. Simulation is an important tool used to design, run, and optimize the experiments. Also, it plays an important role in the interpretation, analysis, and discussion of big and complex data to obtain logical physical results [39]. Aspen Plus is a simulation software which is designed to handle complex chemical processes with multiple unit operations [39].

Simulation of hydrogen production by alkaline electrolysis using Aspen Plus has been proposed by Sanchez et al. [40] in which a new custom model of an alkaline electrolysis plant is developed including both stack and balance of the plant. Their objective was to analyse the performance of a complete electrolysis system. Their simulation results show that overall performance of the system can be improved by increasing temperature and reducing pressure.

Based on our best knowledge from the literature there is no simulation work on the production of hydrogen using dark fermentation. Therefore, this study is used to model and analyse the production of biohydrogen using Aspen Plus simulation software. Effects of simulation parameters such as temperature and pressure on the production yields hydrogen, CO2, and acetic acid with the aim of selecting optimum conditions for energy efficiency and production yield.

2. Simulation Analysis and Modeling

This simulation study helps to optimize the optimum production rate of the hydrogen by using sewage water as a raw material. Also, to investigate the byproducts which will be the result of the side reactions. The aim of this paper is to explore, the effect of substrate, temperature, and pressure in hydrogen production, in addition, to decreasing the discharge of treated water into sea and use as raw material of hydrogen gas production. This study was done for a selected Sewage Treatment Plant (STP) in Oman as a case study for utilization of hydrogen gas production. Also, Aspen-Plus software is used as a tool to know the best conditions for producing hydrogen gas by using the bioreactors.

2.1 Case study of hydrogen production

In this section the case study of the hydrogen production is divided into sub-case studies. This includes software used for the study, the data of raw material and the usage of treated effluent.

- *Simulation Software*

Aspen Plus has been used in this study for the simulation of bio hydrogen production from the treated effluents taken from sewage treatment plant in Muscat, Oman. This software provides the performance of chemical processes or process modelling tool, which is utilized for optimization, design, run a sensitivity study or controlling the chemical processes. It is used for research studies and in industries such as oil and gas sector.

- *Raw material*

Feed stock of the simulation study is treated effluent which contains of water and organic matter. The raw material is taken from one of the sewage treatment plants in Oman and their production rate is 92,800 m3/day [41]. The plant makes benefit of only 50 percent of the production which is used for cooling system and irrigation. On the other hand, around 46,400 m3/day of treated water will discharge it to the sea. From here, the remaining treated water will be used for producing hydrogen gas and it will be the input for the raw material [42].

- *Usage of Treated effluent*

The STP is selling the treated effluent for cooling system such as heat exchangers and chillers, water for firefighter and irrigation. Furthermore, in some countries they use the treated effluent as drinking water. Nowadays, most countries are shifting to produce hydrogen based on water specifically the sludge and treated effluent. Thus, Aspen Plus is used for simulating the process of producing hydrogen gas from STP [42].

2.2 Simulation Model Setup of the Study

- *Aspen-Plus Software*

Aspen Plus software is the leading solution for process modelling that gives lot of economic benefits throughout the process engineering lifecycle [43]. It is the energy industry's leading process simulation software that is used by top oil and gas producers, refineries, and engineering companies for process optimization in design and operations.

Aspen Plus provides a wide range of thermodynamic models and property methods, allowing users to select the most appropriate model for the specific chemicals and reactions involved in bio-hydrogen gas production [43].

Selecting methods and reaction types for simulating bio-hydrogen gas processes in Aspen Plus involves a systematic approach. Begin by defining the specific production pathway and identifying key chemical reactions. Choose thermodynamic models and reaction types that accurately represent the biochemical processes, considering factors such as kinetics for microbial reactions. Validate the simulation results against experimental data and perform sensitivity analyses to understand parameter influences [44].

- *Properties Setup*

The use of computer-aided process engineering is essential to reach the goal of providing the best system for producing hydrogen gas. This section is for considering the reactions that happened during the production of hydrogen gas. As it is noted, there are several gasses that can be produced in parallel with hydrogen gas production. As seen from Figure 2 that there are seven components used for the main reaction and side reactions. The present work analyses the Non-Random Two-Liquids (NRTL) mode model to check the relation between components and the production of hydrogen gas using a conversion reaction as a reaction type.

Figure 2 Components, method, and reaction type of hydrogen gas production.

As mentioned earlier, there are two methods to produce hydrogen gas from water by using biohydrogen reactor. However, this study will focus on the Dark Fermentation. In this type of reactor, the main chemical reaction is:

$$CH_{12}O_6 + 6\,H_2O \rightarrow 6CO_2 + 12H_2 \qquad (1)$$

Also, there are different side reactions that will produce acetic acid as volatile fatty acids, Methanol, Carbon dioxide, Carbon Monoxide and Hydrogen Peroxide as shown below:

$$CO_2 + H_2O \rightarrow H_2O_2 + CO \quad (2)$$

$$2CO_2 + 4H_2O \rightarrow 2\,CH_3OH + 3O_2 \quad (3)$$

$$CO_2 + H_2O \rightarrow H_2O_2 + CO \quad (4)$$

$$CH_3OH + CO \rightarrow CH_3COOH \quad (5)$$

It can be seen from the above equations that the CO and CO2 must be liquefied for simple control, storage and selling it to plants which needs this byproduct is also feasible.

- *Proposed Process Flow Diagram (PFD)*

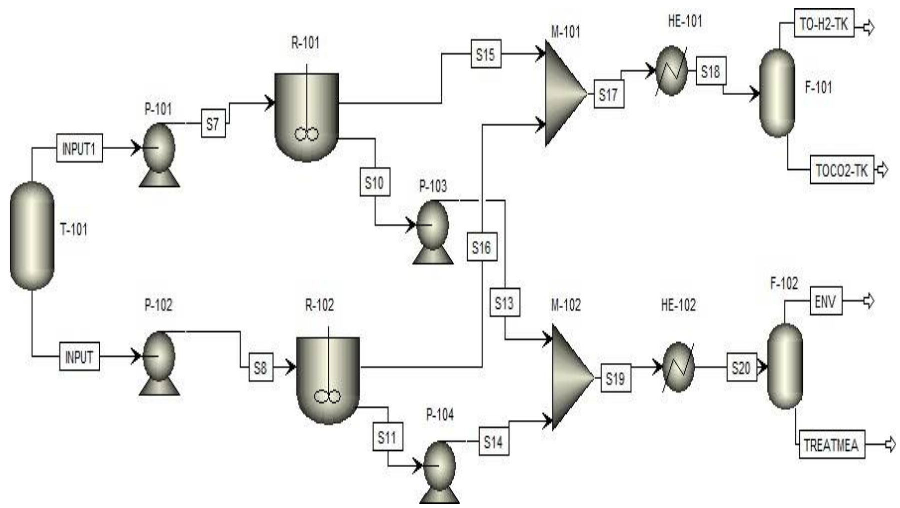

Figure 3 Simulation flow diagram for Hydrogen gas production.

From Figure 3, the treated effluent and glucose is stored in tank then it is separated to two reactors by using a divider with the help of a pump. Each reactor will receive around 1,160,000 kg/h of raw material at standard condition. Then the top product which contains mostly hydrogen gas and carbon gases will be mixed by using a mixer and cooled to have vapor fraction less than 1 to enhance the separation. At the end, the two-phase flow will enter the flash unit to produce Hydrogen as top product and the carbon will leave as bottom product. In another hand, the bottom product of reactor will be pumped to a mixer which contains mostly water, unreacted glucose, and acetic acid. After the mixer the mixture will be heated to reach vapor fraction above 1 to separate the unwanted gases such as CO2 and CO. At the end, the two-phase will enter the flash to separate mostly water with traces of dissolved gases at the bottom and carbons as gas phase from the distillate.

3. Results and Discussion

The simulation part focuses on analysing the outcome of the results obtained, based on utilizing different graphs comparison technique, for hydrogen production. These results obtained from Aspen Plus simulation software by sensitivity analysis include the effect of temperature, substrate flow rate, and pressure of the stream inlet on the hydrogen, CO2, and acetic acid production. The weight percent of the substrate in water is described in Table 4. The amount of water is 46,400 m3/day.

Table 4. Mass flow and weight percentages for the substrate

Input of Substrate (Kg/h)	Substrate in Water (wt.%)
500	0.022%
600	0.026%
700	0.030%
800	0.034%
900	0.039%
1000	0.043%
1100	0.047%
1200	0.052%
1300	0.056%
1400	0.060%
1500	0.065%

3.1 Temperature change

The effect of temperature on the research appears to aim at understanding how temperature changes affect hydrogen gas, carbon dioxide (CO2), and acetic acid production, while maintaining a constant pressure of 101.325 Kpa. The results of temperature effects on the reactor products at a fixed substrate rate of 1500 kg/hr with reference temperature of 37 oC are listed in Table 5. As seen from the results decreasing temperature has no impact on hydrogen production however it enhances CO2 production and decreases the acetic acid.

Table 5. The effect of temperature with fixed substate rate on the production rates

Temperature (C)	**Hydrogen Production (kg/h)**	**Difference (%)**	**CO_2 Production (kg/h)**	**Difference (%)**	**Acetic Acid Production (kg/h)**	**Difference (%)**
7	254.5492409	-0.014%	1211.576434	-20.322%	218.6941884	9.957%
37	254.5838036	0.000%	1520.585458	0.000%	198.890415	0.000%
67	254.6033791	0.008%	1588.450038	4.463%	168.4883795	-15.286%
97	254.6195359	0.014%	1606.659383	5.661%	123.7898137	-37.760%

- *Hydrogen Production with Temperature change and glucose rate change*

The data from Figure 2 can be used to understand the relationship between glucose input, temperature, and hydrogen production by using Aspen Plus Software. To analyse the data presented in

Figure 4, it would typically be fine to observe how the changes in glucose input levels for different number of runs affect the production of hydrogen gas at each of the specified temperatures (7°C, 37°C, 67°C, and 97°C) [44], while maintaining a constant water input as 2,000,000 (Kg/h).
From Figure 4 increasing the temperature has very small effect in hydrogen production [45]. However, the major change occurs for changing glucose input rate. For example, input of 500 (Kg/h) of glucose which will react with fixed amount of water will generate hydrogen with production rate of almost 84.79 (Kg/h) with different given temperatures. Also, for the glucose input of 1,500 (Kg/h) with the same input rate of water and temperature conditions, the hydrogen production is almost same 254.58 (Kg/h) for all temperatures [45]. The hydrogen gas will be separated with separation column (F-101) as the output of stream coming out from top product of reactor (R-101 and R-102).

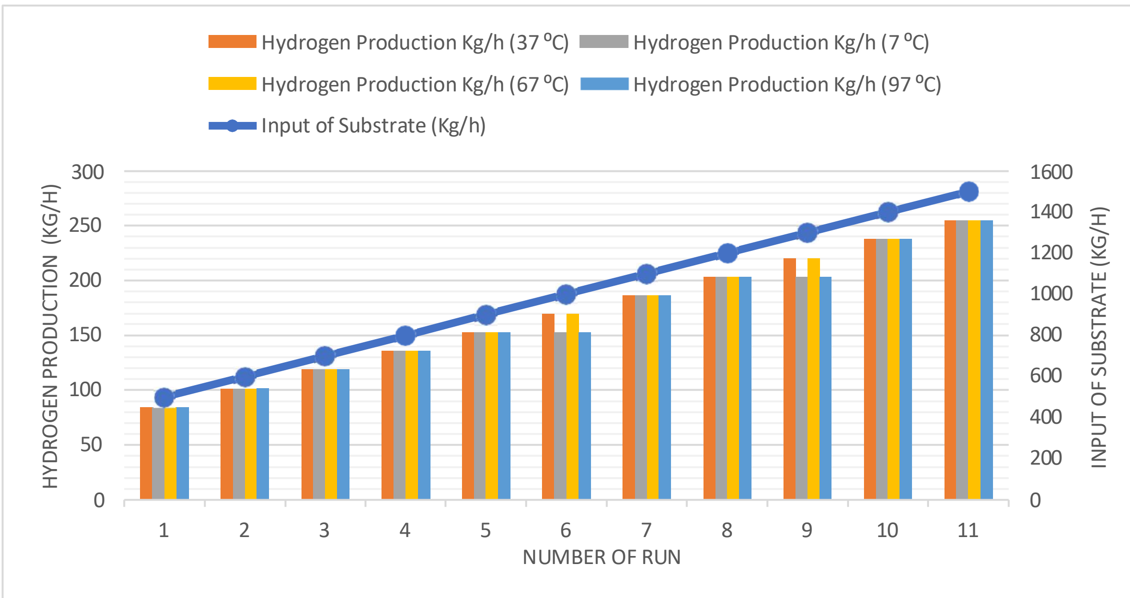

Figure 4. Hydrogen Production with Temperature and Glucose rate change.

- *Carbon Dioxide Production with Temperature and glucose rate change*

The observations highlight the influence of the glucose input rate on carbon dioxide production in the system. While temperature does have some effect, it appears to be secondary to the impact of varying the glucose input rate.
As represented in Figure 5, rising the temperature has small impact in carbon dioxide production as by product but, the major change occurs for changing glucose input rate. For instance, input of 500 (Kg/h) of glucose which will react with 2,000,000 (Kg/h) of water at 37 oC and 97 oC will produce carbon dioxide with production rate of approximately 459.78 (Kg/h) and 533.56 (Kg/h), respectively. Also, for the glucose input of 1500 (Kg/h) with the same input rate of water and temperature of 37 oC and 97 oC, the carbon dioxide production will increase significantly to reach 1211.57 (Kg/h) and 1606.65 (Kg/h), respectively. The carbon dioxide will be liquefied by heat exchanger and will be separated with separation column (F-101) as the output of stream coming out from top product of reactor (R-101 and R-102).

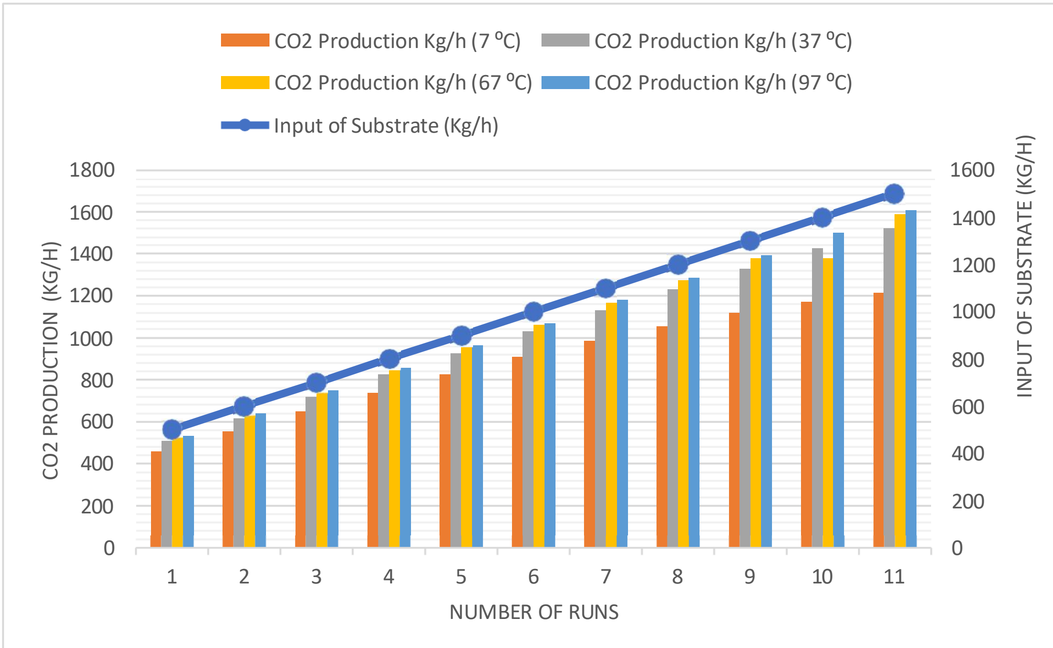

Figure 5. CO2 Production with temperature and glucose rate change

- *Acetic Acid Production with Temperature and glucose rate change*

The observations suggest that temperature has a significant and inverse effect on the production of acetic acid in your system, while glucose input rate positively influences its production. This information can be valuable for controlling and optimizing the production of acetic acid.

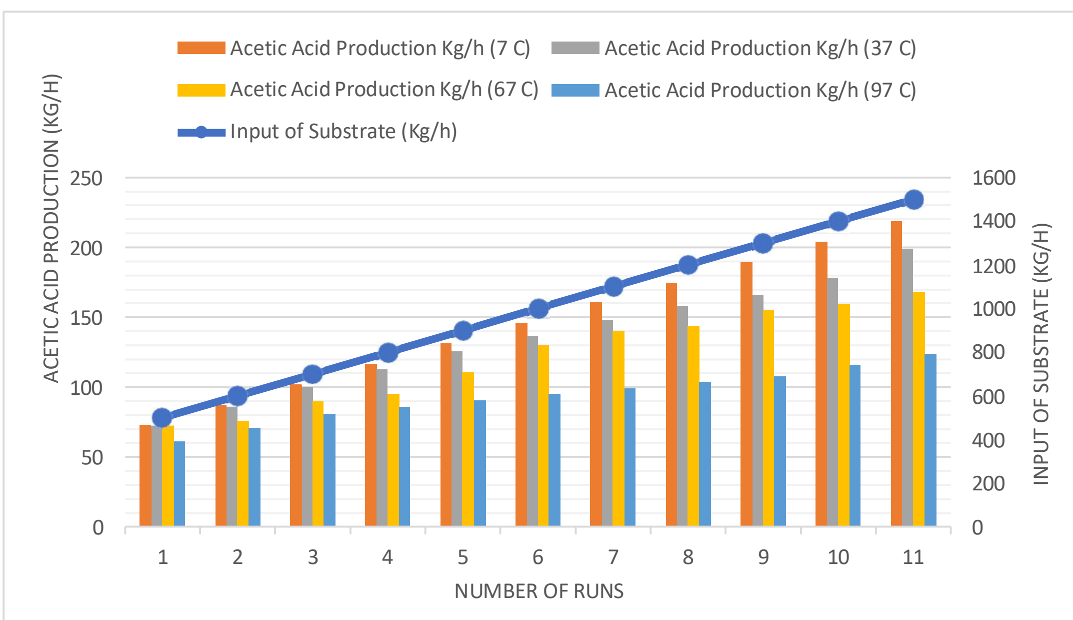

Figure 6. Acetic Acid Production with Temperature and Glucose rate change

When the glucose input is 1500 Kg/h and the temperature is 7°C, the production rate of acetic acid is 218.69 Kg/h. However, when the temperature is increased to 97°C under the same glucose input conditions (1500 Kg/h), the production rate of acetic acid decreases significantly to 123.78 Kg/h. Similarly, when the glucose input is reduced to 500 Kg/h at 7°C, the production rate of acetic acid is 72.89 Kg/h. But when the temperature is increased to 97°C under the same glucose input conditions (500 Kg/h), the production rate of acetic acid decreases to 60.87 Kg/h.

3.2 Pressure Changes

The influence of pressure on the production of hydrogen, carbon dioxide, and acetic acid has been studied at constant temperature at 37°C, constant substrate flow rate of 1500 kg/hr, and reference pressure of 101.325 kPa and the results are shown in Table 6 with. As can be seen from the results increasing pressure has no influence on the hydrogen and acetic acid production rate but reduces the CO2 production.

Table 6. The effect of pressure on the production rate at a fixed substrate flow rate

Pressure (kPa)	Hydrogen Production (kg/h)	Difference (%)	CO2 Production (kg/h)	Difference (%)	Acetic Acid Production (kg/h)	Difference (%)
101.325	254.5492409	0.000%	1520.585458	0.000%	218.6679415	0.0000%
202.65	254.4648304	-0.033%	1428.549447	-6.053%	218.6823717	0.0066%
303.975	254.3433192	-0.081%	1346.040299	-11.479%	218.6871273	0.0088%
405.3	254.2195235	-0.130%	1271.049655	-16.411%	218.6895234	0.0099%

Figure 7 illustrates the hydrogen output under different pressure conditions while varying the glucose input. The water input is mentioned as being fixed or constant throughout the experiment, with a value of 2,000,000 kg per hour.

Increasing the pressure in the reactor has relatively little impact on the production of hydrogen. The primary factor influencing hydrogen production appears to be the rate at which glucose is consumed. The largest change in hydrogen production occurs when the rate at which glucose is consumed changes. When 2,000,000 kilograms per hour of water and 1,500 kilograms per hour of glucose are combined, hydrogen is produced at a rate of almost 254 kilograms per hour.

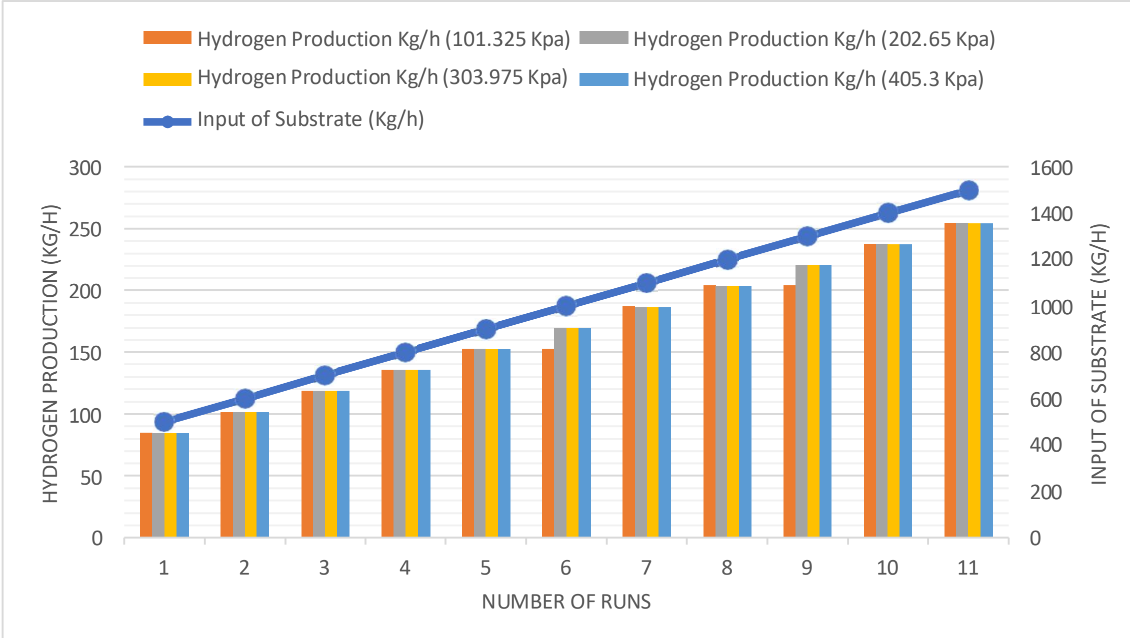

Figure 7. Hydrogen Production with pressure and glucose rate change

- *Carbon Dioxide Production with Pressure change*

Figure 8 shows a different aspect of the study process, specifically the production of Carbon Dioxide in response to varying glucose input, pressure levels, and a constant temperature of 37°C. Increasing pressure has little effect on Carbon Dioxide production as a byproduct. This suggests that changes in pressure levels do not significantly impact the rate of CO2 production. The significant shift in CO2 production is primarily determined by the rate of glucose input, as indicated by temperature analysis. Higher glucose input rates result in higher CO2 production.

When 500 kilograms per hour of glucose reacts with 2,000,000 kilograms per hour of water at 101.325 Kpa and 202.65 Kpa, it produces roughly 510.17 kilograms per hour and 481.728 kilograms per hour of CO2, respectively. This demonstrates the impact of pressure on CO2 production at a lower glucose input. When using a glucose input rate of 1,500 kg/h, a water input rate of the same amount, and pressures of 101.325 Kpa and 202.65 Kpa, the CO2 flow rates are 1520.58 kg/h and 1428.54 kg/h, respectively. This illustrates the relatively small effect of pressure on CO2 production at a higher glucose input.

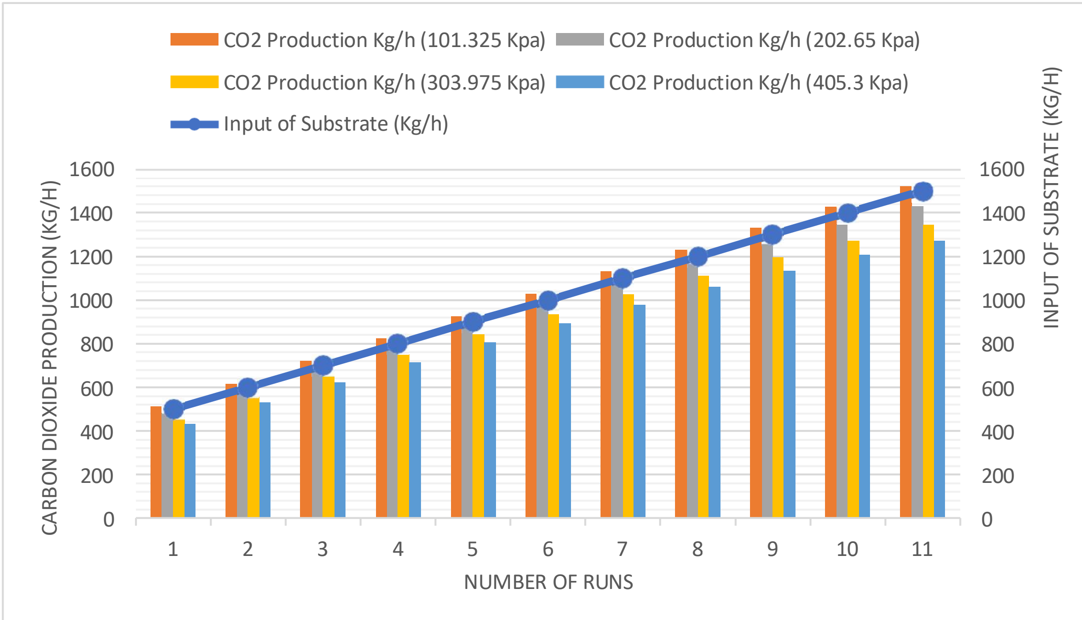

Figure 8. Carbon Dioxide Production with Pressure change

Carbon Dioxide will exist in two phases (gas and liquid) under high pressure. These phases are separated using separation columns (F-101 and F-102). The output streams from the top and bottom products of the reactor (R-101 and R-102) are processed to separate and collect the different phases of CO_2.

- *Acetic Acid Production with Pressure change*

Changes in glucose input and pressure levels affect the production of acetic acid in a chemical process with a constant temperature and fixed water input. Figure 9 shows how these variables impact acetic acid output. Figure 9 illustrates the production of acetic acid as an output in response to varying glucose input, pressure levels, and a constant temperature of 37°C. As it is clear from Figure 9, the production of acetic acid is not affected by the pressure. When glucose is added at a rate of 500 kg/h, acetic acid is produced at rates of around 72 kg/h for different levels of pressure. This demonstrates that pressure has a minimal impact on acetic acid production.

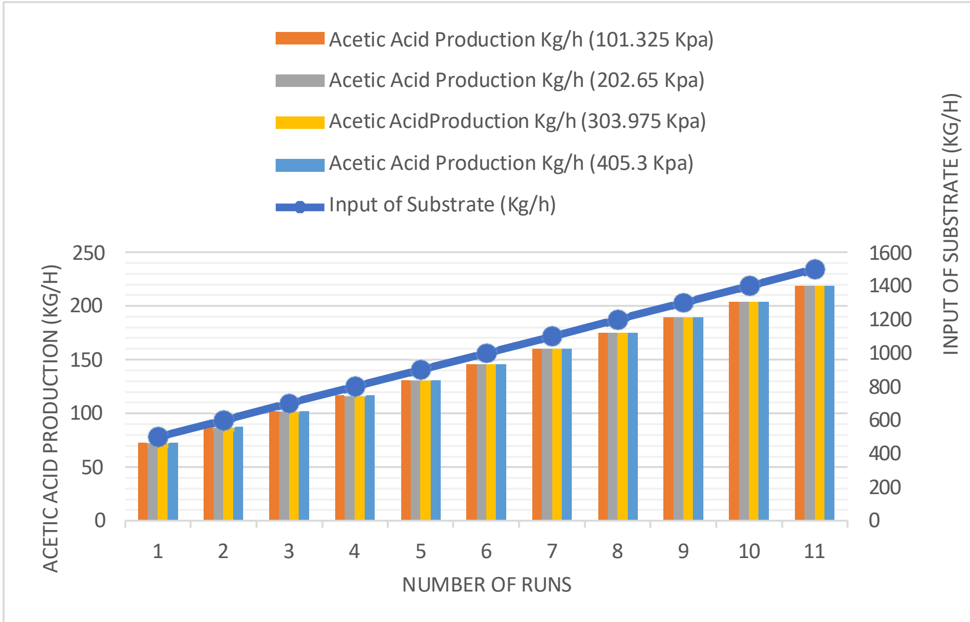

Figure 9. Acetic Acid Production with pressure change

3.3 Selection of Optimum Temperature and Pressure for Outputs

The findings of the biohydrogen gas process suggest that controlling the glucose input rate and maintaining a specific temperature and pressure can optimize the production of hydrogen, carbon dioxide, and acetic acid in the process. It's essential to consider these factors when designing or optimizing the production process for these chemicals.

Hydrogen and carbon dioxide production rates are not significantly influenced by changes in temperature. On the other hand, acetic acid production is negatively impacted by increasing temperature, as higher temperatures lead to a decrease in acetic acid production.

Pressure changes do not have a significant impact on hydrogen and acetic acid production rates. However, carbon dioxide production rates increase with higher pressure, indicating a positive correlation between pressure and carbon dioxide production.

The most significant factor affecting the production rates of hydrogen, carbon dioxide, and acetic acid is the glucose input rate. Increasing the glucose input rate leads to higher production rates of hydrogen, carbon dioxide, and acetic acid.

Based on the analysis, to save energy and increase acetic acid production, the recommended operating temperature is 37°C. Also, the best operating pressure condition is 101.325 kPa to mitigate the negative impact of CO2 production [45]. These conditions result in the production of approximately 84.76 kg/h of hydrogen to almost 254.54 kg/h of hydrogen when the glucose input rate varies between 500 and 1,500 kg/h.

4. Conclusions

Simulating the production of hydrogen gas can be a valuable tool for understanding and optimizing the processes involved. Computer simulations allows to model the behaviour of hydrogen production systems, assess various parameters, and predict outcomes without the need for physical experimentation. Aspen-Plus is widely used in industries such as petrochemicals, refining, and energy production, where hydrogen plays a crucial role. Engineers and researchers use it to design, analyse, and optimize hydrogen production systems, assess the impact of process changes, and ensure the efficiency and safety of hydrogen-related processes. It is a versatile tool that can be tailored to specific applications, including hydrogen gas production from various feedstocks. For Biohydrogen gas production process from sewage treatment plants, Aspen-Plus software is used to study the impact of changing the temperature and the pressure to the hydrogen, carbon dioxide, and acetic acid production as presented in this paper, considering optimum temperature and pressure. Based on the analysis, hydrogen and carbon dioxide production rates are not significantly influenced by changes in temperature. On the other hand, acetic acid production is negatively impacted by increasing temperature, as higher temperatures lead to a decrease in acetic acid production. In order to save energy and to increase the production of acetic acid which can be used for other purposes, the operating condition for the temperature is 37°C. Also, pressure changes do not have a significant impact on hydrogen and acetic acid production rates. However, carbon dioxide production rates increase with higher pressure. The best operating condition for the pressure is 101.325 kPa, this will help to reduce the negative impact of CO2 production. The production of hydrogen gas using these optimum operating conditions improved the obtained results from approximately 84.76 kg H2/h to almost 254.54 kg H2/h, by varying the glucose input rates between 500 and 1,500 kg/h.

Funding: The research leading to these results has received funding from the Ministry of Higher Education, Research and Innovation (MoHERI) of the Sultanate of Oman under BFP. MoHERI Block Funding Agreement No **BFP/RGP/EI/23/455.**

Acknowledgments: The authors would like to gratefully acknowledge the funding for the project provided by Ministry of Higher Education, Research and Innovation (MoHERI) of the Sultanate of Oman under BFP. MoHERI Block Funding Agreement No BFP/RGP/EI/23/455. The authors would like to express their gratitude to NAMA Water Services, Oman, for their support in data collection and the sampling process throughout the entire period of the project. Special thanks also go to GUtech for providing access to facilities, laboratories, materials, and the use of Aspen Plus software, which were instrumental in the completion of this project.

References

1. Depren, S. K., Kartal, M. T., Çelikdemir, N. Ç., & Depren, Ö. (2022). Energy consumption and environmental degradation nexus: A systematic review and meta-analysis of fossil fuel and renewable energy consumption. Ecological Informatics, 70, 101747.
2. Paramati, S. R., Shahzad, U., & Doğan, B. (2022). The role of environmental technology for energy demand and energy efficiency: Evidence from OECD countries. Renewable and Sustainable Energy Reviews, 153, 111735.
3. Olabi, A. G., & Abdelkareem, M. A. (2022). Renewable energy and climate change. Renewable and Sustainable Energy Reviews, 158, 112111.
4. Abbasi, K. R., Shahbaz, M., Zhang, J., Irfan, M., & Alvarado, R. (2022). Analyze the environmental sustainability factors of China: The role of fossil fuel energy and renewable energy. Renewable energy, 187, 390-402.
5. Ang, T. Z., Salem, M., Kamarol, M., Das, H. S., Nazari, M. A., & Prabaharan, N. (2022). A comprehensive study of renewable energy sources: classifications, challenges and suggestions. Energy Strategy Reviews, 43, 100939.
6. Mousavi, Y., Bevan, G., Kucukdemiral, I. B., & Fekih, A. (2022). Sliding mode control of wind energy conversion systems: Trends and applications. Renewable and Sustainable Energy Reviews, 167, 112734.
7. Kannan, N., & Vakeesan, D. (2016). Solar energy for future world:-A review. Renewable and Sustainable Energy Reviews, 62, 1092-1105.
8. Ozturk, M., Bezir, N. C., & Ozek, N. (2009). Hydropower–water and renewable energy in Turkey:

Sources and policy. Renewable and Sustainable Energy Reviews, 13(3), 605-615.

9. BP. (2018). Statistical review of world energy. https://www.bp.com/content/dam/bp/en/corporate/pdf/energy-economics/statistical-review/bp-stats-review-2018-full-report.pdf
10. BP. (2020). Statistical review of world energy—full report—BP statistical review of world Energy; 69th edition. https://www.bp.com/content/dam/bp/business-sites/en/global/corporate/pdfs/energy-economics/statistical-review/bp-stats-review-2020-full-report.pdf
11. Al-Sarihi, A., & Mason, M. (2020). Challenges and opportunities for climate policy integration in oil-producing countries: The case of the UAE and Oman. Climate Policy, 20(10), 1226–1241. https://doi.org/10.1080/14693062.2020.17810
12. IRENA. (2019). Renewable energy market analysis: GCC 2019. International Renewable Energy Agency.
13. Samour, A., Tawfik, O. I., Radulescu, M., & Baldan, C. F. (2023). Do Oil Price, Renewable Energy, and Financial Development Matter for Environmental Quality in Oman? Novel Insights from Augmented ARDL Approach. Energies, 16(12), 4574.
14. Bahgat, G. (2023). A New Dawn in Oman: Challenges and Opportunities. Journal of South Asian and Middle Eastern Studies, 47(1), 76-89.
15. Edwards, P. P., Kuznetsov, V. L., & David, W. I. (2007). Hydrogen energy. Philosophical Transactions of the Royal Society A: Mathematical, Physical and Engineering Sciences, 365(1853), 1043-1056.
16. Rosen, M. A., & Koohi-Fayegh, S. (2016). The prospects for hydrogen as an energy carrier: an overview of hydrogen energy and hydrogen energy systems. Energy, Ecology and Environment, 1(1), 10-29.
17. Ngoh, S. K., & Njomo, D. (2012). An overview of hydrogen gas production from solar energy. Renewable and Sustainable Energy Reviews, 16(9), 6782-6792.
18. Arun, J., Sasipraba, T., Gopinath, K. P., Priyadharsini, P., Nachiappan, S., Nirmala, N., ... & Pugazhendhi, A. (2022). Influence of biomass and nanoadditives in dark fermentation for enriched bio-hydrogen production: A detailed mechanistic review on pathway and commercialization challenges. Fuel, 327, 125112.
19. Ram, M., & Mondal, M. K. (2022). Biomass gasification: a step toward cleaner fuel and chemicals. In Biofuels and Bioenergy (pp. 253-276). Elsevier.
20. Kumar, J. A., Sathish, S., Krithiga, T., Praveenkumar, T. R., Lokesh, S., Prabu, D., ... & Rajasimman, M. (2022). A comprehensive review on bio-hydrogen production from brewery industrial wastewater and its treatment methodologies. Fuel, 319, 123594.
21. Singh, N., & Sarma, S. (2022). Biological routes of hydrogen production: a critical assessment. In Handbook of Biofuels (pp. 419-434). Academic Press.
22. Kamran, M. (2021). Fuel cell. Renewable energy Conversion Systems, 221.
23. Koutra, E., Tsafrakidou, P., Sakarika, M., & Kornaros, M. (2020). Microalgal biorefinery. In Microalgae Cultivation for Biofuels Production (pp. 163-185). Academic Press.
24. Singh, N., & Sarma, S. (2022). Biological routes of hydrogen production: a critical assessment. In Handbook of Biofuels (pp. 419-434). Academic Press.
25. Paesi, S., Schiavenin, A., Almeida, L. G., Andreis, D., Magrini, F. E., Marconatto, L., ... & Giongo, A. (2022). Comparison of two different kinds of seed sludge and characterization of microorganisms producing hydrogen and soluble metabolites from raw glycerol. Brazilian Journal of Chemical Engineering, 39(2), 387-402.
26. Longfor, N. R., DONG, L., Wang, J., & Qian, X. A Techno-Economic Review on Biomass Waste-to-Energy Potential in Cameroon. Available at SSRN 4241699.
27. Fu, S., Lian, S., Angelidaki, I., & Guo, R. (2022). Micro-aeration: an attractive strategy to facilitate anaerobic digestion. Trends in Biotechnology.
28. Cao, Y., Liu, H., Liu, W., Guo, J., & Xian, M. (2022). Debottlenecking the biological hydrogen production pathway of dark fermentation: insight into the impact of strain improvement. Microbial Cell Factories, 21(1), 1-16.
29. Khan, S. A. R., Ponce, P., Yu, Z., Golpîra, H., & Mathew, M. (2022). Environmental technology

and wastewater treatment: Strategies to achieve environmental sustainability. Chemosphere, 286, 131532.

30. Chen, X., Zhao, B., Shuai, C., Qu, S., & Xu, M. (2022). Global spread of water scarcity risk through trade. Resources, Conservation and Recycling, 187, 106643.
31. Fu, H., Niu, J., Wu, Z., Xue, P., Sun, M., Zhu, H., & Cheng, B. (2022). Influencing factors of stereotypes on wastewater treatment plants-Case study of 9 wastewater treatment plants in Xi'an, China. Environmental Management, 1-10.
32. Chen, R., Yuan, S., Chen, S., Ci, H., Dai, X., Wang, X., ... & Dong, B. (2022). Life-cycle assessment of two sewage sludge-to-energy systems based on different sewage sludge characteristics: Energy balance and greenhouse gas-emission footprint analysis. Journal of Environmental Sciences, 111, 380-391.
33. Zhang, X., Ye, P., & Wu, Y. (2022). Enhanced technology for sewage sludge advanced dewatering from an engineering practice perspective: A review. Journal of Environmental Management, 321, 115938
34. Ananthi, V., Ramesh, U., Balaji, P., Kumar, P., Govarthanan, M., & Arun, A. (2022). A review on the impact of various factors on biohydrogen production. International Journal of Hydrogen Energy.
35. Elbeshbishy, E., Dhar, B. R., Nakhla, G., & Lee, H. S. (2017). A critical review on inhibition of dark biohydrogen fermentation. Renewable and Sustainable Energy Reviews, 79, 656-668.
36. Usman, T. M., Banu, J. R., Gunasekaran, M., & Kumar, G. (2019). Biohydrogen production from industrial wastewater: an overview. Bioresource Technology Reports, 7, 100287.
37. Mikheeva, E. R., Katraeva, I. V., Vorozhtsov, D. L., Kovalev, D. A., Kovalev, A. A., Grigoriev, V. S., & Litti, Y. V. (2022). Dark fermentative biohydrogen production from confectionery wastewater in continuous-flow reactors. International Journal of Hydrogen Energy.
38. ROY, Partho S.; AMIN, M. Ruhul. Aspen-HYSYS simulation of natural gas processing plant. Journal of Chemical Engineering, 2011, 26: 62-65.
39. Apostolakis, J., Bandieramonte, M., Banerjee, S., Bartosik, N., Corti, G., Cosmo, G., ... & Paganetti, H. (2022). Detector simulation challenges for future accelerator experiments. Frontiers in Physics, 10, 913510.
40. Sanchz M., Amores E., Abad D., Rodriguez L., and Clemente-Jul C., (2020). Aspen Plus model of an alkaline electrolysis system for hydrogen production, International Journal of Hydrogen Energy, 45, 3916-3929.
41. Nasser, M., & Emad, M. Steady state simulation of production of sulfuric acid by contact process using Aspen-Plus V8. 8.
42. Barghash, H., Al Farsi, A., Okedu, K. E., & Al-Wahaibi, B. M. (2022). Cost benefit analysis for green hydrogen production from treated effluent: The case study of Oman. Frontiers in Bioengineering and Biotechnology, 10, 1046556.
43. Barghash, H., AlRashdi, Z., Okedu, K. E., & Desmond, P. (2022). Life-Cycle Assessment Study for Bio-Hydrogen Gas Production from Sewage Treatment Plants Using Solar PVs. Energies, 15(21), 8056.
44. Haydary, J. (2019). Chemical process design and simulation: Aspen Plus and Aspen Hysys applications. John Wiley & Sons.
45. Barghash H, Okedu KE and Al Balushi A (2021) Bio-Hydrogen Production Using Landfill Leachate Considering Different Photo Fermentation Processes. Front. Bioeng. Biotechnol. 9:644065. doi: 10.3389/fbioe.2021.644065

Autopilot Triple Modular Redundancy Approach for Unmanned Aerial Vehicles

Mohammad Kdaisat[1].

[1] MARSROBOTICS;
***** *Corresponding authors: kdaisat@marsrobotic.com; Tel.: +962780375885*

Abstract: Tactical or MALE UAVs have a very high price components and any failure could lead to catastrophic consequences. By improving fault tolerance and reliability, this project aims to maintain safe navigation and mission continuity even in challenging conditions. The Triple Modular Redundancy (TMR) for UAV autopilot ensures reliable operation despite potential autopilot failures. The current phase of the autopilot TMR project focuses on autopilot outputs only, excluding redundancy for other components, such as sensors. TMR utilizes three parallel autopilot systems, with a voter that work based on a logic to determine the correct output by comparing the autopilots output and eliminating any deviating signals. This system ensures continuous functionality in complex environments and avoids risks associated with malfunctions. The voter logic employs a majority principle to manage differences among autopilot outputs, ensuring that any faulty output is excluded from the control process. Currently, the ground station connects to the TMR system via external transceiver, while autopilots communicate internally with the voter through a CAN bus. Data from each autopilot is compared in the voter system based on control surfaces deflections. The system checks for Variances, values outside the normal behavior, and noise. A scoring system is included to prioritize reliable autopilots.

Keywords: Triple Modular Redundancy; Reliability; Fault Tolerance; Fault Detection.

1. Introduction

This study focuses on enhancing the reliability of systems that require high availability, such as those used in safety-critical applications. The Triple Modular Redundancy (TMR) approach uses three identical components to provide fault tolerance. If one component fails, the other two can still function correctly, allowing the system to continue operating. Previous research has shown that TMR can significantly reduce the risk of system failure. The aim of this work is to design and implement a TMR system that maintains performance and reliability.

F S Pranoto et al. [1] designed a preliminary redundancy management system for the LAPAN Surveillance Aircraft (LSA-02) automatic flight control system (AFCS). Their approach used a combination of cold standby redundancy for critical actuators and dual modular redundancy (DMR) for flight control computers. The results indicated that the redundant system enhances safety by mitigating risks during critical component failures.

Li et al. [2] presented a Triple Modular Redundancy (TMR) solution aimed at enhancing hardware security, specifically to counteract potential supply chain attacks such as hardware Trojans. Using an FPGA-based implementation of soft-core processors, they tested the system with four benchmark applications, including UAV autopilot systems. Their results showed that the TMR setup successfully prevented hardware Trojans from causing significant harm.

Feldstein et al. [3] designed a fault-tolerant flight control system based on a Triple Modular Redundancy (TMR) configuration. Implemented on a PC/104 embedded platform, their system was tested using Microsoft Flight Simulator to validate its ability to tolerate a single fault during flight operations. Their results indicated that while the system could handle one fault, further work is required to meet real-time performance requirements necessary for operational flight control systems

2. Materials and Methods

The TMR system consists of three identical processing units and a voting mechanism to ensure accurate decision-making. Each component operates independently but provides its output to the voter, which selects the most common output.

2.1 Software in the loop simulation (SILS) components

The TMR SILS model consists of three independent autopilot models that receives the same data from the ground station. The outputs of these three autopilots then goes into the mathematical model of the aircraft. The states of the UAV are then sent from the mathematical model to the three autopilot models. Based on these states, each autopilot then evaluates the deflection for the UAV control surfaces.

The output deflections then go into the voting algorithm to check the validity of each autopilot outputs and select one autopilot outputs to be sent to the ground station.

2.2 Hardware in the loop simulation (HILS) components

The HILS model consists of three autopilot boards and a voter processing unit mounted on to the redundancy management board. The TMR management board powers the autopilot boards and connects them to the sensors and actuators through the main connector. An illustrative structure is shown in the following figure

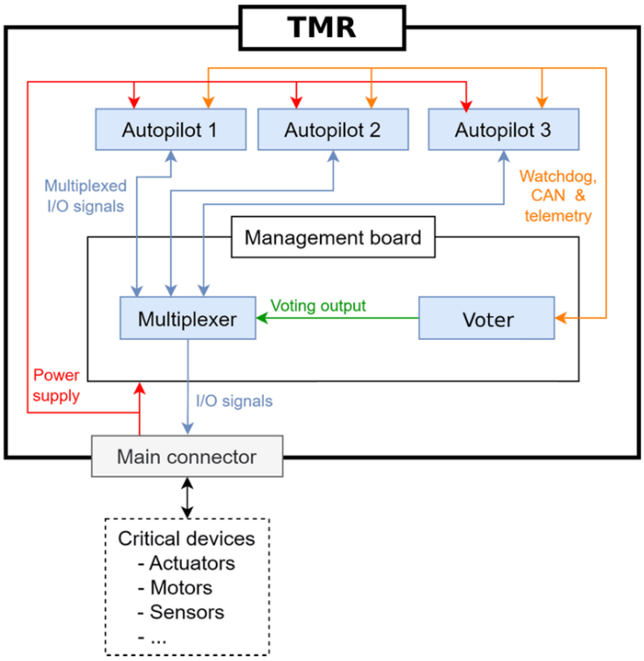

2.2 Voting method and algorithm

The main method used in the voting process is the majority voting, where the output data of each autopilot is compared relative to each other, if the error between one of the autopilots with the other two exceeds a certain threshold, this auto pilot is labeled as failure autopilot and excluded from the voting process.

There is a scoring system used to indicate which autopilot is more reliable than others. The score of each autopilot depends on the healthy operating time. So, when one of the autopilots is declared as a failed autopilot, its score will drop down rapidly.

3. Results and Discussion

Currently, the project is in the development phase, and final results are pending. Initial tests have shown that the design works as expected under controlled conditions.

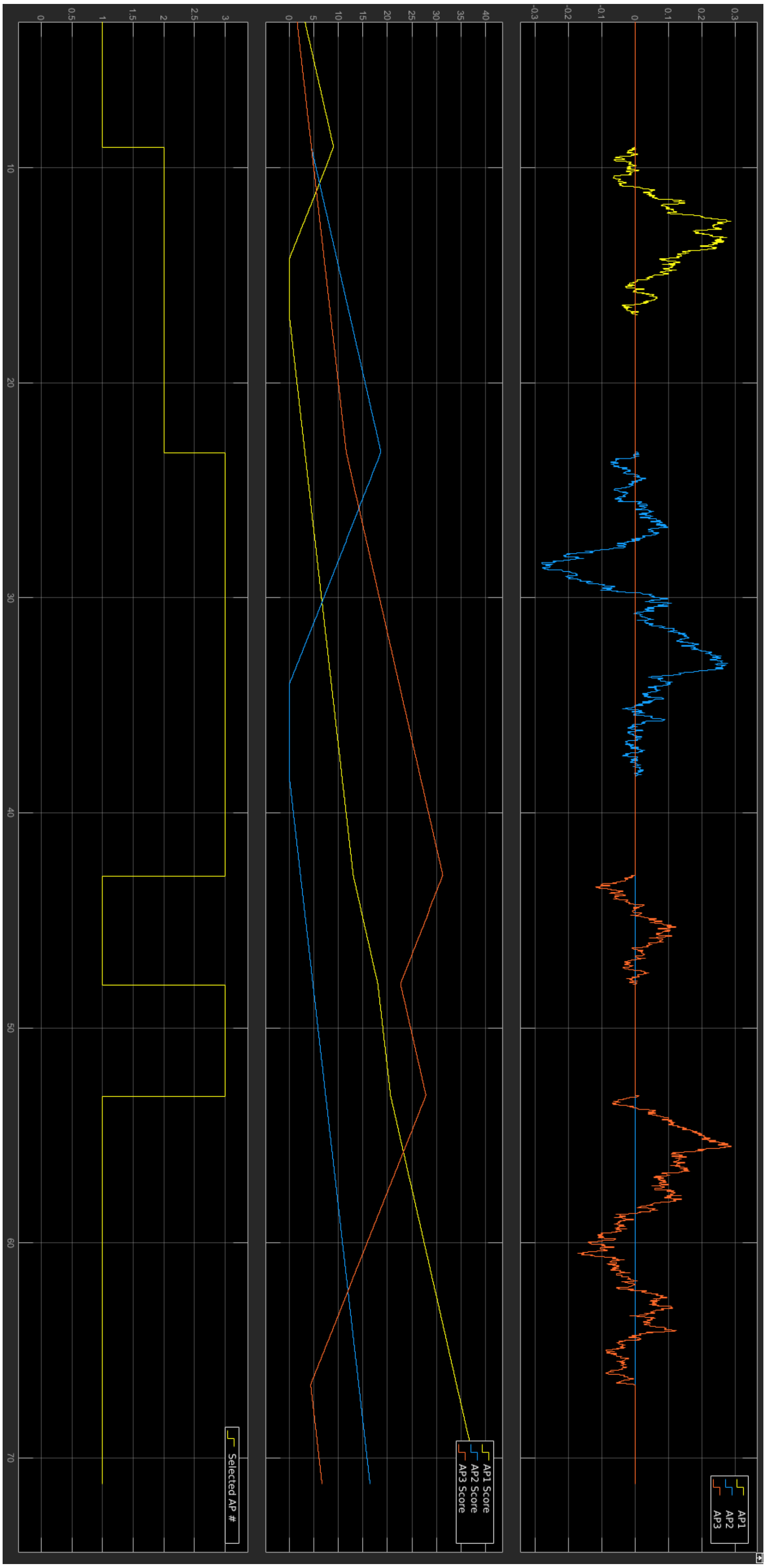

Figure 1: SILS Model Results

In the above figure, the first section shows the health of each autopilot outputs, where the fluctuation indicates a failure in the autopilot. The second section shows the score of each autopilot, a positive slope indicates increase in the score and a negative slope indicates decrease in the score when a failure occurs. The last part shows the number of the selected autopilot.

4. Conclusions

In the conclusion, the preliminary tests show promising results, where the system behaves as it should. If an autopilot fails, the voter switches the selected autopilot to the highest score healthy autopilot, and the score of the failed autopilot will drop rapidly. Future tests will evaluate the system's performance under various failure scenarios.

Funding: This research received no external funding.

Acknowledgments: I want to express my gratitude to my team for their continuous support whenever I needed it.

References

1. Pranoto, F. S., and A. Wirawan. "Preliminary design of redundancy management for LSA-02 automatic flight control system." *Journal of Physics: Conference Series*. Vol. 1130. No. 1. IOP Publishing, 2018.
2. Li, Yubo, and Kevin Skadron. "TMR: A Solution for Hardware Security Designs." (2015).
3. Feldstein, Cary Benjamin, and J. C. Muzio. "Development of a fault tolerant flight control system." *The 23rd Digital Avionics Systems Conference (IEEE Cat. No. 04CH37576)*. Vol. 2. IEEE, 2004.

Translator from Arabic/English languages to Braille Using Solenoid Motors and Arduino Microcontroller

Ramzi Saifan (1) r.saifan@ju.edu.jo
Hadeel Saleh (1) HadeelAhmadSaleh@gmail.com
Heba Tawfeq (1) HebaTawfeq49@gmail.com
Musa AlYaman (2) m.alyaman@ju.edu.jo

(1) Department of Computer Engineering
University of Jordan
Amman, Jordan

(2) Department of Mechatronics Engineering
University of Jordan
Amman, Jordan

Abstract - People are blessed with five senses. Losing any of them, makes the life of that person as well as the surrounding people very hard. This paper presents a system that focuses on helping people who lost the sight sense (i.e., blind people), their families, and their close people to live easier and to engage the blind people in the society and in the life, especially in the educational process. In this paper, we propose a system that can translate Arabic and English text files into Braille Language. Specifically, the proposed system is composed of two parts: a hardware device that performs Braille translation and an Android application. The application is used to send a text file via Bluetooth to the hardware device. The hardware device is composed of 48 solenoid motors controlled by an Arduino-Mega2560 to translate text files into Braille language word by word. To achieve this goal, the microcontroller reads a text file word by word, and starts moving a set of solenoid motors up and down to form a word that can be read by visually impaired people. Additionally, the user can choose to convert the text file into voice record.

The proposed system was tested on visually impaired people and people who want to learn Braille language. The results were impressive where we found that 100% of the people who did the test agree that the suggested system contributes in enhancing the education process for visually impaired people. Also, they agreed that the proposed system facilitates the communication and involvement of blind people in the society. Results demonstrated the effectiveness of our device in correctly reproducing alphanumeric content, and opening promising perspectives in every-day life applications.

Keywords: embedded systems; Braille language; solenoid; blind people

I. Introduction

Sight is a blessing that not all people have it. People who have a visual disability are called Visually Impaired people (VI) or blind people. Visual impairment can be defined as the reduced ability to see which causes problems in vision that are not fixable by usual means, such as glasses [1]. The estimated number of people who are visually impaired in the world is 285 million divided into 39 million blind and 246 million low vision [2].

VI people face difficulties to perform everyday routines and activities such as learning, writing, and especially reading. Therefore, a special language called Braille language was invented in 1824. Even though Braille has made reading easier for the VI people, there are still problems with the size of the printed materials. In addition, Braille printers are of high cost and unavailable everywhere. Also, printing one Braille page costs between (30$ to 50$) [3], which is very expensive, especially for VI students and those who need printed materials around the clock.

On the other hand, technological solutions are being increasingly used in different areas. Also, they have a massive impact on many aspects of our lifestyle. Therefore, it is necessary to use technology to simplify the life of regular as well as disabled people.

The Main idea of our system is to present a solution that assists blind people who use Braille language for reading. We present a hardware device which simplifies the process of converting any text file whether it is in Arabic or in English into Braille language, and consequently eliminates the need for physical Braille printers. We will use 48 Solenoid motors instead of Braille printers to translate a text file into Braille language. Specifically, each six solenoids on the device will represent a letter, and each set of letters will represent a word.

For the proposed system to be more complete and usable by the VI people, the proposed system has the option of translating the text file into voice record. Additionally, the proposed system includes a learning feature which allows regular people to learn Braille language in Arabic and English.

The outline of the paper is as follows: in Section 2, some background and similar systems are introduced. The design and implementation details of the proposed system are presented in Section 3. Then, the results from using the system are summarized in Section 4. Finally, we conclude and give some future work directions in Section 5.

II. Background and Related Work

This section is divided into two parts: the first part gives background information about Braille language, Arduino, and Solenoid motors. The second part introduce a survey of some related work.

A. Background

Braille is a special language that was invented in 1824. In Braille, letters are formed as six touchable dots that can be touched by VI people to represent letters. Based on which dots are raised and which are not, the letters are formed. Different letters have different patterns of these dots. Also, each language has its own representation of the letters using these dots. The dots' positions are identified by numbers from one to six [4]. Interestingly, reading is from left to right in all languages. Each six dots form a cell, where the cell can be used to represent a letter, number, punctuation mark, or even a word as shown in Figure 1 and Figure 2 for English and Arabic Braille alphabets, respectively.

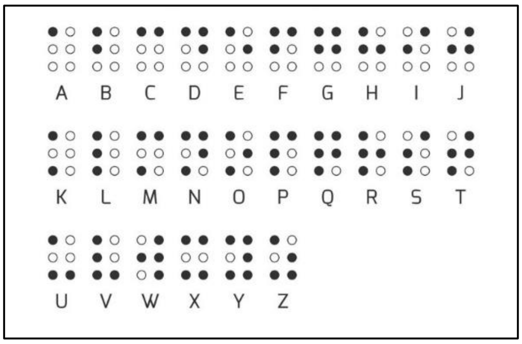

Figure 1 - English Braille alphabets [5]

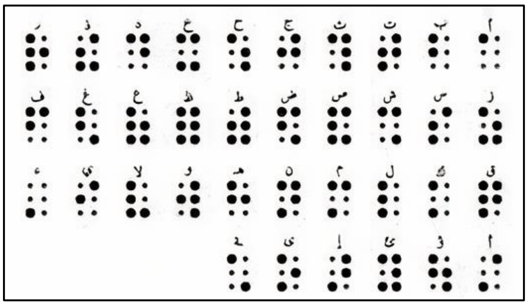

Figure 2 - Arabic Braille alphabets [6]

The microcontroller to be used for this system is Arduino. Arduino boards can read inputs and turn them into outputs. To do so, the Arduino programming language (based on Wiring) can be used.

Solenoids are basically electromagnets motors which result in linear motion: they are made of a big coil of copper wire with a piece of metal in the middle. When the coil is energized, the metal is pulled into the center of the coil. This makes the Solenoid motor to pull and push (ON or OFF).

B. Related Work

To overcome the problem of high cost Braille books, development of efficient Braille reading devices has been investigated by many researchers. Zhou et. al. developed a portable Braille reading system based on electro-tactile display technology [7]. Their system has three main parts: six-channel electro-tactile stimulator, a flexible electrode array for Braille display, and a graphical user interface (GUI) for monitoring and control. The authors proposed two Braille reading strategies, these are: spatial mode and sequential mode. In the spatial mode, the six dots are ON and OFF at the same time to represent one letter. On the other hand, in Sequential mode, the six dots are raised sequentially one after the other. Electro-tactile display is a haptic device that directly generates sensations with electric current [8]. By using surface electrodes, the electro-tactile display can stimulate receptors within the skin.

Aranyanak et. al. [9] designed a high-resolution finger-tracking system which utilizes components which provide temporal and spatial resolution of finger movements. They used a Nintendo Wii gaming device in their system which contains built-in infrared camera, which can calculate the positions of up to four infrared light sources. The used tracking system comprises a refreshable braille display, a Wiimote, four infrared LEDs, and a laptop that integrates the components. Hand tracking is accomplished by attaching an infrared LED to one or two of a subject's reading fingers and using feedback from the Wiimote's infrared camera to determine the locations of the two light sources. To display braille characters under computer control, they used the Easy Braille refreshable display. This is an electromechanical device that comprises 40 braille cells. To display the braille dot patterns, small rounded pins are raised and lowered through holes in the cell surface.

Breidegard et al. [10] introduced an automatic finger-tracking system (AFTS) for identifying finger location in video recordings of braille readers. The AFTS used an algorithm based on template matching and filtering to detect and track the readers' fingertips. The system had two cameras. The first camera was placed underneath a semitransparent braille sheet mounted on a transparent glass plate. Its spatial resolution was 768×576 pixels, and the resolution of a second camera, located at an angle above the fingers, was 320×240 pixels. The frame rates of both cameras were 25 FPS.

Hughes [11] constructed a device for examining the movement kinematics of braille readers. The equipment comprised a digitizing tablet about 30 cm square with a spatial resolution of 0.1 mm. The tip of a digitizing pen was attached to the end of the dominant reading fingertip and connected to the pen's electronics, which were mounted separately on the reader's forearm. The tip of the pen was 3–10 mm distant from the reading finger's center, and the reading surface was not touched by the pen. The sampling rate of the system was 100 Hz.

A system called Tactile was invented by a team from MIT [12]. Their device can display six characters at a time, and has a built-in camera. Users can place it down on a line of text with the press of a button then the device takes a picture. Optical character recognition (OCR) then takes over, identifying the characters on the page using Microsoft's Computer Vision API. Then the software translates each character into braille and subsequently triggers the mechanical system in the box to raise and lower the pins.

In [13], the authors designed a Braille display device operates by electronically lowering and raising different combinations of pins to produce in Braille what appears on a portion of the computer screen. The Braille display takes the information that appears on the computer screen, translates it, and displays it in Braille one line at a time. A line of refreshable Braille consists of a series of electronically driven pins that pop up to form Braille characters. When the cursor on screen moves across a line or down the page, the Braille line changes to reflect what is currently under or near the cursor. This is called refreshable.

Since Braille Language Translator is an enhancement of Braille Translators, showing differences between them is very important. First, translation will be for both English and Arabic text files into Braille language. Also, the proposed system can be used by people without visual or hearing problems to learn Braille and Sign language and simplify the communication with blind and deaf people.

III. Solution Description and Implementation

The proposed system is a Braille translator that consists of two parts: An Android application and a hardware device. The Android application is used to upload text a file and consequently send it via Bluetooth to translate it into Braille language. Then, the hardware will start mapping the received text letters with the proper Braille characters and view them in sequence. Another option is supported by the Android application for blind users is translating the uploaded text file into a record. In Figure 3, the overall structure of the system is displayed. The objective behind using potentiometer is to control the speed of displaying the text in Braille language.

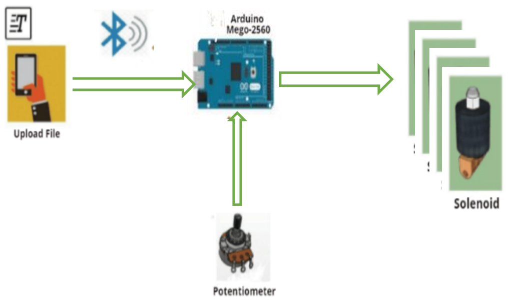

Figure 3 - System structure

Figure 4 shows the workflow of the system. Specifically, if the user clicks “Braille Language” button; the two “upload text file” buttons will appear to enable the user to upload a text file written in English or Arabic. After uploading a text file, the user can choose to translate the text file either into record or by the hardware device. If the user clicks on “Translate into Record” button; then the selected text file will be translated into voice record. But if the user clicks on “Translate by device” button; then a socket between the sender side (the application) and the receiver side (the hardware device) will be opened which establishes a connection. Then, the sending process begins sending the selected text file to the device.

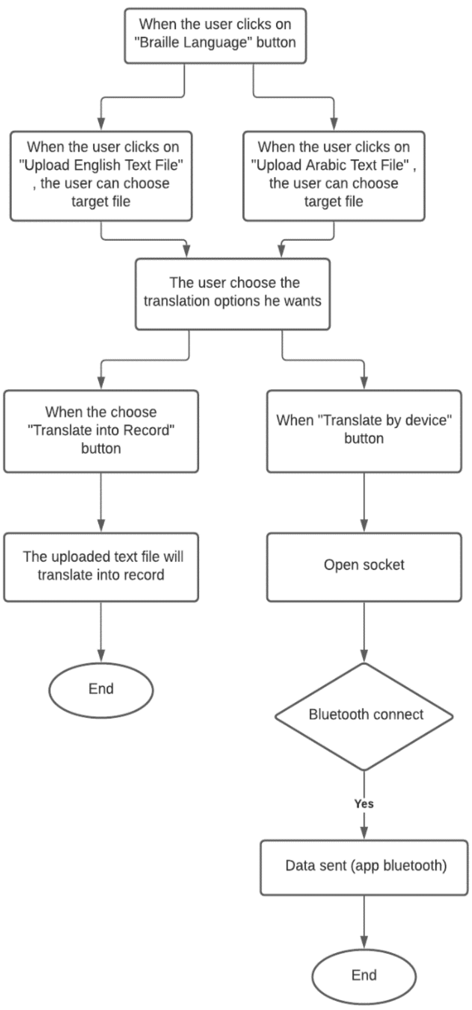

Figure 4 - Braille translator flow diagram

If the user clicks on the “to learn button”, either in Arabic or in English, another page will be opened to enable him/her to insert the needed text to translate.

The proposed Braille Language Translator (BLT) mobile application was simulated via Android virtual device (AVD) simulator. AVD is a simulator which allows the developer to define the characteristics of any Android device. The AVD simulator can be managed from an AVD manager which can be launched from the Android Studio.

The application is designed to be easy and simple for blind people to use because they will asked to click three buttons only which can be done with the help of TalkBack feature or somebody else. To send the text file to the hardware translator or to translate the uploaded text file into record, “Braille Language” button must be clicked as shown in Figure 5, where the screen in Figure 6 will be displayed. This screen allows the user to select any English or Arabic text file from the mobile storage to be translated.

Figure 5 – Main menu

Figure 6 - Upload Arabic or English text file

After the user chooses a certain Arabic or English text file, another page will automatically open which shows additional buttons as shown in Figure 7.

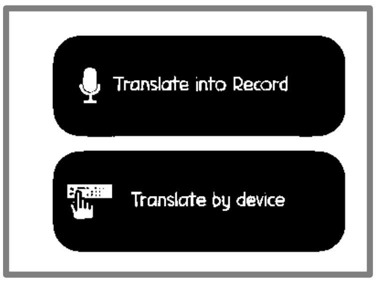

Figure 7 - Braille translation options

If the user chooses “Translate into Record” button, the uploaded text will be translated into voice record using the text to speech (TTS) feature of the Android operating system, whether the text is in Arabic or in English. This design enables the uneducated blind people to read text files by listening to their records. If the user chose “Translate by device”, the text file will be sent to the hardware device via Bluetooth which will perform Braille language translation.

The proposed system also allows any person to learn Braille language using the hardware device. To do this, when the user clicks on "To learn" in Figure 8, the screen in Figure 8 will be displayed. Then, the user can first enter the target text in the "Enter text" space, and press "Translate into Braille" button, then the entered text will be translated into Braille language by the hardware device.

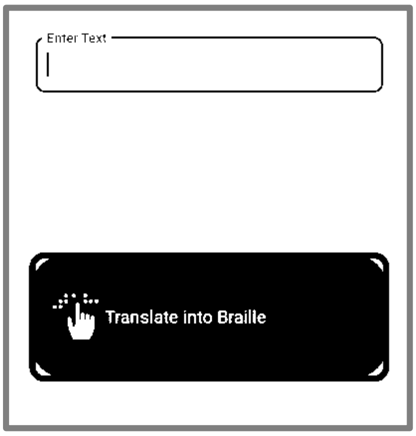

Figure 8 - Translate into Braille

A. *The Hardware Translator Design*

In this section, the hardware part will be explained in detail. The hardware part consists of: Arduino controller, Bluetooth module, Potentiometer, and Solenoids.

The Arduino is the main brain and controller of the whole system. It has the following main functions: 1) controls the Bluetooth to receive the data from the application, 2) map the text received from the application to the proper Braille character, 3) controls the solenoid motors to switch them ON and OFF to represent characters, and 4) control the speed of showing the words in Braille language with the help of the potentiometer.

The communication between the mobile application and the hardware device is done in Bluetooth because it consumes low power compared to other communication systems like radio or Wifi. The Bluetooth module is an external component used to connect smartphones, computers, and tablets to an Arduino board. It is designed for transparent wireless serial communication. In the proposed system, the Arduino needs to receive a text from the application via Bluetooth. To achieve that, a HC-06 Bluetooth module was programmed and installed.

As mentioned earlier, Braille language represents a character using six cells. In the proposed system, solenoid motors correspond to those tiny cells such that when the solenoid motor is ON, the bump is there, and when the solenoid is OFF, the bump is not existing. Solenoids have a very important role in this project; even though several technologies were considered before choosing Solenoids such as Servomotors, but eventually Solenoid was the best choice because it is reliable, gives linear motion, and works in ON/OFF mode rather than rotate in specific angles. Also, it is fast and resistant to errors.

To control the speed of displaying the words in Braille language on the Solenoid motors, a potentiometer is used. Effectively, the potentiometer is a variable resistor and a voltage divider. To control the potentiometer resistance, it has a knob that helps the user to control the resistance value manually. The potentiometer is connected to the Arduino as an Analog pin, so it works as a value sensor, and this value is mapped to speed value through a mapping function.

IV. Results

In this section, the results of the proposed system will be demonstrated along with the testing criteria that was followed.

A. *Application Testing*

Several test cases were used to verify any feature or functionality in any software application. In order to verify the proposed application functionalities, we must test Android availability on the devices and other functionalities that are implemented in the system.

As mentioned earlier, Talkback feature is very important when it comes to VI applications. Thus, it was very important to ensure that all buttons and pop-ups would support the Talkback feature and that the device would clearly speak each button's name out loud. All buttons were tested against the talkback feature, and they were read in voice. Therefore, the talkback feature is working fine.

Table 1 shows the time needed for the application to send the chosen text file according to its size to the hardware device. As Table 1 shows, the application proved sufficiency when it comes to delays, as the average delay needed was not that long (i.e., in seconds per file). Additionally, the application supports both ".txt" and ".pdf" files.

Table 1 - Transmission time for different file sizes

Text Size (KB)	Transmission Time (Sec)
0.5	1.5
1.5	4.34
2.5	5.2

B. *Hardware Testing*

As a first step of hardware testing, the code should be checked before constructing the actual circuit. This is because Solenoids are relatively expensive. Consequently, LEDs were connected instead of Solenoids as shown in Figure 9. They were mapped to represent what the Solenoids would do in the final circuit. For example, to raise the solenoid, we turned ON the LED. Specifically, we connected 48 LEDs to represent a word of up to 8 letters, 6 LED per letter. We started displaying the words on LEDs. The result was completely true. Controlling LEDs and Solenoid motors will have the same code (motor High is LED on, and motor Low is LED off). Therefore, the code was fully ported without any modification.

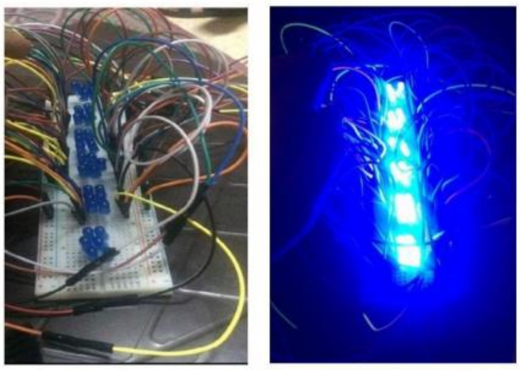

Figure 9 - LEDs connection

After making sure the Arduino code and other system components are correctly running and completely functional, the final circuit was constructed using Solenoids. Then, extensive tests were done on Arabic and English letters and words. The results were excellent, where the Braille language translation device is functioning 100% correct. We are showing a sample of the results in Table 2 and Table 3. In these tables, the output of the translator and its corresponding Braille is displayed for Arabic and English letters in sequence.

Table 2 - Sample of Arabic letters in Braille and on the translator

Arabic character	Braille Representation	Translator Representation
أ	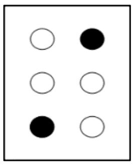	
ب	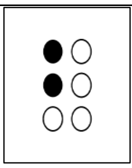	
ت	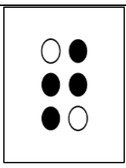	

Table 1 - Sample of English letters in Braille and on the translator

English Character	Braille Representation	Translator Representation
A	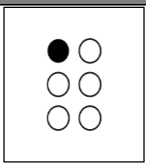	
B	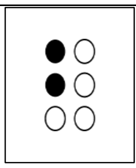	
C	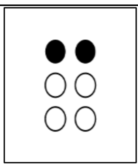	

A text file containing the Arabic word “مرحبا” (Merhaba) which means “Hi” in English was also sent and it was displayed correctly as shown in Figure 10.

Figure 10 - Arabic word "مرحبا" (means hello) in Braille

One challenge and limitation which exist in the Arduino programming language is that it does not support Arabic letters. We overcame this restriction by using an encoding technique to map the Arabic letters into non-English symbols that can be understood by Arduino. Therefore, when the user uploads an Arabic text to be translated into Braille, the application will read each character and replace it with symbols as shown in Table 4.

Table 4 - Coding Arabic letters into Braille

Arabic Letter	Encoded Symbol	Arabic Letter	Encoded Symbol
ا	0	ع	*
ب	1	غ	(
ت	2	ف	)
ث	3	ق	_
ج	4	ك	-
ح	5	ل	=
خ	6	م	+
د	7	ن	?
ذ	8	ه	[
ر	9	و	]
ز	~	ي	{
س	!	ء	}
ش	@	أ	|
ص	#	ؤ	:
ض	%	ئ	;
ط	^	إ	<
ظ	&	ى	>
		ة	,

C. Survey Results

To ascertain whether the proposed system achieves its objectives or not, we prepared a survey on the quality and effectiveness of this system. The survey checks whether the targeted users have benefited from the services provided by the application. The survey was distributed among 106 people including both blind and people who want to learn Braille. The survey questions and statistical results are shown in Table 5 below.

Table 5 - Braille translator survey results

Q1: Select age group:			
12-20 years	**21-30 years**	**Older than 30 years**	
30.2%	**43.4%**	**26.4%**	
Q2: The purpose of using the application?			
Blind	**To learn**		
5.7%	**94.3%**		
Q3: Have you ever used a phone app specifically designed for blind?			
Yes	**No**		
35.8%	**64.2%**		
Q4: Do you want to translate the text by audio record or device?			
Audio recording	**Device**		
64.2%	**35.8%**		
Q5: Do you think Braille's translated texts are understandable and clear?			
Clear	**Medium Clarity**	**Unclear**	**Unacceptable**
73.6%	**22.6%**	**3.8%**	**0%**
Q6: If you choose a translation by voice recording, is the recording clear and clear?			
Clear	**Medium Clarity**	**Unclear**	**Unacceptable**
86.8%	**11.3%**	**1.9%**	**0%**
Q7: In case you choose to translate through the device, is the device's translation of the text clear?			
Clear	**Medium Clarity**	**Unclear**	**Unacceptable**
77.4%	**20.8%**	**1.9%**	**0%**
Q8: If the app is used for the purpose of education, do you think it will enhance the educational process?			
Yes	**No**		
100%	**0%**		
Q9: Do you think this system could help communicate better in society?			
Yes	**No**		
100%	**0%**		

Based on the survey results, it is estimated that most of the people who fill the form (43.4%) are from the range of age between (20-30 years). Most of them (94.3%) want to learn Braille language. There were (64.2%) of them who have never seen an application specially designed for blind people, which means that the applications for blind people are not popular enough.

We asked the surveyed people to select the way which they wanted to translate the text file either by the hardware device or by voice, we found that (64.2%) prefer to translate the text file into a record, and (35.8%) prefer to translate it by the hardware device.

People who chose to translate the text file by the hardware device (73.6%) see that the translated text is clear and (22.6%) of them see that it is medium clarity, also people who prefer to translate the text into the record most of them (86.8%) have seen that the record is clear enough.

The result shows that most of them think that if we use our application in both communicating and education it will enhance each of them.

V. Conclusion

We have designed and built a system that allows a user to choose a text file from the user's mobile phone, establishes a Bluetooth connection with a hardware Braille translator and send the file to the translator. The Braille translator, when receives the file from the application, represents each character with its corresponding Braille letter, and displays the words clearly for the user with the help of 48 solenoid motors. Additionally, the application can translate the selected file into a voice record. The proposed system helps people who are willing to learn Braille language using a feature dedicated for that.

References

[1] Patil, S., Raut, A. and Jaiswal, S., E-VISION Eyes for Visually Impaired using Smartphone Implementing Object Detection.

[2] https://www.who.int/news-room/fact-sheets/detail/blindness-and-visual-impairment accessed 27/7/2022

[3] Chowdhury, D., Haider, M.Z., Sarkar, M., Refat, M., Datta, K. and Fattah, S.A., 2018. An intuitive approach to innovate a low cost Braille embosser. *International Journal of Instrumentation Technology*, *2*(1), pp.1-17.

[4] Kitchings, R.T., Antonacopoulos, A. and Drakopoulos, D., 1995. Analysis of scand braille documents. *Document Analysis Systems, Bd*, *14*, p.413.

[5] Padmavathi, S., Reddy, S.S. and Meenakshy, D., 2013. Conversion of braille to text in English, Hindi and Tamil languages. *arXiv preprint arXiv:1307.2997*.

[6] Abualkishik, A.M. and Omar, K., 2008. Quranic braille system. *International Journal of Computer and Information Engineering*, *2*(10), pp.3306-3312.

[7] Zhou, Z., Yang, Y. and Liu, H., 2022. A Braille Reading System Based on Electrotactile Display With Flexible Electrode Array. *IEEE/CAA Journal of Automatica Sinica*, *9*(4), pp.735-737.

[8] H. Kajimoto, N. Kawakami, T. Maeda, and S. Tachi, "Electro-tactile display with tactile primary color approach," Graduate School of Information and Technology, The University of Tokyo, Japan, 2004.

[9] Aranyanak, I., Reilly, R.G. A system for tracking braille readers using a Wii Remote and a refreshable braille display. *Behav Res* **45,** 216–228 (2013). https://doi.org/10.3758/s13428-012-0235-8

[10] Breidegard, B., Eriksson, Y., Fellenius, K., Jonsson, B., Holmqvist, K., & Stromqvist, S. (2008). Enlightened: The art of finger reading. *Studia Linguistica*, *62*, 249–260.

[11] Hughes, B. (2011). Movement kinematics of the braille-reading finger. *Journal of Visual Impairment and Blindness*, *105*, 370–381.

[12] Wei-Haas, M., 2017. This Device Translates Text To Braille in Real Time. *Smithsonian Magazine*.

[13] Shinali, M.C., Mnjokava, C. and Thinguri, R., 2014. Adaptation of the curriculum to suit children with visual impairment in integrated ECD centres in Kenya: a case of Narok sub-county.

Studying the Improvement of Production Processes at JOPETROL Lubricants Plant Using Lean Methodology

Mohammad D. AL-Tahat [1], and Hisham M. S. Alghwiri [2]* , Sa'ed Awni Musmar[3]

* *Corresponding authors: hisham.alghwiri@gmail.com; Tel.: +962 772155157.*

Abstract: The study aimed to implement the TOYOTA production system, and Lean approach to reduce the waste of filling volume of (5) liter production line during the processes in Jordan Petroleum Refinery, at the Lube Oil Plant from 2021 to 2022, by using the quality control and process improvement tools; Pareto chart, KIZEN, root-cause analysis, and five S, to identify the eight waste types. The results summarized revising the standard operation procedures for the system to contribute professional practices to minimize the volume of eight kinds of waste, and wide benefits from improving production processes, by controlling supply chains when applying the five S's in the raw materials warehouse and controlling the ordered according to need, and the speed of obtaining information due to understanding the documenting work procedures correctly, and avoid excess processes, transportation, motion, waiting, and overproduction wastes.

Keywords: Lean Production; TOYOTA production system, Five S System; Process Improvement.

1. Introduction

Global marketplaces today make it more important than ever for companies to stay competitive by working smarter, not harder. The state of technology today makes it possible to gather and analyze a variety of data efficiently, which helps organizations better understand their operations and pinpoint areas where they may make improvements.

In addition, the data are either not sufficiently examined or, worse, are incorrectly assessed, producing inaccurate findings (Subagyo et al., 2020). Since many organizations lack the skills necessary for data analysis, complex problem solutions frequently rely solely on intuition. More data-driven judgments are required.

Nowadays, with the economic inflation left by the political situation in the whole world, especially in the Middle East, and fears that are increasing after the Covid-19 pandemic passed, which can cause problems in the economy, such as poverty and unemployment, companies have become towards reducing operating costs in manufacturing processes and improving them continuously to maintain improvement and competition (Swanson and Santamaria, 2021).

The industrial sector looks forward to searching for the best waste-free manufacturing practices, maintaining the continuity of the facility's work within strategic plans, and advancing industry and products more, which hold for the industrial sector in Jordan to change the old work methodologies and replace them with approaches of entrepreneurship and sustainability for continuous improvement. Therefore, the Lean approach was applied for continuous improvement in the Jordan Petroleum Refinery Company - a lubricant plant for the manufacture of engine and industrial lubricants under the brand name (JOPETROL).

In the industrial sector, Lean tools have delivered more than 20 benefits. The top ten benefits mentioned are increased profitability and financial savings; minimized cost; reduced cycle time in production; improved key performance indicators; fewer defects; reduced machine breakdown time; reduced inventory; enhanced quality; and increased production capacity. Other soft benefits such as detecting different types of waste, improving employee morale toward inventive thinking, and lowering workplace accidents while applying the five S's of housekeeping procedures were highlighted in a few cases (Albliwi et al., 2015).

The current performance measures and Key Performance Indicators (KPIs) are satisfactory for the top management, the company is looking to improve the efficiency of its work, keeping with global technological improvements in the production and packaging of products, and keep the market share in Jordan due to decrease of lubricants products consumption because spread the electrical vehicles, seeking to improve the level of performance and support success.

The study aims to review the current state of the operations in the production sections and search for a solution to the observations and problems they face. The top management aspires to raise the level of factory performance and believes that the positive change to raise the performance level of the JOPETROL oil factory directly affects the efficiency of the entire plant, which leads to reducing operating costs and using resources better to increase profits and ensure the quality of products.

2. Materials and Methods

According to Krajewski et al. (2022), lean systems are "operational systems that optimize the value generated by each of a company's activities by eliminating waste and delays." The eight categories of waste are motion, defect, overproduction, waiting, underutilized resources, transportation, inventory, and over-processing. Lean systems' strategic features include process level consideration, supply chain level consideration, and the TOYOTA production system (TPS), which serves as an industry best practice example.

The strategic elements of lean systems include continuous improvement, just-in-time, pull-and-push workflow techniques, poka-yoke, the five (S) methodology, standard work, total predictive maintenance (TPM), heijunka, and jidoka. (TPS) reduced time and activity waste to achieve the best quality, lowest cost, and shortest lead time, as illustrated in Figure 1.

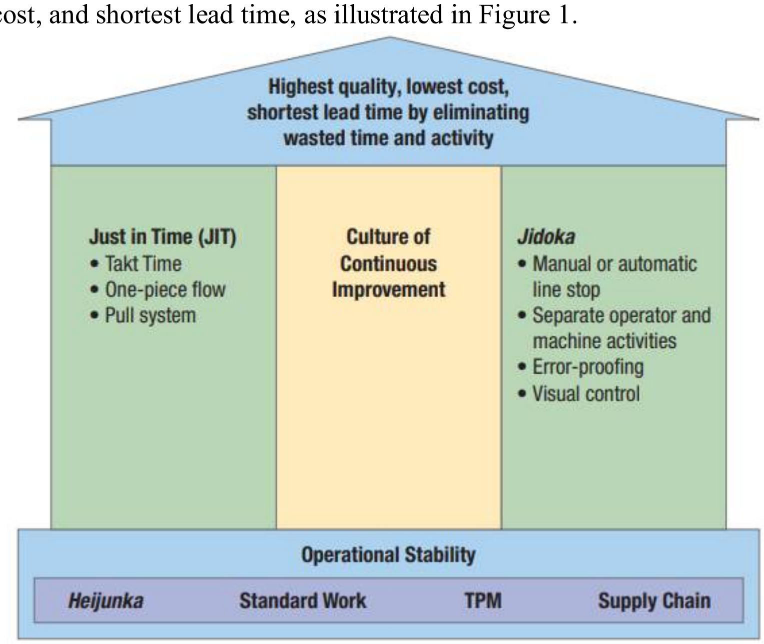

Figure 1: The house of TPS (Krajewski, et al., 2022).

The notion of lean production (LP) is a continual improvement approach to waste detection and reduction in the manufacturing process. When it comes to lean, it all boils down to doing more with less: fewer time, inventory, space, people, and money. LP seeks to eradicate waste from supplier networks, customer relations, product design, plant management, and all other areas of the production process (Jha and Kumar, 2020).

Table 1: The eight types of waste according to Krajewski, et al. (2022).

NO.	Waste	Definition
1	**Overproduction**	Producing an item before it is required makes it difficult to spot flaws and results in long lead times and extra inventory.
2	**Inappropriate Processing**	When lesser devices might suffice, expensive high-precision equipment is used. It leads to an overuse of costly capital assets. Smaller, more flexible equipment, well-maintained older machines, and combining process steps where possible all help to reduce waste associated with improper processing.
3	**Waiting**	Operators lose time due to unbalanced workstations because if one process step takes longer than the next, the operators will either wait idly or execute their jobs at a rate that makes it look like they have work to complete. Operators may also have to wait if a preceding process step fails, has quality concerns, is missing parts or information, or requires a lengthy switch.
4	**Transportation**	Extra product movement and material handling between operations, can result in product damage and deterioration without adding any consumer value.
5	**Motion**	Reaching, lifting, and walking requires unnecessary effort due to ergonomics. Jobs that require a lot of movement should be redesigned.
6	**Inventory**	Excess inventory hides difficulties on the shop floor, takes up space, raises lead times, and makes communication difficult. Overproduction and waiting result in work-in-progress inventory.
7	**Defects**	Quality faults lead to rework and scrap, as well as wasted expenses such as lost capacity, effort, higher inspection, and a loss of customer goodwill.
8	**Underutilization of Employees**	The organization's lack of knowledge of the capabilities and creativity of its employees, for a long time

The production order in manufacturing processes originates with the customer and travels through a number of stages before arriving at the production lines. The production order flow of the JOPETROL company is depicted in Figure 2.

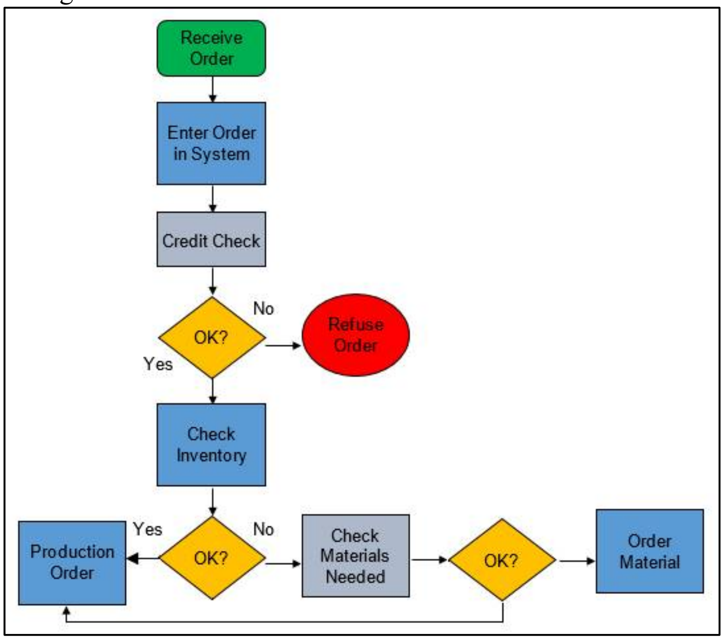

Figure 2: The flow chart from receiving customer's order to the actual production request in JOPETROL company

The blending department confirms that raw materials are available in the right quantities once the manufacturing request has reached the production departments. Everything is set up for the mixing procedure. In order to create the final product, which is subject to detection and sample procedures before consenting to store it or send it to the final packaging department, JOPETROL depends on the blending stage, in which numerous components are blended in precise quantities. The high-level process map for the JOPETROL corporation is displayed in Figure 3.

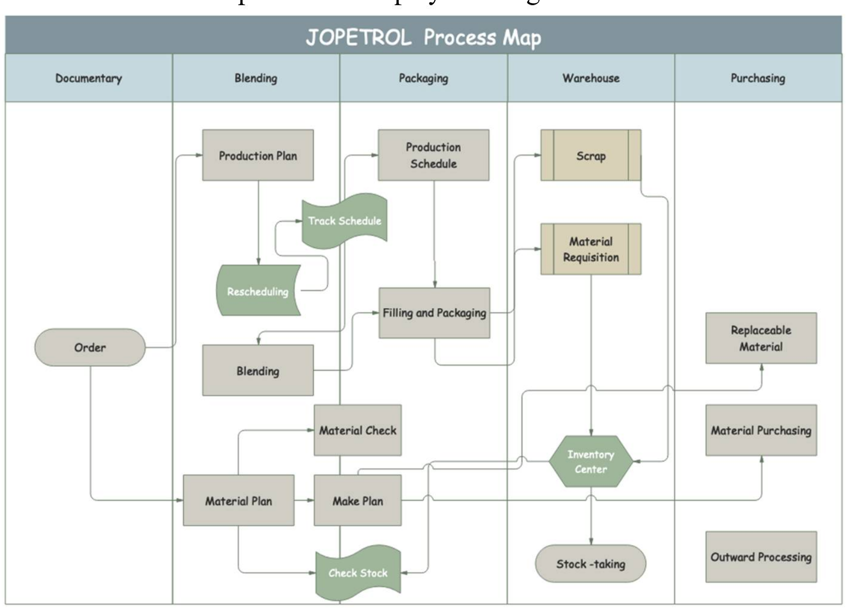

Figure 3: JOPETROL process map.

One of the most popular approaches in the services and industries is the lean approach. The goal of Lobo et al. (2018) was to examine how the oil and gas chain's operations use the Value Stream Mapping (VSM) tool. The review of published research in the Scopus database from 2012 to 2017 served as the study's foundation. The study concluded that there is a research gap because no particular framework was utilized in the studies that used the VSM tool.

The impacts of the variations in the filling machine volumes of (5) liters containers of oil product on the added value time and the total lead time were clarified by the researcher using the Current Value Stream Map (CVSM). Observations on the Thomason production line provided the data for the CVSM. This production line's CVSM is displayed in the figure below.

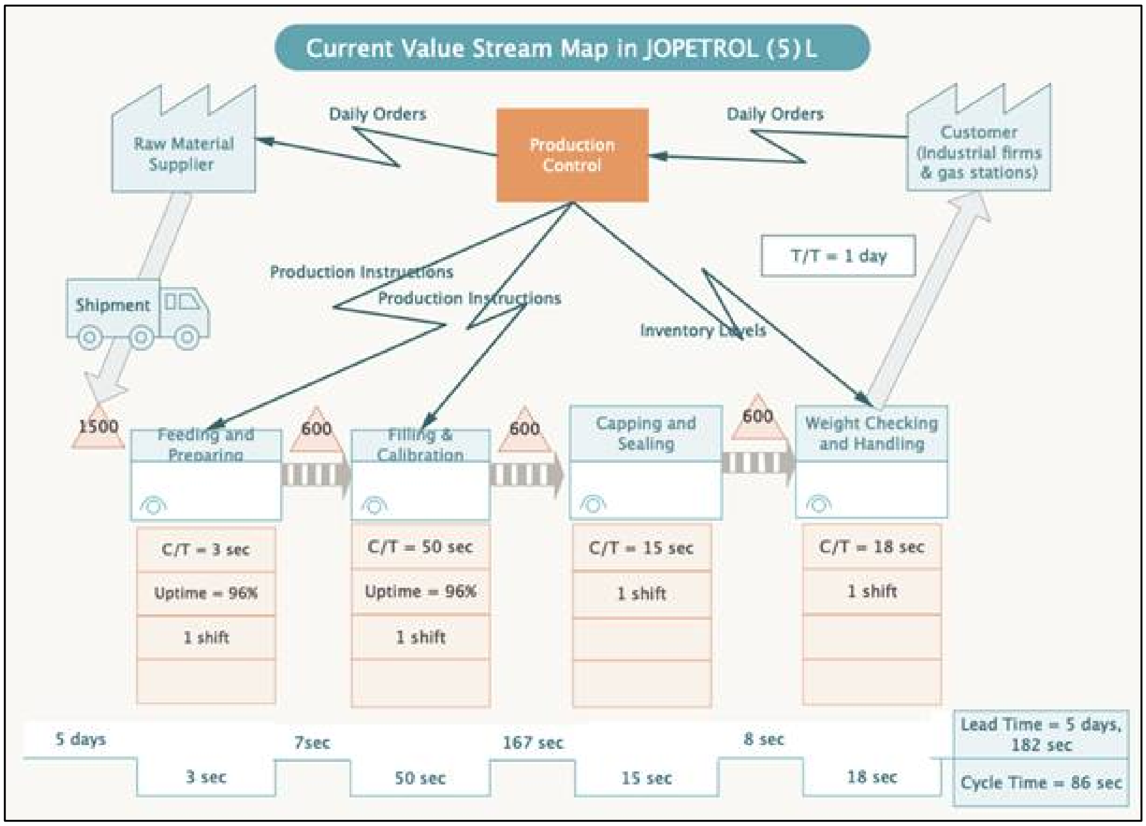

Figure 4: Current value stream map for filling machine (5) liters.

The CVSM shows that the total cycle time for the oil product equals 86 seconds (in the packaging department). The total lead time is 5 days and 182 seconds. The majority of the lead time in the production line (92%) or (167 seconds out of 182 seconds) is for the delay between actual filling and capping process which includes the manual calibration work due to the variability of oil volume. The containers exit the filling with a volume below or higher than the tolerance limits which requires corrective manual calibration. After ensuring that the volume of the oil containers is correct, the same operator manually inserts a cap on the container. The CVSM has been developed to illustrate the effect of the problem of volume variations for the oil product on the total lead time. It is clear from Figure 4 that the variability in filling volumes has increased the total lead time and specifically the time between filling and capping which reached 167 seconds.

An average of 5.5% of oil products were categorized as faults between February and June 2021, according to reports from JOPETROL's Quality Control Department and data connected to the quantities recorded in the production line. Between February and June 2021, the total output and number of flaws in the oil product are displayed in Figure 5.

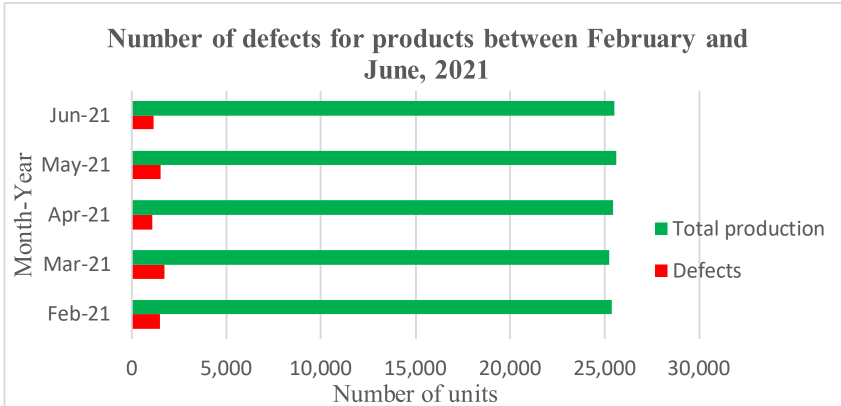

Figure 5: Total number of defects of the oil product between August and December 2021.

The primary reasons behind the variation in volume filling for oil products in the production line machine are found using a cause and effect diagram, commonly referred to as a fishbone diagram. This instrument breaks down the rationale into categories about people, things, processes, machinery, and the environment (Smith et al., 2011). One of the fundamental instruments in the measure phase that seeks to identify the primary causes of the variability issue is the fishbone.

Fishbone was created to identify the underlying causes through observations made on production lines, frequently asked questions, and interviews with management involved in the oil product. Initially, broad factors about the apparatus, humans, supplies, and techniques were determined. Each root cause, after that, was then categorized by the researcher under the relevant heading. The volume variability problem's fishbone diagram is displayed in Figure 6.

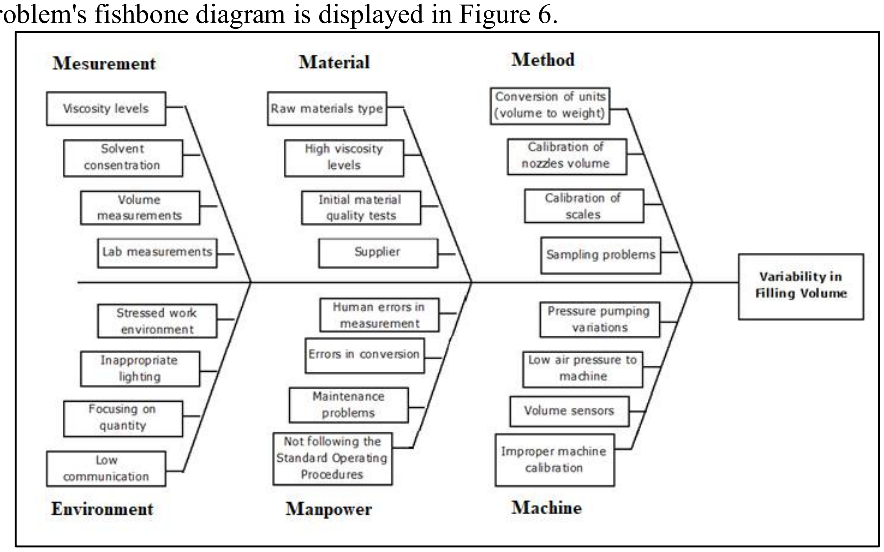

Figure 6: Cause and effect diagram for the volumes variability problem

The application of a fishbone diagram aids in the process of determining the underlying reasons of the issue of variation in the oil product's filling volumes. As seen in figure 6, six primary factors have been identified: measurement, materials, techniques, machinery, labor, and environment. Each category's underlying causes have been identified.

3. Results and Discussion

For oil products, the high and the low limit is 50 grams whereas the allowed tolerance by the Jordanian Standards is 75 grams for both high and low limits. Finally, a semi-automated handler is used to move the finished product to the pallet. Figure 7 shows the flow of processes in the production line for oil in JOPETROL company.

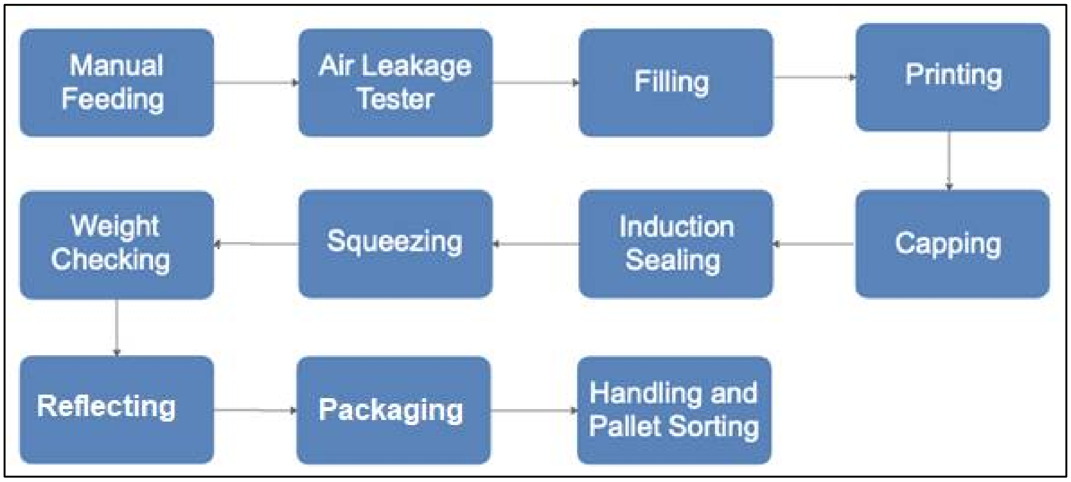

Figure 7: The processes in the production line

Upon approval of the filling of the products, an eleven-stage production line is prepared as shown in the above figure. The production line is an intersection of human and machine factors. The manufacturing process begins with feeding the bottles manually as shown in the above figure and goes through the process of leakage testing, filling, printing, capping, induction, squeezing, weight checking, reflecting, packaging, and ending with placing the product on the pallet by the worker.

The methods used are one of the main reasons for the emergence of the problem. There may be a defect in the conversion from unit volume to weight since the density of oil differs from the density of water. The calibration of the filling nozzles is one of the most prominent problems related to the methodology, and the calibration that is done on the scales periodically can cause this kind of problem.

Problems caused by the machine may be a result of miss-calibration, wrong in the machine's sensors, the presence of some electronics or mechanical problems, interruptions in the air pressure entering the machine, and the occurrence of rust or corrosion in the pipes. It is possible that the human being is one of the factors that cause the problem of differences in volume filling, for example, there may be problems in measuring, converting, or reading the scale.

These problems may arise as a result of the lack of regular maintenance or mistakes in manual calibration. Lack of training and non-compliance with operation procedures may lead to the variability of volume filling in the production line.

3.1. Statistics

3.1.1. The boxplot is a graph that identifies the outliers in the dataset which may support the conclusions of the previous descriptive statistics. Figure 8 shows the boxplot for the filling weight dataset between February and June 2021.

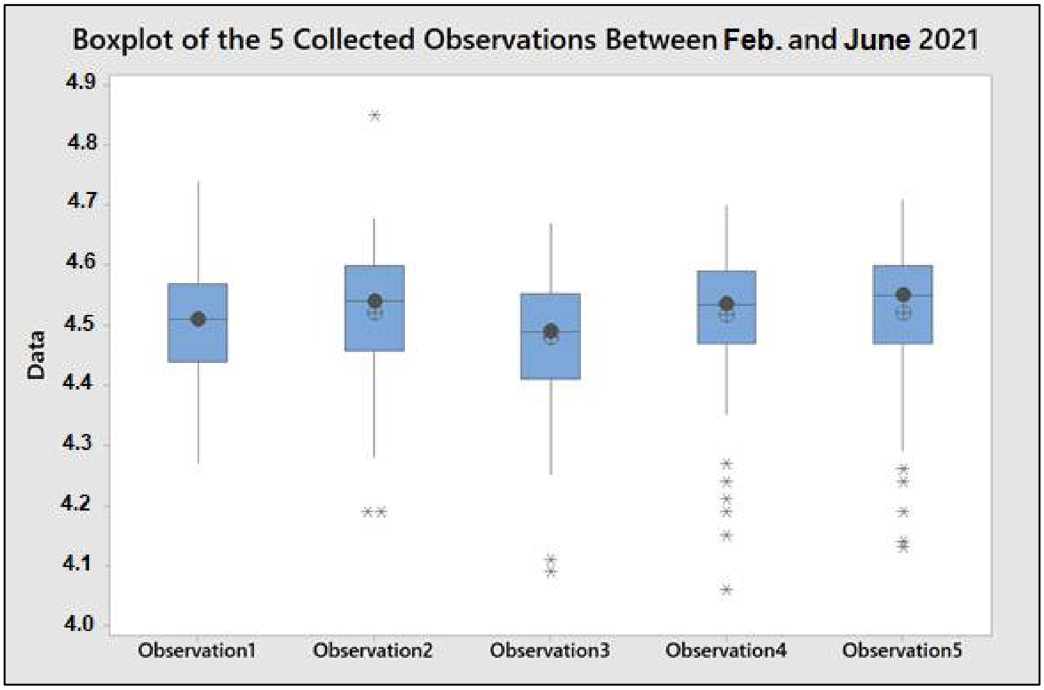

Figure 8: Boxplot for the filling weight dataset under analysis

3.1.2. During analysis all plots except the (for observation 1) have outliers. The results of the first observation have a mean value close to the target filling weight rate, the first observation is usually taken in the morning (at the beginning of work) which can be a reason for the result. The second observation indicates the presence of three outliers' points that usually have a cause. It appears that the average weight of the filling in the second observation is higher than the average weight of the first observation.

3.2. Control Charts page 56 theasis

Bulleted lists look like this:

- First bullet
- Second bullet
- Third bullet

Numbered lists can be added as follows:

1. First item
2. Second item
3. Third item

The text continues here.

3.2. Figures, Tables and Schemes

All figures and tables should be cited in the main text as Figure 1, Table 1, etc.

(a) **(b)**

Figure 1. This is a figure, Schemes follow the same formatting. If there are multiple panels, they should be listed as: (**a**) Description of what is contained in the first panel; (**b**) Description of what is contained in the second panel. Figures should be placed in the main text near to the first time they are cited. A caption on a single line should be centered.

Table 1. This is a table. Tables should be placed in the main text near to the first time they are cited.

Title 1	**Title 2**	**Title 3**
entry 1	data	data
entry 2	data	data [1]

[1] Tables may have a footer.

3.3. Formatting of Mathematical Components

This is an example of an equation:

$$a = 1, \tag{1}$$

the text following an equation need not be a new paragraph. Please punctuate equations as regular text.

Theorem-type environments (including propositions, lemmas, corollaries etc.) can be formatted as follows:

4. Conclusions

This section is not mandatory, but can be added to the manuscript if the discussion is unusually long or complex.

Funding: Please add: "This research received no external funding" or "This research was funded by NAME OF FUNDER, grant number XXX" and "The APC was funded by XXX". Check carefully that the details given are accurate and use the standard spelling of funding agency names at https://search.crossref.org/funding, any errors may affect your future funding.

Acknowledgments: In this section you can acknowledge any support given which is not covered by the author contribution or funding sections. This may include administrative and technical support, or donations in kind (e.g., materials used for experiments).

References

References must be numbered in order of appearance in the text (including citations in tables and legends) and listed individually at the end of the manuscript. We recommend preparing the references with a bibliography software package, such as EndNote, Reference Manager or Zotero to avoid typing mistakes and duplicated references. Include the digital object identifier (DOI) for all references where available.

Citations and References in Supplementary files are permitted provided that they also appear in the reference list here.

In the text, reference numbers should be placed in square brackets [ ], and placed before the punctuation; for example [1], [1–3] or [1,3]. For embedded citations in the text with pagination, use both parentheses and brackets to indicate the reference number and page numbers; for example [5] (p. 10), or [6] (pp. 101–105).

1. Author 1, A.B.; Author 2, C.D. Title of the article. *Abbreviated Journal Name* **Year**, *Volume*, page range.
2. Author 1, A.; Author 2, B. Title of the chapter. In *Book Title*, 2nd ed.; Editor 1, A., Editor 2, B., Eds.; Publisher: Publisher Location, Country, 2007; Volume 3, pp. 154–196.
3. Author 1, A.; Author 2, B. *Book Title*, 3rd ed.; Publisher: Publisher Location, Country, 2008; pp. 154–196.
4. Author 1, A.B.; Author 2, C. Title of Unpublished Work. *Abbreviated Journal Name* stage of publication
(under review; accepted; in press).
5. Author 1, A.B. (University, City, State, Country); Author 2, C. (Institute, City, State, Country). Personal communication, 2012.
6. Author 1, A.B.; Author 2, C.D.; Author 3, E.F. Title of Presentation. In Title of the Collected Work (if available), Proceedings of the Name of the Conference, Location of Conference, Country, Date of Conference; Editor 1, Editor 2, Eds. (if available); Publisher: City, Country, Year (if available); Abstract Number (optional), Pagination (optional).
7. Author 1, A.B. Title of Thesis. Level of Thesis, Degree-Granting University, Location of University, Date of Completion.
8. Title of Site. Available online: URL (accessed on Day Month Year).